

Eau Terre Environnement

Étude de la dynamique d'écoulement dans le système hydrothermal du rift d'Asal, République de Djibouti

Par

Abdek Hassan Aden

Thèse présenté(e) pour l'obtention du grade de
Philosophiae Doctor (Ph.D.)
en sciences de la Terre

Jury d'évaluation

Président du jury et
Examineur interne

Professeur Erwan Gloaguen
INRS

Examineur externe

Professeur Michel Chouteau
École Polytechnique de Montréal

Examineur externe

Professeur Philippe Pasquier
École Polytechnique de Montréal

Directeur de recherche

Professeur Jasmin Raymond
INRS

Codirecteur de recherche

Professeur Bernard Giroux
INRS

REMERCIEMENTS

Cette thèse a été réalisée avec l'aide et le soutien précieux de mes deux superviseurs : Jasmin Raymond et Bernard Giroux. Je voudrais les remercier tous les deux pour m'avoir encouragé, soutenu et motivé à devenir un chercheur indépendant tout au long de ces quatre dernières années. Ils m'ont aidé à comprendre en profondeur la physique des géosciences par des messages clés. Merci à Jasmin Raymond qui m'a initié et guidé aux avantages de l'utilisation de la modélisation numérique de l'écoulement multiphasique pour mieux comprendre les systèmes hydrothermaux en m'apprenant les rudiments de la modélisation numérique et en me motivant à devenir un géo-scientifique très curieux. Merci à Bernard Giroux qui m'a donné les directives pratiques de l'inversion géophysique, m'a introduit à la méthode magnétotellurique pour la caractérisation de la subsurface et m'a initié à l'importance des outils open-source.

Je tiens également à remercier grandement le Docteur Bernard Sanjuan qui a contribué à cette thèse notamment au premier article en partageant son expérience et ses connaissances scientifiques sur le rift d'Asal. Un grand merci également à Professeur Erwan Gloaguen pour avoir accepté d'examiner cette thèse de doctorat. Je tiens à remercier sincèrement le Professeur Michel Chouteau et le Professeur Philippe Pasquier d'avoir accepté d'évaluer et de juger cette thèse de doctorat.

Cette thèse n'aurait pas pu être achevée sans le soutien constant et l'aide de Gaetan Sakindi. Un grand merci à toi cher ami Gaetan Sakindi pour les informations et l'aide précieuses.

Merci à mes amis et à tous les collègues des équipes Géothermie et Géophysique de l'INRS.

Et bien sûr, des milliers et des millions de mercis à mon adorable famille. Un grand merci à tous.

Financement : Ce programme de doctorat a été financé principalement par la Banque Islamique de Développement (BID) et un complément de bourse de l'INRS à travers les crédits de bourse octroyés aux Professeurs Jasmin Raymond et Bernard Giroux.

“ We know accurately only when we know little; with knowledge, doubt increases “

Johann Wolfgang von Goethe

GENERAL ABSTRACT

Geophysical data inversion and hydrogeological modeling provide a better understanding of hydrothermal systems and the key factors that control fluid flow dynamics. The influence of permeability anisotropy within the geological units of the Asal rift, which is coveted for its geothermal resources, has not been evaluated to date. The objective of this PhD thesis is to better understand the hydrothermal system that constitutes the Asal rift by interpreting its deep geoelectric structures with the magnetotelluric method and by simulating the hydrothermal fluid movements by multiphase numerical modeling considering this permeability anisotropy. The joint interpretation of 1D inversion results of magnetotelluric (MT) data from 81 stations and temperature measurements of geothermal wells allowed us to infer the presence of a hydrothermal system in the north-east of the Asal rift. The 1D inversion results suggest that a major fault parallel to the rift axis (H fault) acts as a hydrogeological barrier separating the rift into two distinct resistivity zones. Multiphase numerical modeling of a section parallel to the rift axis indicates that the direction of flow of hydrothermal fluids is toward both Lake Asal and the Ghoubbet Sea and suggests that the deep hydrothermal circulation plays a dominant role in the distribution of fluid directions. Furthermore, dimensionality analysis of MT data from a section perpendicular to the rift axis suggests the presence of a north-east direction of electrical anisotropy for the upper crust and a north-south direction of electrical anisotropy for the lower crust and/or upper mantle. These electrical anisotropy directions would be parallel to the directions of plate motions that change or deviate according to the direction of the prevailing fields stresses. A 2D inversion model of electrical conductivity developed from a section perpendicular to the rift axis indicates the presence of a near-surface aquifer that covers a set of superimposed porous mediums that are associated with a large hydrothermal system. The latter overlies a potential magmatic system containing molten rocks and would be located under the vertical projection of the H fault. Multiphase numerical modeling perpendicular to the rift axis has highlighted two main zones of upward hydrothermal fluid movement. Results show that major faults (H and F) in the rift center would act primarily as hydrothermal fluid discharge zones while major faults on the rift margins (J and β faults) would act primarily as recharge zones. The hydrological behavior of the faults is modified when changing the number of faults considered in the conceptual model, but also according to the injection of magmatic fluid which seems to affect the hydrogeological behavior of the external faults (J and β faults) which under this last assumption may become fluid discharge zones. The horizontal hydraulic anisotropy considered in the simulations reproduces the thermal state observed in geothermal wells. The presence of a saddle point for fluid flow is suggested here according to which four directions of fluid flow can

exist in the Asal rift with rising fluids at the center. The area between the H and F faults are promising future drilling target for potential exploration of geothermal resources in the Asal rift.

RÉSUMÉ GÉNÉRAL

L'inversion des données géophysiques et la modélisation hydrogéologique permettent de mieux comprendre les systèmes hydrothermaux et les facteurs clés qui contrôlent la dynamique de circulation des fluides. L'influence de l'anisotropie de perméabilité au sein des unités géologiques du rift d'Asal convoité pour ses ressources géothermiques n'a jusqu'à maintenant pas été évaluée. L'objectif de cette thèse de doctorat est de mieux comprendre le système hydrothermal qui constitue le rift d'Asal en interprétant ses structures géo-électriques profondes avec la méthode magnétotellurique et en simulant les mouvements des fluides hydrothermaux par modélisation numérique multiphasique considérant cette anisotropie de perméabilité. L'interprétation conjointe des résultats d'inversion 1D des données magnétotelluriques (MT) provenant de 81 sondages et les mesures de températures des puits géothermiques ont permis d'inférer la présence d'un système hydrothermal au nord-est du rift d'Asal. Ces résultats d'inversion 1D suggèrent qu'une faille majeure parallèle à l'axe du rift (faille H) agirait comme une barrière hydrogéologique séparant le rift en deux zones de résistivité distinctes. La modélisation numérique multiphasique d'une section parallèle à l'axe du rift indique que la direction d'écoulement des fluides hydrothermaux est à la fois vers le Lac Asal et vers la mer de Ghoubbet et suggère que l'écoulement hydrothermal profond joue un rôle prépondérant sur la répartition des directions des fluides. De plus, l'analyse de la dimensionnalité des données MT d'une section perpendiculaire à l'axe du rift suggère la présence d'une direction nord-est d'anisotropie électrique pour la croûte supérieure et une direction nord-sud d'anisotropie électrique pour la croûte inférieure et/ou le manteau supérieur. Ces directions d'anisotropie électriques seraient parallèles aux directions des mouvements des plaques qui changent ou dévient selon la direction des contraintes dominantes. Un modèle d'inversion 2D de conductivité électrique développé à partir d'une section perpendiculaire à l'axe du rift indique la présence d'un aquifère proche de la surface qui couvre un ensemble de couches poreuses superposées et qui sont associées à un large système hydrothermal. Ce dernier recouvre un potentiel système magmatique contenant des roches en fusion et serait localisé sous la projection verticale de la faille H. La modélisation numérique multiphasique perpendiculaire à l'axe du rift a permis de mettre en lumière deux principales zones de fluides hydrothermaux avec mouvements ascendants. Les résultats montrent que les failles majeures (H et F) au centre du rift agiraient principalement comme zones de décharge du fluide hydrothermal alors que les failles majeures situées sur les marges du rift (failles J et β) agiraient principalement comme zones de recharge. Le comportement hydrologique des failles est modifié selon le nombre de failles considérées dans le modèle conceptuel, mais aussi selon l'injection de fluide magmatique qui semble affecter le comportement hydrogéologique des failles externes (J et β) qui sous cette hypothèse peuvent devenir des zones

de décharge du fluide. L'anisotropie hydraulique horizontale considérée dans les simulations permet de reproduire l'état thermique observé dans les puits géothermiques. La présence d'un point de selle pour l'écoulement des fluides est ici suggérée selon lequel quatre directions d'écoulement du fluide existeraient dans le rift d'Asal avec une remontée des fluides au centre. La zone entre les failles H et F serait la cible de choix pour des forages profonds lors d'éventuels travaux d'exploration des ressources géothermiques du rift d'Asal.

TABLE DES MATIÈRES

REMERCIEMENTS	3
RÉSUMÉ GÉNÉRAL	8
1. INTRODUCTION GÉNÉRALE	18
1.1. Mise en contexte	18
1.2. Problématique.....	19
1.3. Revue générale de la littérature	20
1.3.1. Le contexte géodynamique et géologique du rift d'Asal	20
1.3.2. Les manifestations thermales à la surface	21
1.3.3. L'inventaire des différentes études d'exploration géothermique	21
1.3.4. Les champs hydrothermaux.....	24
1.3.5. Objectifs et structure de la thèse.....	26
2. PREMIER ARTICLE: NEW INSIGHTS INTO HYDROTHERMAL FLUID CIRCULATION AFFECTED BY REGIONAL GROUNDWATER FLOW IN THE ASAL RIFT, REPUBLIC OF DJIBOUTI	29
2.1. Introduction	31
2.2. Geodynamic and Hydrogeological Context.....	32
2.3. Methods.....	36
2.3.1. Magnetotelluric Data Acquisition and Processing.....	37
2.3.2. Conceptual Model and Numerical Simulations	38
2.4. Results.....	43
2.4.1. 1D Electrical Resistivity Model	43
2.4.2. 2D Conceptual Model	43
2.4.3. Numerical Simulations	48
2.5. Discussion.....	52
2.6. Conclusions	58
3. DEUXIÈME ARTICLE: POTENTIAL HYDROTHERMAL SYSTEM INSIDE ANISOTROPIC MEDIA INFERRED FROM MAGNETOTELLURIC DATA ANALYSIS BENEATH ERODED ASAL RIFT, REPUBLIC OF DJIBOUTI	61
3.1. Introduction	63
3.2. Geological Background.....	64
3.3. Methods.....	66
3.3.1. Magnetotelluric data acquisition and processing	66
3.3.2. Dimensionality analysis of MT data	67

3.3.3.	Electrical anisotropy.....	70
3.3.4.	Static shift correction and strategy for 2D inversion models	70
3.4.	Results.....	71
3.4.1.	Dimensionality	72
3.4.2.	Electrical anisotropy.....	79
3.4.3.	2D Inversion models	83
3.5.	Discussion.....	88
3.5.1.	Geoelectric strike direction dependent of the periods.....	88
3.5.2.	Two main directions of anisotropy varying with depth	90
3.5.3.	Subsurface conductivity structure and associated interpretations	93
3.6.	Conclusions	97
4.	TROISIÈME ARTICLE: NUMERICAL MODELING OF HYDROTHERMAL SYSTEM CIRCULATION BENEATH ASAL RIFT, REPUBLIC OF DJIBOUTI.....	99
1.	Introduction	101
2.	Geodynamic background and geological context.....	102
3.	Methodology	105
3.1.	2D Conceptual model	105
3.2.	Hydraulic and thermal properties	106
3.3.	Boundary and initial conditions for fluid flow and heat transfer	108
4.1.	Fluid circulation.....	111
5.	Discussion.....	121
5.1.	Rock permeability	121
5.2.	Fault permeability and number of actives faults	122
5.3.	Permeability anisotropy and asymmetry.....	123
5.4.	Heat source and magmatic volatile release.....	124
5.5.	Fluid flow pattern and thermal state of the Asal hydrothermal system	126
5.6.	Implications for geothermal energy exploration	127
6.	Conclusions	128
5.	DISCUSSION GÉNÉRALE ET CONCLUSIONS.....	130
6.	References	137
	151
	Appendix A for Chapter 2	151
	Appendix B for Chapter 3	152
	Appendix C for Chapter 4	154

LISTES DES FIGURES

Fig.1.1. Modèle conceptuel des systèmes hydrothermaux volcaniques actives (Hedenquist and Lowenstern 1994).	25
Fig.1.2. Modèle conceptuel pour un fluide hydrothermal influence structurellement dans un segment de système de rift magmatique (Rowland and Sibson 2004).	26
Fig. 2.1. (a) Topographic map of Djibouti with the main geothermal potential sites. Red rectangle is Djibouti. (b) Structural map of the Asal Rift modified from (Stein et al. 1991). MT: magnetotelluric.....	35
Fig. 2.2. Temperatures measured at equilibrium in Asal geothermal wells.	36
Fig. 2.3. Comparison of observed and simulated electrical resistivity at MT sites along 2D MT profile in Fig. 2.1.	45
Fig. 2.4. Interpolation at selected depth of inverted electrical resistivity.....	47
Fig. 2.5. Above) Resistivity model and below) 2D conceptual model interpreted along 2D MT profile in Fig. 2.1.	48
Fig. 2.6. Simulated temperature and flow vectors at time equal to 100 000 years in scenario 1. The direction of flow is from the point to the end of the straight lines. The length of each line indicates the water flow vector magnitude, where $1.2 \text{ km} = 1e^{-5} \text{ g s}^{-1} \text{ cm}^{-2}$. (a) Results with a grid of 100×100 and initial time step of 0.001 year. (b) Results with a grid of 40×100 and initial time step of 0.01 year.	50
Fig. 2.7. Simulated temperature and flow vectors at time equal to 100 000 years. The direction of flow is from the point to the end of the straight lines. The length of each line indicates the water vector magnitude where $1.2 \text{ km} = 1e^{-5} \text{ g s}^{-1} \text{ cm}^{-2}$	51
Fig. 2.8. Comparison between the observed and simulated temperatures at well Asal 6.....	52
Fig.3.1. Topographic and main structural elements, (a) Djibouti and (b) Asal rift. Red rectangle is Djibouti; MT : Magnetotelluric (modified from Hassan Aden et al. 2021).....	65
Fig.3.2. Phase sensitive skew or regional skew.	73
Fig.3.3. Rose diagram of the orientation of the phase tensor strike for the stations along 2D profile (Fig.3.1) where each rose diagram corresponds to the mean strike estimated over all 14 MT stations along with the corresponding periods range.....	74
Fig.3.4. A) Strike angle from impedance invariants (B) strike angle from decomposition model. The major and minor axes of ellipse respectively correspond to the Φ_{\max} and Φ_{\min} of phase tensor ellipse defined in the precedent section 3.4.1.2.	75
Fig.3.5. Induction vectors with phase tensor ellipse.....	78

Fig.3.6. Phase difference between the two orthogonal components (TE and TM) phases. The dashed black triangles indicate the locations of MT stations.	79
Fig.3.7. Pseudo-section of phases tensor ellipses along 2D profile MT sites (Fig. 3.1).....	81
Fig.3.8. Magnitude of the real induction vectors.	83
Fig.3.9. Inversion models. A) TM resistivity model. B) Invariant resistivity model	86
Fig.3.10. Observed versus modeled apparent resistivity and phase data. A) TM model, B) Invariant model, C) TE model and D) TE-TM model.....	87
Fig.4.1. Topography and main structural elements of (a) Djibouti and (b) Asal rift. The red rectangle is Djibouti and MT abbreviates Magnetotelluric (modified from Hassan Aden et al. 2021).	103
Fig.4.2. 2D hydrothermal conceptual model interpreted along 2D profile (Fig.4.1). F-J, F-H, F- β indicate the emplacement of faults with their name, for example F-J is the fault J location. A6, A-4P (projected A4 well) and A5 are the geothermal wells (Fig.4.1). A5 is located at the same position of F-F and is denoted A5: 'A5/F-F'.	106
Fig.4.3. Simulated temperature and flow vectors at time 800 000 years, a) scenario 1 and b) scenario 2.	112
Fig.4.4. Simulated temperature and flow vectors, c) scenario 3 at time 230 000 years, and d) scenario 4 at time 800 000 years.	114
Fig.4.5. Simulated temperature and flow vectors at time 500 000 years, e) scenario 5 and f) scenario 6.	115
Fig.4.6. Simulated temperature and flow vectors at time 500 000 year, S5B) scenario 5B and S6B) scenario 6B.....	117
Fig.4.7. Simulated temperature and flow vectors, g) scenario 7 at time 200 000 years and h) scenario 8 at time 130 000 years.	118
Fig.4.8a. Comparison between the observed and simulated temperatures at well A4. The word S represent or means scenario.....	119
Fig.4.8b. Comparison between the observed and simulated temperatures at well A6. The word S represent or means scenario.....	120

LISTE DES TABLEAUX

Table 2.1. Hydraulic and thermal properties for simulation of the base case scenario.....	42
Table 4.1. Thermo-hydraulic properties for the base case (scenario 1).....	107
Table 4.2. Modification of each different scenario from the base case scenario 1.....	110

LISTE DES ÉQUATIONS

Equation 2.1.	37
Equation 2.2.	39
Equation 2.3.	39
Equation 3.1.	67
Equation 3.2.	68
Equation 3.3.	68

NOMENCLATURE

	Symbol	Unit
E_x, E_y	elements of electric field	$V\ m^{-1}$
g	gravitational constant	$m\ s^{-2}$
H_x, H_y	elements of magnetic field	T
h	specific enthalpy of the fluid phase	$J\ kg^{-1}$
h_r	specific enthalpy of the solid phase	$J\ kg^{-1}$
I	identity matrix	----
K_a	effective thermal conductivity	$W\ m^{-1}\ K^{-1}$
k	porous-medium permeability tensor	m^2
k_r	relative permeability	----
P	fluid pressure in the liquid phase	Pa
P_g	fluid pressure in the gas phase	Pa
q_{sf}	flow-rate intensity of a fluid-mass source	$kg\ s^{-1}\ m^{-3}$
q_{sh}	flow-rate intensity of an enthalpy source	$W\ m^{-3}$
S_w	saturation of liquid phase (water)	----
S_s	saturation of gas phase (steam or air)	----
T	temperature	$^{\circ}C$
t	time	s
Z	impedance tensor	$V\ A^{-1}$
$Z_{xx}, Z_{xy}, Z_{yx}, Z_{yy}$	elements of Z	$V\ A^{-1}$

Greek letters

β	skew angle	$^{\circ}$
∇	spatial gradient	m^{-1}
μ	viscosity of fluid	Pa s

ρ	fluid density	kg m^{-3}
ρ_r	density of the solid phase	kg m^{-3}
Φ	phase tensor angle	$^\circ$
φ	porosity	%

1. INTRODUCTION GÉNÉRALE

1.1. Mise en contexte

L'indépendance énergétique est un défi majeur pour le développement économique de la République de Djibouti à l'instar des nombreux pays africains puisque le taux d'électrification demeure relativement faible. L'énergie électrique est principalement fournie par l'interconnexion transfrontalière du réseau hydro-électrique de l'Éthiopie voisine qui répond à 94 % de la consommation nationale du Djibouti. Des combustibles fossiles importés des pays du Golfe Persique sont aussi utilisés localement à Djibouti pour la production d'électricité. Cependant, la politique de gestion des ressources hydrauliques communes et transfrontalières (exploitation du fleuve du Nil) entre l'Éthiopie, le Soudan et l'Égypte divise les autorités de ces trois pays. De plus, la volonté du gouvernement éthiopien de construire un grand barrage hydraulique en amont du fleuve Nil (Éthiopie) pourrait facilement causer une diminution du débit du fleuve en aval (Soudan et Egypte). Cette situation n'est pas très rassurante à moyen et à long terme dans la mesure où l'énergie électrique de Djibouti provient principalement de l'hydro-électricité éthiopienne gérée à partir d'une seule entente. La température moyenne et les précipitations totales annuelles dans la capitale qui regroupe à elle seule presque 70 % de la population totale, sont respectivement de 38.1 °C et de 122 mm. Les conditions climatiques ne sont pas très favorables au développement et à la production d'énergie hydro-électrique et/ou la biomasse. Avec une population majoritairement très jeune et une position géostratégique qui se situe au carrefour régional du détroit de Bab-el-Mandeb reliant la mer Rouge au golfe d'Aden dans l'océan Indien, dans lequel presque un tiers du trafic maritime mondial transite chaque année via le canal de suez, Djibouti est au carrefour de trois continents. Par conséquent, l'activité économique du pays est dépendante du secteur tertiaire. La construction d'infrastructures et d'installations portuaires modernes qui sont indispensables afin de dynamiser le secteur tertiaire ainsi que la diversification de l'économie qui pourrait créer plus d'emplois sont des objectifs de développement issue d'une volonté politique mais le coût de l'électricité élevé de 0.42 \$ CAD/kWh est un frein pour les atteindre rapidement. Par ailleurs, l'exploitation des ressources géothermiques locales permettrait la production continue d'électricité propre sans dépendre des variations climatiques (contrairement au solaire et à l'éolien).

Djibouti se situe sur la dépression de l'Afar, une région tectoniquement active où trois grandes structures majeures, soit la vallée du Grand Rift, la mer Rouge et le golfe d'Aden, sont en extension et forment ensemble la jonction triple d'Afar. Le pays disposerait d'un potentiel géothermique évalué à 1000 MW, dont 340 MW sont associés au rift d'Asal (Houssein and Axelsson 2010).

1.2. Problématique

Les caractéristiques géologiques du rift d'Asal-Ghoubbet, qui est un rift océanique émergé similaire à celui de l'Islande, ont attiré la curiosité des scientifiques et explorateurs. Entre 1975 et 1988, des études géologiques, géophysiques et géochimiques menées par le gouvernement djiboutien avec la collaboration scientifique franco-italienne ont guidé la réalisation de six forages géothermiques profonds. Ces forages ont confirmé l'existence d'un réservoir intermédiaire situé entre 400 et 700 m de profondeur avec une température maximale de 185 °C ainsi qu'un réservoir potentiel qualifié de profond qui serait localisé entre 1200 et 2000 m de profondeur avec une température maximale de 359 °C. Les essais de production se sont toutefois avérés inefficaces pour une production commerciale continue dans le temps pour deux raisons :

- Le fluide géothermique dans les puits forés au sud-ouest du rift (Asal 1 à 3 et 6) qui atteignent le réservoir profond a une salinité élevée d'environ 120 g/l et peut entraîner des problèmes d'entartage et de corrosion. Les solutions envisagées à l'époque de réalisation des forages et impliquant des inhibiteurs chimiques n'étaient pas satisfaisantes.
- Les puits forés au centre du rift (Asal 4 et 5), qui recoupent le réservoir potentiel profond, ont interceptés des formations peu perméables bien que des températures très élevées ont été enregistrées.

L'étude magnétotellurique menée par le gouvernement djiboutien en collaboration avec la société islandaise ISOR en 2008 a suggéré l'existence de trois champs géothermiques exploitables dans le rift d'Asal (Houssein et Axelsson, 2010). Un programme d'exploration de trois forages géothermiques profonds a été prévu dans la zone la plus prometteuse du rift (Caldera de Fiealé) mais la crise économique mondiale de l'époque (2008) a obligé le gouvernement Islandais à réduire ses dépenses et ses investissements à l'étranger. Le projet qui avait été abandonné est toutefois relancé depuis le 11 juillet 2018 par le gouvernement djiboutien. Les experts souhaitent trouver une température de 300 °C ou plus afin que le fluide hydrothermal permette l'extraction de la vapeur pour produire l'électricité. L'étude de préfaisabilité pour une éventuelle exploitation est toujours en cours et est supervisée par l'EDD (Electricité de Djibouti).

Composé essentiellement de roches volcaniques, le rift d'Asal-Ghoubbet est bordé au nord-est et au sud-ouest par des hauts plateaux de 400 à 1500 m d'altitude. La mesure du potentiel électrique naturel à la surface appelée la méthode de potentiel spontanée (SP), a montré l'existence de deux grandes zones d'anomalies positives (Mlynarski and Zlotnicki 2001). Ces anomalies sont dues à l'infiltration de l'eau de mer de Ghoubbet vers le lac Asal, réchauffé par le flux de chaleur terrestre élevé présent sous le rift. La présence d'une anomalie négative de largeur

de 1 km qui sépare les deux anomalies positives serait liée probablement au transfert rapide des eaux de mer froides via les failles de directions nord-ouest - sud-est (Mlynarski et Zlotnicki, 2001).

L'interprétation de la résistivité électrique dans le milieu volcanique est importante pour mieux identifier la présence des fluides. En effet, la résistivité électrique dans de tels milieux peut être influencée par un certain nombre des paramètres tels que par un gradient élevé de température, par un écoulement multiphasique, par des saumures hypersalines ou encore par la présence de minéraux d'altération riches en argile. Séparer les effets de tous ces phénomènes afin de déterminer avec précision la présence des eaux thermales est une tâche relativement complexe qui demande une interprétation adéquate.

L'activité magmatique et tectonique génère des déformations horizontale et verticales dans le rift d'Asal qui est une zone de divergence. Les études antérieures n'ont pas porté un grand intérêt sur la structure géo-électrique profonde du rift qui demeure inconnue. De plus, l'influence de la variation de conductivité électrique par rapport à la déformation horizontale et verticale des structures profondes dans un contexte de rift n'a pas été bien élucidée. En outre, l'activité sismique enregistrée dans la zone active du rift serait attribuée au dynamisme du système magmatique sous le rift, qui serait actuellement en état de sur pression (Dobre and Peltzer 2007; Dobre et al. 2007; Smittarello et al. 2016). Ces auteurs estiment que ce dynamisme conditionne la circulation des fluides dans le réseau de fractures par le biais d'un gradient de pression. Néanmoins, la nature exacte du fluide associé à ce dynamisme n'est pas bien déterminée. Des travaux de recherche apparaissent nécessaires pour bien comprendre la dynamique des fluides dans le système hydrothermal par le biais d'une analyse et interprétation conjointe des résultats de sondages magnétotelluriques et de modélisation numérique multiphasique de l'écoulement et du transfert de chaleur.

1.3. Revue générale de la littérature

Dans les rifts océaniques, la croûte est mince et dense et le manteau s'étend à faible profondeur de part et d'autre de la dorsale sous la région. Les anomalies magnétiques sont symétriques de part et d'autre de l'axe du rift et le flux géothermique est élevé (Hermance 1982). Les environnements tectoniques extensifs sont connus pour abriter d'importantes ressources géothermiques affectées par des écoulements de fluide à l'échelle régionale (Bellani et Gherardi, 2013).

1.3.1. Le contexte géodynamique et géologique du rift d'Asal

L'ouverture du segment de rift d'Asal date du Miocène et sa géologie est caractérisée par l'abondance des roches volcaniques formées dans un environnement d'extension et d'ouverture. Ayant une faible épaisseur et des laves basaltiques à la surface sous forme de séries des basaltes stratoides datant de 2 Ma, la croûte terrestre du rift d'Asal est considérée de type « transitionnel », soit un intermédiaire entre la croûte continentale et océanique naissante (Dobre 2004). Le rift d'Asal est long de 15 km et large de 14 km et est marqué par une activité tectonique et des failles extensives de directions principales nord-ouest - sud-est. Les formations et séries basaltiques dont l'âge varie entre 8 à 1 Ma illustrent une activité volcanique et tectonique récente dont la dernière éruption du volcan Ardoukoba date de 1978. La vitesse d'ouverture du rift a été estimée à 1.6 cm an⁻¹ (Vigny et al. 2007). L'activité volcanique et tectonique actuelle serait concentrée dans la partie centrale du rift émergée, caractérisée par un réseau de failles verticales et de fissures alors que les marges externes du rift sont caractérisées par des grandes failles normales.

Trois épisodes d'extension se sont produits dans le rift. Le premier est caractérisé par des émissions basaltiques de type Dalha abondants avec un effondrement, suivi d'un deuxième épisode volcano-tectonique calme avec des émissions de rhyolites et finalement un dernier épisode d'extension continue avec un important effondrement et des émissions de basaltes tholeitiques (Abdallah et al. 1979). La corrélation litho-stratigraphique des forages géothermiques profonds montre trois principaux types de formation qui se succèdent (Zan et al. 1990; Jalludin 2007). La série de basalte de Dalha qui date de 6-8 Ma est la plus ancienne et elle est recouverte par la série de basalte de stratoïde datant de 1-4 Ma. Depuis 800 000 ans, la plus jeune série d'Asal s'est déposée sur les marges externes du rift et dans le rift interne où elle est associée au volcanisme récent de l'axe du rift. L'activité volcanique continue et les mouvements tectoniques récents qui affectent la région depuis le quaternaire indiquent l'existence d'une source de chaleur magmatique peu profonde (Stieltjes et al. 1976).

1.3.2. Les manifestations thermales à la surface

Les sources thermales, les fumerolles et l'existence d'altération à la surface du rift d'Asal sont des indicateurs d'une activité volcanique et de la présence de ressources géothermiques en profondeur. Les sources chaudes sont abondantes dans l'est du lac Asal avec des températures variant de 30 à 80 °C (Sanjuan et al. 1990). Entre le lac Asal et la mer de Ghoubbet, seules les fumerolles peuvent être observées à la surface parce que le niveau hydrostatique est sous la surface topographique (Demange and Puvilland 1993).

1.3.3. L'inventaire des différentes études d'exploration géothermique

En 1970, le BRGM (Bureau de Recherches Géologiques et Minières) a lancé la première campagne d'exploration géothermique avec des études géophysiques, géologiques et géochimiques pour évaluer les ressources géothermiques dans la République de Djibouti, notamment dans le rift d'Asal. Un premier réseau géodésique a été installé en 1973 puis une première carte géologique a été publiée en 1975. Sur la base des résultats d'exploration de l'ensemble des études menées, onze forages exploratoires ont été réalisés dans le rift allant de 50 à 180 m de profondeur (Jalludin 2007). Les valeurs de gradient géothermique élevées de ces forages ont confirmé l'existence d'un potentiel géothermique et la présence de ressource à haute enthalpie (Stieltjes et al. 1976). La deuxième phase d'exploration géothermique a débuté en 1975 avec la réalisation des deux forages géothermiques profonds (Asal 1 et 2) par le BRGM. L'éruption volcanique du volcan Ardoukoba en 1978 a suscité un grand intérêt des scientifiques pour mieux comprendre le contexte géologique qui aura aidé à l'exploration géothermique. La compagnie italienne Aquater a exploré les ressources géothermiques de la plaine de Hanlé qui est située à 60 km au sud-ouest du rift d'Asal et a réalisé deux forages profonds. La température trouvée à 2000 m de profondeur était de 124°C et cela a provoqué le délaissement de cette plaine pour reconduire les recherches vers le rift d'Asal. De ce fait, Aquater réalisa quatre autres forages profonds dans le rift d'Asal (Asal 3 à 6).

Les sondages magnétotelluriques (MT) réalisés en 2008 par les équipes ISOR de Reykjavik Energy Iceland (REI) en collaboration avec le gouvernement djiboutien dans le rift d'Asal ont permis une première analyse de la structure géo-électrique profonde du rift. L'analyse et l'interprétation de la résistivité montre un ensemble de couches résistantes et conductrices qui se superposent depuis la surface jusqu'aux plus grandes profondeurs. La faible conductivité de la première couche superficielle est due à la nature sèche des roches présentes au-dessus de la nappe phréatique. La conductivité de la seconde couche ayant quelques centaines de mètres d'épaisseur est associée aux minéraux d'altération conducteurs (smectite et zéolithes) et cette analyse est en accord avec les logs des forages profonds (Sakindi 2015). La faible conductivité de la troisième couche résulte soit de la présence en quantité des minéraux résistants à haute température (chlorite et épidote) comme le montrent les données des forages, soit de la diminution de la porosité des roches. Finalement, des zones très conductrices plus profondes, s'étendant jusqu'à 5 km, ont été identifiées, comme dans la plupart des champs géothermiques à haute enthalpie, sans pour autant en connaître exactement la nature. En comparaison aux champs géothermiques d'Islande, ces zones très conductrices peuvent être caractérisées par des températures très élevées d'environ 700°C et correspondraient à des saumures d'origine magmatique piégées dans la zone de transition de l'état ductile à l'état fragile des roches (Árnason et al. 2010).

Les études géochimiques, décrivant notamment les corrélations entre éléments majeurs et éléments de traces, tel que strontium, lithium, bore et brome, ainsi les rapports isotopiques du strontium des échantillons prélevés dans les sources thermales du rift d'Asal, indiquent que la composition du fluide géothermique est affectée par une interaction de l'eau de mer avec le basalte et par une évaporation qui n'est pas significative (Sanjuan et al. 1990; Jalludin 2007, 2012). Cette interaction est plus ou moins importante selon la localisation des sources thermales et selon la proportion d'eau d'origine météorique et d'origine marine présente dans les roches. Néanmoins, la composition du fluide thermique de la source K1 qui est localisé au Sud du lac Asal, montre que l'eau continentale a interagi uniquement avec le basalte sans contact avec l'eau de mer. La circulation de l'eau de mer de Ghoubbet vers le lac Asal ne s'étendrait pas au-delà du lac Asal. De plus, la faible valeur du rapport bore/chlore mesurée dans les forages peut être associée à la présence d'une zone où la vapeur domine dans le système hydrothermal d'Asal (Sanjuan et al. 1990). Cette interprétation est en accord avec les résultats des forages. L'eau hautement salée du lac Asal contribue aussi à la recharge du réservoir géothermique mais cette contribution reste encore superficielle à nos jours dans la mesure où l'eau du lac Asal était une eau douce et que sa salinité a été acquise récemment (Gasse and Fontes 1989; Sanjuan et al. 1990). Cela contraint le temps de circulation des fluides dans le système hydrothermal profond de haute enthalpie. Les études géochimiques des échantillons de fluides prélevés dans les forages profonds montrent que l'eau de mer recharge le fluide géothermique des aquifères peu profonds du rift. La température d'équilibre calculée à partir de toutes les espèces réactives gazeuses, à part le H₂S, est très proche de celle mesurée au fond des forages Asal 3 et 6. Cette température correspond à celle du réservoir géothermique identifié et varie entre 250-265°C. Le lac Asal contient une eau de mer évaporée dont la teneur en CaSO₄ change en raison de la précipitation et l'eau géothermique profonde semble n'avoir aucun contact avec l'eau du lac Asal (D'Amore et al. 1998).

En 1979 puis en 1983, des équipes du BRGM ont réalisé des études gravimétriques pour déterminer la répartition de la densité des roches dans la région d'Asal (Jalludin 2007). Les anomalies positives sont associées aux roches les plus anciennes sur les marges externes du rift et dans la baie de Ghoubbet nord ainsi que dans la Caldera de Fiealé et au sud. Ces anomalies coïncident avec le volcanisme récent. L'anomalie positive identifiée dans la partie centrale du rift serait attribuée à une injection magmatique présente en profondeur (Jalludin 2007). Généralement, l'altération n'affecte pas significativement les roches denses. La faible anomalie gravimétrique dans la partie sud-ouest du rift est interprétée comme étant liée à la présence des hyaloclastites de faible densité qui se sont déposées depuis le Pléistocène et au début de l'Holocène durant la période où le rift était sous l'eau de mer (Jalludin, 2012.). Cette interprétation corrobore avec la lithologie identifiée dans les forages Asal 1, 2, 3 et 6 (Zan et al. 1990).

La présence d'une activité sismique qui est concentrée principalement au nord-est du rift avec une forte sismicité au-dessous de la zone de Caldera de Fiealé est due à une activité volcanique récente et deux principales zones de sismicité existent sous le rift d'Asal (Dobre 2004). Sous la zone de Caldera Fiealé, des séismes se produisent entre 1 et 4 km alors qu'au nord-est du rift, la sismicité est plus profonde et atteint jusqu'à 5 km (Dobre et al. 2007). L'observation des ondes S qui se propagent jusqu'à 5 km de profondeur et leur atténuation avec une vitesse minimale dans les roches qui sont partiellement fondues confirme l'absence d'une chambre magmatique (Dobre et al. 2007) qui serait localisée à 4 km de profondeur comme il a été suggéré par les études antérieures (Stieltjes et al. 1976; Abdallah et al. 1979; Van et al. 1981). En outre, la sismicité enregistrée serait plutôt associée à la variation du gradient de pression d'un fluide hydrothermal et/ou magmatique qu'à un mouvement tectonique des failles (Dobre and Peltzer 2007). La profondeur sismogénique montre la limite entre les roches cassantes ou fragiles dont la pression du magma sous-jacent provoque les mouvements horizontaux et verticaux, et les roches ductiles à température élevées. De plus, l'anomalie de basse vitesse des ondes P (V_p) est probablement due à la présence d'un fluide à dominance de vapeur ou de gaz piégés dans les pores des roches plutôt qu'à la saturation d'un fluide à dominance liquide (Dobre et al. 2007).

1.3.4. Les champs hydrothermaux

Dans les systèmes hydrothermaux à haute enthalpie, la circulation convective des eaux souterraines est contrôlée par la variation du gradient thermique lié aux intrusions magmatiques profondes. Le corps intrusif et/ou le magma est à l'origine de la source de chaleur, qui fournit un flux thermique conductif aux zones et roches environnantes. En raison du gradient de température élevé entre le corps intrusif et les roches environnantes, ces dernières se déforment et passent de l'état ductile à l'état fragile. Cette déformation des roches permet le développement des voies d'écoulement des fluides qui sont perméables. La différence entre le gradient de pression vertical hydrostatique élevé des eaux souterraines qui sont généralement froides et le gradient hydrostatique du fluide hydrothermal profond est à l'origine de la circulation hydrothermale, qui facilite la remontée des eaux réchauffées vers la surface (Fig.1.1). Si ces eaux sont très chaudes, lors de la remontée, le fluide hydrothermal se dépressurise jusqu'à une profondeur où la pression est égale à la pression de la saturation de vapeur. Par conséquent, à cette étape se produit la séparation de la phase de vapeur et la phase de liquide.

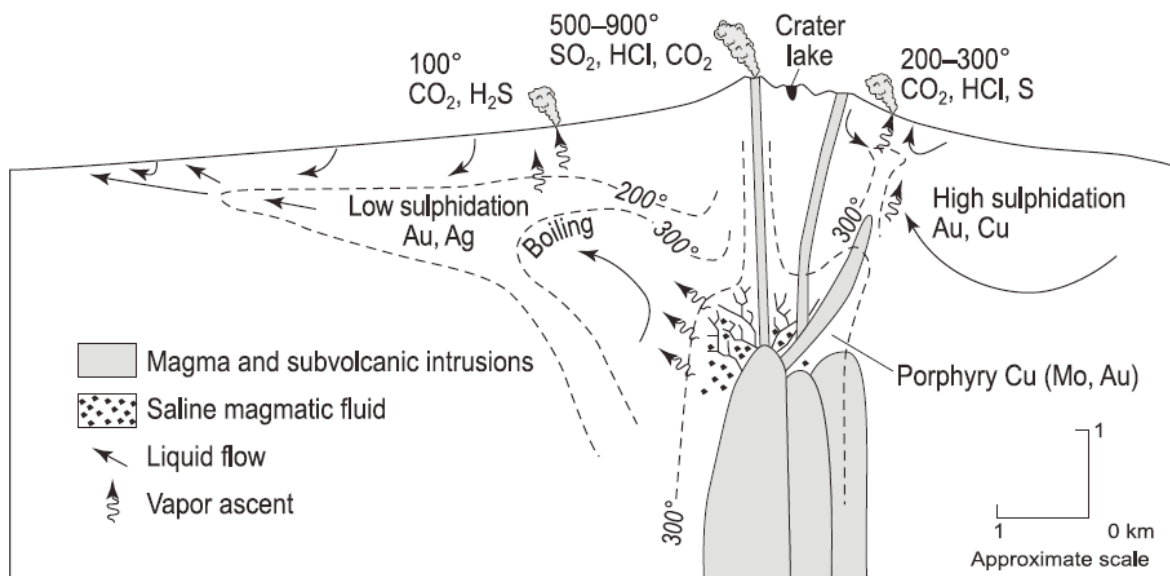


Fig.1.1. Modèle conceptuel des systèmes hydrothermaux volcaniques actifs (Hedenquist and Lowenstern 1994).

Dans les zones d'ébullition, le système hydrothermal présente des températures proches de celle de la courbe du point d'ébullition. Par ailleurs, dans le cas où le fluide est uniquement de l'eau pure, la saturation volumétrique de l'enthalpie, de la densité de la phase de vapeur et de la densité de la phase liquide, varient en fonction de l'enthalpie du fluide et les propriétés thermodynamiques de l'eau pure. Il est aussi important de noter que la profondeur maximale des zones d'ébullition et leur enthalpie varient également selon les propriétés thermodynamiques des fluides. À l'échelle mondiale, les systèmes dominés par le liquide ayant un gradient de pression avoisinant de la pression hydrostatique sont généralement plus fréquents par rapport aux systèmes dominés par la vapeur qui a un gradient de pression statique proche du gradient de la vapeur (Scott et al. 2016). L'importance des éléments structuraux contrôlant l'écoulement des fluides hydrothermaux dans une zone de rift tectonique extensive ont été étudiés par Rowland et Sibson (2004) et ils ont proposé un modèle conceptuel pour l'écoulement hydrothermal influencé par l'architecture structurale dans un système de rift magmatique. Ces auteurs ont conclu la coexistence d'un écoulement de fluide horizontal axial et le développement de panaches géothermiques (Fig.1.2).

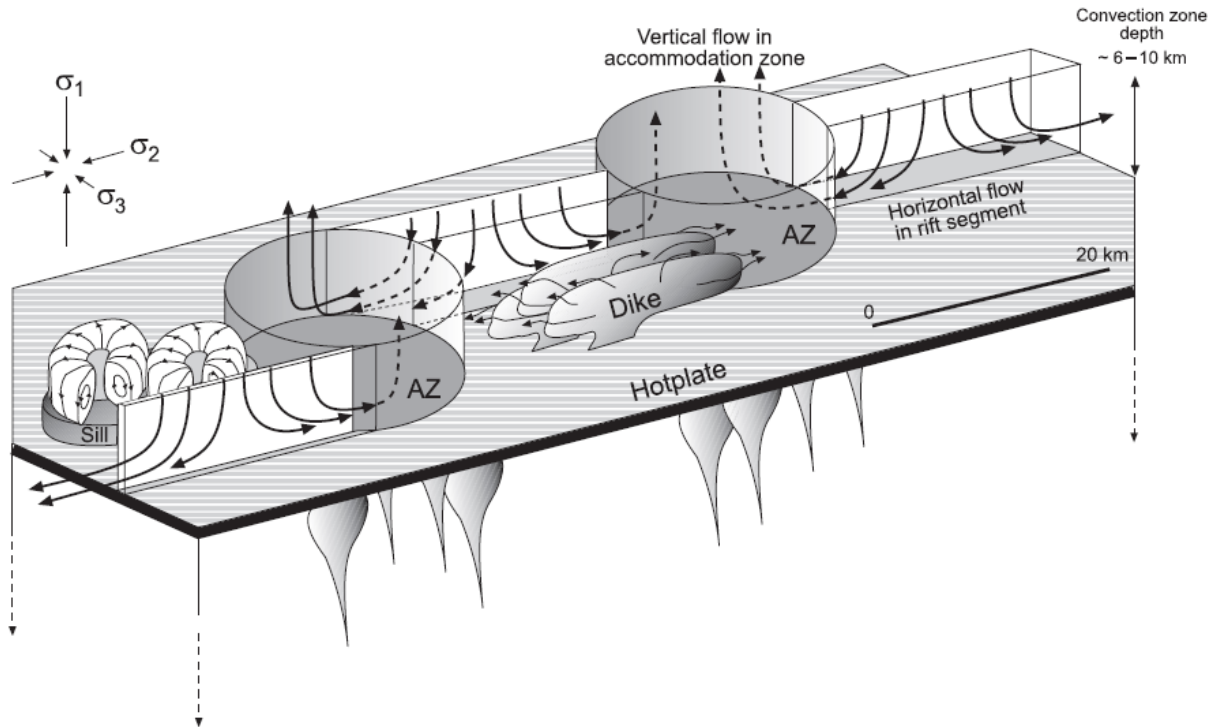


Fig.1.2. Modèle conceptuel structural pour la criculation du fluide hydrothermal dans un segment de système de rift magmatique (Rowland and Sibson 2004).

1.3.5. Objectifs et structure de la thèse

1.3.5.1. Objectifs

- Objectif global

L'objectif global des travaux scientifiques menés durant cette thèse de doctorat a été d'identifier et d'évaluer la dynamique des fluides hydrothermaux dans le contexte du rift d'Asal.

- Objectifs secondaires

Afin d'atteindre cet objectif principal, trois objectifs secondaires ont été étudiés à travers une série de trois articles. De ce fait, le premier article intitulé «<Nouvelles connaissances sur la circulation des fluides hydrothermaux affectés par l'écoulement régional des eaux souterraines dans le rift d'Asal, République de Djibouti>> a pour objectif de mieux comprendre l'influence et l'interaction de l'écoulement régional (de la mer de Ghoubbet au Lac Asal) sur la circulation hydrothermale profonde et l'importance des failles majeures sur la circulation régionale des fluides. Par conséquent, l'objectif du deuxième article intitulé «<Système hydrothermal potentiel dans un milieu anisotrope sous le rift érodé d'Asal, République de Djibouti>> est de proposer une analyse quantitative des structures géo-électrique profondes dans le but de présenter un modèle

conceptuel 2D du système hydrothermal. Et finalement, un troisième article intitulé <<Modélisation numérique de la circulation d'un système hydrothermal sous le rift d'Asal, République de Djibouti>> a été préparé. L'objectif est de mieux comprendre et d'évaluer quantitativement le rôle de l'anisotropie de la subsurface et des failles dans l'écoulement des fluides et le transport de chaleur. Ainsi des éléments de réponses complémentaires à la littérature antérieure sur la circulation des fluides hydrothermaux et de nouvelles connaissances sur la dynamique quantitative d'écoulement des fluides hydrothermaux sont proposés.

1.3.5.2. Aperçu de la méthodologie

Pour atteindre le but principal de l'article 1, un modèle 3D construit à partir des résultats d'inversion 1D de conductivité électrique a été développé. Par la suite, un modèle conceptuel hydrogéologique 2D parallèle à l'axe du rift a été interprété à partir d'une section de modèles 1D juxtaposés (le modèle 3D cité dans la phrase précédente). Ensuite, des simulations numériques multiphasiques de l'écoulement et du transfert de chaleur ont été réalisées avec le précédent modèle conceptuel hydrogéologique 2D parallèle à l'axe du rift. Pour essayer de parfaire notre connaissance sur la structure profonde du rift et mieux la définir sur la base de l'objectif général de l'article 2, deux approches complémentaires ont été développées. La première approche a permis de montrer l'existence d'une direction géo-électrique bien définie et à inférer la présence d'anisotropie électrique sous le rift d'Asal par une étude de la dimensionalité des données magnétotelluriques (MT) d'un profil 2D perpendiculaire à l'axe du rift comportant 14 stations. La seconde approche a été basée sur les conclusions de l'étude de la dimensionalité des données MT pour supposer la présence de structure régionale 2D. Cela a nécessité le développement d'un modèle 2D de conductivité électrique régionale afin d'analyser et interpréter les structures géologiques profondes du rift et notamment la présence d'un large système hydrothermal et un système magmatique. Dans l'optique de réaliser l'objectif principal et final de l'article 3 et mieux évaluer quantitativement la structure thermique et le fonctionnement du système hydrothermal, plusieurs scénarios de simulations numériques de l'écoulement multiphasique et du transfert de chaleurs ont été réalisés avec le modèle conceptuel 2D perpendiculaire à l'axe du rift qui a été développé dans l'article 2. Les principaux paramètres susceptibles d'affecter la circulation régionale des fluides hydrothermaux qui ont été étudiés et considérés dans les modèles sont les systèmes des failles majeurs (géométrie simplifiée), la perméabilité, l'anisotropie de la perméabilité et l'injection du fluide magmatique.

1.3.5.3. Structure de la thèse

Les principaux résultats de cette thèse permettent la compréhension des structures profondes du rift d'Asal afin d'inférer la distribution des températures du système hydrothermal et la dynamique de la circulation hydrothermale profonde. Les résultats de l'article 1 mettent en évidence la présence d'une faille majeure parallèle à l'axe du rift (faille H) qui agirait comme une barrière hydrogéologique où le nord-est du rift est plus conducteur et plus perméable que le sud-ouest. Cet article montre également que l'écoulement des fluides est à la fois vers la mer de Ghoubbet et vers le lac Asal, et que la circulation hydrothermale profonde et la tectonique affecte et conditionne les directions des écoulements souterrains. L'existence d'anisotropie électrique qui serait associée à la direction des contraintes dominantes des mouvements de trois plaques a été proposé dans l'article 2. De plus, l'interprétation des résultats obtenus dans l'article 2 illustrent la présence d'un large système hydrothermal au sein du rift et un potentiel réservoir/système magmatique qui serait localisé au centre du rift d'Asal. Les résultats des simulations numériques développés dans l'article 3 attestent que les principaux paramètres affectant la circulation hydrothermale régionale sont la perméabilité des unités géologiques et celle des failles, le nombre des failles actives et perméables, l'anisotropie de perméabilité des roches et l'injection du fluide magmatique. Même si tous ces paramètres peuvent jouer un rôle dans la quantification des mouvements horizontaux et verticaux des fluides, le rôle de l'anisotropie horizontale de la perméabilité est plus significatif et prépondérant dans le rift d'Asal. En effet, l'état thermique observé dans les puits géothermiques est reproduit sous l'hypothèse de l'anisotropie de perméabilité et serait représentatif des conditions thermiques actuelles du système hydrothermal d'Asal. En comparant les résultats de l'article 1 et l'article 3, l'existence d'un point de selle serait suggérée et les directions d'écoulements des fluides seraient vers le nord-est, nord-ouest, sud-ouest et sud-est sous le rift d'Asal.

2. PREMIER ARTICLE: NEW INSIGHTS INTO HYDROTHERMAL FLUID CIRCULATION AFFECTED BY REGIONAL GROUNDWATER FLOW IN THE ASAL RIFT, REPUBLIC OF DJIBOUTI

Nouvelles connaissances sur la circulation des fluides hydrothermaux influencée par l'écoulement régional des eaux souterraines dans le rift d'Asal, République de Djibouti

Autheurs:

Abdek Hassan¹, Jasmin Raymond¹, Bernard Giroux¹ and Bernard Sanjuan²

¹ Institut national de la recherche scientifique, 490 de la Couronne, Québec, QC G1K 9A9, Canada

² Bureau de recherches géologiques et minières, 3 Avenue Claude Guillemin, la CEDEX 02, 45062, Orléans, France

Titre de la revue :

Energies

22 Février 2021

<https://doi.org/10.3390/en14041166>

Abstract for Article 1

The Asal Rift hosts a lake located in a depression at 150 m below sea level, where recharge is influenced by regional groundwater flow interacting with the Ghoubbet Sea along the coast of Djibouti. This regional groundwater flow is believed to influence hydrothermal fluid circulation, which we aim to better understand in this study, having the objective of developing concepts for geothermal exploration in the area. To this end, magnetotelluric data acquired in the Asal Rift were processed and analyzed. 1D inversion models of electrical conductivity were interpolated for interpretation. These data were then used to build a 2D hydrogeological model, allowing multiphase flow and heat transfer simulations to be performed, considering the regional groundwater flow near the surface and the site topography, in order to confirm the preferred path of fluid flow. Geophysical data analysis indicates the presence of normal faults, notably the H fault, which may act as a conduit for the circulation of hydrothermal fluids and where the hanging wall can be a hydrogeological barrier within the hydrothermal system of the Asal Rift. The results from the 2D numerical flow and heat transfer modelling show the importance of groundwater flow responsible for thermal springs located at the periphery of Asal Lake. Reservoir temperature inferred by means of geothermometry ranging from 200 to 270 °C was shown to correspond to simulated temperature at potential reservoir depth. Moreover, simulated temperature between 600 and 1700 m depth is close to the temperature profile measured in the geothermal well Asal 6 of the area, with less than 20 °C difference. Simulations indicate that hydrothermal fluid circulation is likely influenced by the regional groundwater flow controlled by the topography and the major water bodies, the Ghoubbet Sea and Asal Lake, feeding buoyant fluids interacting with a deep magmatic source and where tectonic activity created normal faults offering a preferred path for fluid circulation.

2.1. Introduction

Extensive tectonic environments are known to host significant geothermal resources with large scale fluid flows (Bellani and Gherardi, 2013). The Asal Rift is located in the central part of the Republic of Djibouti in the Afar depression, a tectonically active region where three major structures, the Great Rift Valley, the Red Sea, and the Gulf of Aden, are in extension and together form the Afar Triple junction (Sanjuan et al. 1990; Mlynarski and Zlotnicki 2001), an emerged oceanic rift like that of Iceland. This region is a geological laboratory, where several scientific studies have been conducted to understand the processes and mechanisms related to the rifting phenomenon. The geological, geophysical, and geochemical studies carried out with French–Italian scientific collaboration between 1975 and 1988 guided the drilling of six deep geothermal exploration boreholes. A 3D geophysical model was built from passive seismic data (Dobre et al. 2007) and indicated that the dip of normal faults far from the rift axis is about 50°–60° in the NE–SW direction, whereas normal faults close to the rift axis are sub-vertical. The tectonic activity of these faults and the volcanism of the area, including the last eruption of the Ardoukoba volcano in 1978, are sources of seismic activity and drivers of hydrothermal fluid circulation. The results of seismic tomography indicate that most of the seismic events are located in the first 3 km below the surface (Dobre et al. 2007). Nevertheless, seismicity within the Asal Rift does not seem to be related to vertical fault planes, but rather to the opening of the fractures through a pressure gradient caused by hot fluids rising under the rift (Dobre and Peltzer 2007). This mechanism implies that the planes of normal faults begin to tilt away from the rift axis (Dobre et al. 2007) and could act as natural conduits allowing hydrothermal fluid circulation.

Asal Lake, which is 150 m below sea level, is affected by saline groundwater originating from the Ghoubbet sea located 12 km southeastward (Sanjuan et al. 1990; Mlynarski and Zlotnicki 2001). The role of normal faults in groundwater circulation in the Asal Rift appears important, especially for the circulation of groundwater interacting with Asal Lake, the Ghoubbet Sea, and the deep hydrothermal circulation of hot fluids, which has not been studied with modern physical models that can reproduce multiphase flow and heat transfer mechanisms. The present study is based on this hypothesis, for which work was conducted to better understand the importance of normal faults in the circulation of groundwater and hydrothermal fluids. This study was conducted in the context of geothermal exploration to provide fundamental knowledge analyzing the role of faults and considering the impact of groundwater flow between the Ghoubbet Sea and the Asal Lake. The work aims to define which faults can act as conduits or barriers to groundwater flow within the Asal Rift. To achieve this goal, electrical resistivity data were analyzed to build a conceptual model of the rift, followed by quantitative multiphase and heat transfer modelling of the hydrothermal system in 2D.

2.2. Geodynamic and Hydrogeological Context

The westward propagation of the Gulf of Aden at a velocity of 30 mm/year gave rise to the emergence of the Asal Rift (Mlynarski and Zlotnicki 2001). The opening of the Asal Rift segment dates from the Miocene and its geology is characterized by the abundance of volcanic rocks formed in an environment of extension and opening. This emerged rift segment is 15 km long and 14 km wide. The opening velocity is approximately 16 mm/year (Vigny et al. 2007) in the direction of N°45°E. The structure of this rift is characterized by a set of fracture networks and normal faults in the N130°E direction between Asal Lake and Ghoubbet Bay (Fig. 2.1). Having a thin thickness and basaltic lavas at the surface in the form of basalt series, the land crust of the Asal Rift is considered transitional, i.e., an intermediate between the continental and nascent oceanic crust (Dobre et al. 2007). The first effusive event linked to the birth of the rift dates from 853,000 to 315,000 years ago (Manighetti et al. 1998). Effusive magmatic activity continued in the northern part of the Asal Rift for 315,000 years and the southern part has been under seawater level for 326,000 years, with the formation of hyaloclastites (Manighetti et al. 1998). The activity of the central Fieale Caldera controlled the evolution of the rift between 326,000 and 100,000 years ago. Indeed, it allowed the injection of large volumes of basaltic lava into the interior floor that masked the previous faults (Pinzuti et al. 2010). Over the last 50,000 years, volcanic activity has decreased and the successive basaltic flow formations that make up Fieale Caldera have gradually been shifted by normal faults (Manighetti et al. 1998). The modern rift structure began about 40,000 to 30,000 years ago with the development of the faults with outer margins H and δ (Stein et al. 1991). From this period, the Fieale Caldera gradually extinguished and volcanic activity continued along the interior floor with small volcanic edifices and eruptive fissures (Manighetti et al. 1998). With the most recent magmato-tectonic event dated in November 1978, two earthquakes of magnitude 5 and 5.3 were recorded in the Asal-Ghoubbet Rift and, following this event, 0.7 m of vertical subsidence and 2 m of horizontal extension in the direction N°40 E occurred in the rift (Stein et al. 1991). A one-week eruption accompanied by basaltic fissures to the northwest of the rift gave rise in November 1978 to the axial volcanic chain and then to the eruption of the Ardoukoba volcano (Fig. 2.1). At present, most of the rift deformation is concentrated in its north-eastern part and around the edifice of the Fieale Caldera (Dobre and Peltzer 2007; Dobre et al. 2007; Vigny et al. 2007).

Thermal springs, fumaroles, and the existence of alteration on the surface of the Asal Rift are indicators of volcanic activity and the presence of potential geothermal resources at depth. Hot springs are abundant around the Asal Lake, especially in the eastern part, with temperatures ranging from 30 to 90 °C (Fig. 2.1). Between the Asal Lake and the Ghoubbet Sea, only fumaroles are observed at the surface because the hydrostatic level is below the topographic surface.

Chemical analyses of gases and determination of δD and $\delta^{18}O$ water stable isotopes of steam condensate have been performed for some of these fumaroles (Correia et al. 1983; Marini 1987). The results allowed estimating the source temperature at a depth higher than 230 °C, and even than 300 °C, in the studied Asal Rift. The isotopic data from the steam condensate suggest the existence of primary steam (likely separated at high temperature) originating from a deep heavy brine in this area (Marini 1987). The existence of this primary steam is in good agreement with the presence of a dominant vapor zone in the conceptual geothermal model proposed by BRGM.

Owing to the high salinity of Asal Lake and according to geochemical analyses, about 90% of the recharge of Asal Lake is believed to be due to infiltration and evaporation of Ghoubbet seawater (Sanjuan et al. 1990), depleted in sulfate because of $CaSO_4$ precipitation (D'Amore et al. 1998b). From a geochemical study of water sampled from the rift thermal springs, the authors of (Sanjuan et al. 1990) showed that the chemical and Sr isotope composition of these waters can be explained by variable seawater interaction with basaltic rocks at different temperatures and evaporation processes. Among thermal waters, those of the Manda group (Fig. 2.1) indicate the lowest seawater–basalt interaction and evaporation degree, suggesting that their source temperature is not high and their circulation rate is relatively significant between the Ghoubbet Sea and the Asal Lake. The thermal waters of the Eadkorar group, located in the northeastern part of the lake (Fig. 2.1), constituted by a mixing of seawater, Asal Lake water, and meteoric water, as suggested by the δD and $\delta^{18}O$ water stable isotopes (Fouillac et al. 1983; Awaleh et al. 2017), indicate the highest seawater–basalt interaction grade and seem to be the only direct leaks of a deep fluid discharged from a geothermal reservoir at 200–210 °C, as estimated by chemical geothermometry (Sanjuan et al. 1990a). The Korilii and Kalou thermal waters (Fig. 2.1) can result from a mixing between the deep geothermal water at 260–270 °C with seawater and Asal Lake water. The stable isotopes suggest the Korilii water is also diluted by meteoric waters (Fouillac et al. 1983; Awaleh et al. 2017). The Eounda Alifitta waters, located in the north-eastern most part of the lake (Fig. 2.1), indicate relatively low basalt–seawater interaction degrees and significant contributions of Asal Lake water. A contribution of meteoric water is also suggested by the water stable isotopes (Fouillac et al. 1983).

The geothermal wells A1, A3, and A6 are within a radius of 300 m (Fig. 2.1). These wells have confirmed the existence of an intermediate reservoir located between 300 and 700 m depth, with a maximum temperature of 185 °C, and another potentially deep reservoir located between 1200 and 2000 m depth, with a maximum temperature of 260–280 °C (Fig. 2.2). However, production tests proved to be ineffective for a continuous commercial geothermal energy production over time for two reasons:

The geothermal fluid produced in the wells drilled south-west of the rift (wells A1, A2, A3, and A6), which reached the deep reservoir, had a salinity ranging up to 120 g/l, and wells were subject to scaling and corrosion problems. The solutions considered at that time with chemical inhibitors were not satisfactory (Houssein and Axelsson 2010). The wells drilled in the center of the rift (wells A4 and A5) intercepted formations with low permeability, even if a higher temperature (345 and 360 °C, respectively) was measured at their base. The authors of (Sanjuan et al. 1990) showed that the deepest geothermal fluid from the wells is constituted by a mixing of seawater and Asal Lake water, interacting with basalt rocks at 260–270 °C. The water stable isotopes also suggest a contribution of meteoric water (Fouillac et al. 1983), similar to that observed in the Korilii, Eadkorar, and Eounda Alifitta thermal waters, which could mainly be the meteoric water that transits from Asal local rift to Sakalol-Harralol depression, located at the north-west of Asal Lake, or/and the meteoric water coming from the deep circulating regional aquifers (Marini 1987; Awaleh et al. 2017). The low boron concentration observed in these deep waters suggests the existence of a steam phase in the geothermal system (Sanjuan et al. 1990). The existence of such a zone with dominant vapor is in agreement with the conclusions relative to the gas and steam condensate data drawn by (Marini 1987) and the conceptual geothermal model proposed by BRGM (Correia et al. 1983; Gadalia and Traineau 1984). The equilibrium temperature calculated from all gaseous reactive species associated with these well waters, except H₂S, is very close to that measured at the bottom of the geothermal wells Asal 3 and Asal 6. This temperature corresponds to that of the identified geothermal reservoir and varies between 250 and 270 °C. According to (Sanjuan et al. 1990a), the geothermal waters located at a depth between 300 and 700 m correspond to a mixing between the deepest geothermal fluid and seawater. The circulation of hydrothermal fluids in the northern part of the rift is believed to happen deeper than in its southern part (Demange and Puvilland 1993).

Assuming the highly saline water of Asal Lake contributes to the recharge of the geothermal reservoir, this contribution is relatively recent as the water of Asal Lake was fresh and its salinity was recently acquired (Sanjuan et al. 1990a; Stein et al. 1991). This constrains the fluid circulation time in the deep hydrothermal system located between 1 and 3 km, having high enthalpy. The water level of Asal Lake 9 to 6 thousand years ago was 160 m above sea level. Over the past 5 to 6 thousand years, the level has declined by 310 m and the lake level is currently 150 m below sea level (Stein et al. 1991). This level has remained constant for the last centuries. Therefore, this suggests that, despite the intense evaporation from the arid climate of the area and the infiltration of water from the lake, this evaporation of lake water is compensated by a constant recharge mainly supplied by the Ghoubbet Sea.

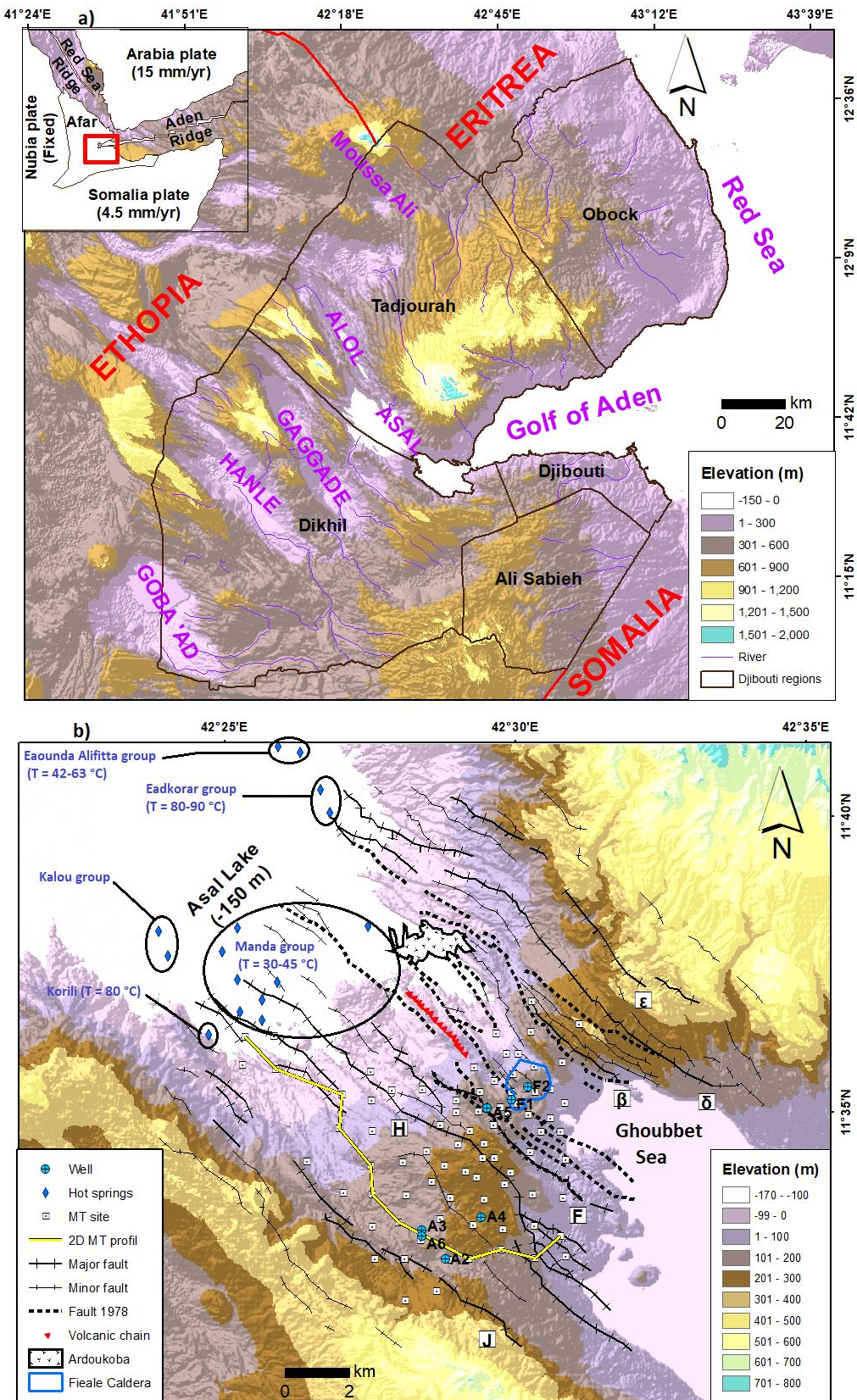


Fig. 2.1. (a) Topographic map of Djibouti with the main geothermal potential sites. Red rectangle is Djibouti. (b) Structural map of the Asal Rift modified from (Stein et al. 1991). MT: magnetotelluric.

The Asal 2 and Asal 3 wells are believed to penetrate the potential deep reservoir unit, but Asal 2 well was non-productive, although a temperature of 230 °C was measured at a depth of 923 m, while the Asal 3 and Asal 6 (located with a distance of about 300 m) were producers with permeable zones at a depth of 1030 m (Fig. 2.2). The fluid produced was hyper saline and essentially composed of liquid at 260° C (Houssein and Axelsson 2010).

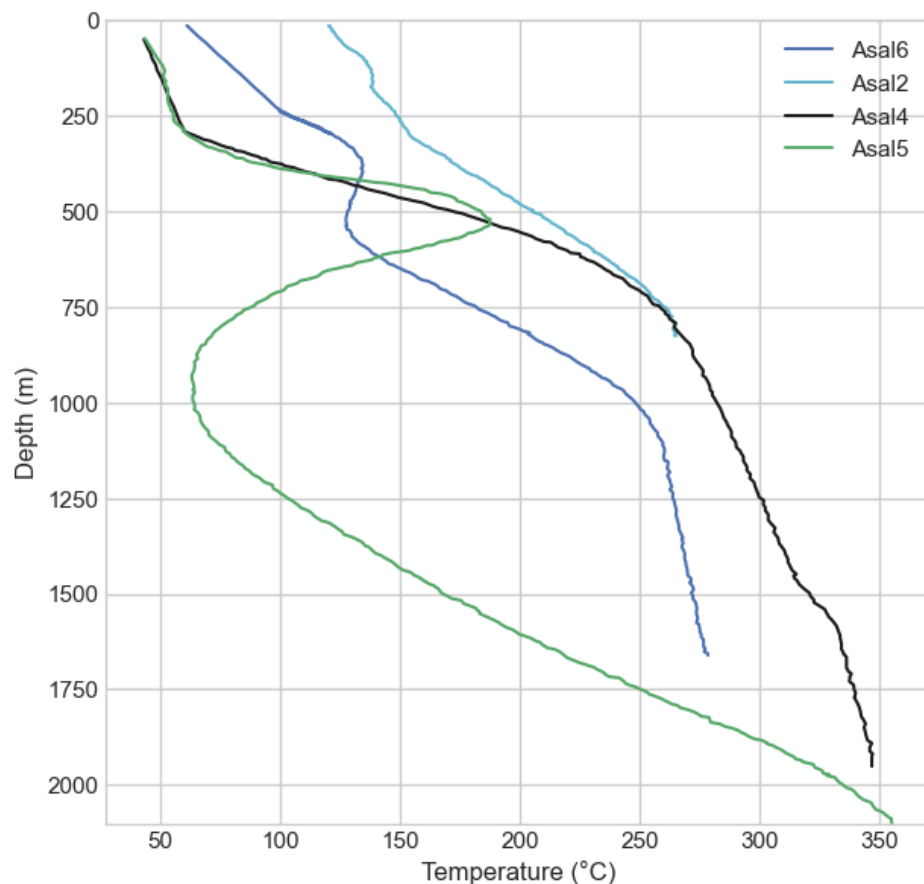


Fig. 2.2. Temperatures measured at equilibrium in Asal geothermal wells.

2.3. Methods

An electrical resistivity model deduced from magnetotelluric surveys was used in this study to better understand the circulation of seawater through normal rift faults. Using the geoelectrical model, a 2D hydrogeological model was developed for numerically simulating multiphase flow and heat transfer, in order to better understand and quantify the flow dynamics and the development of possible hydrothermal reservoirs.

To better understand the role of seawater and the origin of thermal springs at the periphery of the Asal Lake, the 2D numerical model of coupled and multiphase flow and heat transfer was

developed with the HYDROTHERM software provided by USGS (Hayba and Ingebritsen 1997; Kipp et al. 2008).

2.3.1. Magnetotelluric Data Acquisition and Processing

Generally, the presence of fluids in porous rocks and their interconnections, the types of minerals, and the temperature and pressure in the rocks contribute to the variation of electrical resistivity. Hydrothermal fluids and the existence of a layer of clay that acts as a cap rock present on the roof of a hydrothermal reservoir are usually identified as highly conductive areas, while, on the other hand, gas reservoirs and cooled magma are identified as less conductive areas (Yamaya et al. 2013).

Between 2007 and 2008, a survey including 81 magnetotelluric (MT) stations was carried out in the Asal Rift by the Icelandic company ISOR (Houssein and Axelsson 2010). The geographical distribution of the MT stations, which are roughly 1 km apart, covers a large part of the Asal Rift (Fig. 2.1). The instrument used to record the data was a Phoenix MTU-5 system and has the ability to record the temporal variation of the three components of the magnetic field (H_x , H_y , and H_z) and the two components of the telluric field (E_x and E_y). A reference station, located 10 km from the study area, was used to correct and reduce the local noise of the MT signals (Simpson and Bahr 2005). The data collection time was 48 h. For each site, time series were converted from time domain to frequency domain impedance tensor (Sakindi 2015). The frequency range of the data varies from 12.9×10^{-6} Hz to 400 Hz and corresponds approximately to a depth of investigation of the MT signal of more than 12 km inside the earth.

In this study, a 1D inversion of each station of the MT data was achieved. The apparent resistivity of the squared sum of the components of the invariant impedance (Szarka and Menvielle 1997) was inverted using the Occam algorithm (Constable et al. 1987). This impedance is expressed as follows:

$$Z_{SSQ} = \sqrt{\frac{Z_{xx}^2 + Z_{xy}^2 + Z_{yx}^2 + Z_{yy}^2}{2}} \quad (2.1)$$

where Z_{xx} , Z_{xy} , Z_{yx} , and Z_{yy} are the elements of the impedance tensor Z . Generally, the invariant determinant model is used, but, recently, (Rung-Arunwan et al. 2016, 2017) have shown that the determinant model is affected by galvanic distortion at depth. These authors argue that this model tends to reveal more conductive geological structures in the presence of distortion. Another invariant type of model named SSQ (sum of squared elements) is used because it is less affected

by the distortion and more appropriate to obtain a first representative approximation of the regional electrical resistivity (Rung-Arunwan et al. 2016, 2017).

In this study, an uncertainty of 10% apparent resistivity was assigned for most soundings, except seven with up to 20% uncertainty. The signal in the so-called dead-band, which corresponds to the 5 to 20 s period interval, was low and the resulting uncertainty higher. Moreover, the uncertainty assigned for the phase was 2.5°. The number of layers is 100 and the initial starting model has an electrical resistivity of 100 Ω .m. With this approach, an electrical resistivity model was developed, where data from all sites were interpolated and interpreted to infer concepts about underground fluid flow. The inversion results of an electrical conductivity model are presented in Section 4 below, helping to evaluate the role of the Asal Rift in groundwater circulation interacting with deep hydrothermal fluids and to delineate the presence of a hydrothermal system located at a depth between 1.2 and 2 km.

2.3.2. Conceptual Model and Numerical Simulations

High enthalpy geothermal resources required to generate electricity are generally found in areas where magma is introduced into the shallow crust (<10 km) and hydrothermal convection takes place over intrusive hot bodies. For a convective-type geothermal system such as the Asal Rift, the most appropriate conceptual model consists of the following elements (Spichak and Manzella 2009). A deep magmatic intrusion that is covered by a host rock. The latter hosts permeable reservoir formations that are covered by a cap rock close to the surface. Based on the structure of this type of geothermal system and the results of the geothermal wells data (Fig. 2.2), a conceptual model of the Asal Rift was set up, helping to approximate the thickness of the seawater intrusion towards Asal Lake. The 2D conceptual model used to define the geometry of the numerical model was based on an interpreted resistivity section inferred from the 1D electrical resistivity model developed in this study. This 2D section is parallel to the rift axis (Fig. 2.1) and was chosen because of the presence of productive geothermal wells (Asal 3 and Asal 6) along this section, and is parallel to the believed direction of regional groundwater flow. The temperature profile of the Asal 6 well was used to calibrate the numerical model.

2.3.2.1. Multiphase Flow and Heat Transport

Simulation of multiphase flow and heat transport is challenging because it is difficult to consider the critical point to set the appropriate thermodynamic state of the fluid in two phases. The pressure–enthalpy formulation that defines the thermodynamic state of the fluid in two phases can be used to avoid this problem, which was done in the HYDROTHERM code (Sanford 2005).

The governing equations used in the HYDROTHERM code are expressions of mass and energy conservation formulated in terms of pressure and enthalpy. As no potentiometric-head function exists for density fields that depend on temperature, pressure is chosen as the dependent variable for fluid flow. All pressures are expressed as absolute and the water-component flow equation is based on the conservation of water mass in a volume element, coupled with Darcy's law for multiphase flow through a porous medium (Kipp et al. 2008):

$$\frac{\partial}{\partial t} [\varphi(\rho_w S_w + \rho_s S_s)] - \nabla \cdot \frac{k k_{rw} \rho_{rw}}{\mu_w} [\nabla P + \rho_w g] - \nabla \cdot \frac{k k_{rs} \rho_{rs}}{\mu_s} [\nabla P_g + \rho_s g] - q_{sf} = 0 \quad (2.2)$$

where φ is the porosity (dimensionless), ρ is the fluid density (kg m^{-3}), S_w is the saturation of liquid phase (water) and S_s is the saturation of the gas phase (steam or air; dimensionless), k is the porous-medium permeability tensor (m^2), k_r is the relative permeability (dimensionless), μ is the viscosity of fluid (Pa s), P is the fluid pressure in the liquid phase (Pa), P_g is the fluid pressure in the gas phase (Pa), g is the gravitational constant (m s^{-2}), q_{sf} is the flow-rate intensity of a fluid-mass source (positive into the region; $\text{kg s}^{-1} \text{m}^{-3}$), t is the time (s), and ∇ is the spatial gradient (m^{-1}). The phase subscripts w and s refer to water (liquid phase) and steam (gas phase or vapor phase), respectively. In the single-component (water) zone, $p_g = p$ because the capillary pressure is assumed to be zero. As any point in the mesh, it can be a single component or two component zone and the saturation constraint is $S_w + S_g = 1$.

The thermal-transport equation is based on the conservation of enthalpy in both the fluid phases and the solid phase of the porous medium, in a volume element of the region. So, enthalpy is a derived property containing both internal energy and flow energy. Thus,

$$\frac{\partial}{\partial t} [\varphi(\rho_w h_w S_w + \rho_s h_s S_s) + (1 - \varphi) \rho_r h_r] - \nabla \cdot K_a I \nabla T + \nabla \cdot \varphi(\rho_w h_w S_w v_w + \rho_s h_s S_s v_s) - q_{sh} = 0 \quad (2.3)$$

where h is the specific enthalpy of the fluid phase (J kg^{-1}), h_r is the specific enthalpy of the porous-matrix solid phase (J kg^{-1}), ρ_r is the density of the porous-matrix solid phase (kg m^{-3}), K_a is the effective thermal conductivity of the bulk porous medium (combined liquid, gas, and solid phases) ($\text{W m}^{-1} \text{K}^{-1}$), I is the identity matrix of rank 3 (dimensionless), T is the temperature ($^{\circ}\text{C}$), and q_{sh} is the flow-rate intensity of an enthalpy source (positive into the region; W m^{-3}).

The main assumptions underlying Equations (2) and (3) that are solved in HYDROTHERM are the following: capillary pressure effect is negligible, porous medium and fluid are in local thermal equilibrium, the fluid is pure water, heat transfer by radiation and dispersion can be neglected,

Darcy's law is valid with two phase forms, and relative permeability is a nonhysteretic function of liquid volume saturation.

2.3.2.2. Spatial and Temporal Discretization

The 2D conceptual model to simulate extends 14 km horizontally (Fig. 2.1) and 3 km vertically from the land surface. The model geometry in the HYDROTHERM simulator is discretized with a regular 100×100 grids. The simulation time span to reach a quasi-steady state temperature regime was 100,000 years and an initial time step of 0.001 year was considered. An automatic time step algorithm is used in the simulator, where smaller time steps are selected when conditions are changing rapidly and maximum values for changes in pressure, enthalpy, and liquid saturation are specified before running the simulation (Kipp et al. 2008). In our study the maximum changes in pressure, enthalpy, and saturation are 10%, 5%, and 0.03, respectively. This results in a maximum time step of 1000 years. The independence of the mesh is presented to demonstrate the accuracy of the solution. In this study, two different grids were considered with two different initial time steps.

2.3.2.3. Initial and Boundary Conditions

Numerical modeling of continental or subaerial hydrothermal systems often considers the upper system flow boundary to be the water table of shallow aquifers affected by topography (Hayba and Ingebritsen 1997; Driesner and Geiger 2007; Ragueneil et al. 2019). Therefore, initial conditions are an initial temperature of 20 °C with an atmospheric pressure of 1 atm at the surface of the 2D model, a geothermal gradient of 49 °C/km, and hydrostatic pressure increasing with depth. A heat flux of 100 mW/m² was fixed at the base of the model and the surface boundary has a constant temperature of 20 °C. A pressure of 1 atm was also considered at the surface boundary. The base of the model is considered impermeable with no flux. Constant temperature and pressure determined from the initial conditions were imposed on the lateral boundaries of the model in order to take into account the variation of the geothermal and the pressure gradients at depth. This allowed to establish the temperature and pressure gradients according to the topography and the water table depth inferred from the conceptual model. Five different simulation scenarios are presented below. For all scenarios, a deep resistive structure named R2 was taken as a magmatic intrusion or heat source, and a heat flux of 2700 mW/m² was fixed at the base of this R2 structure. This is the base case scenario where the boundary conditions presented above are used. Numerical simulations conducted in magmatic hydrothermal systems (Hayba and Ingebritsen 1997; Weis 2015) showed that the representation of the topography is an important factor to reproduce regional groundwater flow driven by the topography. This was taken into

account to better evaluate the dynamic of groundwater flow between the Asal Lake and Ghoubbet Sea. In addition, the influence of infiltration from rainfall in geothermal systems is not negligible, but the impact of rainfall in the hydrothermal activity is commonly limited in the upper part (Gaudin et al. 2015) and may not prevail in the deeper part of the hydrothermal system, as in the case of Asal Rift. The impact of rainfall was not simulated as the numerical simulations considered confined flow.

2.3.2.4. Hydraulic and Thermal Properties

The geological units considered in the conceptual 2D model were interpreted from the 1D electrical resistivity model developed in this study. Hydraulic and thermal properties of each unit were defined according to Table 2.1, used as the base case scenario and noted as scenario 1. Then, four other different scenarios were conducted in order to evaluate the sensitivity of the results to changes in the main hydraulic parameter (permeability) of the geological units. Three permeable vertical conduits that can be associated with fault zones were added and coexist to evaluate the possible impact of fault zones. The choice of emplacement and geometry of these faults was based on the interpretation of the inverted electrical resistivity profile developed in this study. Thus, properties of faults remain the same of those of unit C1 (Table 2.1), but with higher isotropic permeability equal to $2.17 \times 10^{-14} \text{ m}^2$. In scenario 2, a permeability dependent temperature in the potential deep reservoir unit was adopted with an isotropic permeability of heat source equal to 10^{-17} m^2 . Scenario 3 was simulated to understand the behaviour of the system in the deeper part without permeability dependent temperature. To do this, an isotropic permeability was assigned to both the heat source (10^{-17} m^2) and the potential deep reservoir unit (10^{-15} m^2). This permeability value assigned in the potential deep reservoir unit is of the same order of the one estimated from the production test of well Asal 3, which reached the potential deep reservoir, which was equal to $6.3 \times 10^{-15} \text{ m}^2$ (Jalludin 2007). The conditions of scenario 4 are similar, but a permeability dependent temperature inside the heat source unit was used. Finally, scenario 5 was simulated with permeability anisotropy within the near-surface aquifer C1, which was assigned to the model to investigate how it can influence the regional groundwater flow. Horizontal permeability was set one order higher than the one of the base case scenario. The purpose of this scenario 5 was to simulate the predominance of horizontal fluid movements over vertical movements within this geological formation and hypothesize the behavior of the system in such conditions. The properties of all units remain the same as those of scenario 1, except for the horizontal permeability in the unit C1, which was equal to $2.17 \times 10^{-14} \text{ m}^2$.

In the crust, thermal conductivity decreases with increasing temperature (Vosteen and Schellschmidt 2003). The formulation developed by Vosteen and Schellschmidt (2003) for

crystalline rocks with a temperature range between 20 and 500 °C was taken into account, where the thermal conductivity value at 20 °C is 2.5 W m⁻¹ °C⁻¹. To consider the effect of latent heat of crystallization, a linear temperature-dependent rock heat capacity relation was adopted, which doubles from 900 at temperatures below 100 °C to 1800 J kg⁻¹ at temperatures greater than 500 °C. This linear relationship was based on the approach initially developed by Vosteen and Schellschmidt (2003) and then used by Scott et al. (2017) for similar modeling work.

Temperature-dependent rock permeability was formulated for both the potential deep reservoir and heat source (Table 2.1). This formulation is the same as that developed by Driesner and Geiger (2007) for magmatic hydrothermal systems, where permeability increases with the decreasing temperature. Thus, the permeability of the heat source with a temperature range of 400–500 °C is one order of magnitude less than the one of the deep reservoir with a temperature range of 200–400 °C.

Table 2.1. Hydraulic and thermal properties for simulation of the base case scenario.

Formations	Unsaturated Formation : R1	Aquifer : C1	Cap rock : C2	Potential Deep Reservoir	Heat Source : R2
Porosity (-)	0.12	0.12	0.12	0.27	0.12
Horizontal permeability (m ²)	2.17 × 10 ⁻¹⁶	2.17 × 10 ⁻¹⁵	2.17 × 10 ⁻¹⁸	Temperature dependent	Temperature dependent
Vertical permeability (m ²)	2.17 × 10 ⁻¹⁶	2.17 × 10 ⁻¹⁶	2.17 × 10 ⁻¹⁸	Temperature dependent	Temperature dependent
Thermal Conductivity (W m ⁻¹ k ⁻¹)	Temperature dependent	Temperature dependent	Temperature dependent	Temperature dependent	Temperature dependent
Density (kg m ⁻³)	2700	2700	2700	2800	2900
Specific heat (J kg ⁻¹)	1000	1000	1000	Temperature dependent	Temperature dependent
Compressibility (Pa ⁻¹)	10 ⁻²⁰	10 ⁻²⁰	10 ⁻²⁰	10 ⁻²⁰	10 ⁻²⁰

In such systems, fluid flow is mainly controlled by processes such as thermal pressurization, buoyancy, and magmatic exsolved fluid. Our hypothesis is based upon the existence of deep hydrothermal circulation in the Asal Rift and the absence of a magma chamber at a depth less than 5 km (Dobre et al. 2007). Thus, the fluid pressure originating from the heat source unit may have allowed rocks to fail and created permeability within the potential deep reservoir unit.

2.4. Results

The results of 1D electrical conductivity model are initially presented and followed by the results of fluid flow simulations.

2.4.1. 1D Electrical Resistivity Model

Observed and simulated electrical resistivity data fit with an average root mean square (RMS) misfit of about 0.1. The match of electrical resistivity and phase at each MT station appears reasonable, as can be seen for resistivity, and phase curves of all MT sites along the 2D MT profile (Fig. 2.1) presented in Fig. 2.3.

The H fault (Fig. 2.1, Fig. 2.4) delineates two distinct zones of electrical resistivity. The north-east part of this fault is defined as a conductive zone, while the south part is less conductive (more than 20 Ω .m). The geometry of the Fieale Caldera corresponds to a well-defined zone of electrical resistivity of the order 20–30 Ω .m (Fig. 2.1, Fig. 2.4). The different electrical iso-resistivity maps in Fig. 2.4 show a gradient of electrical conductivity that increases in the direction from the south-west to the north-east. This change of the conductivity gradient is clearly visible and evident at depths of 1640 and 1840 m (Fig. 2.4).

2.4.2. 2D Conceptual Model

The conceptual model of Fig. 2.5 was defined using the available electrical resistivity data interpreted along a cross section more or less parallel to the Asal rift axis (Fig. 2.1). A top layer of high resistivity (R1) is associated with unsaturated formation near the surface. The underlying layer with a low resistivity C1 is considered as an aquifer, which can host shallow or intermediate reservoirs, as evidenced by temperature profiles of wells Asal 6 and Asal 3 (Fig. 2.2). These temperature profiles show convection cells with a change in geothermal gradient at a depth between 300 and 600 m that can only occur in permeable layers with fractures. Layer C2 can be a cap rock covering the formations hosting deep hydrothermal reservoirs, which is referred to

here as the potential deep reservoir unit in the numerical model. The highly resistive R2 structures can mostly likely be associated with intrusive bodies.

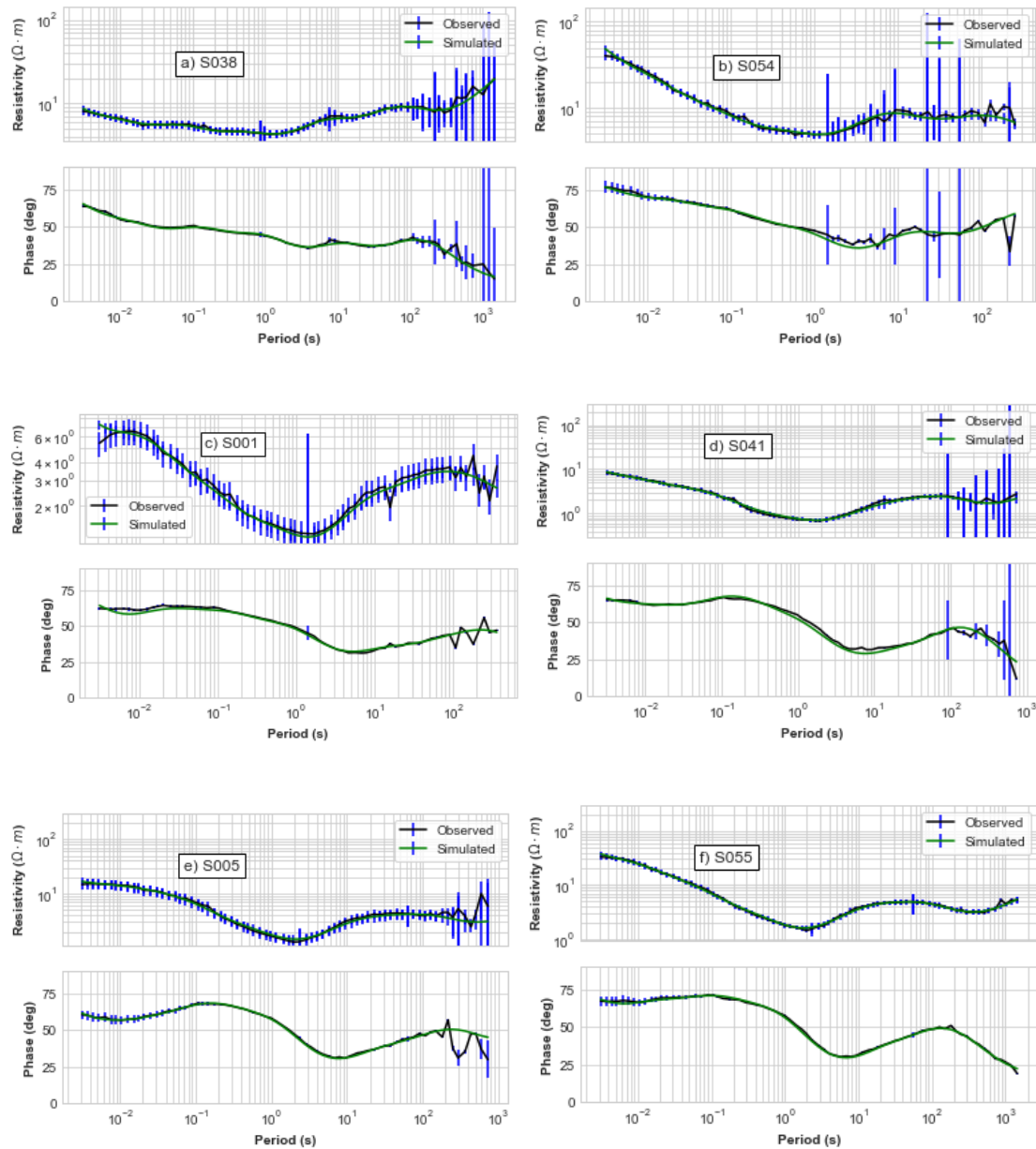


Fig.2.3. Cont

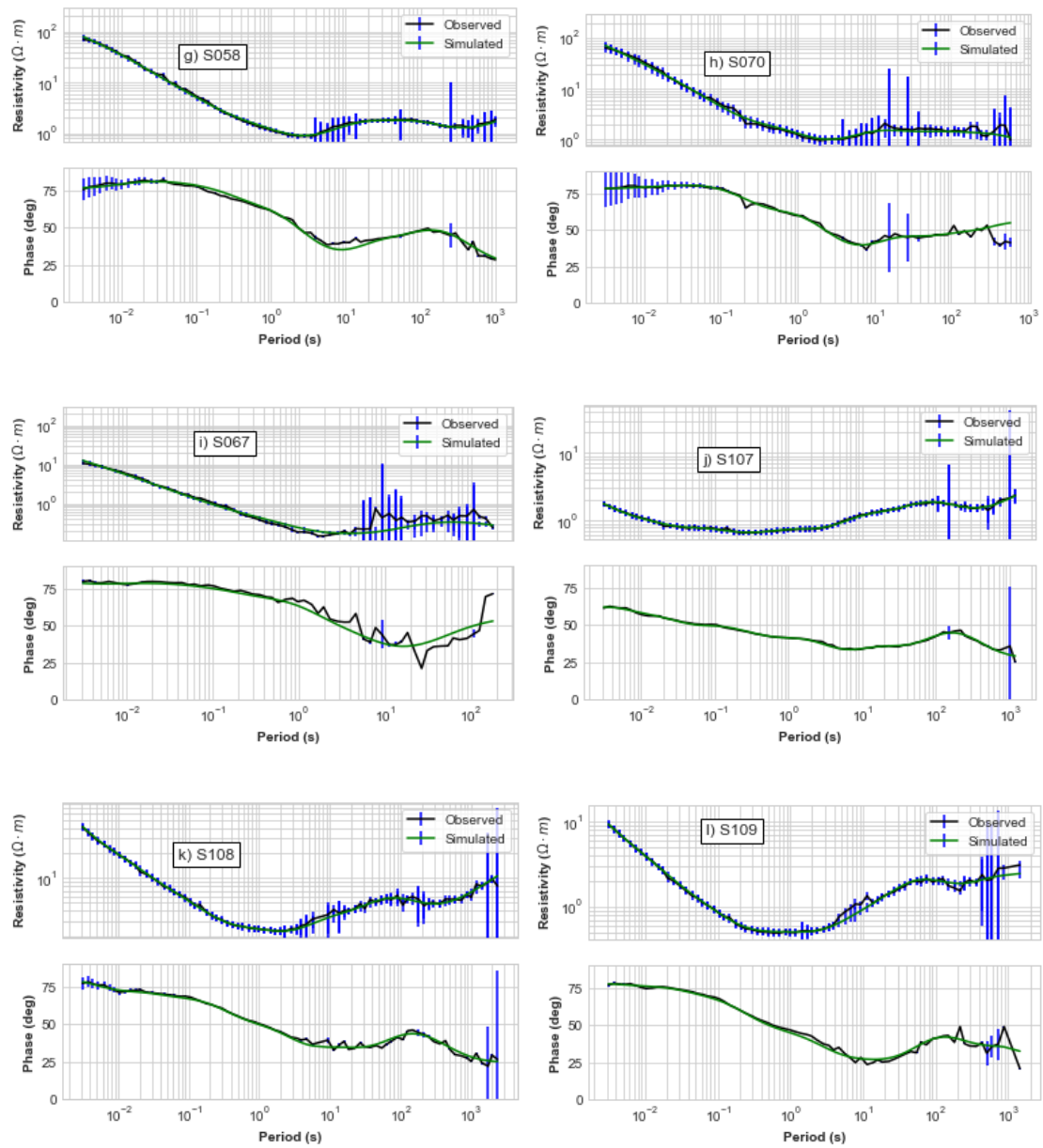


Fig. 2.3. Comparison of observed and simulated electrical resistivity sounding data at MT sites along 2D MT profile in Fig. 2.1.

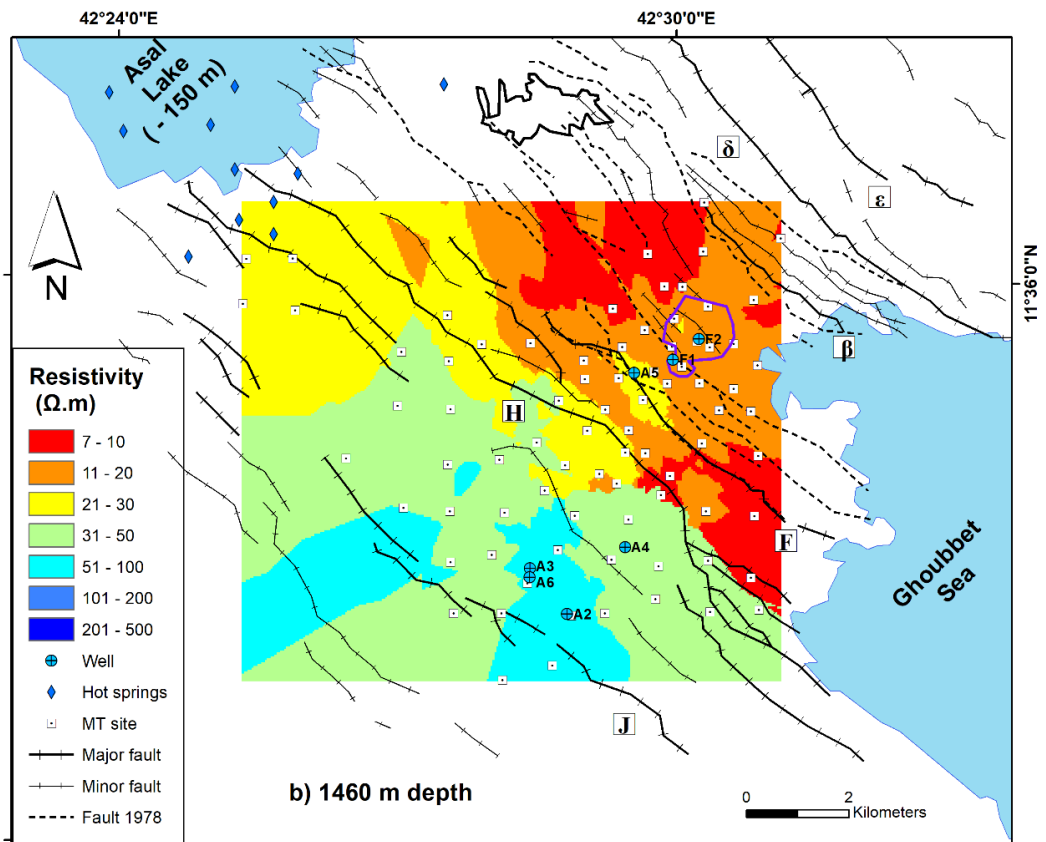
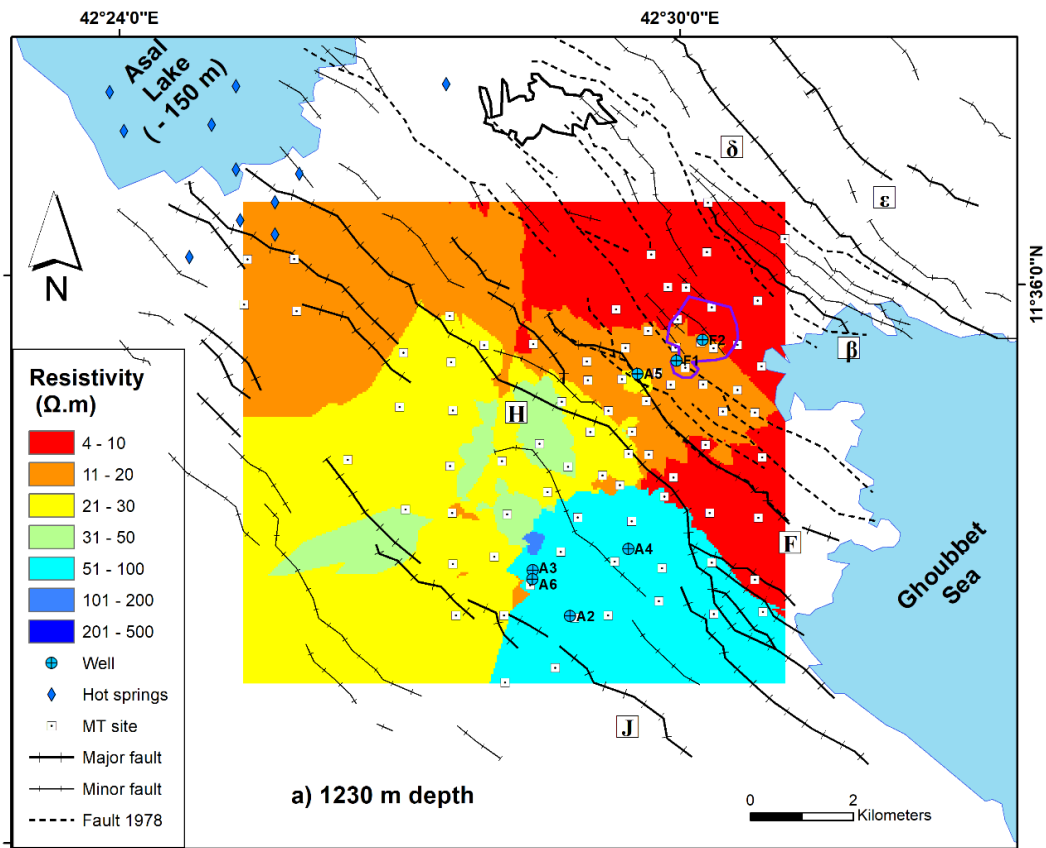


Fig. 2.4. Cont

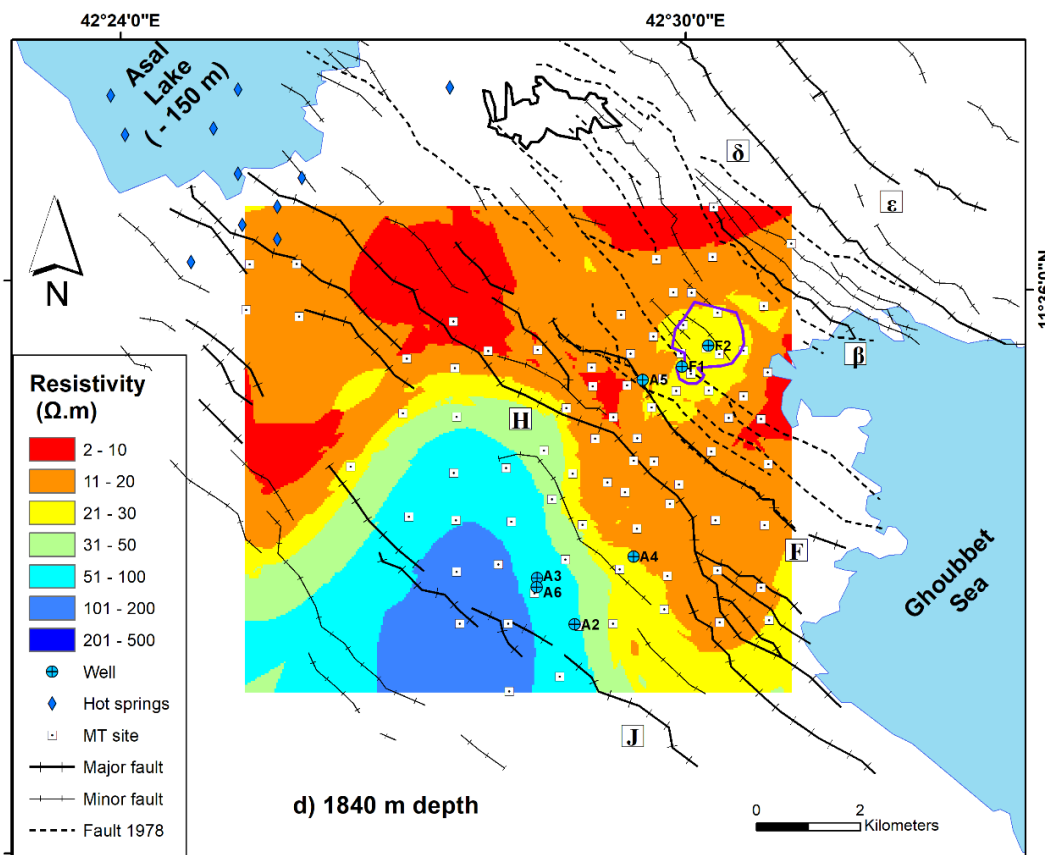
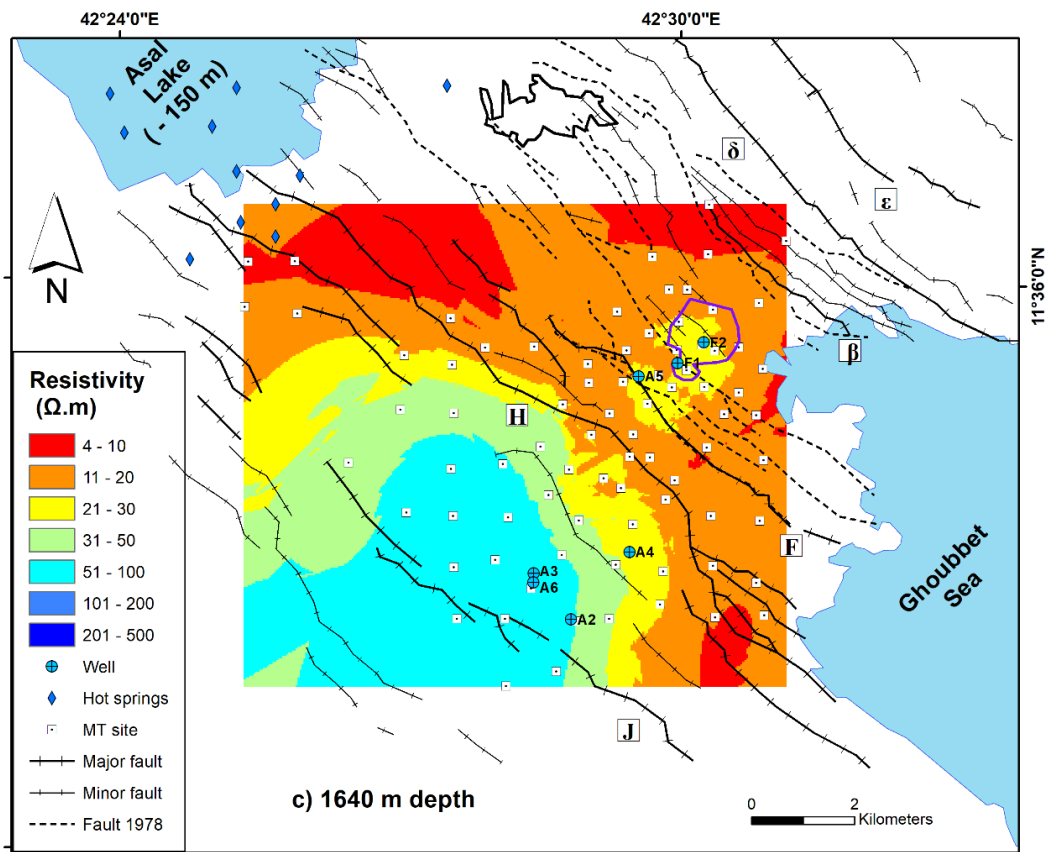


Fig. 2.4. Interpolation at selected depth of inverted electrical resistivity.

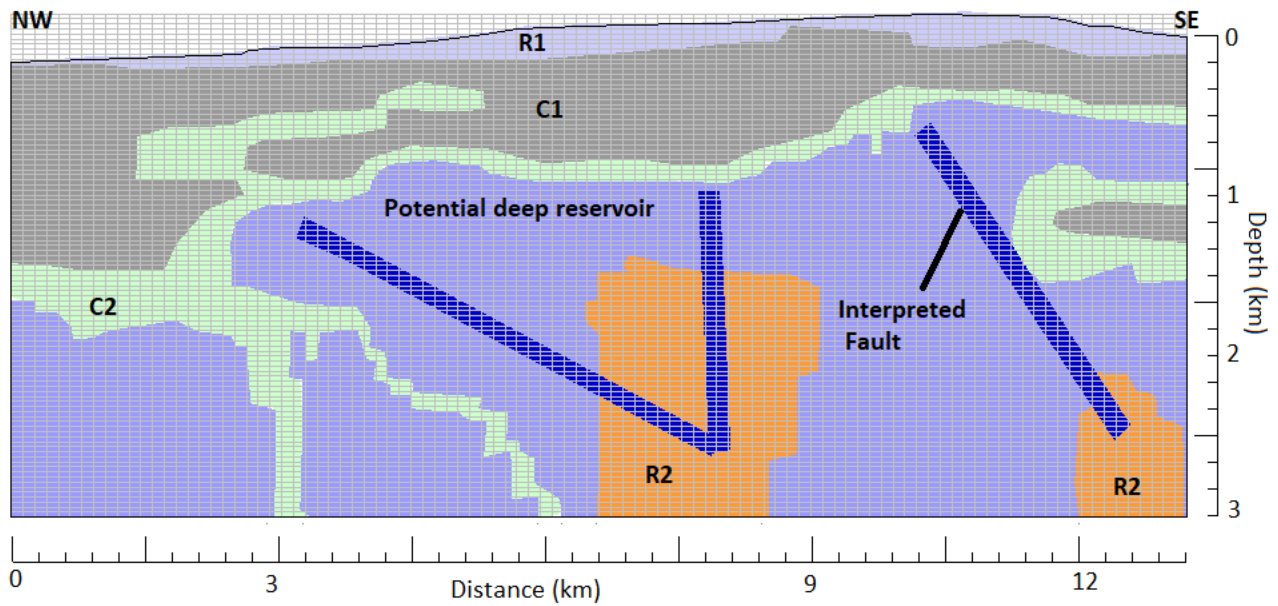
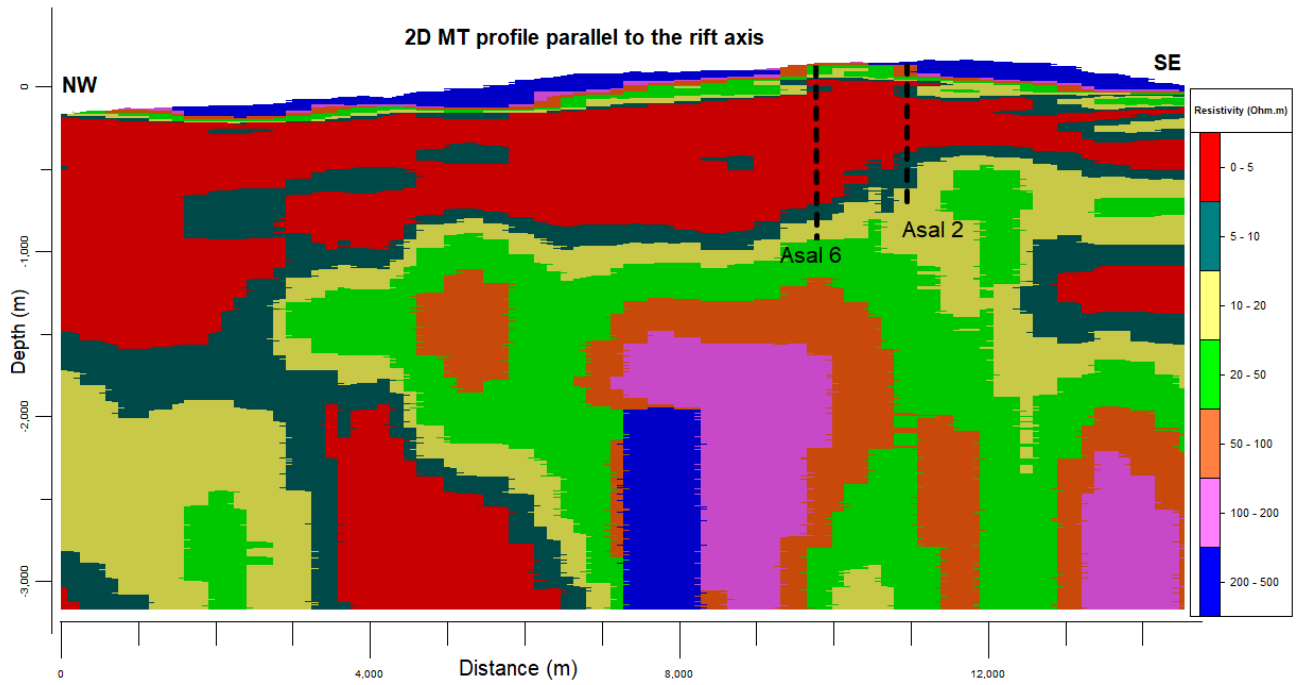


Fig. 2.5. Above) Resistivity model and below) 2D conceptual model interpreted along 2D MT profile in Fig. 2.1.

2.4.3. Numerical Simulations

Mesh and time step independence were investigated to make sure numerical simulations are reliable. A comparison between different grids for scenario 1 at the location of Asal 6 well at a depth of 1500 m is presented in Appendix 1. The results with a 100 × 100 grid and initial time step

of 0.001 year are presented in Fig. 2.6 and 2.7. Furthermore, a mesh with a 40 × 100 grid with an initial time step of 0.01 year was considered (Fig. 2.6) and the patterns of flow and heat transport observed were similar to those of mesh with a 100×100 grid (Fig. 2.7). We can deduce and argue that our solution is independent of the choice of the grid and the choice of the initial time step. One should keep in mind that the HYDROTHERM software uses an algorithm allowing an automatic time step (Kipp et al. 2008) in which only the initial time step is set by the user.

The simulation results of scenario 1 and scenario 2 (Fig. 2.6 and 2.7) show the upwelling of a warm fluid or an upflow zone that propagates from the heat source at the model center toward Asal Lake and toward the sea, but to a lesser intensity. The development of convection movements is visible inside the deep potential reservoir unit that can likely host localized hydrothermal reservoirs. Scenarios 3 and 4 present similar flow and temperature patterns with the presence of three flow zones at a distinct depth. Groundwater circulation toward Asal Lake inside the aquifer C1 can be identified and the widening of the deep upflow zone of hydrothermal reservoir from the center to the sea can be observed. High velocity flow vectors also appear in the center of the rift at a depth between 900 and 1800 m, particularly inside the faults zones, where hot ascent fluid in the fault close to the sea and cold descendant fluid in the fault close to Asal Lake can be observed. This can be associated with a mixture of descending cold groundwater with the ascending deep hydrothermal circulation over a depth of about 500 m and driven by the temperature gradient (Fig. 2.7). Scenario 5 captures the same temperature patterns as the results of scenarios 1 and 2, but with strong flow vectors inside the unit called C1, noted here as a shallow aquifer. Obviously, the system behavior remains the same in the deeper part even with the presence of significant lateral flow in the upper part of the system (Fig. 2.7).

The Asal 3 and Asal 6 wells are believed to be penetrating the deep potential reservoir unit. The full comparison between simulated and observed temperature in well Asal 6 for each scenario is shown in Fig. 2.8. The simulated temperature is about 255 °C in scenario 1 at a depth of 1600 m, which approximately corresponds to the measured temperature at the bottom of Asal 6 well (265 °C at a depth of 1700 m). In fact, the measured temperature matches with the simulated temperature of scenarios 1, 2, and 5, except in the upper part above 600 m depth (Fig. 2.8). The comparison between the measured and simulated temperature for scenario 3 is not presented as it is the same as scenario 4 (Fig. 2.8).

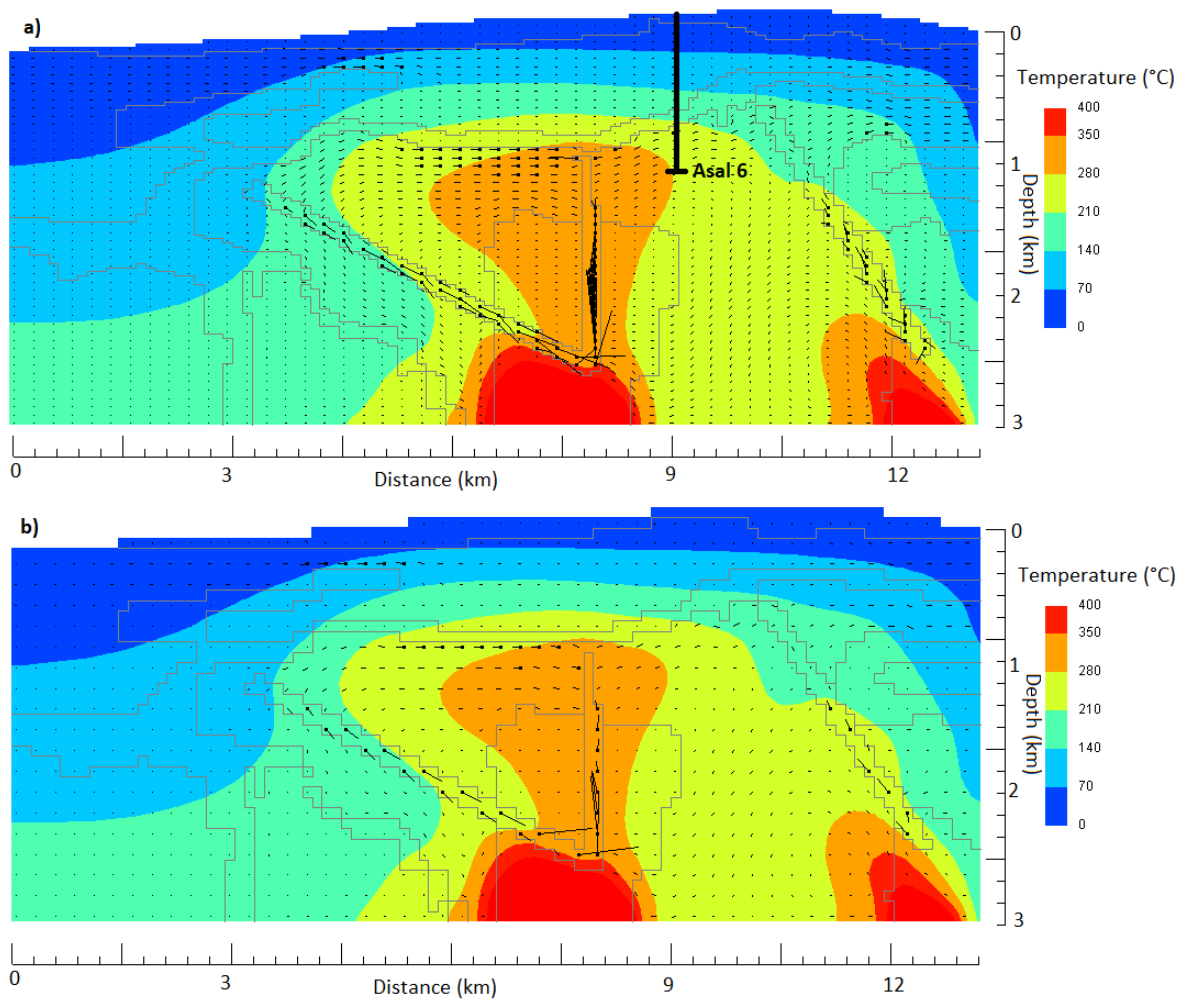


Fig. 2.6. Simulated temperature and flow vectors at time equal to 100,000 years in scenario 1. The direction of flow is from the point to the end of the straight lines. The length of each line indicates the water flow vector magnitude, where $1.2 \text{ km} = 1e^{-5} \text{ g s}^{-1} \text{ cm}^{-2}$. (a) Results with a grid of 100×100 and initial time step of 0.001 year. (b) Results with a grid of 40×100 and initial time step of 0.01 year.

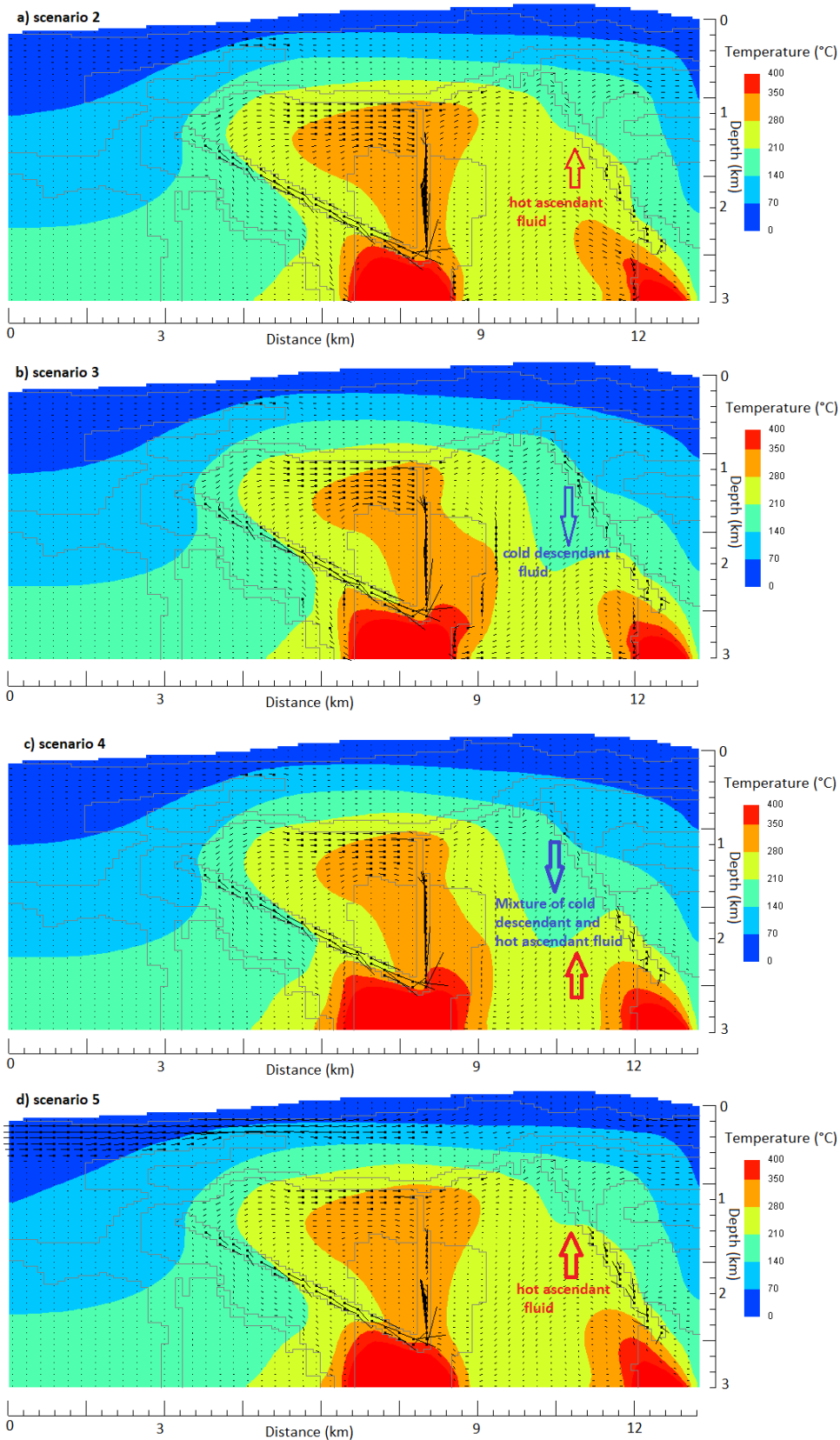


Fig. 2.7. Simulated temperature and flow vectors at time equal to 100 000 years. The direction of flow is from the point to the end of the straight lines. The length of each line indicates the water vector magnitude where $1.2 \text{ km} = 1e^{-5} \text{ g s}^{-1} \text{ cm}^{-2}$.

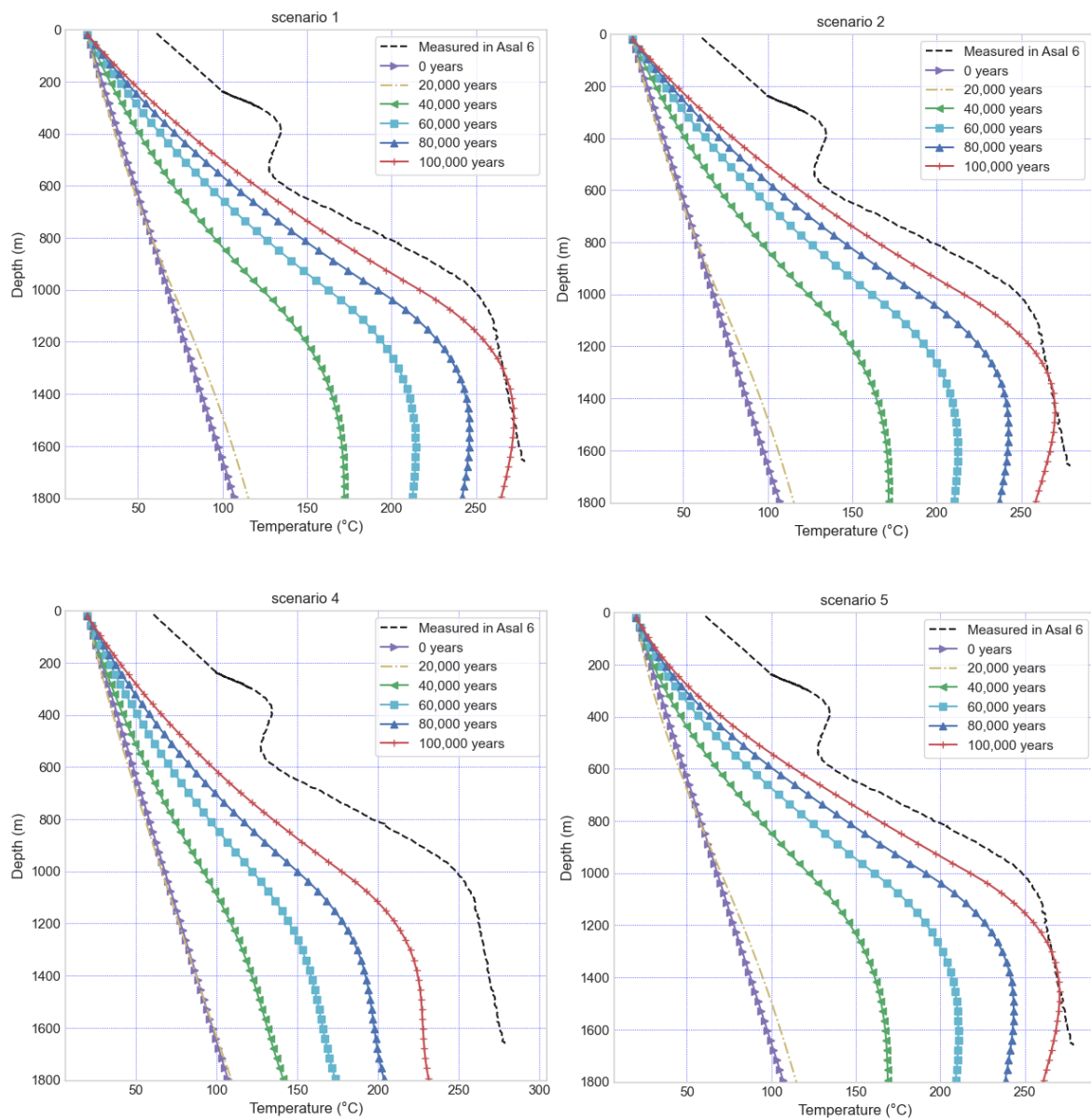


Fig. 2.8. Comparison between the observed and simulated temperatures at well Asal 6.

2.5. Discussion

The directions of faults and fractures are parallel to the direction of believed groundwater flow (Fig. 2.1 and 2.4). Unfortunately, the available MT data do not cover the entire area of the emerged Asal Rift. A lack of data in the area of the normal faults ϵ and δ to the north-east of the rift limits the interpretation (Fig. 2.1). However, previous geochemical analyses conducted by Houssein et al. (1993) in littoral thermal springs could help to place our interpretations in a logical context and may explain the origin and the evolution of thermal waters that are not far at the

eastern flank of the normal faults ϵ and δ located at the north-east of the rift. These authors conclude that a mixture of hot seawater with cold seawater emerges through the fractures. Moreover, the presence of deep hot seawater-derived geothermal fluid with a temperature of 210 °C was confirmed (Sanjuan 2011). Despite the lack of data in this zone, our interpretation of pronounced fluid circulation at the north-east of the rift can be justifiable. The comparison between the $^{87}\text{Sr}/^{86}\text{Sr}$ ratio and strontium concentration of the brine waters from the Red Sea bottom and Asal Lake have indicated that Asal Lake is a better location to study how hydrothermal fluids of seawater origin may evolve in the Red Sea rift (Boschetti et al. 2018).

The descriptive lithology of the wells drilled in the Asal Rift consists mainly of a succession of basaltic series, which were deposited over geological time and have different ages (Zan et al. 1990). Even if the abundance of shale and/or graphite is known to cause a decrease in electrical resistivity (Simpson and Bahr 2005), no significant quantity of the latter is found in the wells drilled, and more precisely between 1 and 2 km depth (Zan et al. 1990). Within the Earth's crust, the dominant electrical conduction mechanism is electrolytic (Simpson and Bahr 2005). Therefore, low electrical resistivity in the context of the Asal Rift is generally interpreted as an indicator of the presence of a fluid. At depths of 1200 and 1400 m (Fig. 2.4), groundwater seems to be present mainly between the H fault and the δ fault according to the following evidence. In this zone, observed fractures were caused by the tectonic and volcanic activity associated with the eruption of the Ardoukoba volcano that occurred in 1978 (Fig. 2.1). The low electrical resistivity suggests the presence of water and hence more important flow to the southeast between the H and F faults, and to the north-east of Fieale Caldera. The existence of dykes at an approximate depth of 4 km near the rift axis (between the F and β faults) has been hypothesized based on the deformations observed at the surface (Stein et al. 1991). In this case, rift extension and subsidence are controlled by dyke injection. Moreover, the stretching model of Asal Rift is likely accommodated by the magma activity (Smittarello et al. 2016). This extension can result in open cracks where groundwater flows easily. The proximity of the sea and the coexistence of recent open faults and fractures is fair evidence for such flow illustrated with the simulations. The electrical resistivity model, especially images obtained at a depth between 1.2 and 2 km (Fig. 2.4), indicates a possible hydrothermal system in the north-east part of the Asal Rift and with more pronounced regional groundwater flow in this area rather than in the south-west zone (Fig. 2.4). Considering the contrast in electrical resistivity between the north-east and south-west parts of the Asal Rift, it seems likely that the hanging wall of the H fault acts as a hydrogeological barrier separating the Asal Rift between two zones. A first conductive zone, whose high electrical conductivity is due to the presence of groundwater, as well as a second less conductive zone with an increase of the electrical resistivity gradient towards the south of the rift, imply lower porosity and/or less groundwater in pore space and fractures. Only the major J fault and the minor fault passing

through well Asal 4 exist in the south zone of the Asal Rift. In addition, according to the bathymetry map of the region, the J fault is not connected to the Ghoubbet sea. The absence of the open cracks or fractures observed with the November 1978 eruption in the southern zone of the Asal Rift is another argument that limits the possibility of possible fluid flow or water infiltration in this sector, while the presence of activated faults in 1978 in the northern part is dominant (Fig. 2.1).

Wells A5, F1, and F2 were drilled in the north-east zone of the H fault, but only the temperature profile of well A5 was available for this study (Fig. 2.2). This temperature profile shows a first convection cell from 300 to 500 m and a second convection cell from 500 to 1200 m, and then a constant geothermal gradient that can be related to heat conduction between 1.2 and 1.8 km. This information, therefore, correlates with the conductive zone to the north-east of fault H. Furthermore, the geothermal gradient estimated between 1.2 and 1.8 km in well Asal 5 is 18.7 °C/100 m. In addition, well Asal 5 is located in a relatively conductive zone with an electrical resistivity greater than 20 Ω m, which can corroborate the absence of groundwater that can have a high salinity associated with electrical resistivity less than or equal to a value of 10 Ω m (Simpson and Bahr 2005). This Asal 5 well can be close to a heat source where heat is transferred by deep conduction, resulting in a strong conductive geothermal gradient at a depth between 1.2 and 1.8 km. The absence of groundwater circulation between 1.2 and 2 km in this well is corroborated by both its temperature profile and the electrical resistivity model presented in this study. The latter also shows the Fieale Caldera in close proximity to well Asal 5 has a particular electrical resistivity range of 20–30 Ω m. It is highly probable that this resistivity is characteristic of the nature of the rock in this Caldera zone, which can be hot, but less permeable, limiting the circulation of fluid. Another important fact is that hydrothermal mineral assemblage is in good agreement with the measured temperatures in all geothermal wells of Asal Rift, except for well Asal 5 (Zan et al. 1990), where a chlorite-epidote mineral assemblage zone that normally should exist at a high temperature was observed at a depth between 500 and 1200 m, where an important temperature inversion was measured (Fig. 2.2). This piece of information allows to assume that a pre-existing high temperature reservoir can have existed before the infiltration of cold sea water, and the temperature inversion may likely be related to a recent infiltration of seawater.

Geodetic measurements indicate that the opening of the Asal–Ghoubbet Rift has a velocity of 16 mm/year and an opening direction perpendicular to the rift axis, highlighting the asymmetrical behavior of the Asal Rift (Vigny et al. 2007). These authors studied the horizontal and vertical deformation of the rift in directions parallel and perpendicular to the rift axis. They consider that the north-eastern part of the Asal Rift is the site of significant continuous deformation, whereas for its south-western part, the deformation is weak and practically non-existent. These results corroborate the presence of active normal faults in the north-eastern part of the rift and the existing

seismic activity (Doubre et al. 2007). The rate of deformation along the axis perpendicular to the rift axis increases towards the north-east of the rift (Vigny et al. 2007). This is a surprising correlation between the increase in this deformation rate and the increase in electrical conductivity highlighted by the model developed in this work pointing in the same direction (Fig. 2.4).

The regional groundwater flow affected by sea water was believed to be the main source of recharge to Asal Lake (Sanjuan et al. 1990), but our simulation results show the groundwater flow is directed toward both the Asal Lake and the Ghoubbet Sea, with a maximum point on the SE side diving flow in the two directions and a pronounced flow to Asal Lake. This can limit the potential depth of penetration of sea water intrusions near the surface. In this case, recharge of Asal Lake can occur through aquifer (C1), potentially containing fossil seawater that is likely fed by a deep hydrothermal circulation. In all the different simulation scenarios, it is important to highlight the evidence of groundwater flow into Asal Lake and hydrothermal circulation beneath Asal Lake and the Ghoubbet sea.

The superposition of three permeable zones with the predominance of flow towards Asal Lake and the Ghoubbet sea are important elements to advance the hypothesis of the existence of a large hydrothermal system under the rift that would be compartmentalized into these three permeable zones, which can be individualized under the tectonic activity and the injection of a deep heat source since the formation of the rift over the geological time. The subsurface flow at a depth between 300 and 700 m (Fig. 2.7) can be influenced by the Ghoubbet sea and the local rift topography, while the intermediate flow at a depth between 1200 and 2000 m (Fig. 2.7) is interpreted as the result of the development of a hydrothermal system, and the deep flow can be linked to a deep hydrothermal circulation feed by a heat source originating from a deep magmatic system (Fig. 2.7). The presence of the cap rock layer limits possible communications between the second permeable layer, identified here as a potential deep reservoir, and the shallow aquifer C1 (Fig. 2.5 and 2.7), and facilitates the development of a hydrothermal reservoir in the formation, where this cap rock layer covers and helps to contain thermal energy in the potential deep reservoir.

Similar simulation results obtained with scenario 5 (Fig. 2.7) support the idea that regional flow variation is not strongly influenced by the permeability anisotropy in layer C1 of the conceptual model (Fig. 2.5). In other words, the regional flow is mainly controlled by tectonics that affect deep structures and allow the deep heat source to be directed to shallower geological strata and formations. Simulations with an isotropic permeability of 10^{-15} m² inside the deep reservoir and equal to 10^{-17} m² inside the heat source were conducted for scenario 3 to indirectly evaluate the vertical dependence of permeability, which can decrease with depth. The development of hot convection cells within this unit was less pronounced than in scenarios 1 and 2 (Fig. 2.6 and 2.7).

Scenarios with permeability dependent temperature (scenarios 1, 2, and 5) seem to be more realistic than scenario 3 with isotropic permeability. However, the results from scenario 3 are not representative of conceptual hydrothermal models proposed in previous studies (Harris et al. 2004; Schardt et al. 2006), where hydrothermal activity is concentrated in areas with elevated topography. Hydrothermal activity in permeability dependent temperature scenarios better correlates with the central zone of high topography (Fig. 2.6 and 2.7). In scenarios 1, 2, and 5, the lateral extension of the hydrothermal reservoir with the isotherm 210 °C becomes important compared with the results of scenarios 3 and 4 (Fig. 2.6 and 2.7). This pattern is in good agreement with a previous study conducted in a tectonically active rift-ridge zone in Iceland (Lupi et al. 2010). The authors of this study confirm that emplacement and geometry of the upflow zones are mainly controlled by the location and the permeability values of fault zones. The geometry, location, and permeability values of fault zones remain the same in all the different scenarios for this study, but we deduce from our results that the permeability dependent temperature rock formulated in both heat source and potential deep reservoir can play a major role to reproduce a representative dynamic heat transfer in hydrothermal systems. Permeability dependent temperature formulated solely for the heat source unit may not produce significant variation when the potential deep reservoir is set with a constant permeability like the simulated conditions of scenario 4. In addition, the results are approximately the same as the results of scenario 3, where isotropic permeability was set for both the heat source and potential deep reservoir units. In such cases, we hypothesize that permeability dependent temperature would be an appropriate formulation in a hydrothermal system as in the Asal Rift, when it is adopted for both the heat source and potential deep reservoir or, uniquely, for the potential deep reservoir like in scenario 2.

The comparison between the temperature profile measured in the Asal 6 well and the temperature simulated appears more realistic with scenarios 1, 2, and 5 compared with other scenarios (Fig. 2.8). This indicates that the conditions used are representative of the rift and the associated thermal anomaly can be related to the injection of a magma forming a heat source and the development of vertical conduits qualified as active faults to convey this internal thermal energy. In scenario 4 (Fig. 2.8), the system at the end of the simulation began to cooled down, as the temperature at 100,000 years is less than the temperature measured in well Asal 6. It can be reasonable to interpret this as a consequence of an extinguished deep hydrothermal fluid circulation inside the heat source layer, where permeability could be higher than that assigned in scenario 4. However, the shape of the simulated temperature profile at the location of well Asal 6 is maintained and has the same appearance as the measured temperature in well Asal 6. Furthermore, the same reservoir was recognized at a depth between 1050 and 1300 m in three wells, Asal 1, 3, and 6, and the geologic formation hosting this reservoir is called Dalha basal,

which has an average age of 4 to 9 My, where temperatures measured in this reservoir range from 260 to 280 °C (Jalludin 2007) and are close to the simulated temperatures in this study. In addition, permeability anisotropy considered in scenario 5 inside the C1 layer does not lead to cooling of the system and the simulated thermal state at well Asal 6 is close to the measured one (Fig. 2.8). It can be assumed that the thermal anomaly caused by this near-surface groundwater flow has less effect at the global scale of the system. Nevertheless, the assumption of pronounced horizontal flow near Asal Lake in scenario 5 is corroborated by our interpreted conceptual model based on electrical resistivity inversion (Fig. 2.5), where the thickness of the shallow aquifer called C1 increases toward Asal Lake. As results of MT inversion and numerical simulations showed, this study is focused for the potential deep reservoir between 1 and 3 km. The developed 2D model simulate a regional groundwater flow that gives a capture of fluid circulation in a regional scale. Then, the lack of a better correlation between measured and simulated temperature at Asal 6 well for the shallow part of the system above 600 m of depth (Fig. 2.8) may be related to a localized fractures or convections cells. Another possible interpretation would be resulted by the difference of density fluid between the upper part of the system and the lower part. May be if a higher density fluid (as saline fluid) was considered in the shallow part than the deeper part, the shallow part of temperature profile measured at Asal 6 well could be well represented.

Temperatures measured in the thermal springs emerging on the periphery of Asal Lake range from 30 to 90 °C (Sanjuan et al. 1990), and the results of the different scenarios show approximate emergence temperatures that corroborate with those measured in the thermal springs (Fig. 2.7). Based on the chemical and isotopic characteristic of water in the Asal region, three main types of water may co-exist in the subsurface: seawater intrusion from Ghoubbet sea, Asal Lake water, and meteoric infiltration probably originating from the meteoric water that transits from Asal Rift to Sakalol-Harralol depression or/and the meteoric water coming from the deep circulating regional aquifer (Awaleh et al. 2017). The low temperature emergence observed in the hot springs of group Manda (Sanjuan et al. 1990a), their chemical composition of which is close to that of seawater, and the high rate of flow show that seawater circulation through the faults and fractures is the main source of their recharge (Fouillac et al. 1983). This information can be related to the emplacement of the hot springs group Manda that are close to the H fault and are aligned more or less to this H fault and with two other major faults located south of the H fault (Fig. 2.1). Moreover, in this case, the information corroborates our hypothesis that seawater intrusion occurs where faults/fractures exist (Fig. 2.1 and 2.4).

Dissolved salts in water can change the phase conditions of liquid–vapor system and the phase relation of saline water approximated by the H₂O-NaCl system is not the same as those of pure water considered in this study. In conditions of an H₂O-NaCl system such as that of the Asal Rift,

the temperature and pressure of liquid–vapor co-existence are above the critical values of pure water (Bischoff and Pitzer 1989). Despite that the fluid simulated from HYDROTHERM code is pure water (Kipp et al. 2008), for saline geothermal fluid, the emplacement depth of intrusion controls significantly whether phase separation is dominantly carried out by boiling or by condensation (Scott et al. 2017). Obviously, in this case, numerical simulations considering a saline geothermal fluid are expected to reveal the presence of a vapor phase, as proposed by the BRGM conceptual model (Demange and Puvilland 1993). This model is in good agreement with the gas chemical results of the Asal fumaroles and the water stable isotope data of their steam condensates (Marini 1987), as well as the decrease of boron concentrations in the well geothermal fluids evidenced by geochemical analyses (Sanjuan et al. 1990).

The total flow rate of geothermal fluid produced in well Asal 3 showed a considerable decrease of production rate and a decrease of bottom hole pressure, which were related to sulphide and silica deposits in the well with a TDS (Total dissolved solids) of 116,000 ppm (Jalludin 2007), suggesting a high potential of permeability reduction.

The δD and $\delta^{18}O$ water stable isotope data for the geothermal fluids of the Asal wells and for some hot springs (Korilii, Eadkorar, and Eounda Alifitta groups; Fig. 2.1) indicated contributions of meteoric water (Sanjuan et al. 1990a). This meteoric contribution probably originates from the meteoric water that transits from the Asal Rift to the Sakalol-Harralol depression or/and the meteoric water coming from the deep circulating regional aquifer (Awaleh et al. 2017). These authors showed, in the area of Sakalol-Harralol, the presence of hot springs, with high TDS Na-Cl waters, aligned in NW-SE along the main faults like in the Asal Rift. The high-altitude zones of rift margins at the north and south do not seem to be potential recharge sources. However, a more representative numerical model can incorporate these zones and be tested to confirm or invalidate these hypotheses. As suggested by Awaleh et al. (2017), the existence of a deep regional aquifer that may have a wide extension in Djibouti and where the Asal geothermal water has apparently common features in terms of chemical and water-isotope compositions is a good argument to highlight the need for a numerical multiphase model developed at a large regional scale. Coastal aquifers in Djibouti hosted geothermal water that could be more evolved in terms of water–rock interaction between deep fossil water and sea water intrusions (Boschetti et al. 2018).

2.6. Conclusions

This study emphasizes the importance of fault activity and its role in hydrothermal circulation. More specifically, the hypothesis of groundwater infiltration into Asal Lake is supported by

numerical flow and heat transfer simulations performed after considering an electrical resistivity model of the area. The electrical conductivity model obtained after inversion of MT data indicates that faults can act as conduits for the circulation of water, notably the H fault, where the hanging wall of the fault behaves as a hydrogeological barrier. The variation of the electrical conductivity gradient and its increase from the south-west to the north-east of the rift are in agreement with previous work that brings to light the presence of horizontal and vertical deformation in the south-west to north-east direction. The 2D numerical model of flow and heat transfer developed in this study was used to better understand the groundwater flow and hydrothermal circulation. Furthermore, this model confirmed that flow is generally controlled by the presence of faults acting as conduits and driven by deep heat sources. Three flow zones were defined based on the interpretation of electrical resistivity and temperature profiles. The temperature simulated with our model having these three zones is correlated with the temperature measured in well Asal 6, and is thus considered representative of the heat transfer dynamics of the system. These three flow zones are shallow groundwater flow affected by seawater and topography, an intermediate flow with a hydrothermal circulation, and a deep flow related to the hot hydrothermal circulation originating from the magmatic heat source.

In the context of geothermal energy research, future exploration drilling can be located either along this major H fault or in the northeastern part of the rift to capture a significant flow of geothermal fluid that mainly comes from the underground circulation heated by the strong geothermal gradient existing under the Asal Rift. The target drilling zone could be the deep potential reservoir unit down to a depth of 3 km to better intercept permeable zones containing supercritical water or inside the potential deep reservoir at an intermediate depth between 1 and 2 km. The Fieale Caldera and its surrounding zones should be avoided as the presence of hot rocks is thought to produce low permeability in this area.

It could be interesting to complete the present study with a second electrical resistivity model including more MT sites covering the entire surface area of the Asal–Ghoubbet Rift and extending to the north-east of the rift, notably the north Ghoubbet zone, in order to better understand the limits of the hydrothermal system identified in our study and to establish a correlation on a larger scale between the electrical resistivity gradient and the deformation velocity gradient estimated by geodetic measurements (Vigny et al. 2007). In other words, such a complementary study will help estimate which are the underground circulation paths and proportions of seawater and meteoric water recharged through the faults in the hydrothermal systems identified in this study. According to the water stable isotopes data (Awaleh et al. 2017), infiltration of meteoric water can possibly occur from the meteoric water that transits from Asal Rift to Sakalol-Harralol depression or/and the meteoric water coming from the deep circulating regional aquifer. Similarly, the

development of a 2D numerical model of flow and heat transfer down to a depth of 10 km can help to elucidate the role of magmatic intrusion in the deep hydrothermal circulation.

3. DEUXIÈME ARTICLE: POTENTIAL HYDROTHERMAL SYSTEM INSIDE ANISOTROPIC MEDIA INFERRED FROM MAGNETOTELLURIC DATA ANALYSIS BENEATH ERODED ASAL RIFT, REPUBLIC OF DJIBOUTI

System hydrothermal potentiel contenu dans des milieux anisotropes inféré à partir de l'analyse des données Magnétotelluriques sous le rift érodée d'Asal, République de Djibouti

Autheurs:

Abdek Hassan¹, Bernard Giroux¹ and Jasmin Raymond¹

¹ Institut national de la recherche scientifique, 490 de la Couronne, Québec, QC G1K 9A9, Canada

Titre de la revue :

Journal of Applied Geophysics

Submission date: June 2022

Lien avec le chapitre précédent : Généralement la structure géo-électrique de la subsurface est 2D ou 3D. Le modèle d'inversion 1D des données MT du chapitre précédent permet d'évaluer approximativement la distribution de la résistivité régionale mais ne peut à lui seul expliquer clairement le lien entre les directions des champs des contraintes régionales dans un contexte d'ouverture d'un rift. La présence d'une direction géo-électrique régionale 2D ou d'une direction d'anisotropie électrique est ici posée comme hypothèse. Afin de mieux appréhender la validité de cette hypothèse et inférer l'extension du réservoir hydrothermal associée, l'analyse effectuée dans le chapitre 3 offre quelques éléments de réponses.

Abstract for Article 2

At the center of the Republic of Djibouti, an eroded rift called Asal is located where tectonic and magmatic activities can be observed at the surface. Multiple studies were done with different exploration methods to understand rifting processes and characterize the subsurface of this rift. Among those methods, the deep geoelectrical structures need to be better defined with the geoelectrical sounding method (MT) to better delineate the deep resistivity structures. With the objective of improving our understanding of the deep rift structure, magnetotelluric (MT) data acquired in the Asal rift were analyzed and inverted to build a 2D conductivity model of the hydrothermal system. To achieve this, a dimensionality analysis of the MT data along a 2D profile perpendicular to the rift axis was made. Results of this analysis justify the approximation of 2D conductivity structure. Then, 2D inversion models were achieved to build models of the conductive structures. Dimensionality analysis results revealed existence of electrical anisotropy. Consistent correlation between geoelectric strike and electrical anisotropy direction was suggested. While electrical anisotropy direction determined from the ellipticity of the phase tensor for the short periods was interpreted as the consequence of tectonic activity and horizontal deformation of the rift, the electrical anisotropy direction for the long periods was assumed to be related to the effects of combined magmatic-tectonic activities with predominant magma/dyke intrusion which implies the vertical deformation and the subsidence of the rift. Moreover, the variation and rotation of paleo and actual stress fields direction of plate motion in Asal rift located at the junction of three diverging plates -Arabia, Nubia and Somalia - over geological time can generate both magmatic and tectonic activities which in turn can induce a preferred direction of electrical anisotropy. While the north-south electrical anisotropy direction is parallel to the direction of Red Sea Rift propagation, the north-east electrical anisotropy direction is aligned with the extension direction between Arabia and Somalia plates. Result of 2D inversion models presented for the Asal rift allowed to identify two superimposed conductive units close to the surface and interpreted as a shallow aquifer and a wide potential hydrothermal system. Those conductive mediums are overlying a relatively resistive medium. The latter is associated to a magmatic system likely containing hot and/or molten rocks. 2D conductivity model developed in this study could be considered as conceptual model of Asal rift prior to modeling multiphase fluid flow and heat transfer and/or could be used to identify the hydrothermal system for future drilling target depth of geothermal exploration

3.1. Introduction

Rifts zones with divergent plates host high potential geothermal resources and large hydrothermal systems. The Asal rift is an impelling place to study many features related to the characterization of such hydrothermal systems, as seismicity, ground deformation, high ground temperature, fumaroles activities and geomagnetic anomalies have been observed in the area during the past decades (Sanjuan et al. 1990; Manighetti et al. 1997; Doubre and Peltzer 2007; Doubre et al. 2007). Earthquake monitoring was consequently made for a long period in the Asal rift in order to image the thermal structure of the crust (Doubre et al. 2007). Thus, the presence of a hydrothermal system was suggested as seismicity can be related to fluid movement in the crust (Mlynarski and Zlotnicki 2001; Doubre et al. 2007; Hassan Aden et al. 2021). However, the high linear geothermal gradient, the permeability reduction from 1 to 2 km observed in deep geothermal wells located at the center of rift (A5, F1, F3, and the absence of significant hydrothermal circulation, are fair evidence that the active hydrothermal system can be compartmented.

Characterization of the subsurface with geophysical methods is an important prior step in geothermal exploration. The magnetotelluric (MT) method is suitable to highlight conductivity contrasts at depth and electrical properties are among the most useful parameters for imaging deep geothermal structures, especially in a volcanic context. Electrical conductivity varies with clay content, temperature, rock type, water content. Particularly, the presence of interconnected pore or fracture filled by a fluid or conductive minerals drastically changes the electrical resistivity. Combined with other information, this parameter can help to identify the presence of a magmatic system, hydrothermal reservoir, shallow aquifer, regional aquifer, vertical conduits as faults and an the existence of cap rocks (Giroux et al. 1997; Meju 2002; Spichak and Manzella 2009; Piña-Varas et al. 2018).

Dimensionality analysis of magnetotelluric data and the determination of geo-electric strike are useful tools to evaluate the existence of anisotropic layers in the subsurface. In fact, geo-electric strike dependence on the penetration depth of electromagnetic fields can be used to determine the past and remanent tectonic activities in a rift zones (Simpson 2000), where tectonic and magmatic activities are dominant processes of rifting, like in the Asal rift. Our aim was to infer the presence of both geo-electric strike and electrical anisotropy direction that may be related to the remanent and current stress fields in an extension context of rift prior to delimit the deep structure and assess the extent of the hydrothermal system in Asal rift. To achieve this objective, MT data acquired in 2008 by ISOR (Houssein and Axelsson 2010) were reinterpreted in this study. Detailed dimensionality analysis of the MT soundings was performed, followed by 2D inversion of

resistivity sections across the rift. Joint analysis of dimensionality and 2D inversion model were done to infer the geoelectric strike direction, existence of electrical anisotropy, presence of potential hydrothermal system, and to reinterpret the main potential conduction mechanism which accommodate the subsurface resistivity distribution.

3.2. Geological Background

The junction of three diverging plates - Arabia, Somalia and Nubia - in East Africa is a well-known depression called Afar depression, where the expression of tectonic and magmatic activity is manifested as rift segments. Asal is the first inland rift segment of the Afar depression resulting from the westward propagation of the Aden oceanic ridge (Fig.3.1).

The emerged part of the Asal-Ghoubbet rift is bounded in the east by Ghoubbet Bay and in the west by Lake Asal (Fig.3.1). The opening date of this rift is close to 1 My (Manighetti et al. 1998). Normal faults with principal direction of north-west – south-east that can have subvertical scarp over 100 m and a deep rift valley of about 300 m are the main observed structural elements at the surface. The central emerged part of the rift is narrower than the marginal parts. Such structural and topographic settings are common features of slow spreading oceanic ridges. Deformed paleo shoreline from a preexisted freshwater lake high stand dated to 9 ky and the recent basaltic lava flow that cover mainly the rift axis zone highlight that this area has been subject to recent volcanic and tectonic activity (Gasse and Fontes 1989; Stein et al. 1991). The topography of the emerged rift resulted from successive steps of magmatic-tectonic activity. At the early time, almost 100 ky ago, the Fieale volcano was built by magmatic activity, then following tectonic activity faulted the crater that went under a last period of weak magmatic activity. Volcanic edifices of this later period can be observable at the surface but actives normal faults have dismantled most of them (De Chabalier and Avouac 1994; Manighetti et al. 1998).

Micro seismic activity, fumaroles and faults creep activity concentrated at the surface of Fieale Caldera, low seismic velocity zone under Fieale and surrounding areas are evidences supporting the idea that the central volcanic system cited above persisted up to now under the Fieale Caldera (Dobre and Peltzer 2007; Dobre et al. 2007). Intense seismic swarm with an earthquake of magnitude greater than 5 that happened on November 1978 in the Asal-Ghoubbet rift was followed by a fissured basaltic eruption lasting one week and which ended by the extrusion of an approximate volume of $2 \times 10^7 \text{ m}^3 \text{ yr}^{-1}$ of lava that gave rise to the Ardoukoba volcano (Stein et al. 1991).

Observed deformation and geodetic data between 1972 and 1979 allowed deducing an absolute uplift of the rift shoulders of about 0.2 m, 2 m extension with direction perpendicular to

the rift axis (north-east) and 0.7 m absolute subsidence of the inner floor controlled by normal faults activity (Stein et al. 1991; Manighetti et al. 1998; Vigny et al. 2007).

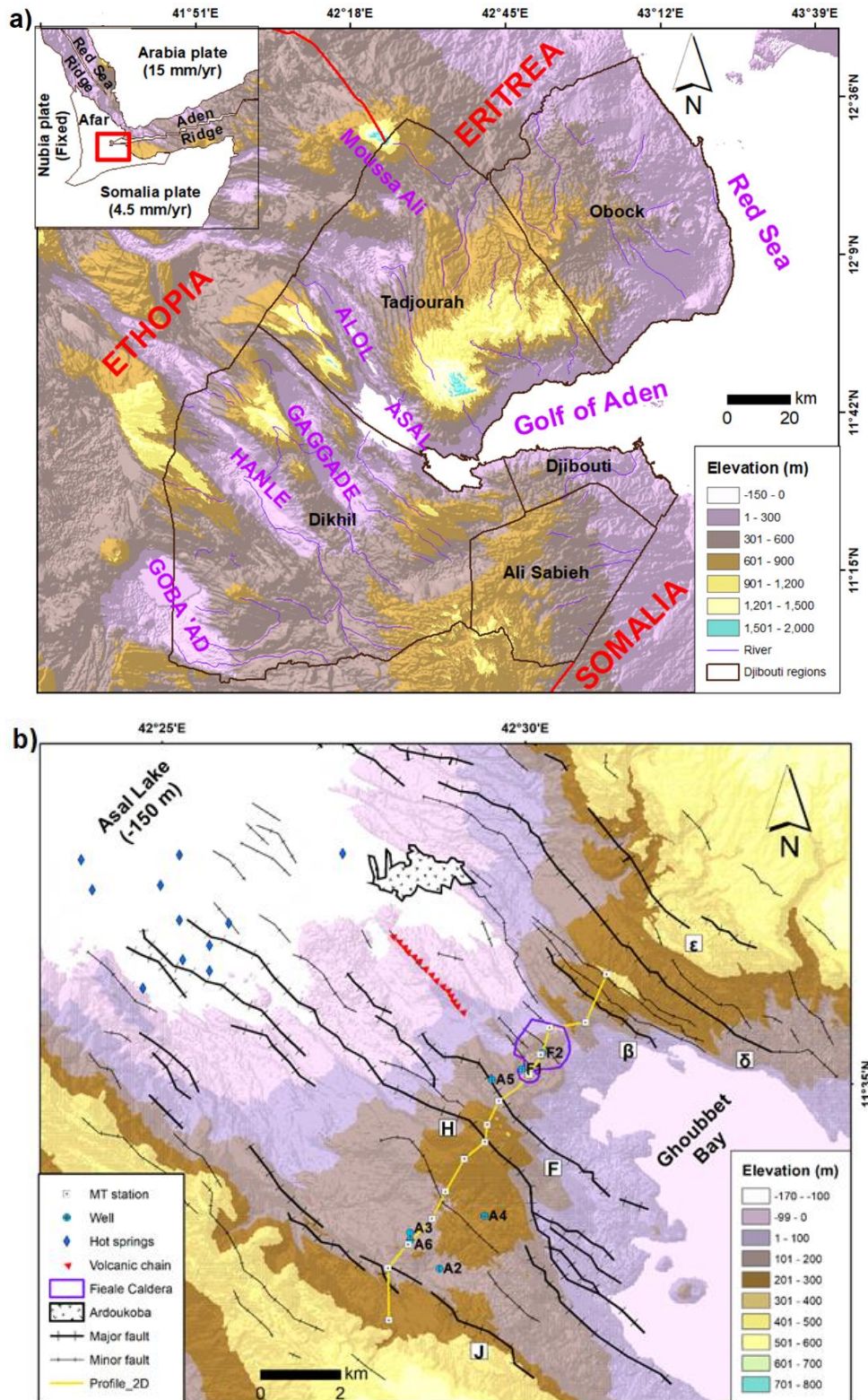


Fig.3.1. Topographic and main structural elements of (a) Djibouti and (b) Asal rift. The red rectangle is Djibouti; MT : Magnetotelluric (modified from Hassan Aden et al. 2021).

Observed deformation at the surface was interpreted as the result of injection of two magma filled dykes, one under the Ghoubbet bay and another under the emerged Asal rift (Stein et al. 1991; Cattin et al. 2005). In addition, co-seismic period in 1978 of earthquake epicenters record during 5 days at the same episode of deformation in the Ghoubbet Bay had a trending direction of N120°E, which corroborates with the direction of dyke injection described above (Manighetti et al. 1998). Two months of continuous seismicity recorded after that event indicated extension of the seismic activity in the Ghoubbet pass and the transfer zone between the Asal-Ghoubbet rift and Tadjoura submerged rift segment (Stein et al. 1991; Manighetti et al. 1998). In their study, Audin et al. (2001) hypothesized that rift extension at shallow depth is mainly controlled by opening fissures and normal faulting in both the Ghoubbet seafloor and the emerged Asal rift. Unfortunately, detailed structural and kinematic features that could explain how fissures, faults and dyke are related are still missing. Seismicity recorded between 1979 and 1984 with moderate magnitude was concentrated in the north-east of the rift axis, in the emerged part of the rift (Dobre et al. 2007).

Local geodetic measurements performed at different times suggest that extension in the Asal rift has stabilized since 1990 to an approximate velocity extension of 16 mm/y (Vigny et al. 2007). According to the latter authors, this rate is practically the same as the regional extension rate inferred from large scale geodetic measurements between the Arabia and Somali plates. The long term opening velocity of the Asal-Ghoubbet rift is also close to the previous local and regional extension velocity (De Chabaliier and Avouac 1994; Manighetti et al. 1998). Therefore, even with the existence of some minor transients slip events on fissures and faults inferred from InSAR data (Dobre and Peltzer 2007) and a weak localized seismic activity (Dobre et al. 2007), it is believed that a steady state extensional regime has been reached.

3.3. Methods

3.3.1. Magnetotelluric data acquisition and processing

A MT survey was made in the Asal Rift between 2007 and 2008 by the Icelandic company ISOR (Houssein and Axelsson 2010). The geographical distribution of the MT stations, which are roughly 1 km apart, covers a large part of the Asal Rift (Fig.3.1). Phoenix MTU-5 systems were used to record the data, i.e. the temporal variation of the three components of the magnetic field (H_x , H_y and H_z) and the two components of the telluric field (E_x and E_y). In order to reduce random noise in the MT signals, a remote reference station located 10 km away from the study area was used (Sakindi 2015). The data collection time was 48 hours. For each site, time series were converted from time domain to frequency domain impedance tensor with the Fourier transformation method (Sakindi 2015). Then, a least square technique estimated was used in

order to reduce and remove the noise related to the electric and magnetic fields that are not naturally induced but resulting from human activities. The frequency range of the data varies from 12.7×10^{-6} Hz to 400 Hz and corresponds roughly to a skin depth of the electromagnetic fields up to 24 km in the Earth if we assume a resistivity of 20 $\Omega \cdot m$.

Horizontal and orthogonal components of electric and magnetic fields are related to the impedance tensor by the following equation:

$$\begin{bmatrix} E_x \\ E_y \end{bmatrix} = \begin{bmatrix} Z_{xx} & Z_{xy} \\ Z_{yx} & Z_{yy} \end{bmatrix} \begin{bmatrix} H_x \\ H_y \end{bmatrix} \quad (3.1)$$

where

$$\mathbf{Z} = \begin{bmatrix} Z_{xx} & Z_{xy} \\ Z_{yx} & Z_{yy} \end{bmatrix}$$

is the complex impedance tensor.

3.3.2. Dimensionality analysis of MT data

Dimensionality analysis is a useful way to understand whether a 3D, 2D or 1D conductivity model should be developed to fit the data. This is made with common analysis methods used by MT community like induction vectors, phase tensor, superimposition model and invariant impedance tensor (Bahr 1987; Caldwell et al. 2004; Weaver et al. 2006). Thus, to determine if the Earth can be approximated by a 2D conductivity structure, we will investigate in the following sections the presence of a well-defined geoelectric strike, which can be a good argument to assume a 2D structure.

3.3.2.1. Phase tensor

The phase tensor corresponds to the regional phase tensor relationship between the electric and magnetic fields and is not affected by galvanic distortion of electric fields (Caldwell et al. 2004). This phase tensor can be represented by an ellipse where the ellipticity can indicate the degree of split between the orthogonal xy and yx components of the complex impedance tensor (see equation 3.1 in paragraph 3.3.1), for which a magnitude and phase can be determined. The ellipticity of the phase tensor can be a tool to investigate the presence of lateral and vertical gradient of resistivity which is aligned to the direction of the major axis of the ellipse where the presence of dominant 2D conductivity structure or anisotropy can be inferred (Caldwell et al. 2004; Heise et al. 2006). The direction with maximum inductive current flow is inferred by the orientation of the major axis of the ellipse, which correspond to the strike angle estimated from the phase

tensor. As we don't know or don't have prior information for which axe of ellipse correspond to the maximum or the minimum phase, the orientation of the induction vectors will be jointly use (see section 3.3.2.4) to eliminate the 90° ambiguity. An approximate circular phase reveals no preferential inductive current flow direction and indicates 1D conductivity structure, while a large ellipticity indicates a preferred direction of current flow (Caldwell et al. 2004). Phase tensor ellipses pointing parallel or perpendicular to the geoelectric strike is often known to indicate a dominant 2D conductivity structure. Another parameter used by MT practitioners is phase tensor skew (β), which describes the asymmetry of the phase tensor (Caldwell et al. 2004) and is expresses by equation 3.2 :

$$\beta = \frac{1}{2} \tan^{-1} \left(\frac{\Phi_{xy} - \Phi_{yx}}{\Phi_{xx} + \Phi_{yy}} \right) \quad (3.2)$$

where Φ_{ij} is the phase tensor components defined by

$$\Phi = X^{-1}Y \quad (3.3)$$

where X and Y are respectively the real and imaginary parts of Z .

3D conductivity structure can be inferred when the phase tensor skew angle is greater than 5° (Caldwell et al. 2004; Booker 2014). Furthermore, values of skew angle less than 5° are practically found but can't be a good argument to advance and conclude on the absence of 3D conductivity structure (Heise et al. 2006).

3.3.2.2. Strike angle from impedance invariants

Rotational invariants quantities computed from MT data have been extensively used in the past decades at various stages of MT data processing. Two common examples are the determinant invariant and the squared sum of components of the impedance tensor (Szarka and Menvielle 1997). With the determination of seven invariants of impedance tensor, Weaver et al. (2006) have proposed some tools and guidance for analyzing MT dimensionality, i.e. to assess whether a 1D, 2D or 3D conductivity structure interpretation is required prior to modeling or inverting MT data. Moreover, they presented some necessary conditions for considering a regional 2D resistivity structure and advanced that a mean geoelectrical strike angle can be easily calculated in the presence of dominant 2D resistivity structure. In this study, the geoelectric strike angle was determined following this approach to verify the possible extent of a 2D conductivity structure and determine the associated geoelectric strike.

3.3.2.3. Strike angle from decomposition model

Separating the impedance tensor of a regional 2D/1D earth model and local 3D effects has commonly made to distinguish between regional induction and local galvanic distortion (Bahr 1987; Lilley 2020). Where local distortion affects the impedance tensor, the impedance phase derived from decomposition model of a regional 2D conductivity structure and local 3D structure, or an ideal 2D and near 2D MT data, can be a useful indicator of dimensionality of the regional conductivity structure in cases of 2D or 3D Earth (Lilley 2020). The regional strike determined from Bahr (1987) for 2D regional MT data but locally distorted with the presence of 3D galvanic effects will be along strike. In the case of 3D regional MT data, the strike determined from decomposition model (Bahr 1987) may be considered as an approximate along strike as being a near 2D regionally MT data (Lilley 2020). The same method was used in this study to determine the geoelectric strike angle and to compare the result with the strike angles determined in the above sections and at the same time to better confirm the presence of 2D structure. The frequency dependence of the geoelectric strike angle with the periods can't be ignored and must be considered when evaluating the appropriate geoelectric strike at the corresponding period that is often assumed to be the geological strike. The latter is influenced by the dimension and depth of a body and the inductive length of electromagnetic fields.

3.3.2.4. Induction vectors

Induction vectors or tipper vectors are calculated from the vertical magnetic field data, which is generated by lateral conductivity gradient. They are used to determine the presence or absence of lateral conductivity variations at the corresponding depth. Parkinson convention was adopted in this study where the vectors point towards anomalous internal concentrations of current. The presence of high magnitude induction vectors can indicate the presence of large conductors and where the lateral changes in conductivity are important (Fig.3.5). Because tipper vectors are computed from the frequency-domain tensor components, the mean direction/strike inferred from the real component of tipper vector pointing toward a conductor can help to identify the existence of lateral conductivity contrast at the corresponding periods. If the length of the induction vectors is close to zero, a 1D resistivity structure at depth can be suggested; otherwise 2D or 3D structure should be considered. Furthermore, if the regional conductivity structure is 2D, the orientation of the tipper vector is mainly orthogonal or parallel to the geoelectric strike direction and this could be helpful in order to eliminate the 90° ambiguity of geoelectric strike (because we don't know or don't have prior information for which axe of ellipse correspond to the maximum or the minimum phase). In the case of inconsistent orthogonality between strike direction and orientation of tipper, a 3D conductivity structure may be more appropriate.

3.3.3. Electrical anisotropy

Existence of electrical anisotropy was analyzed with three methods, the phase split or phase difference between the two polarizations, the consistency of constant electromagnetic strike in a particular period range with the magnitude and direction of the induction vectors and the ellipticity of the phase tensor. Phase split or phase difference between the TE and TM polarization of the phase tensor can indicate the existence of anisotropy. Phase split greater than 10° is often associated to bulk anisotropy of a medium or to a dipping boundary separating two different conductivity regions, or to lateral resistivity variation (Heise et al. 2006). The values Φ_{\max} and Φ_{\min} are the invariants quantities of the phase tensor and represent the length of the major axis and the length of the minor axis of the phase tensor ellipse, respectively (Caldwell et al. 2004). The resistivity contrast can be inferred from the difference of Φ_{\max} and Φ_{\min} and the direction of the principal axis of ellipse that correspond to the phase tensor angle (Caldwell et al. 2004; Heise et al. 2006). This method was used to verify the correlation between the shape of the ellipse, the ellipticity degree and the geoelectric strike in order to infer the presence of anisotropy at depth. Some insights based on electromagnetic strike and induction vector will be analysed to identify the presence of electrically anisotropy beneath Asal rift. In addition, we conducted a prior test to confirm the extent of 2D regional conductivity structure and the possible phase sensitive skew or regional skew increase that can result from potential anisotropic structures (Eisel et al. 2001). The value of phase sensitive skew or regional skew is generally greater than 0.3 in the presence of 3D regional resistivity (García Juanatey et al. 2019) and a sudden increase of the phase sensitive skew value is often related to the presence of anisotropy or the increase of uncertainty in some MT sites. Anisotropy can be related to other parameters like mechanical deformation or paleo/actual stress field, melt intrusion, conductive faults and reactivated faults or fractures. Different directions of anisotropy at different depth generated by different mechanisms can exist both in the crust and/or in the mantle. That means anisotropy direction may change with increasing periods of the natural electromagnetic fields or with the skin depth of MT signals.

3.3.4. Static shift correction and strategy for 2D inversion models

Heterogeneity of small size bodies and resistivity discontinuities across a geological boundary can generate a local distortion of electric field amplitudes and can produce a static shift of the apparent resistivity curve (Tournerie et al. 2007, Arnason, 2015). Thus, measured resistivity curves are shifted up or down by an unknown real factor. On the other hand, the shape of the true level of the resistivity curve remains at least same to the shifted resistivities curves. This effect should be removed to correctly infer the geoelectrical properties of the area under investigation.

For the last two decades, researchers tried to find which method is most appropriate to correct the static shift phenomenon (Tournerie et al. 2007, Gómez-Treviño et al. 2014, Moorkamp et al. 2020, Arnason, 2015). The Time Domain Electromagnetic Method (TDEM) is unaffected by static shift and this method is usually used to perform the correction when TDEM surveys can be done coincidentally with MT soundings (Krivochieva and Chouteau 2003; Spichak and Manzella 2009). In this study, the TDEM method is thus used in order to correct the static shift of each MT sounding where MT stations are close to the TDEM stations for the 2D profile perpendicular to the rift axis (Fig.3.1). TDEM survey was done by ISOR with the collaboration of Djibouti government and the TDEM penetration overlapped with shallow MT penetration. Static shift correction was done to find and determine the proportionality coefficient between apparent resistivity derived from TDEM data and apparent resistivity derived from MT data. At the surface and in the shallow subsurface of geothermally active regions like the Asal rift, resistive environments and dry volcanic rock are more common, and small-scale resistivity contrasts are likely to significantly distort the amplitudes of electric fields (Arnason, 2015) and static shift should be corrected to avoid the distortion generated by the small-scale bodies near surface. In addition, in some area with hilly landscape, topography effect can cause a misinterpretation of MT data because the induced current density can be concentrated in valleys and spread out on hills. In this study, we did not take account the topography effect for the 2D inversion. The topography of the study area where electromagnetic soundings are available varies from 100 to 300 m (Fig.3.1) and this can be approximate by a slope angle of less than 9 %. 3D topography and bathymetry effect on MT data was studied by Nam et al. (2009), who suggested that this effect is small for a short period range (for the depth of the crust) and can be neglected if the slope angle is less than 9°. So, in the Asal rift, we assumed that the topographic effect is negligible and used a 2D mesh where the top of the 2D inversion model didn't vary with the altitude of MT stations along the 2D profile. We assumed that 3D galvanic distortion was adequately corrected by the TDEM data, whereas the potential 3D inductive effect or 3D inductive regional conductivity was checked by analysing the value of phase sensitive skew where value greater than 0.3 are correlated by the presence of 3D inductive effects (García Juanatey et al. 2019). In cases where 3D inductive effects are not dominant, 2D inversion can be a good reasonable solution.

3.4. Results

Results obtained from dimensionality analysis are presented and the results from 2D inversion models follows.

3.4.1. Dimensionality

3.4.1.1. Extent of 2D regional conductivity and the regional skew

In order to determine the absence of dominant 3D regional conductivity and generalize the presence of dominant 2D regional conductivity in the study area, values of the regional skew were analyzed. It is reasonable and safe to advance that a 2D regional conductivity structure can be considered in this study as there are few points that have a regional skew value greater than 0.3 (Fig.3.2). Some points with greater regional skew are likely due to the influence of uncertainty in MT fields or impedance estimates (see Appendix B). Relative increase of regional skew values can demonstrate the deviation of the conductivity distribution from the ideal or the exact 2D conductivity structure where the diagonal elements of impedance tensor are neglected and should be zero or close to zero (Bahr 1987; García Juanatey et al. 2019). Increasing values of the regional skew for the intermediate and long periods can be interpreted as due to the presence of anisotropic layers as suggested in previously studies by Eisel and Bahr (1993) and Eisel et al.(2001) with an assumed 2D resistivity structure. It is also correlated with the high vertical gradient magnitude induction vectors (Fig.3.8). What we have is very interesting to suggest that anisotropy exists for the area where both the values of regional skew and the magnitude of the tipper increase. In addition, a phase split, ellipticity and a well-defined geoelectric strike exist for the same periods range, which also support the presence of anisotropy at the corresponding depth.

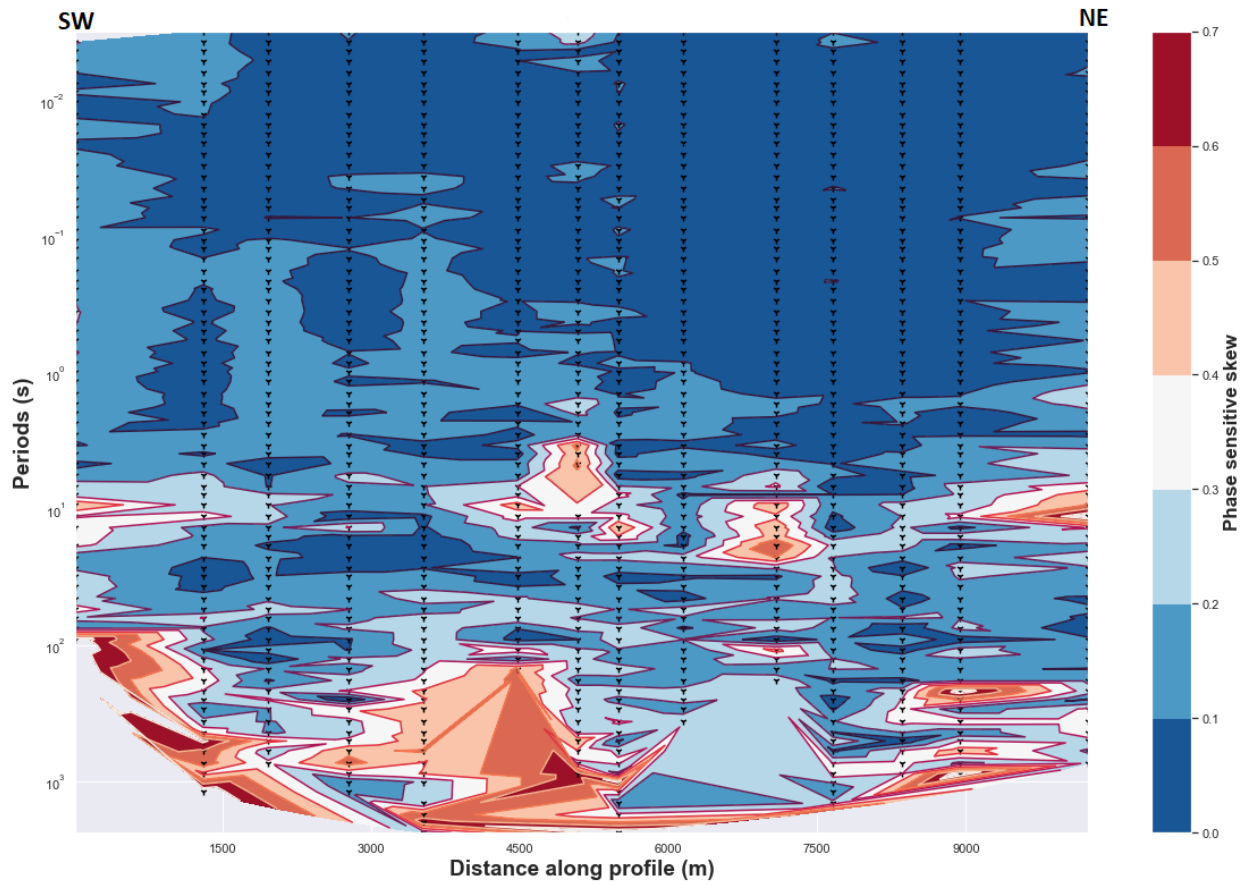


Fig.3.2. Phase sensitive skew or regional skew.

3.4.1.2. Phase tensor analysis

The convention adopted in this paper is that the phase tensor angle is measured counter-clockwise, with the east direction corresponding to 0° . The analysis reveals that two main geoelectric strikes appear over two bandwidths for the phase tensor strike (Fig.3.3), a mean north-east strike of about 40° for the short periods and another sensitive north-north-east strike for the long periods. The mean strike of phase tensor (Fig.3.3) is estimated over all 14 MT stations along 2D profile (Fig.3.1) with the corresponding periods range regrouped by decades.

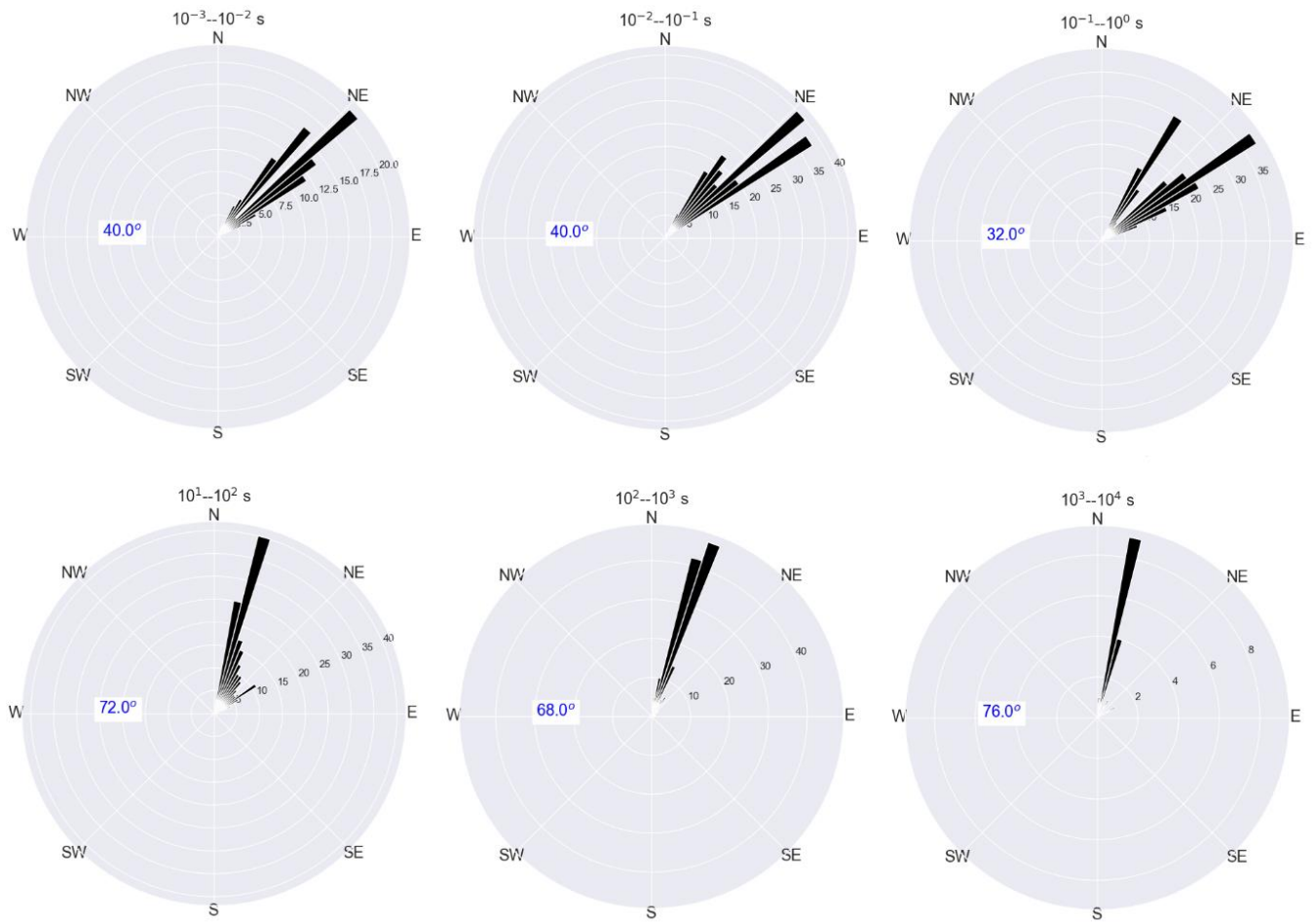


Fig.3.3. Rose diagram of the orientation of the phase tensor strike for the stations along 2D profile (Fig.3.1) where each rose diagram corresponds to the mean strike estimated over all 14 MT stations along with the corresponding period range.

3.4.1.3. Impedance invariant and decomposition model

The geoelectric strike estimated from two different approaches (impedance invariant and decomposition model) are in the same range (Fig. 3.4).

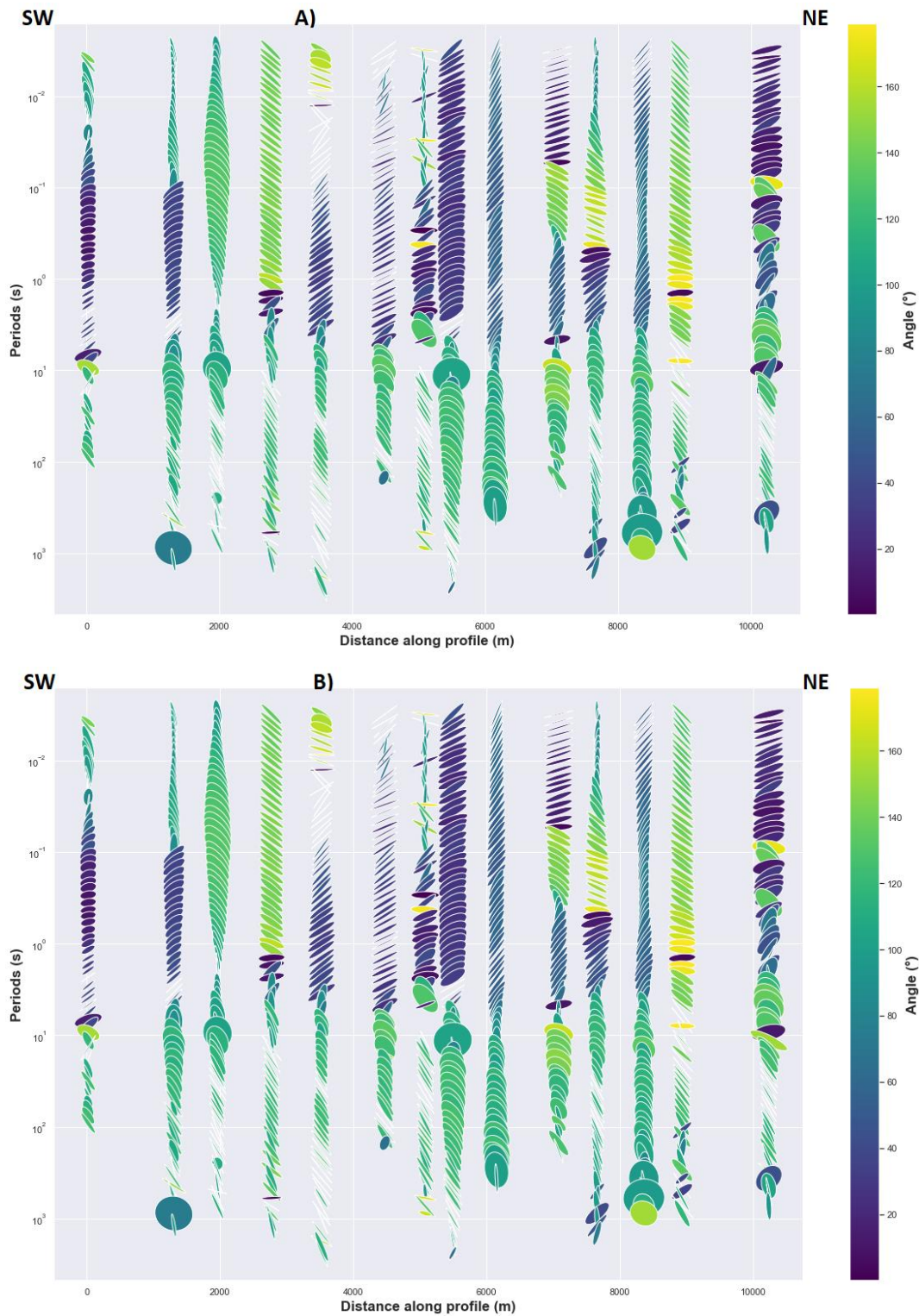


Fig.3.4. A) Strike angle from impedance invariants (B) strike angle from decomposition model. The major and minor axes of ellipse respectively correspond to the Φ_{\max} and Φ_{\min} of phase tensor ellipse defined in the precedent section 3.4.1.2.

The two methods give consistent results, and indicate how geoelectric strike is dependent on period and site location. As evidenced in Fig. 3.4, the strike at short-intermediate periods for most

MT stations is relatively north-east with an average of 45° but some stations have a $N120^\circ E$ strike that can be described as an orthogonal strike direction of the north-east strike, which can result from 3D effects or local 2D heterogeneity. Further reinterpretation related to the position of those MT stations is given in discussion. For the long period, an approximate north-north-west strike direction with an average of $N120^\circ E$ can be seen (Fig. 3.4). In a 2D Earth, the strike determined from impedance invariant is mathematically same to the strike determined from decomposition model of Bahr (Weaver et al.2006), which corresponds to the observed results in Fig.3.4.

3.4.1.4. Tipper orientation with phase tensor ellipse

Tipper vectors represent the relation between the vertical magnetic field to the horizontal magnetic fields. And lateral conductivity variation induces variation of horizontal magnetic fields, which generate a vertical magnetic field. The tipper vector as illustrated in Fig.3.5 have a magnitude and direction that varies with period and with site location. For short periods, vectors with strong magnitudes are observed in the center of the rift and in the south-west. The orientation of the tipper angle is approximately $N45^\circ E$ for the stations located in the south-west, while for the sites located at the center, the tipper angle is close to north-north-east and sometimes close to the north-south direction. Furthermore, for the long periods, the features are almost the same for sites located in the center and in the south-west, where the high magnitude vectors are aligned close to the north-south direction. The induction vectors are weak in the case of dominant 1D resistivity structure as evidenced in Fig.3.5 for some MT sites. In addition, the circular form of the ellipse of those sites indicates the dominant 1D structure (Fig.3.5, Caldwell et al. 2004). The filled color of the ellipse corresponds to the skew angle, which is commonly used to infer the presence of 3D effects where values greater than 5° are generally linked to the existence of 3D effects (Bibby et al. 2005; Booker 2014). In Fig.3.5, values less than 5° of skew angle are common and could be associated to the dominant 2D regional conductivity structure (Caldwell et al. 2004). Another important element is that the principal axes of the ellipse are either parallel or perpendicular to the geoelectric strike direction in the presence of dominant 2D conductivity structure (Heise et al. 2006) as illustrated in Fig.3.5.

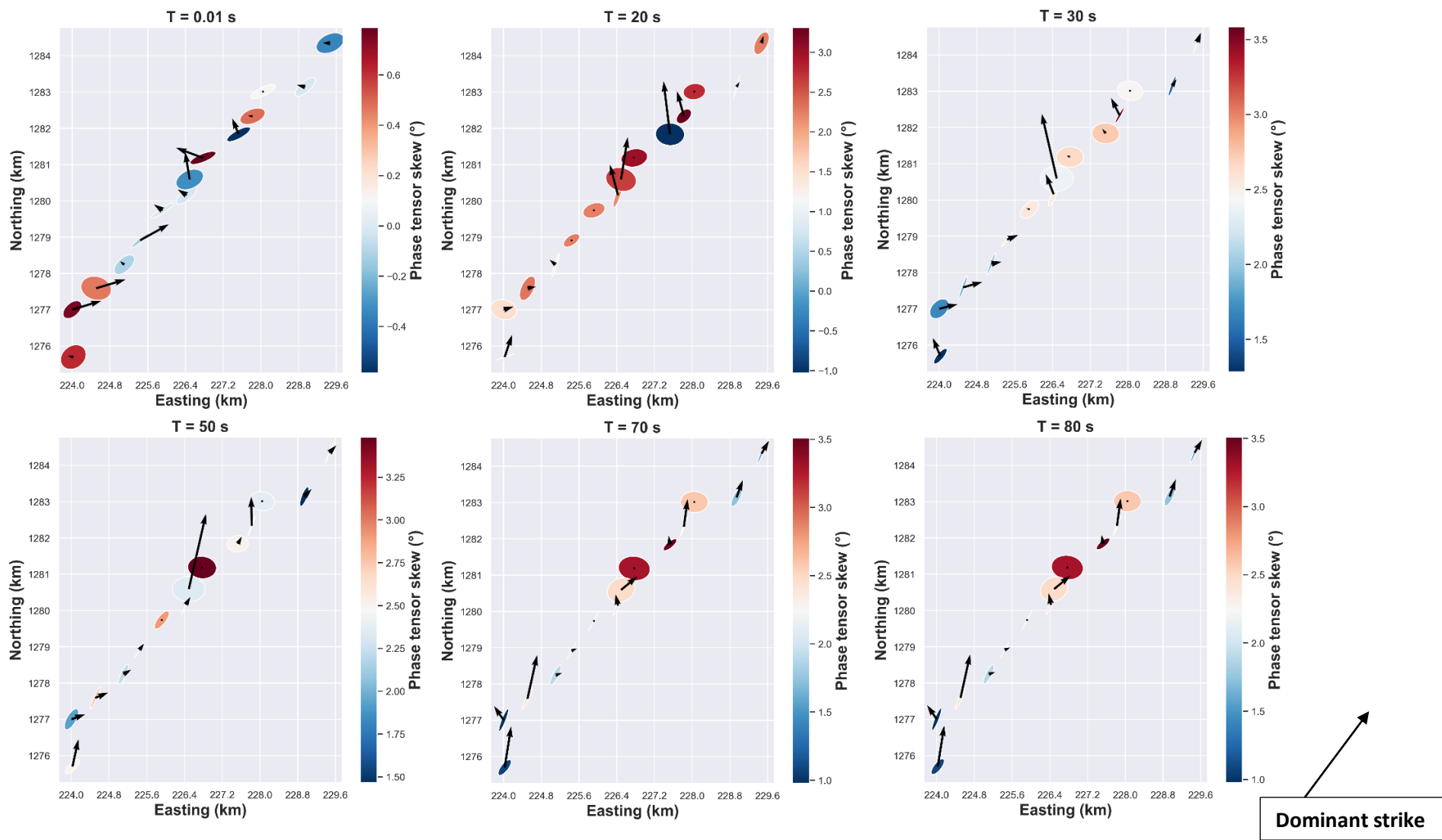


Fig.3.5. Cont

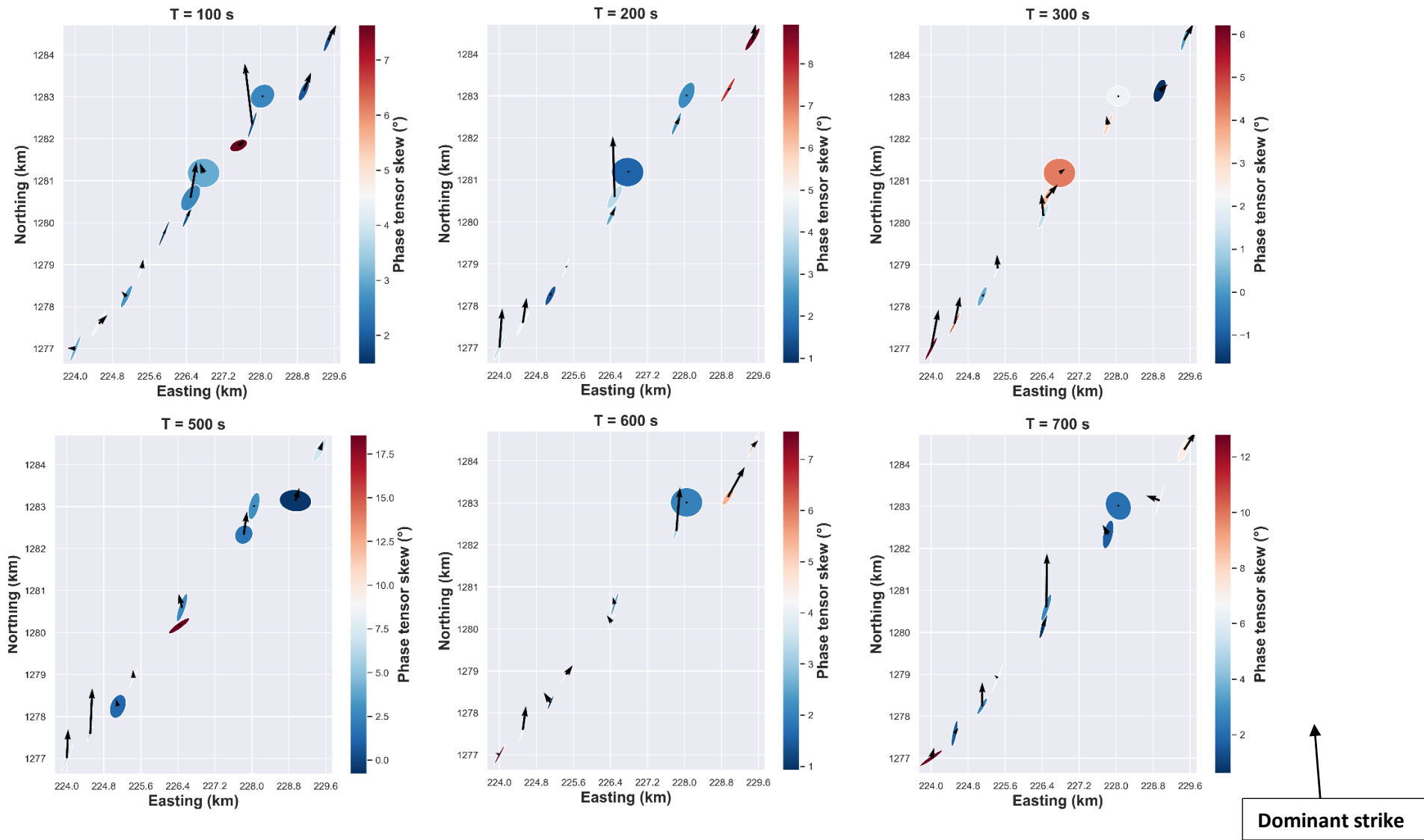


Fig.3.5. Real induction vectors with phase tensor ellipse.

3.4.2. Electrical anisotropy

3.4.2.1. Impedance phase split or difference between TE and TM phases

In case where a dipping boundary from the surface to depth could create a phase split, convergence of phase split values should be observed for MT sites close to that dipping interface. The lack of this convergence along entire 2D profile may exclude this hypothesis. Consequently, the anisotropy hypothesis may be preferred for the long periods.

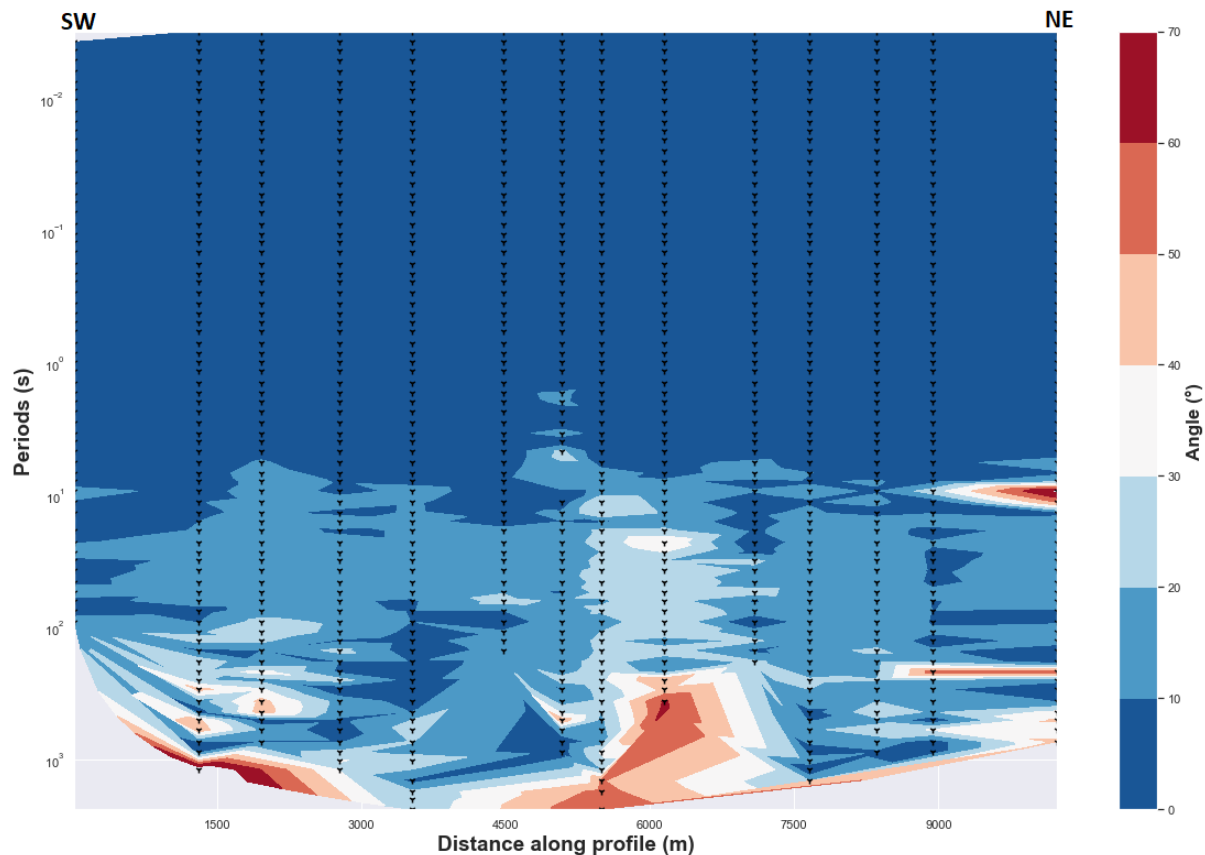


Fig.3.6. Phase difference between the two orthogonal components (TE and TM) phases. The dashed black triangles indicate the locations of MT stations at various periods.

Furthermore, if a consistency of phase split along a 2D profile and with multiple stations is observed as shown in Fig.3.6, the presence of anisotropy is an interpretation that is preferred to the lateral variation of conductivity (Kellett et al. 1992; Eisel et al. 2001). This can be explained considering that if the lateral variation is the cause, the phase split should decrease or disappear for the MT sites far away from any lateral resistivity gradient. This is not what is observed in Fig.3.6, in which the phase split remains for a range of periods and with most of MT sites along

entire 2D profile. It is thus reasonable to attribute this to the electrical anisotropy of geological structures at the corresponding depth. Additionally, the period range (long periods) where the degree of phase split is important corresponds to the period range where an approximate constant geoelectrical strike is well defined for all dimensionality analysis methods described in paragraph 3.4.1. This preferred direction of regional electric fields is roughly north-south and remains almost constant for the entire range of periods that the phase split is manifested. The same pattern was demonstrated by Kellett et al. (1992) to indicate the presence of dyke in anisotropic crust. It is obvious that at the center of the rift the degree of phase difference is more pronounced and increases with depth.

3.4.2.2. The ellipticity of the phase tensor

While evidence of the phase split can be observed in the presence of anisotropy for the long periods where near surface galvanic distortion has less effect on the regional phase response, and in general case this phenomenon can be hidden or difficult to observed for the short periods due to the near surface galvanic distortion effects which are significant (Heise et al. 2006). Thus, phase split derived from impedance phase is distorted as the impedance tensor is distorted for the short periods whereas the phase tensor is not affected by the galvanic distortion for both the long and the short periods (Caldwell et al. 2004; Heise et al. 2006). The maximum and minimum phases of the principal values of phase tensor (Caldwell et al. 2004; Lilley 2020) are invariants quantities, and their geometric mean ϕ_{mean} can be calculated to determine the magnitude of the phase tensor response. Moreover, the ellipticity of phase tensor can help to assess the presence of electrical anisotropy (Heise et al. 2006). The major axes of ellipses are generally oriented N43°E at short periods, but for the long periods their direction tends to be north-south (Fig.3.7). Furthermore, ellipticity and the shape of ellipses for many MT sites are related to the phase split between the xy and yx polarization in a regional 2D resistivity where the minor axis of the ellipse decreased. The consistency of this feature at many periods (Fig.3.7) may be produced either by 2D conductivity structure or electrical anisotropic medium or an interface between isotropic and anisotropic medium. Logically, single large 2-D electrical heterogeneity is not expected at depth in the study area over the entire 2D profile that can generate the consistent ellipticity because there is not one unique direction of induction vectors in Fig.3.5 that support the assumption of single large 2-D electrical heterogeneity. Consequently, the potential cause of this consistent ellipticity with approximate preferred direction can be explained by the presence of anisotropy. The greatest values of the geometric mean $\phi_{\text{mean}} = (\Phi_{\text{max}} * \Phi_{\text{min}})^{1/2}$ that are coincident with obvious ellipticity are observed for intermediate and long periods in the center and in the north-east indicating conductivity increase (Fig.3.7). The pattern displayed by the values of ϕ_{mean} is somehow

different for MT sites between the center and the south-west where this pattern is more localized for the intermediate periods. A relative increase of φ_{mean} values appears in some MT sites in the center, south-west and north-east for short and intermediate periods, which can be interpreted as high contrast resistivity inside a macro-anisotropic medium and the surrounding rocks for the corresponding periods. For long periods, ellipticity reduces in the north-east and at the center of the rift, with an increase of φ_{mean} values. This increase of φ_{mean} values can suggest a possible interface between two anisotropic media with different geoelectric strike and a high conductivity contrast between the two media where the deepest medium is more conductive (Fig.3.7).

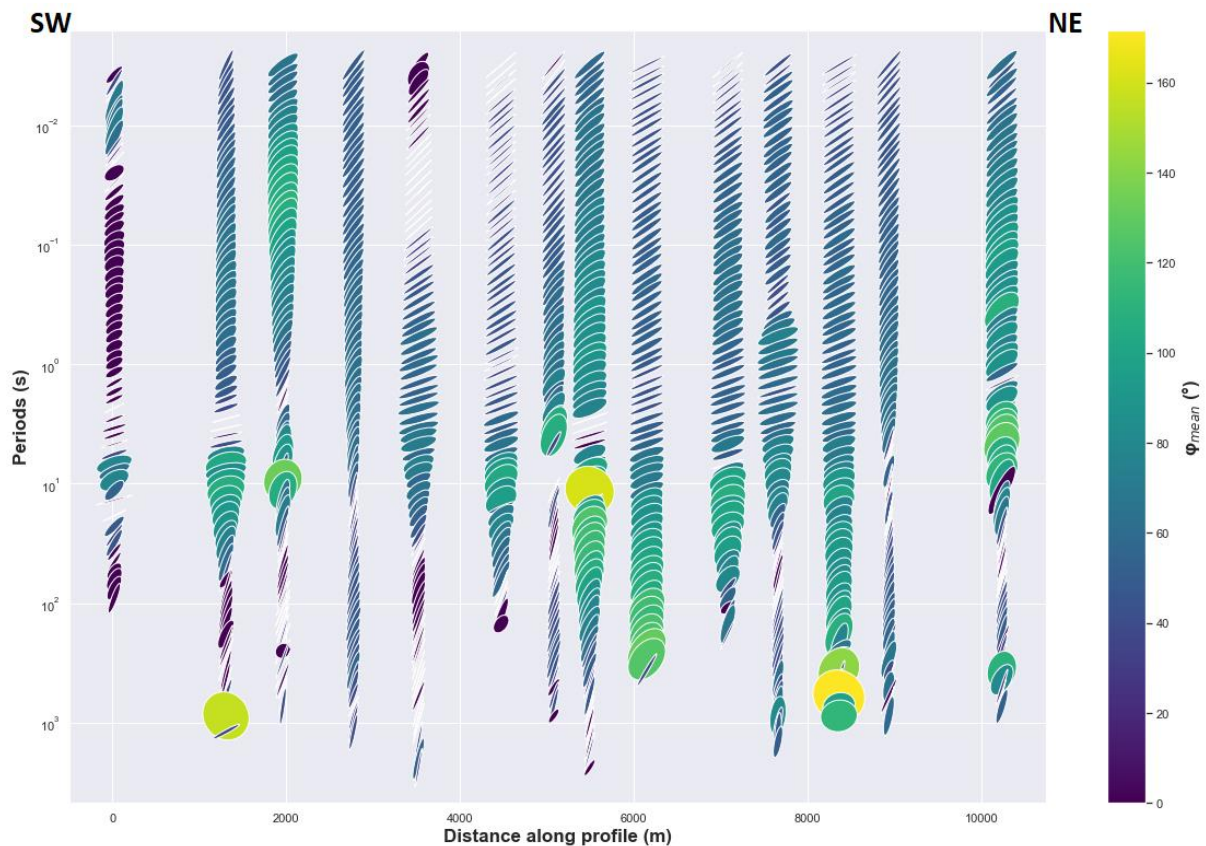


Fig.3.7. Pseudo-section of phases tensor ellipses along 2D profile MT sites (Fig. 3.1).

3.4.2.3. Induction vectors

Orientation of the induction vectors can be related to and depend on the presence of electrical anisotropy or lateral variation of the resistivity and the regional geoelectric strike direction. If the latter is not parallel to the eventual inferred anisotropy direction, it can also influence the direction of the induction vectors (Heise and Pous 2001; Heise et al. 2006). In case where phase split and/or phase tensor ellipticity are generated by a lateral conductivity gradient that also generates

induction vectors, a consistent correlation should be observed between the high magnitude induction vectors, ellipticity of the phase tensor and phase split (shown respectively in Fig.3.8, 3.7 and 3.6). High magnitudes induction vectors seem to be confined to the intermediate periods and appear in a discontinuous form rather than in a lateral and continuous form that could be related to a large single 2D heterogeneity. That means the high magnitudes induction vectors appears as a localized and isolated conductors along 2D profile having more elongated vertical scale rather than the lateral scale particularly at center of the rift (Fig.3.8). This pattern can also be related to the noise or uncertainty of magnitude induction data (Appendix B). On the other hand, a continuous phase split and consistent ellipticity are evidenced for the intermediate and long periods (Fig.3.6 and 3.7) along the same 2D profile. High magnitude induction populated for the intermediate periods may explain high conductivity contrast related to the variation of geoelectric strike of short periods to the long periods, which corresponds to the two different directions of anisotropy (Fig.3.7). Also, the induction vectors may be deflected from isotropic layer to anisotropic layer or from two anisotropic medium having different anisotropy direction where anisotropy period dependent is generated by the magnitude of conductivity gradient or discontinuity between the two medium (Heise and Pous 2001). The latter affirmation may be hypothesized in the Asal rift case and that is why we have high magnitude induction vector at the intermediate periods between the first anisotropic medium corresponding for short periods and the second anisotropic medium for long periods. Additionally, general pattern of low magnitudes induction vectors can be observed where a mean geoelectric strike is well defined for each of both long and short periods (Fig.3.3, 3.4, 3.7 and 3.8). Consequently, with this lack of correlation and the fact that 75 % of magnitude induction vectors data are less than 0.2 (which can be interpreted as low values) unless those related to the increase of uncertainty (Appendix B), the anisotropy signature explains this data pattern and the idea that high induction vectors are generated by lateral conductivity gradient can be excluded in this case. However, another possible explanation of the mechanism that can induce the high magnitude induction may be associated by the presence of oriented conductive dyke that intrudes inside relative resistive anisotropic medium, which in turn generate high magnitude of conductivity gradient between the conductive dyke and relative anisotropic medium. Evidence of vertical conductive zones that could be associated with dyke will be presented in the next section of the 2D inversion models.

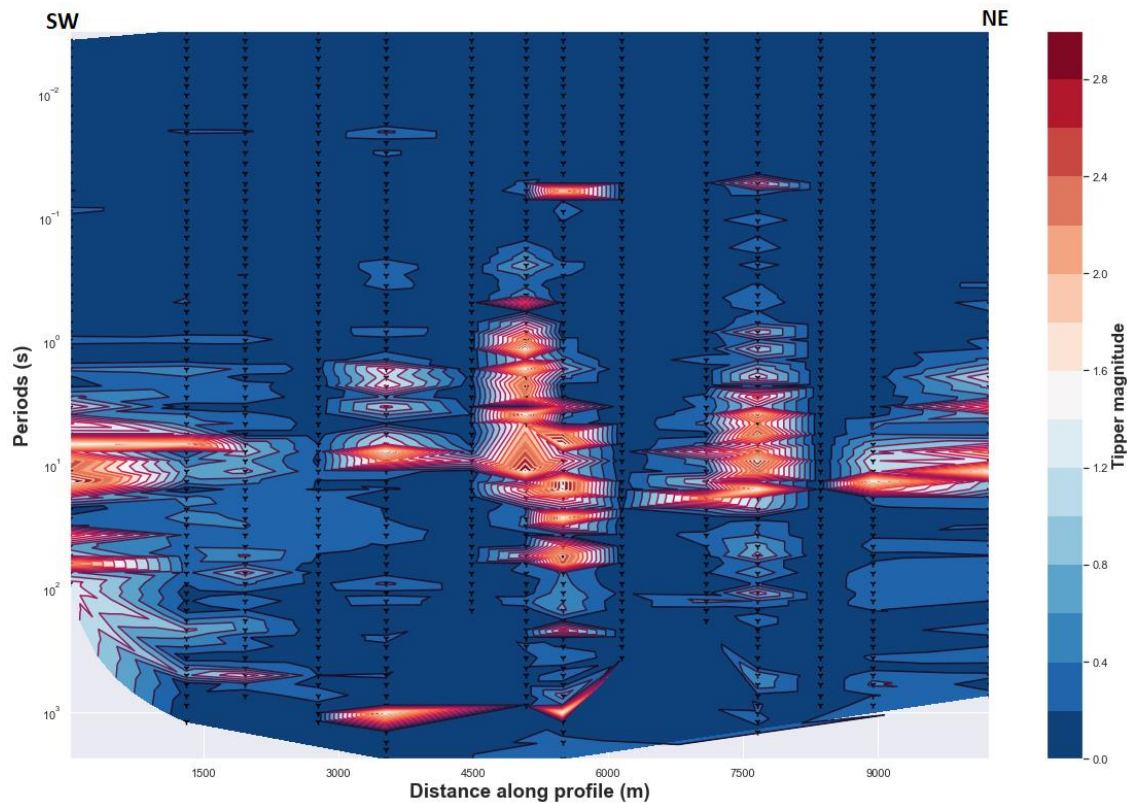


Fig.3.8. Magnitude of the real induction vectors.

3.4.3. 2D Inversion models

Prior to conducting a 2D inversion, a mean geoelectric strike of N45E direction was considered for the inversion models. Then different inversions models were conducted separately. Thus, inversion models of TM (transverse magnetic field parallel to the structure or B polarisation), TE (transverse electric field parallel to the structure or E polarisation), invariant model and TE-TM (joint inversion of TE and TM) modes were run and data are rotated to a mean strike of N45E. The choice of geoelectric strike is not relevant for the derived apparent resistivity from the invariant impedance tensor as the quantity is invariant under any rotation angle and remain the same regardless of the geoelectric strike/rotation angle (Szarka and Menvielle 1997; Tong et al. 2018). We used inversion code performing Occam philosophy with finite difference mesh. This code is Occam2D and is an open-source tool which is available on MTNet. The number of MT stations inverted is 14 as showed by the 2D profile across the rift in Fig.3.1. The width of mesh cell is fixed at 100 m where the number of total layers is 100. The initial model was set to a homogeneous half-space with a resistivity of 100 Ω .m. We used another inversion model with an initial homogeneous half-space of resistivity of 10 Ω .m. The best final 2D inversion that fitted the data

with the lowest RMS misfit was selected which corresponds to the initial model of homogeneous half-space of 100 Ω .m.

The results of the two models (TM and invariant) exhibit similar patterns of subsurface resistivity (Fig.3.9). While the TM mode is considered stable and robust, the TE data are very sensitive to the choice of geoelectrical strike and to the 3D effects of galvanic and inductive origin (Wannamaker et al. 2008). However, inversion model of TE data is presented in Fig.3.9 and the result is in agreement with the TM and invariant models. Although, high conductivity is observed at the center of the TE model at depth of 2 to 5 km. At the same time, the TE model displays lower resistivity at the shallow depth than the TM and invariant models (Fig.3.9). The mechanism that could generate this difference will be discussed in the section 3.5.2. Due to the restrictions or limit of available 2D anisotropic inversion code, a 2D inversion for isotropic models was used and followed the practical approach developed by Heise and Pous (2001). The latter authors proposed that a 2D isotropic inversion model could resolve well macro-anisotropy or structural anisotropy when joint inversion of TE and TM data are rotated to the anisotropy strike that coincide with the geo-electric strike direction and when the anisotropy ratio is higher than five. Joint inversion of TE and TM data rotated to N45°E is presented in Fig.3.9 while another joint inversion of TE and TM data rotated to N120°E is presented in Appendix B. As evidenced, the joint inversion model of TE-TM recovers the anisotropy signature as vertical conductive zone that can be interpreted as conductive dyke.

Resistivity pattern displayed in Fig.3.9 can be described as a succession of different subsurface resistivity from surface up to 10 km of the bottom model. The amplitude and phase of the observed impedance tensor data fit well with the model response (Fig.3.10). The dashed triangle indicates the position of the MT stations along the 2D profile (Fig.3.1).

Near the surface, the high resistivity **R1** layer can be related to the dry volcanic deposit close to the surface or to volcanoclastic rock with low water content. The thickness of **R1** is almost the same in the north-east of the rift for both the TM and invariant models (Fig.3.9) but at the center of the rift and in the south-west, the invariant model shows a relative increase of the thickness of layer **R1**. While both models (TM and invariant) seem to have **C1** layer of comparable width, it is a little thicker in the TM model. This high conductivity **C1** layer can be the result of fluid trapped in the host rock. The **C2** and **C3** layers have a wider extension in the TM model than in the invariant model and their relative high conductivity could be interpreted as aquifers. The resistivity contrast between **R2** and **R3** can be related to the difference between a high resistive rock R3, which was perturbed by a localized hot ascendant material originating from the center of the rift that could be the expression of a magmatic fluid or melt having lower resistivity R2.

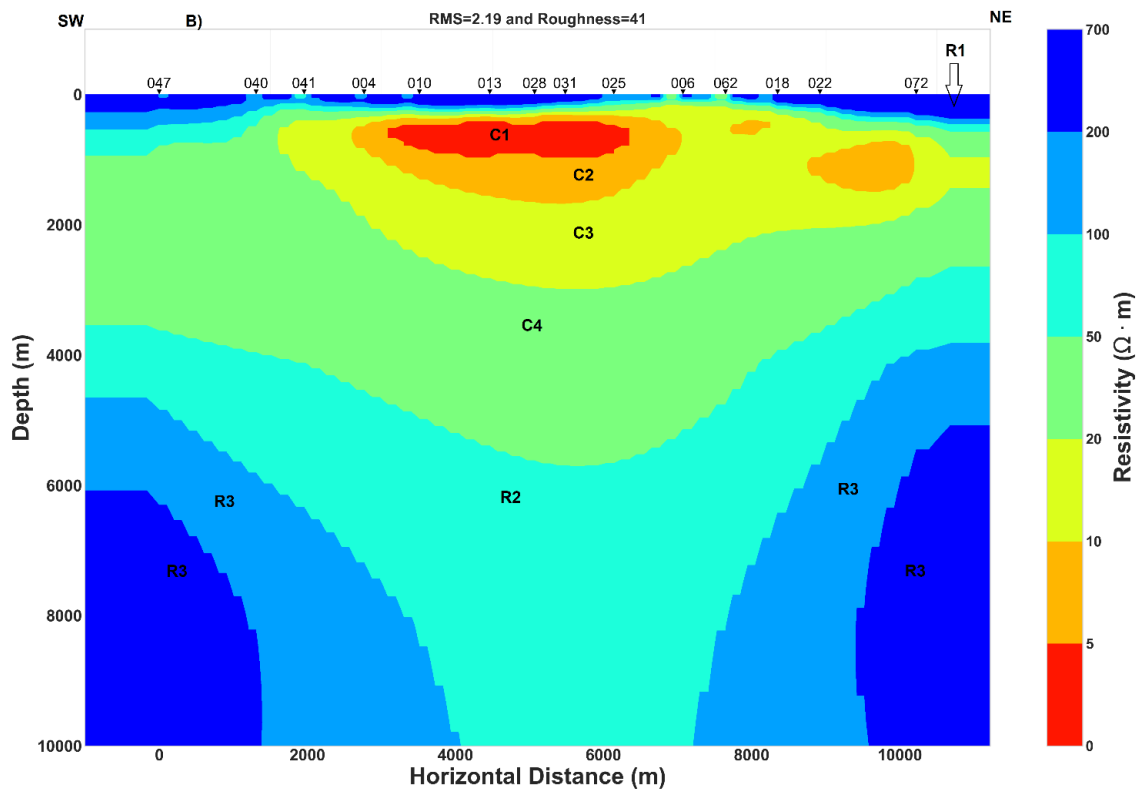
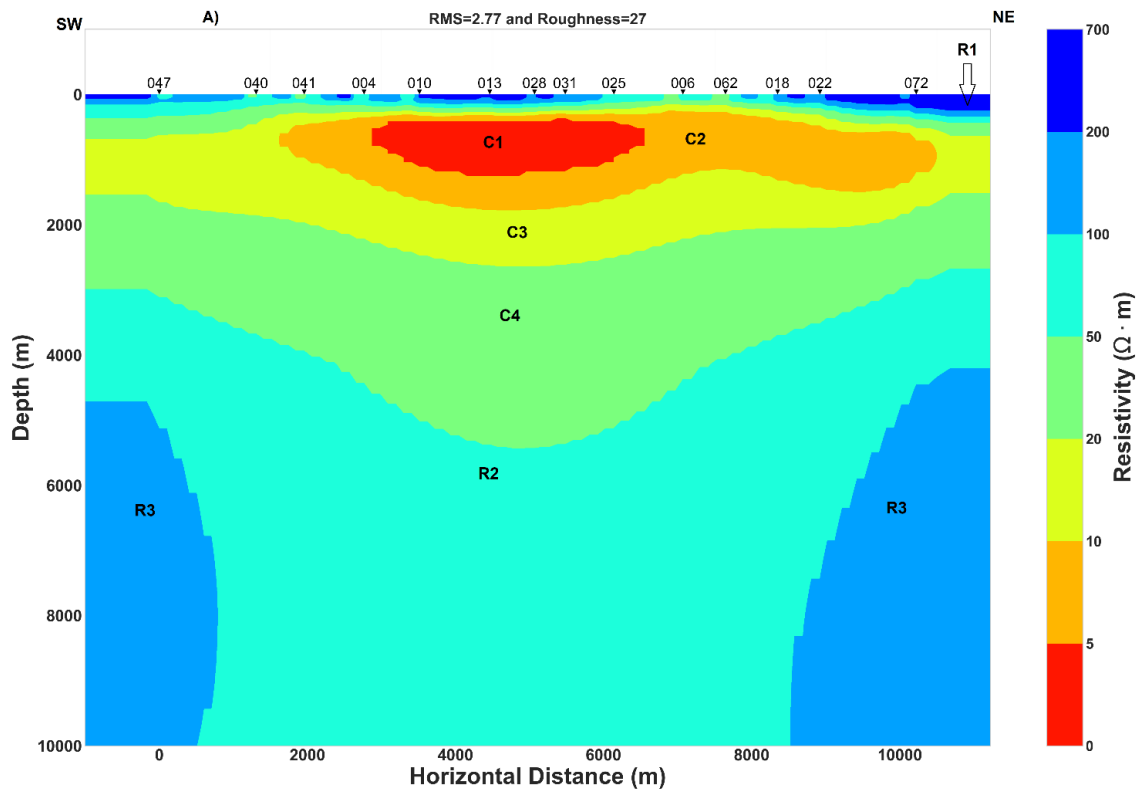


Fig.3.9. Cont.

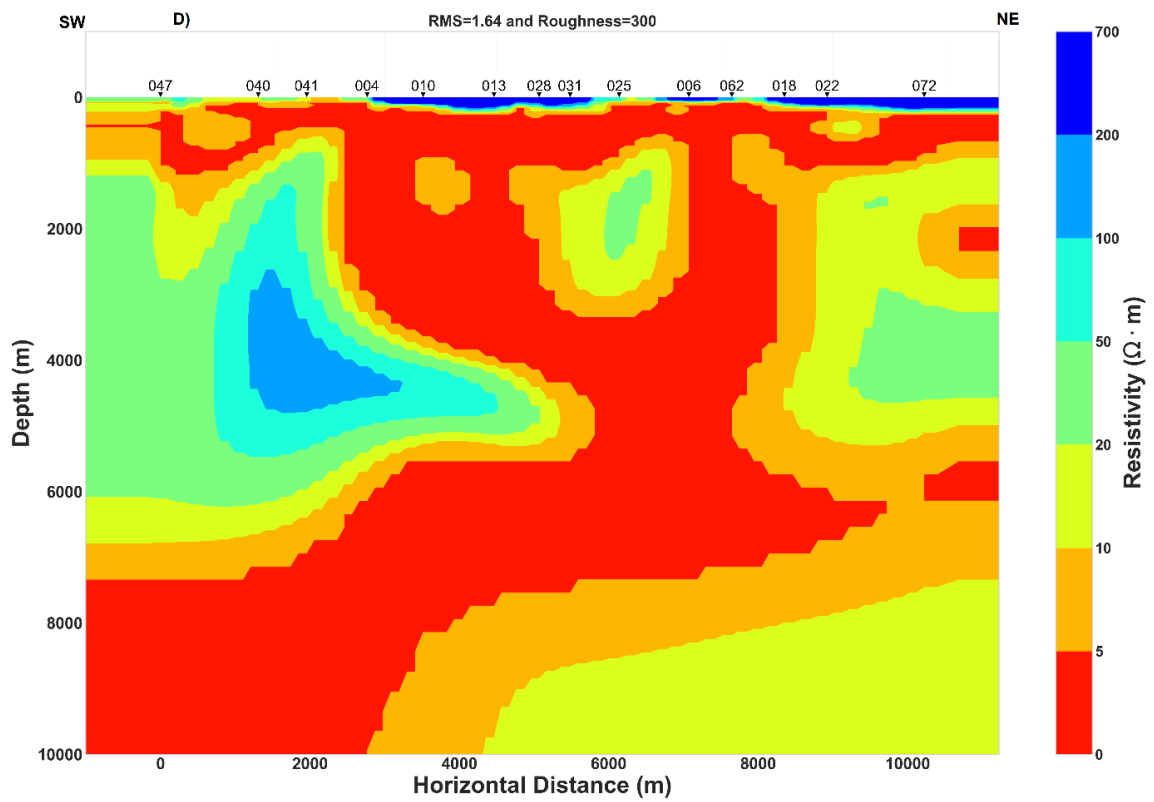
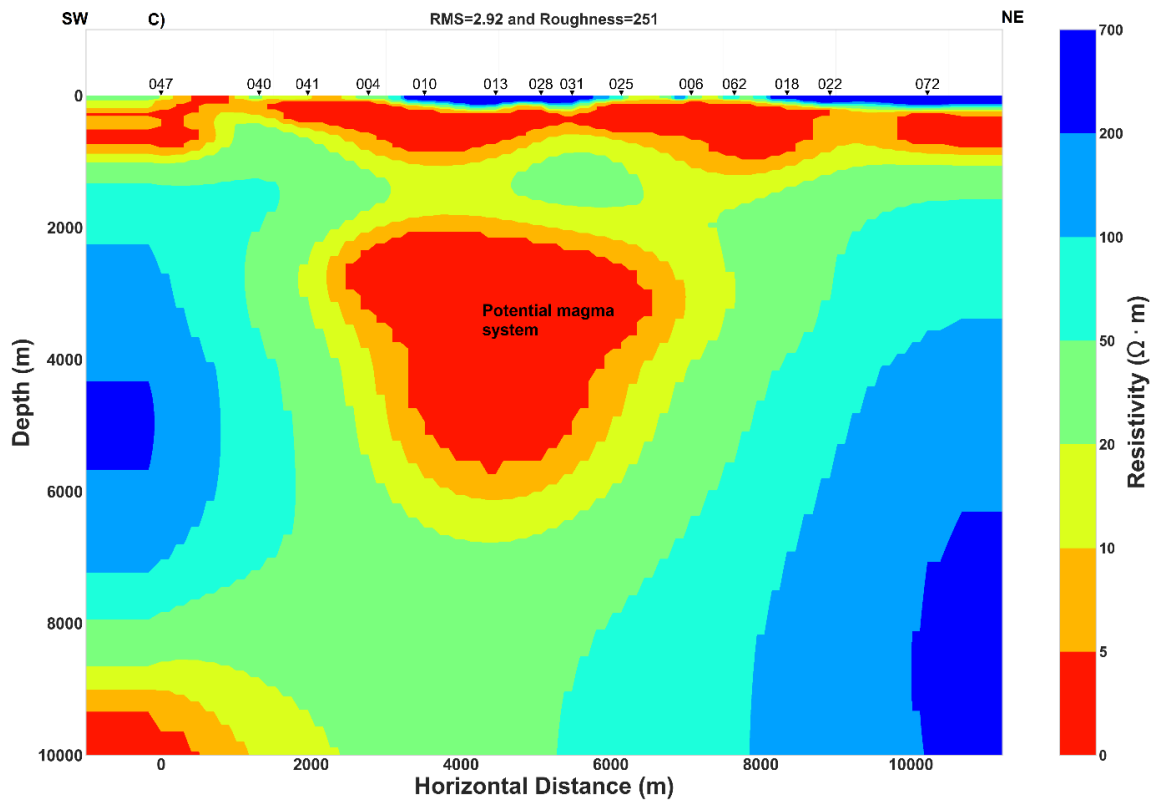


Fig.3.9. Inversion models. A) TM resistivity model, B) Invariant resistivity model, C) TE resistivity model and D) Joint inversion model of TE-TM.

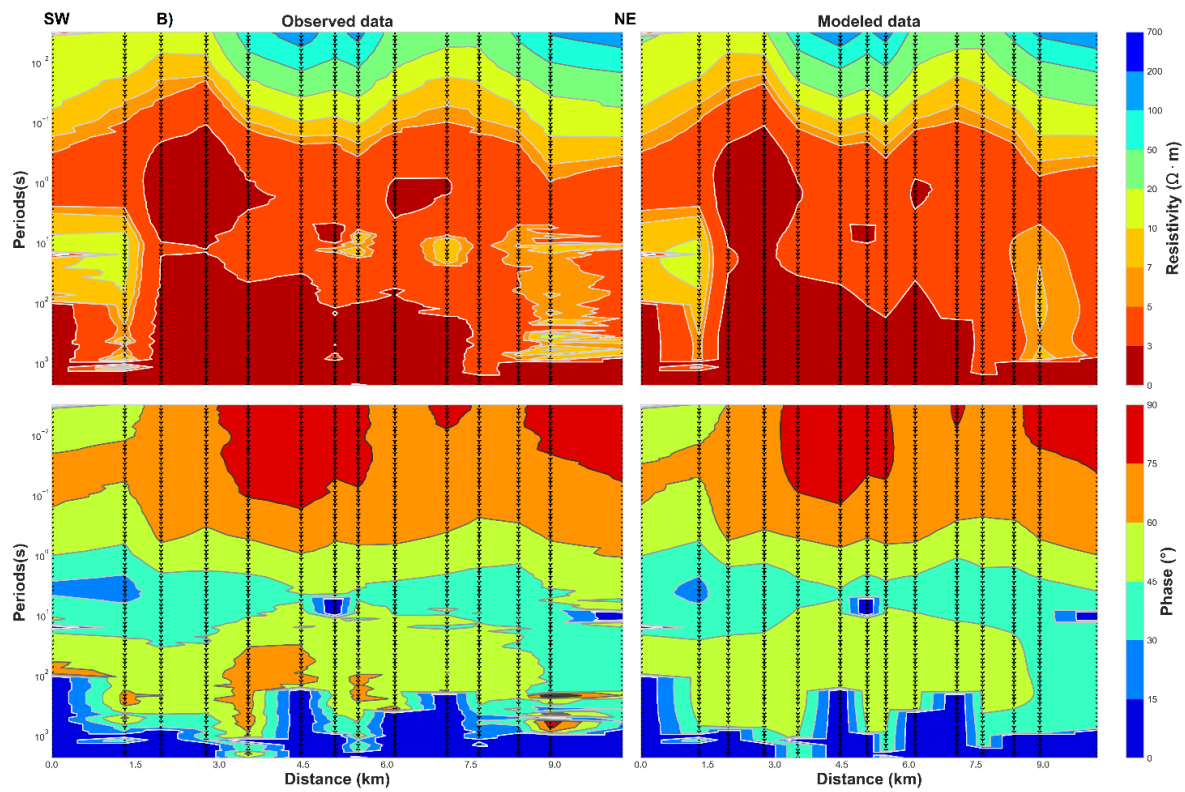
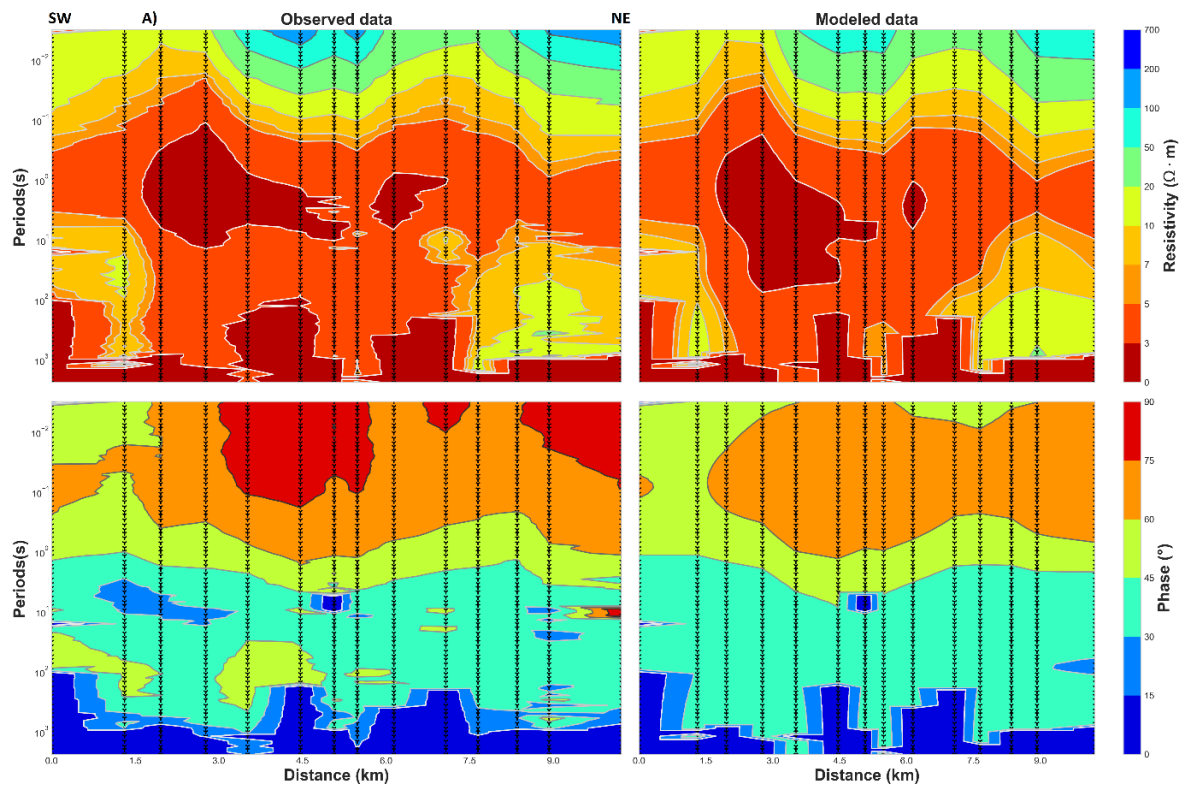


Fig.3.10. Observed vs modeled apparent resistivity and phase data. A) for the TM data and B) for TE-TM data.

Comparing our inversion results, the TE model and joint inversion of TE-TM model resolve better the conductive features (Fig.3.9 and Appendix B), while the invariant model and the TM model may resolve in reasonable way the conductive features (Fig.3.9). The same pattern and characteristic of TE, TM, joint inversion of TE-TM and invariant models was found by Pedersen and Engels (2005). Also, the invariant model is less affected by galvanic distortion and is independent of the value of geo-electric strike and would be the best model. Additionally, previous studies concluded that stable TE inversion model or joint inversion model of the TE and TM data can better resolve both the resistive and conductive feature (Wannamaker et al. 2008; Gómez-Treviño et al. 2014) and similar conclusions can be inferred from the results illustrated in Fig.3.9.

Results of two joint inversion of TE-TM data, one rotated to the strike N45°E (Fig.3.9) and another one rotated to the strike N120°E (Appendix B) display high conductivity areas at great depth. Those results with the 2D inversion models of TM, invariant and the TE model (Fig.3.9) have some similarities and consequently, regional 2D conductivity structure approximation can be considered to explain the subsurface geoelectric structure beneath the Asal rift.

3.5. Discussion

3.5.1. Geoelectric strike direction dependent of the periods

- Comparison of geoelectric strike with strike determined from others studies

Magnetotelluric data analysis allowed us to infer the subsurface conductivity structure with evidence of defined geoelectric strike and anisotropy direction beneath Asal rift. The strike orientation estimated from the phase tensor for short period is north-east close to N40°E, whereas for the long periods it is north-north-east (Fig.3.3). While the geoelectric strike derived from both the invariant impedance and decomposition model showed the same results, a mean strike direction around N120°E can be deduced for the long periods (Fig.3.4). The majority of the induction vectors are parallel to the geoelectric strike derived from phase tensor with low skew angle (Fig.3.5). The latter is generally described as a consequence of a dominant 2D regional conductivity structure in the area (Caldwell et al. 2004; Booker 2014). Structural, geological and bathymetry studies conducted in the Asal-Ghoubbet indicated average strike of fissures and normal faults of N125°E (Stein et al. 1991; Manighetti et al. 1998; Audin et al. 2001). Seismicity was recorded from November 6th to 10th, 1978 with epicenters trending along a N120°E alignment in the Ghoubbet Bay (Manighetti et al. 1998; Audin et al. 2001), which is believed to correspond to the direction of the dyke injection. The seismicity continued for 60 days after the 10 November 1978 event, in the eastern part of the Asal-Ghoubbet rift, particularly in the Ghoubbet Pass and the transfer zone between Asal-Ghoubbet and Tadjourah submerged rift segment (Manighetti et al. 1998). In addition, telluric field polarized in the direction of N100°E was determined by Mlynarski and Zlotnicki (2001) with the Telluric-Telluric (TT) method. This strike is close to the

average strike determined from decomposition model and impedance invariant for the long periods and can be considered an approximate strike with the strike calculated from the phase tensor for the long period. Furthermore, it is surprising to note that some MT stations have an average strike of N120°E for the short periods (approximately at the depth of upper and lower crust) and those MT stations are close to the Major and Minor faults (Fig.3.1 and 3.4). This indicates that a causal relationship between diking, striking, fracturing and dipping may exist. Moreover, in both Asal and Ghoubbet, normal faults are dipping to the north-east direction (Stein et al. 1991; Audin et al. 2001) and the mean strike calculated from all dimensionality analysis for the short-intermediate periods is approximately north-east and north-north-east (Fig.3.3, 3.4, 3.5 and 3.7). Seismological studies have proposed a dipping angle of N50°E for normal faults far from the rift axis and also suggested sub-vertical dipping normal faults close to the rift axis (Dobre et al. 2007). Kinematics and 3D dimensional deformation of Fieale volcano (Fig.3.1) over the past 300 kyr indicated a spreading rate range of 17-30 mm/yr in the N40°E direction that mainly accommodates the separation between Arabia and Somali plates (De Chabaliere and Avouac 1994).

- **Origin and possible mechanism inducing geoelectric strike in a rift context**

Asal rift results from the westward propagation of Aden ridge and has an approximate extension rate of 17 mm/yr in the north-east direction, with many fissures and normal faults striking to the N120°E direction (Manighetti et al. 1998, Vigny et al. 2007). It can be argued that geoelectric strike estimated in this study and the strike determined from others studies (Stein et al. 1991; Audin et al. 2001; Dobre et al. 2007) may have a common origin. It is likely safe to suggest that at the short periods, the geoelectric strike is the result of conductive shear zones which form as echelon structures, and are perhaps cracks or fissures filled by fluids at shallow to intermediate depth corresponding to the upper and middle crust. Those cracks or fissures are mainly accommodated by the extension rate resulting from the horizontal deformation beneath Asal-Ghoubbet into the north-east direction (~N43°E). Additionally, the geoelectric strike estimated for the long periods is more related to the vertical deformation of the Asal rift (at lower lithosphere and/or upper mantle scale) due to the predominant activity of dyke/magma intrusion acting as a highly conductive medium. Then, dyke intrusion triggers the evolution and development of dipping active normal faults acting as conductive zones between the top of the dyke (the maximum depth reached by the magma pressure starting from the great depth to shallow depth) and the faults locations at the surface. This latter mechanism contributes to the subsidence of the volcanic rocks and may explain that both tectonic and magmatic activity controls the rift deformation and the rifting process at different depth scale. Geoelectric strike can be used to reveal structural hints at depth, lateral variation of shallow or deep geological structures, shear zones and can be used to

understand the mantle flow. In a similar geological rifting context of Asal rift like the Kenya rift located in the East African Rift system, geoelectric strike that varies with periods and with site location has revealed hidden structures at depth where the geoelectric strike of north-south for short periods is interpreted as conductive sediments and the north-west – south-east striking for the long periods was interpreted as conductive lineaments (Simpson 2000). Moreover, in an extensional area of Great Basin-Colorado, geo-electric strike determined from the MT phase tensor was interpreted as a faulting trends in the upper-middle crustal basement controlling the Paleozoic and Mesozoic uplifts (Wannamaker et al. 2008). That latter authors found a good correlation between the direction of induction vectors and phase tensor strike to justify the presence of dominant 2D structure as in our case (Fig.3.5), which is an interesting similarity between the two extensional areas.

3.5.2. Two main directions of anisotropy varying with depth

- Presence of 2D anisotropic structure

A straightforward method to identify electrical anisotropy is the presence of consistent phase tensor split with low values of magnitude induction vectors (Kellett et al. 1992; Heise et al. 2006) as shown in Fig.3.6 and 3.8 for short periods. But for the long periods, degree of consistent phase split is more important (Fig.3.6) and a moderate to low values of magnitude induction vectors is present for periods greater than 70 s (Fig.3.8) that can be interpreted again as anisotropy effect from 2D anisotropic structure or 2D heterogeneity. Furthermore, the high regional skew is influenced by induction and is related either to 3D inductive effects or to anisotropy (Bahr 1987; Eisel and Bahr 1993; García Juanatey et al. 2019). Consistent correlation between high regional skew and the high magnitude induction vectors (Fig.3.2 and 3.8) may result from a common origin that could be the consequence of the 2D anisotropic or 3D structure in the study area. Indeed, we should not expect consistent and slightly varying geoelectric strike for the corresponding range of periods if a 3D conductivity structure was the origin of the consistent correlation between high regional skew and the high magnitude induction vectors and we argue that the common origin between them could be the anisotropy signature notably 2D anisotropic structure. Because, the moderate to low value of magnitude induction vectors exclude the assumption of the presence 1D anisotropic structure in which the absence of tipper is expected (Heise et al. 2006; Booker 2014). For the short periods, the consistent ellipticity of the phase tensor with the relative moderate values of geometric mean of the principal values of the phase tensor that has a well-defined geoelectric strike of N43°E (Fig.3.7) in one side, and the minor phase difference between the two polarizations (Fig.3.6) in the other side, can be interpreted together to linked to the presence of regular and homogenous anisotropic medium. Additionally, the assumption of absence 2D isotropic structure as in our case is evidenced by the values of phase tensor skew

angle (Fig.3.5) greater than zero (Booker 2014). The latter author also suggested that a nonzero phase tensor skew angle can indicate structure having azimuthal anisotropy varying with depth if 3D isotropic structure can be excluded. And that suggestion is what can be proposed in Asal rift because a well-defined geoelectric and anisotropy directions in both short and long periods can be inferred (Fig.3.7) and a general low value of regional skew which is produced by 3D inductive structure (Fig.3.2). For the long periods, the consistent moderate phase split, high regional skew and the high geometric mean angle of the principal value of the phase tensor (Fig. 3.2, 3.6 and 3.7) notably for the MT stations close to the center of the rift (rift axis) can be associated to a pattern resulting from anisotropic medium which is more heterogenous, irregular and more conductive than for the MT stations located at the margins of rift (far from the rift center). A similar pattern was found by Bahr et al. (2000) in their study to argue that the middle crust conduction mechanism is governed by electronic conduction due to the graphite rather than electrolytic conduction.

- **Origin of electrical anisotropy and the role of stress field**

There is no published scientific work until now that studied crustal and mantle anisotropy in the Asal rift. However, in case where consistent correlation between the geoelectric strike direction and the anisotropy direction exist as demonstrated in this study, it is likely a reasonable argument to suggest the presence of both paleo-stress field and actual stress direction in a geodynamic context like Asal rift where dynamic plates motion and magmatic activities co-exist and generate different direction of stress field (Stein et al. 1991; Manighetti et al. 1998; Doubre and Peltzer 2007; Smittarello et al. 2016). In others words, stress field can change as plates motions can change their direction. Thus, it is likely possible to advance that electrical anisotropy direction in Asal rift is mainly associated to the dominant stress field of plates motion. Indeed, Asal rift is located at the junction of the three diverging plates (Somali, Arabia and Nubia), which result the westward propagation of Aden ridge, the jump of the Red Sea ridge into Afar depression and their interaction can change, rotate or alter the direction of plate motion over the geological time. Existence of relic strain, possibly resulting from ancient continental collision processes, is interpreted to have induced a general alignment of olivine down to mantle depths beneath the continental rigid plate which in turn generally produce electrical anisotropy direction coincident with the surface trend deformation pattern that was preserved since the last tectono-thermal event responsible for the deformation (Padilha et al. 2006). Additionally, chemical and petrological analysis of Asal rift lavas indicated a presence of olivine with important size up to 1 cm (Pinzuti et al. 2013) and it is likely possible that hydrous olivine may exist in the upper mantle of the Asal rift that can cause electrical anisotropy as proposed previously in similar geodynamic context by Bahr and Simpson (2002). Thus, the preserved traces of past and remanent directions of magmatic-

tectonic activities can be determined from joint analysis of the geoelectric strike and anisotropy direction as proposed previously (Bahr and Simpson 2002; Padilha et al. 2006; Brasse et al. 2009). Moreover, combined magmatic-tectonic activities play important role to define the stress field direction where tectonic activity accommodates the extension, the preferred emplacement direction of recent volcanic materials coming from the cooling magmatic intrusion. Also, both magmatic-tectonic activities can likely change the orientation of old subsurface geological materials to the direction of the existing maximum stress that can be the maximum conductivity direction.

- **Electrical anisotropy direction related to the plates motion**

In others tectonic contexts like Asal rift, geoelectrical strike and electrical anisotropy direction were correlated and electrical anisotropy direction was interpreted to be linked directly or indirectly to plate motion direction, as discussed next. For instance, Frederiksen et al. (2006) found consistent correlation between shear wave splitting (SKS) direction and geoelectric strike direction with the plate motion direction, and interpreted these observations as an upper lithosphere that contain thin anisotropic layers related to the paleo-subduction and a uniform and ductile anisotropic lower lithosphere. Also, consistent phase splitting and low magnitude induction vectors with a geoelectric strike direction oblique to the present day Indian plate-movement were associated to an anisotropic mantle (Shalivahan and Bhattacharya 2005). The discrepancy between the geoelectric strike and the actual Indian plate-movement direction was interpreted by the effects due to the heterogenous and complex convection of the mantle or a resistance to mantle flow by the actual stress field of plate motion (Shalivahan and Bhattacharya 2005). In active extensional at the Great Basin province of north-central Nevada, geo-electrical strike direction parallel to the initial direction of extension was found with small values of magnitude induction vectors that was interpreted as consequence of electrical anisotropy direction (Wannamaker 2005). Also, high conductivity direction which is consistent with the shear wave splitting was found to be close to the direction of plate motion of the western Europe (Prawirodirdjo and Bock 2004). Seismic activity and surface deformation produced by injection of magma into dykes are often occurring during rifting episodes where the velocity of plate opening is mainly controlled by the magmatic intrusion (Einarsson 1991) and intrusive activity mainly controls the faults system activity where magma plumbing system is key of primary control on the rifting process (Medynski et al. 2016).

- **Electrical anisotropy direction related to the fluid-filled in oriented fractures**

In this section we discuss if stress field that induces electrical anisotropy direction is likely a possible mechanism that can also generate fluid-filled oriented fractures or in shear zones in the

study area. In the transpressional regime, existence of shear zones with preferred orientation inducing electrical anisotropy direction is not unexpected. Indeed, in the early stage of transpression region, degree of progressive shearing zones interconnected along strike may increase with the degree of electrical anisotropy and hence shears may act as elements of fluid-driven weakening and growth (Cox et al. 2001). Upper mantle electrical anisotropy is mainly related to the presence of bound water allowing the diffusion of hydrogen (Karato 1990). Although, others mechanism as the presence of aligned high conductive mineral such wet olivine or hydrous olivine may cause electrical anisotropy in the upper mantle (Bahr and Simpson 2002). In contrast, dry olivine is only weakly anisotropic (Duba and Constable 1993). Finally, it is surprising to note that electrical anisotropy directions for both short and long periods determined in our study (Fig.3.3 and Fig.3.7) are in agreement with the electrical anisotropy direction determined in central Germany by Roux et al. (2011). The latter authors found that electrical anisotropy for the lithosphere is close to E40°N and electrical anisotropy direction of the asthenosphere is close to E72°N. Moreover, in the same area of central Germany, the origin of high electrical anisotropy observed, was interpreted to be likely controlled by hydrogen diffusion (Gatzemeier and Tommasi 2006; Roux et al. 2011). Thus, it is possible to hypothesize that the same condition mechanism associated to the hydrogen diffusion in the context of Asal rift. Electrical anisotropy direction was found in the shear zone of Great Slave Lake in Canada (Wannamaker 2005) and the graphitic films along shear zones and wet olivine may be the causes of enhanced electrical anisotropy. Also, another possible explanation is that subsequent retrograde metamorphism can remobilize graphite during fluid-based leaching and redeposit it as vein zones or tabular textures (Wannamaker 2005). Although, presence of over pressured fluid and hydrated clays at the interface of tectonic plates inferred from 3D MT inversion were suggested to be the major factor controlling plate coupling (Heise et al. 2013). Recently, in the Otway Basin of Australia, electrical anisotropy direction inferred from MT data was interpreted in terms of fluid-filled fractures oriented favourably for reactivation in the current stress field that resulting in enhanced electrical and hydraulic conductivity (Kirkby et al. 2015).

3.5.3. Subsurface conductivity structure and associated interpretations

- Hydrothermal system and fluid circulation

Results from 2D inversion show the conductivity structure under Asal rift, with a general pattern of relative conductive environment (C4 and C3) bounded at the bottom by dipping moderately resistive layers (R2 and R3) and at the top by highly conductive layers (C1 and C2). Similar structures found in hydrothermal systems and geothermal prospect zones (Meju 2002; Nurhasan et al. 2006; Spichak and Manzella 2009; Usui et al. 2017) were interpreted as shallow hot aquifer or cap rock that covers high enthalpy hydrothermal/geothermal reservoir. In the present case, the

latter is likely fractured due to the extension rate of rift and the presence of approximate horizontal electrical anisotropy direction and could host significant quantities of fluids (liquid or steam) in the rift zones, where the activity of an overpressure magmatic reservoir at the center inject either a hot material into dyke or magmatic fluid. The latter is often considered as the source of vertical heat mass transfer that can migrate laterally toward the rift segment termination (Ebinger and Casey 2001; Doubre and Geoffroy 2003; Keir et al. 2009).

Surface deformation studies (Cattin et al. 2005; Doubre and Peltzer 2007; Vigny et al. 2007) and related interpretations of the presence of deep hydrothermal fluid circulation will be compared with the conductivity structure model developed in this study (Fig.3.9). Numerical modelling results of 2D thermo-mechanical (Cattin et al. 2005) yielded temperatures consistent with the measured temperatures of deep geothermal wells. However, some disagreement between measured and modeled temperature of well A5 located close to the center of the rift (Fig.3.1) was interpreted as local thermal effects generated by the fluid circulation (Cattin et al. 2005), which corresponds to the high conductance zones of the three conductive layers C2, C3 and C4 (Fig.3.9). Furthermore, Doubre and Peltzer (2007) noted that a faulting process, mainly controlled by deep hydrothermal fluid circulation coming from an overpressurized magmatic system, injects fluid into fractured zones connected to the deep part of the faults and hence triggers in a decrease of the effective normal stress on the locked section at depth of faults which in turn induces faults slip. These authors focused their study on active faults located at the center and at the north-east of the rift. Their results corroborate to the width extension of conductive layers C1, C2 and C3 between the center and the north-east part of the rift (Fig.3.9). In addition, as proposed by Vigny et al. (2007), 70 % of the actual deformation beneath the rift is concentrated toward the northeastern part rather than the southwestern part. The northeastern part was recently interpreted as a preferred zone of fluid filled fractures with a potential deep hydrothermal fluid circulation at shallow crust that can likely be a geothermal target (Hassan Aden et al. 2021). Groundwater circulation between Asal lake and Ghoubbet Bay inferred from self-potential (SP) measurements in the study of Mlynarski and Zlotnicki (2001) proposed a schematic representation of fluid circulation where two large zones at the shoulders of the rift have positives SP anomalies that were interpreted as slow and rewarmed fluid flow, whereas a narrow zone with negative SP at the center of rift separating the two previous zones is more related to a rapid and cold fluid flow. The latter study is in good agreement with our resistivity model, where high conductance of the superposed conductive layers (C2, C3 and C4) is clearly visible at the center whereas at the shoulders of the rift, thickness of those layers decreases. We propose an alternative explanation of the general pattern of fluid circulation that is related to the interaction of a deep heat source likely located in the center with a wide hydrothermal reservoir (C3 and C4) that responds to the pressure changes of fluid-filled rocks deformed due to the extension of the

rift, which create the development of shear zones and fractures at the crust where dyke can intrude. Considering both the low geothermal gradient temperature of A5 well (between 500 and 1200 m depth; see Fig.2.2 in Chapter 2) located in the center of the rift (Zan et al. 1990; Houssein and Axelsson 2010) and associated interpretation of the negative SP anomaly in the same area (Mlynarski and Zlotnicki 2001), it is possible that the high conductivity of C1 layer can be interpreted as a saline (implying high conductivity) aquifer with fluids flowing toward Asal Lake through the faults and fracture networks at the center of the rift.

- **The importance of conductive major normal fault H**

Another interesting feature is the major normal fault **H** (Fig.3.1) which is close to MT station **028** (Fig.3.9). The hanging wall of this fault has been qualified as hydrogeological barrier separating the rift to a conductive northeastern zone and relative resistive southwestern (Hassan Aden et al. 2021). The latter study is in agreement with the 2D conductivity model developed in this work (Fig.3.9), where the extent of C2 layer is more important in the northeastern zone. Additionally, the synclinal form of C3, C4 and R2 at the center close to the vertical projection of **H** fault at great depth (Fig.3.9) may suggest a possible direct link of a sub-vertical dipping and sub-vertical dyke in an approximate north-south striking direction, as inferred by dimensionality analysis at long periods (Fig.3.3, 3.4 and 3.5). We argued that the **H** fault is the main active fault in Asal rift, and it is likely connected to a deep hydrothermal system which change the hydrostatic and lithostatic pressure when the state of the underlying overpressure magma reservoir at the deeper level change. This may be evidenced by the high conductance of conductive layers (C2, C3, C4 in Fig.3.9) observed at the center of rift close to the vertical projection of **H** fault, and the TE and TE-TM models (Fig.3.9 and Appendix B) display high conductive medium between 2 and 5 km depth for the same zone. Similar pattern where high conductance of conductive layer was associated to a reservoir hosting the source of deformation and where upward release triggers micro-earthquakes were found for a hydrothermal system in Japan (Nurhasan et al. 2006). In the hydrothermal system of Unzen graben of Japan, vertical conductive zone having a width of 2 km and an extend down to below 4 km was also interpreted as interconnected fractures network generated by the main active normal fault in which magmatic volatiles are supplied from a deeper pressure source causing surface deformation (Triahadini et al. 2019). Resistivity structure estimated by new 2D inversion models allowed to resolve narrow conductors zones beneath three main faults in the central Japan (Usui et al. 2021). The later authors interpreted the narrow conductive zones under faults as localized ductile shear zones with highly connected fluid which are responsible for the strain accumulation along the active faults. Additionally, in a rift zone, steep crustal-scale faults inferred from MT data analysis were interpreted as preferred path that connect

between the deep dominantly magmatic fluid and upper crustal meteoric regime (Wannamaker et al. 2008).

- **Potential magma reservoir inferred from joint interpretation**

We tried to infer the presence of magma reservoir at depth with joint interpretation of the 2D conductivity model proposed in this study and previous studies. The passive seismic study of Doubré et al. (2007) revealed that the main volcanic activity with the most seismicity recorded under the rift was concentrated beneath Fieale caldera zone (Fig.3.1). Those authors interpreted it as volume of hot rocks where the main seismogenic crust lie between 3-5 km depth overlying above a deeper magma chamber. They argued that the deformation due to the volume of hot molten rocks is mainly aseismic and that the brittle to ductile transition is shallower at the center of the rift than at its shoulders. Thus, in this case the deformed hot molten rock may contain open fissures/fractures that can potentially induce seismicity inferred at depth. Seismic reflection profiles suggested low velocity mantle beneath the Asal rift where the presence of the dyke under the rift axis was inferred (Manighetti et al. 1998). Geochemical and petrological constraints revealed evidence of shallow melting path beneath the rift axis and deeper melting path at the rift shoulders (Pinzuti et al. 2013). Moreover, molten rock or magma reservoir are expected to be highly conductive medium due to the high temperature but neither beneath Fieale Caldera nor beneath the center or close to the rift axis can be found a high conductivity anomaly for the invariant and TM models at great depth (Fig.3.9). Consequently, magma reservoir and/or molten rocks doesn't exist at depth surveyed by the 2D conductivity of the invariant and TM models or those models are not able to detect magma that would result in a high conductive medium. Moreover, the TE and TE-TM models (Fig.3.9 and Appendix B) are able to resolve a high conductivity anomaly at the center of rift between 2 and 5 km depth that may correspond to the magma reservoir. Since the last 30 kyr, the rifting process reached a steady state and a cooling magma is expected under the rift (Stein et al. 1991; Manighetti et al. 1998; Vigny et al. 2007). In this case, a cooling magma intruding the shallow crust during the past magmatic-tectonic events will likely be imaged as relative resistive medium having approximate electrical properties of the embedding geological layer (Partzsch et al. 2000). So, we argue that R2 relative resistive layer (Fig.3.9) may contain potential molten rock based on the following elements. Sub-vertical dipping of R2 can be observed at the center of Asal rift with significant conductance, whereas the conductance decreases at the shoulders of the rift suggesting lateral migration of the injected hot material into dykes. Also, the conductivity contrast between R2 and R3 can indicate a considerable petrophysical properties contrast, notably the temperature which in turn affect the density where the low conductive layer may correspond to the layer of high-density. In this scenario, buoyancy variation generated by the density difference facilitate the migration of the

molten rocks from greater depth level to a shallow depth. And when the buoyancy force is not enough to maintain the upwelling magma reservoir to the shallow strata losing its buoyancy, the hot magmatic materials intruded forms a magmatic reservoir or intrusion at the corresponding depth.

It is surprising that most models of ground deformations (Stein et al. 1991; Cattin et al. 2005) proposed a maximum depth of 4 km from the surface reached by the dyke injection close to the center of the rift where lie the source of deformation which is consistent with the top of the R2 layer and the bottom of C4 layer (Fig.3.9). Vertical resistive structures at the center of Unzen graben in Japan was interpreted as cooled dyke that may have acted previously as volcanic conduit (Triahadini et al. 2019). However, the synclinal form of C4 and R2 can reveal the symmetrical lateral propagation of molten rocks to the shoulders of the rift. It is surprising that this symmetrical propagation can be observed at the surface of the rift where basalt flow vectors seem distributed with the same symmetrical propagation as evidenced in the structural map representation made by Stein et al. (1991). Additionally, potential magma reservoir inferred from our 2D resistivity models (Fig.3.9 and Appendix B) are in agreement with the depth of potential magma or molten rocks determined from the previous conceptual models of the Asal rift developed by Zan et al. (1990), Manighetti et al. (1998), and Doubre et al. (2007). The steep and vertical high conductive zone evidenced by the joint inversion model of TE-TM data (Fig.3.9 and Appendix B) may also be associated to a magmatic fluid pathway. The same pattern was recognized previously by Abdallah et al. (2020) with 3D inversion of MT data in volcanic context where a narrow vertical low resistivity range of about 10 Ω .m (as in our case, see Fig.3.9 and Appendix B). The low resistivity extended from 2 to 9 km at depth and was assumed to correspond to a magmatic fluid pathway. Moreover, many studies conducted in eroded rift zones, passive volcanic margins, slow-spreading mid-oceanic ridge and incipient spreading centers (East Africa) conclude that in the middle of the rift segments exist a central and shallow (< 6 km) magma reservoir that can inject hot material into dykes with magma migrating laterally toward the rift segment termination (Ebinger and Casey 2001; Doubre and Geoffroy 2003; Keir et al. 2009), where the velocity of plate opening is mainly controlled by the intrusion (Einarsson 1991).

3.6. Conclusions

Different methods of dimensionality analysis conducted in this work together with 2D inversion of 14 MT stations along a profile perpendicular to the rift axis allowed us to further understand geoelectric structure beneath Asal rift. Dimensionality analysis was found to determine the dominant geoelectric strike which depend on the periods of natural electromagnetic fields for both the short and long periods. For the short period, a mean strike of N43°E was estimated whereas

a dominant strike of north-south direction was estimated for the long periods. Additionally, electrical anisotropy direction aligned or parallel with the geoelectric strike direction for both the short and long periods was presented in this study. Joint interpretation of electrical anisotropy direction with previous studies demonstrate that anisotropy direction is mainly related to the paleo and actual stress field direction that controls the horizontal and vertical deformation of Asal rift. Electrical anisotropy direction in Asal can be linked to the dominant stress field of three diverging plates (Somali, Arabia and Nubia). However, the westward propagation of Aden ridge, the jump of the Red sea ridge into Afar depression and their interaction can change the direction of plates motion over the geological time which induce a preferred electrical anisotropy direction. The presence of well-defined geoelectric strike permits us to develop 2D inversion models (TM, invariant, TE and TE-TM mode), which justify regional 2D conductivity structure in the study area. Conductive layers in the crust (C1, C2, C3 and C4 in Fig.3.9) were interpreted to be shallow aquifer and potential geothermal/hydrothermal reservoirs, whereas the resistive layer at the bottom of the 2D model (R3 in Fig.3.9) is associated to the basement rocks. The dipping relative resistive layer (R2 in Fig.3.9) can be a magma system or magma domain which hosted molten rock.

For geothermal exploration, we suggest that future drilling can be at the center of rift close to the H Fault where the conductive layers have high conductance and are close to the heat source or magma domain (R2). Additionally, shallow geothermal wells could be made at the north-east part of the rift and should be drilled parallel to the electrical anisotropy direction of north-east, which could align to the oriented fractures direction. Moreover, further numerical modeling of multiphase flow and heat transfer should be carried out to confirm if significant hydrothermal fluid circulation exists inside the high conductance layers (C3 and C4). This latter suggestion is the objective of chapter 4 or article 3 of this PhD thesis.

4. TROISIÈME ARTICLE: NUMERICAL MODELING OF HYDROTHERMAL SYSTEM CIRCULATION BENEATH ASAL RIFT, REPUBLIC OF DJIBOUTI

Modélisation numérique de la circulation d'un système hydrothermal sous le rift d'Asal, République de Djibouti

Auteurs:

Abdek Hassan¹, Jasmin Raymond¹ and Bernard Giroux¹

¹ Institut national de la recherche scientifique, 490 de la Couronne, Québec, QC G1K 9A9, Canada

Titre de la revue:

Energies journal

Submission date: In August 2022

Lien avec le chapitre précédent : L'anisotropie électrique mise en évidence dans le chapitre précédent est associée aux champs de contraintes et les mouvements des plaques qui génèrent des déformations susceptibles de favoriser les écoulements de fluides. Afin de mieux quantifier les directions d'écoulements des fluides et la dynamique de transfert thermique, des résultats de simulations numériques d'écoulement multiphasique considérant que l'anisotropie électrique se traduit en termes d'anisotropie de perméabilité sont présentés au chapitre 4.

Abstract

Asal rift is an aerial rift segment resulting from the westward propagation of the Aden ridge into the Afar Depression. Geothermal manifestations such as hot springs and fumaroles, fault creep, conductivity anomaly and high geothermal gradient were observed both at the surface and in the subsurface. Despite many scientific works conducted in Asal to understand the rifting mechanisms, the hydrothermal fluid circulation still needs to be evaluated since it is based on simplified conceptual models. To further contribute and progress toward a quantitative evaluation of fluid circulation, a 2D numerical model perpendicular to the rift axis was developed with the objective to better understand the role of subsurface anisotropy in fluid flow and heat transfer in the Asal rift. Numerical modeling of multiphase flow and heat transfer was carried out with an equivalent porous medium intersected by faults zones having greater permeability. Horizontal anisotropic permeability and magmatic fluid release were taken in account with different simulation scenarios. The results indicate that faults zones act as recharge/discharge areas depending on to their location, permeability and number. Simulations considering horizontal anisotropic permeability allowed to reproduce the thermal state observed in geothermal wells with the expected general pattern of fluid circulation in Asal rift. Comparing our result with a recent study of 2D numerical modeling parallel to the rift axis, we suggest the presence of a saddle point where fluid flow direction is both to the north-east and to the south-west direction of the rift. Moreover, magmatic fluid release assumed in two simulation scenarios showed to have an impact on the hydrological behavior of faults zones and facilitate the development of super-critical flow at the center of the rift.

Keywords: Multiphase flow, Numerical modeling, Hydrothermal system, Permeability anisotropy, Asal rift, Geothermal, Regional flow

4.1. Introduction

Tectonic activity in volcanic context can create dense normal faulting allowing high geothermal heat releases where crustal permeability is affected by such faulting mechanisms (Rowland and Sibson 2004). In worldwide extensional environment, the role of faults and related fault structures have been widely studied (Rowland and Simmons 2012; Faulds and Hinz 2015). The preferred path for fluid to recharge a hydrothermal system with cold downflow and to allow the hot fluid to rise into the shallow levels was shown to be controlled by faults system in such extensional setting. Active permeable normal faults may act as fluids conduits for both upward and downward flow for some geothermal area with high enthalpy like Laderello in Italy (Bellani et al. 2004). Layered permeability anisotropy characterized with structural analysis was also suggested to be a features controlling flow in rift zones (Rowland and Sibson 2004). However, previous studies conducted in hydrothermal systems of extensional environment still lacks of quantitative assessment to evaluate the role of fault dip angle, abundance and permeability on hydrothermal circulation. This was considered in this study of the Asal rift in Djibouti that also looked at the importance of subsurface anisotropy through numerical simulation of multiphase flow. Previous numerical modeling of hydrothermal systems did not take into account anisotropic permeability, which is believed to be important to reproduce the thermal state of Asal rift.

The importance of understanding the general pattern of fluid flow for geothermal exploration in hydrothermal systems where fluid circulation interacts with magmatic intrusions was highlighted by previous scientific research (Driesner and Geiger 2007; Rojstaczer et al. 2008; Weis 2015). This still needs to be evaluated in several hydrothermal systems, for example in the Asal rift of Djibouti, where the role of faults and their impact on fluid flow affecting recharge and discharge, the pattern of the regional hydrothermal flow, the anisotropic permeability of rocks and magmatic heat flow for the fluid circulation have not been not quantitatively assessed. The Asal rift is a segment of the Afar depression that is an extensional zone between three plates; Somalia, Arabia and Nubia. Asal rift is an eroded and aerial rift where numerous normal faults of north-west – south-east direction intersect the surface of the rift. Both Asal rift and Ghoubbet bay have main normal faults of north-west – south-east direction, which may act as preferred path for hydrothermal fluid circulation (Audin et al. 2001; Mlynarski and Zlotnicki 2001; Cattin et al. 2005; Doubre and Peltzer 2007; Doubre et al. 2007; Hassan Aden et al. 2021). Volcanic and tectonic activity affecting the region since the late quaternary controls the topography and actual structural features of the rift. Our scientific hypothesis is that both fault systems and the presence of anisotropic permeability can facilitate fluid circulation in the Asal rift. Thus, the objective of this work was to better understand fluid circulation by evaluating the role of the faults and permeability

anisotropy in the Asal hydrothermal systems. Numerical simulation of the Asal hydrothermal system was therefore undertaken with different isotropic and anisotropic permeability scenarios defined for subsurface geological units and basement rocks according to a conceptual model developed with interpretation of magnetotelluric surveys (Hassan Aden et al. 2022a). Multiphase flow and heat transfer was simulated to understand how features of fault systems like the geometry of faults, their permeability, location and relative distance between the heat source can play a role for the formation of the hydrothermal system and to determine the preferred recharge and discharge area that influence the general pattern of hydrothermal fluid circulation.

4.2. Geodynamic background and geological context

The Asal rift is close to the western tip of the Aden Gulf rift which propagates to the Afar depression at 30 mm/year (Fig.4.1). The eroded Asal rift is located at the center of the Republic of Djibouti and is bounded to the east by Ghoubbet bay and to the west by the saline Lake Asal. Steep normal faults with principal direction of north-west – south-east with displacement of up to 150 m are the main structural elements observed at the surface (Stein et al. 1991). The latter authors also suggested asymmetric distribution of Holocene faults slip in Asal where faults located at the north-east part of the rift had higher summed slip rate than faults located at the south-west part. The dip angle of faults at the inner of the rift was approximately 60-80° and those faults were active during the Holocene time (Stein et al. 1991). Normal faults dipping to the north-east are predominant both in Asal and in Ghoubbet Bay (Audin et al. 2001). The subaerial rift has 15 km long, a rift valley of 11 km wide and an inner width of 7 km. Those structural and topographic characteristics are common features of slow spreading oceanic ridges with faulting and crustal thickness (Manighetti et al. 1998; Doubre et al. 2007). Faults throughout the Asal rift valley are active, half the rift faults slipped together in the last eruption of Ardoukoba volcano (Fig.4.1), which occurred in Asal rift during November 1978 and could imply that group of faults are activated every 100 years (Stein et al. 1991). Thus, the long term vertical deformation in the Asal rift has not reached steady state movement and it is likely the result of cyclic rifting and filling of lavas (Stein et al. 1991). The deformation of the Asal Lake that preexisted as a freshwater lake and the recent basaltic lava flow that covers the rift axial zone (Zan et al. 1990; Stein et al. 1991) are further evidences that this area was affected by recent volcanic and tectonic activity. The observable Fieale Caldera at the surface (Fig.4.1) was built early, almost 100 ky ago by magmatic eruption, then following tectonic activity faulted the Fieale Caldera crater (De Chabaliere and Avouac 1994).

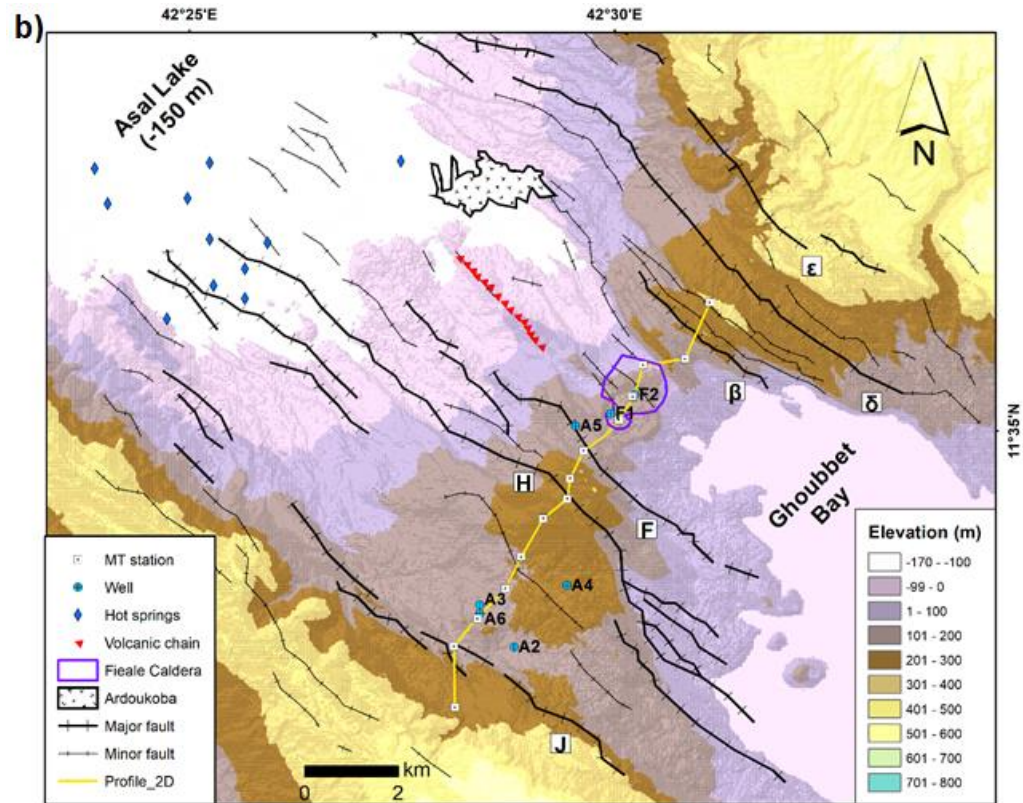
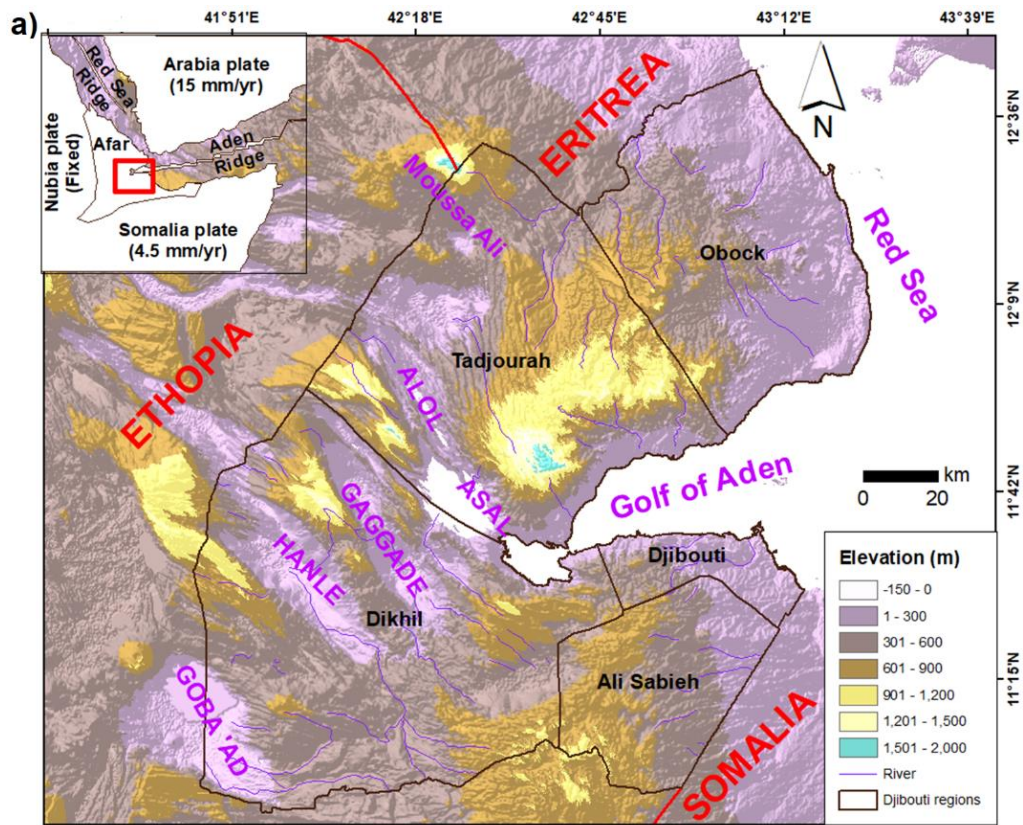


Fig.4.1. Topography and main structural elements of (a) Djibouti and (b) Asal rift. The red rectangle is Djibouti. MT abbreviates Magnetotelluric (modified from Hassan Aden et al. 2021).

Volcanic edifices of that last magmatic period should be observable at the actual surface location of the Fieale Caldera (Fig.4.1), but active normal faults have dismantled most of them (De Chabaliere and Avouac 1994; Manighetti et al. 1998).

Recorded seismicity and inferred faults activity concentrate at the surface and the surrounding areas of Fieale Caldera. Such activities are evidences that a central volcanic system can exist below Fieale Caldera (Dobre and Peltzer 2007; Dobre et al. 2007; Smittarello et al. 2016). Intense seismic swarm with an earthquake of magnitude greater than 5 happened on November 1978 in the Asal-Ghoubbet rift, which was followed by a fissured basaltic eruption lasting one week and ended by the extrusion of an approximate volume of $2 \times 10^7 \text{ m}^3$ of lava (Stein et al. 1991) that giving rise to Ardoukoba volcano previously mentioned (Fig.4.1).

The long term opening velocity of the Asal-Ghoubbet rift is close to the local and regional extension rate estimated by the restoration of horizontal and vertical displacement of the topography (De Chabaliere and Avouac 1994; Manighetti et al. 1998). Therefore, even with presence of few minor transients slip events on fissures and faults determined by interferometric synthetic aperture radar (InSAR; Dobre and Peltzer 2007) and the absence of intense localized seismic activity (Dobre et al. 2007), it is hypothesized that weak tectonic and magmatic activities currently exist under the Asal rift.

Faults dip angle inferred from passive seismic inversion (Dobre et al. 2007) suggest a sub-vertical dipping angle of 90° at the center of the rift and a dipping angle of 60° at the rift margins. Moreover, the dipping angle estimated from mechanical deformation related to the surface morphology of normal faults indicated a nearly constant dipping angle between $50-60^\circ$ (Pinzuti et al. 2010). Recent study of dimensionality analysis of magnetotelluric data additionally suggested the presence of north-east electrical anisotropy direction for the crust, which may be associated to the horizontal deformation of the rift and a north-south electrical anisotropy direction for the lower crust and upper lithosphere, which is associated to the vertical deformation and dike injection (Hassan Aden et al. 2022a). The geo-electric strike and anisotropy direction of magnetotelluric data proposed a sub-vertical dipping (90°) for the MT stations close to the normal faults in Asal rift (Fig.4 in Hassan Aden et al. 2022a). In addition, epicenters during the November 1978 eruptions determined after 5 days of seismic activity indicated a clear trending direction of N120E in the Ghoubbet bay, which corroborate with the direction of dike injection described above (Manighetti et al. 1998). Two months of continued recorded seismicity after that event indicated continuation of the seismicity in the Ghoubbet pass and the transfer zone between the Asal-Ghoubbet rift and Tadjoura submerged rift segment (Stein et al. 1991; Manighetti et al. 1998). Audin et al. (2001) additionally hypothesized that rift extension at shallow depth is mainly controlled by opening fissures and normal faulting in both the Ghoubbet seafloor and emerged

Asal rift. Seismicity recorded between 1979 and 1984 with moderate magnitude was concentrated at the north-east of rift axis in the emerged part of the rift (Dobre et al. 2007).

4.3. Methodology

A 2D numerical model parallel to the rift axis and to the shallow groundwater flow direction believed from Ghoubbet sea to Asal Lake was already developed for the first 3 km of the upper crust (Hassan Aden et al. 2021). This previous work showed the importance of the topography driven groundwater flow interacting with the hydrothermal circulation in such a regional 2D model. Further work was thus needed to better understand deep hydrothermal circulation perpendicular to the rift axis that can shed light on the role of the main normal rift faults. With such model, we believe it can be possible to better understand the relation between the upward magmatic fluids and the permeability of rock and faults considering potential anisotropic layers where lateral fluid circulation can be expected.

The multiphase modeling software Hydrotherm developed by the USGS was used in this study. This code allows to model flow and heat transport where the differential equations describing conservation of mass and energy are coupled to be solved numerically with finite difference method using the Newton Raphson algorithm (Kipp et al. 2008; Ingebritsen et al. 2021). The description of governing equations was presented in the previous work (Hassan Aden et al. 2021) and remain the same in this article. All simulations made in this work considered an equivalent porous medium with the assumption of uniform permeability to represent the different rock and fault zones where fluid transport is governed by Darcy law and phase change occurring gradually. Faults zones were assumed to have a permeability higher than the adjacent units. Consequently, this approach allowed higher fluid flow in the fault zones than in the surrounding rock units.

4.3.1. 2D Conceptual model

The 2D conceptual model perpendicular to the rift axis has a width of 12 km and a depth of 10 km (Fig.4.2). This 2D conceptual model was inferred from interpretation of a 2D conductivity model developed in Hassan Aden et al. (2022a). Reasons that justified the choice of the 2D section (Fig.4.1) are the existence of deep geothermal wells (A6 and A4), where the measured temperature could be used for comparison with simulated temperature. The section was also made perpendicular to the rift axis to enclose the main normal faults and the main geological units identified from outcrops and by geothermal wells (Zan et al. 1990). To simulate the behavior of the hydrothermal system in simplified but realistic conditions, the 2D section across the rift axis encloses the area overlying the seismogenic crust zone between 3-5 km, the assumed deep

magma reservoir and the main normal faults (Cattin et al. 2005, Doubre et al. 2007). The upward flux of magmatic fluids is known to depend mainly on the depth, composition and dimensions of a magma body (Scott et al. 2016). In this context, the hydrodynamic regime of a hydrothermal system is expected to depend primarily on the magmatic heat supply rate and the location of the recharge/discharge areas as well as the permeability structure of the crust.

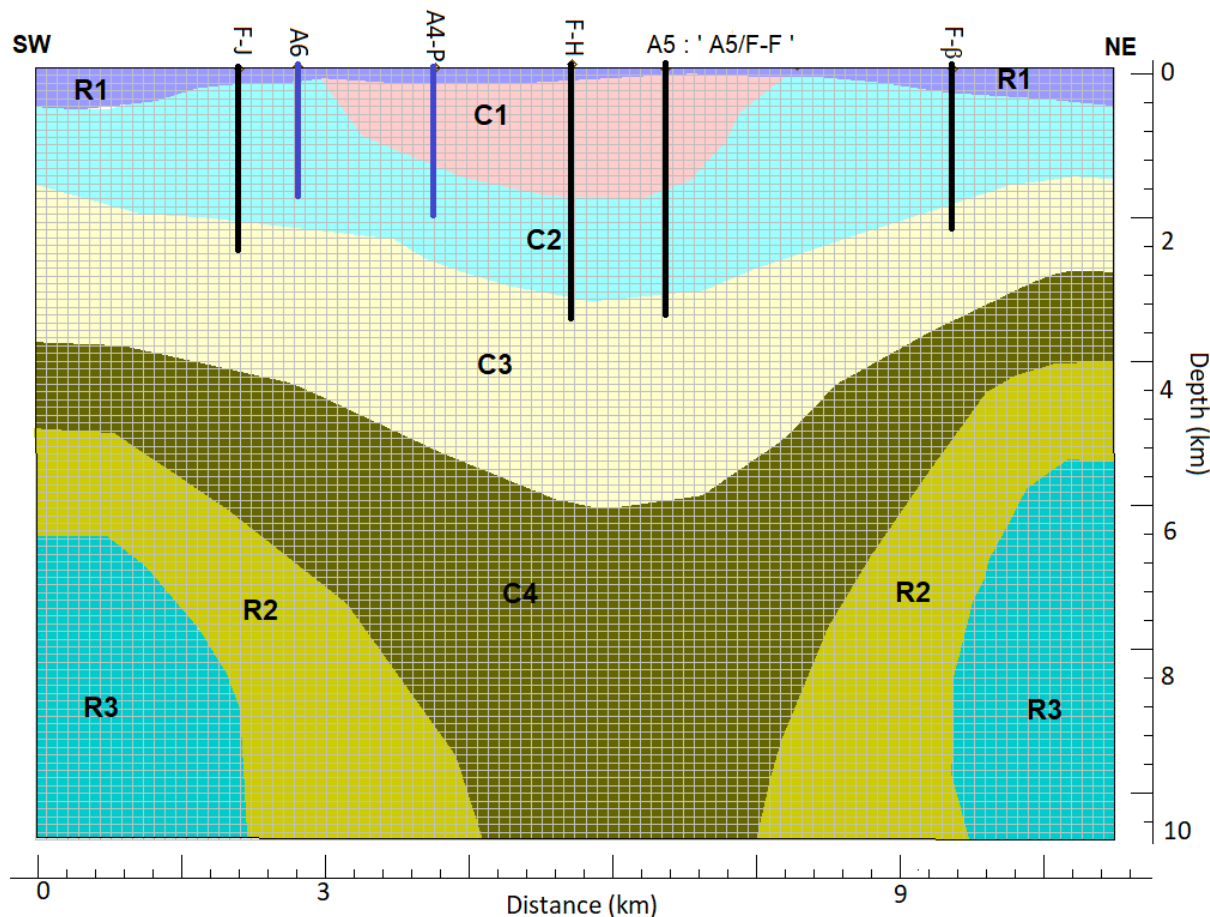


Fig.4.2. 2D Finite difference grid and conceptual model interpreted along a 2D magnetotelluric profile of the Asal rift (Fig.4.1). F-J, F-H, F- β indicate the emplacement of faults with their name, for example F-J is the fault J location. A6, A-4P (projected A4 well) and A5 are the geothermal wells (Fig.4.1). A5 is located at the same position of F-F and is denoted A5: 'A5/F-F'.

4.3.2. Hydraulic and thermal properties

4.3.2.1. Base case scenario

The simplified stratigraphy of the conceptual model is derived from the interpretation of a 2D conductivity model developed recently from the invariant model inversion of MT data by the same

authors (Hassan Aden et al. 2022a). This model, illustrated in Fig.4.2, is composed by a dry volcanic rock (R1) that covers a shallow aquifer (C1). The latter overlies a host rock (C2) that can be considered as potential hydrothermal reservoir. A hydraulically conductive medium having fractures and that could represent a deep reservoir (C3) underlies the C2 potential hydrothermal reservoir.

Table 4.1. Thermo-hydraulic properties for the base case (scenario 1).

Formation	Unsaturat ed formation: R1	Aquifer1: C1	Aquifer2: C2	Host rocks: C3	Medium filled by dikes: C4	Top of the Basement rock: R2	Base of the baseme nt rock: R3
Porosity (-)	0.14	0.13	0.12	0.1	0.07	0.03	0.03
Horizontal permeability (m ²)	2×10 ⁻¹⁷	2×10 ⁻¹⁶	2×10 ⁻¹⁶	10 ⁻¹⁶	10 ⁻¹⁹	10 ⁻¹⁹	10 ⁻¹⁹
Vertical permeability (m ²)	2×10 ⁻¹⁸	10 ⁻¹⁶	10 ⁻¹⁶	10 ⁻¹⁶	10 ⁻¹⁷	10 ⁻¹⁷	10 ⁻¹⁷
Thermal Conductivity (W m ⁻¹ k ⁻¹)	F (T)	F (T)	F (T)	F (T)	F (T)	F (T)	F (T)
Density (kg m ⁻³)	2700	2700	2700	2700	2600	3000	3200
Specific heat (J kg ⁻¹)	900	1000	1000	1000	F(T)	F (T)	F (T)
Compressibility (Pa ⁻¹)	10 ⁻¹⁰	10 ⁻¹⁰	10 ⁻¹⁰	10 ⁻¹⁰	10 ⁻¹⁰	10 ⁻¹⁰	10 ⁻¹⁰

The deep structure considered in the conceptual model is a resistive zone assumed to be the top of the basement (R2) overlying a highly resistive medium (R3) that can be the base of the

basement and a magma system which is a layer likely filled by dikes intrusion (C4) at the center of the rift (Fig.4.2 and Table 4.1).

Four major normal faults are included in the 2D conceptual model (Fig.4.2). The exact dip angle of the fault is unknown and simulations with different dip angles were made to evaluate their impact.

Thermo-hydraulic properties for the base case called scenario 1, which exclude faults, are presented in Table 4.1. The permeability of geological units in this scenario 1 is supposed anisotropic. The simulation of scenario 1 was performed for comparative purposes to later evaluate how anisotropic permeability can influence the deep hydrothermal circulation and to allow lateral fluid circulation. The thermal conductivity that vary with temperature (F(T)) was calculated with the approach presented by Hassan Aden et al. (2021).

4.3.3. Boundary and initial conditions for fluid flow and heat transfer

At the top of the 2D model, constant hydrostatic pressure of 1 bar was assigned with a free flow boundary. Fluid is thus allowed to be recharged/discharged at the top boundary domain. At the bottom of model there is no flow. Lateral boundaries were impermeable. Hydrostatic pressure distribution with depth was used as initial conditions.

At the top of the 2D model, a temperature of 20 °C was assigned. A gaussian bell distribution was used for the bottom the boundary of 2D model to represent the basal heat flow. The conductive heat flow coming from the cooling of the magma system (C4) was represented at the model center with heat flow of 0.4 W m⁻² at the lower boundary of C4 layer whereas the lower boundary segments at location of R2 and R3 on the edges of the model were assigned a basal heat flow of 0.13 W m⁻², which can correspond to the brittle-ductile transition temperatures. Lateral boundaries were adiabatic. A linear geothermal gradient of 40 °C km⁻¹ was used as initial conditions.

4.3.4. Spatial and temporal discretization

Mesh independence was verified in order to confirm the accuracy of numerical simulations. To achieve this, different grids were used with scenario 1 to evaluate temperature at the position of wells A6 and A4 (Fig.4.2) at depth of 1480 m (Appendix C). The geometry of the 2D model was optimally discretized in the simulator with a regular grid of 100 × 100 cells (Fig.4.2). The simulation spans a time long enough to reach a quasi-steady state temperature regime and was set by default as 800 000 years with an initial time step of 0.001 year. The choice of this default

simulation time is close to the duration of the Asal rift opening by intense volcanic activity followed by normal faulting that was estimated about 1 000 000 years (Manighetti et al. 1998). Thus, we assumed that geological materials at depth were present 800 000 years ago. Due to the greater permeability for some simulation scenarios, the simulation time span was reduced. An automatic time step algorithm where smaller time steps are selected when conditions of pressure, enthalpy and saturation are changing rapidly was used by the simulator. The maximum values for changes in pressure, enthalpy, and liquid saturation, which are specified before running the simulations are the factors controlling the length of time step. In the simulations, the maximum changes in pressure, enthalpy, and saturation were found to be 10%, 5%, and 0.03, respectively, and this resulted in a maximum time step of 13 697 years.

4.3.5. Simulation scenarios

Different scenarios were conducted and modifications were made to increase the complexity of the 2D numerical model starting from the base case scenario in 3.2.1 and summarized in Table 4.2. Properties for the shallow units were chosen similar to those determined from the numerical modeling of multiphase flow parallel to the Asal rift axis (Hassan Aden et al. 2021). Properties of the deep model units were determined from compilations of previous scientific works (Hayba and Ingebritsen 1997; Driesner and Geiger 2007; Raguanel et al. 2019; Raymond et al. 2022). We assumed that geological units R1, C1 and C2 have horizontal permeabilities two times higher than the vertical permeability while R2 and R3 have a vertical permeability two order of magnitude higher than the horizontal. We assumed that electrical anisotropy evaluated in the work of Hassan Aden et al. (2022a) can be interpreted as permeability anisotropy.

Faults expression at the surface is well known (Stein et al. 1991; Manighetti et al. 1998; Audin et al. 2001), although uncertainty persist about fault geometry in the subsurface. In scenario 2A, four normal faults were added to the model where a vertical dipping angle of about 90° was considered in agreement with the relation between the direction of diking and faulting (Stein et al. 1991; Audin et al. 2001) and the result of geoelectric strike and anisotropy direction (Hassan Aden et al. 2022a). The faults are simplified to be represented by a zone of high permeability equal to $3 \times 10^{-16} \text{ m}^2$ over a given width of 100 m. Mechanical and chemical process existing in faults were neglected. One will keep in mind that fault width and permeability are not independent on the hydrogeological point of view and are related where their product correspond to the transmissivity. Another simulation scenario called 2B was considered and is only showed in Appendix A where the average dipping angle of faults is 60° as proposed by Doubre et al. (2007) and Pinzuti et al. (2010). We concluded that the flow pattern is less dependent on the dip angle of faults but is more

affected by the location, the number and permeability of faults, explaining why results are shown in appendix C only.

Table 4.2. Modification of each different scenario from the base case scenario 1.

Scenario	Type of modification	Modified Units	Number of faults	Faults permeability	Magmatic fluid considered (Yes or No)
2A and 2B	Adding faults	---	4 Major faults	$3 \times 10^{-16} \text{ m}^2$	No
3	Higher faults permeability	---	4 Major faults	$7 \times 10^{-16} \text{ m}^2$	No
4	Presence of cap rock	C1	4 Major faults	$3 \times 10^{-16} \text{ m}^2$	No
5A and 5B	Anisotropy horizontal permeability	C2 and C3	4 Major faults	$3 \times 10^{-16} \text{ m}^2$	No
6A and 6B	Anisotropy horizontal permeability	C2 and C3	Without faults	$3 \times 10^{-16} \text{ m}^2$	No
7	---	---	4 Major faults	$3 \times 10^{-16} \text{ m}^2$	Yes
8	---	---	4 Major faults	$3 \times 10^{-16} \text{ m}^2$	Yes

Moreover, scenario 3 was made to investigate the effect of the fault permeability, which was set to a higher value equal to $7 \times 10^{-16} \text{ m}^2$. Scenario 4 was made to evaluate the importance of the potential presence of cap rock that is less permeable. In this case, the C1 layer was assumed to act as a cap rock with a low isotropic permeability equal to $2 \times 10^{-17} \text{ m}^2$. Furthermore, to understand

the influence of unit permeability and the importance of significant lateral flow, additional scenarios 5A and 6A were made in which the permeabilities of geological units C2 and C3 (Fig.4.2 and Table 4.2) were horizontally increased by one order of magnitude compared to the base case (Table 4.1). The aim of these scenarios was to evaluate the impact of favorable permeability conditions that can create zones of high hydrothermal fluid velocity and high temperature. Properties selected for scenarios 1 and 2A were reconsidered in scenarios 5A and 6A but with anisotropic permeabilities. A horizontal permeability one order of magnitude higher than the horizontal permeability of scenario 2A was taken into account to simulate scenario 5A, whereas the conditions of scenario 5A were repeated without faults to simulate scenario 6A. We additionally considered scenarios 5B and 6B where the north-east of the Asal rift is assumed more permeable than the south-west in the upper crust. To do this, we reconsidered the properties selected for scenario 5A and assigned a permeability two times higher than the permeability of scenario 5A for geological units (R1, C1, C2 and C3; Fig.4.2) located to the north-east of H fault, whereas the geological units located at the south-west of H fault remained the same as those of scenario 5A in order to simulate scenario 5B. Then, we simulated scenario 6A with the same conditions where geological units located to the north-east are more permeable than those located to the south-west of the rift in order to simulate scenario 6B. Finally, scenarios 7 and 8 were made to quantify the role of the magmatic fluid injection into the hydrothermal system. To this end, conditions of scenario 1 was reconsidered to simulate scenario 7 with a magmatic fluid flux equal to $18 \times 10^4 \text{ m}^3 \text{ year}^{-1}$ as determined by Stein et al. (1991). This magmatic fluid flux is supposed to be located at the bottom of the C4 layer (approximately at 9 km depth) in the 2D conceptual model (Fig.4.2). Scenario 2A was reconsidered to simulate scenario 8 with the same magmatic fluid flux equal to $18 \times 10^4 \text{ m}^3 \text{ year}^{-1}$.

Simulated temperature versus measured temperature in geothermal wells A6 and A4 were compared to better understand the main characteristics that controls the hydrothermal system and infer the most realistic scenarios that represent the thermal state observed in geothermal wells.

4.4. Results

4.4.1. Fluid circulation

Results of scenario 1 and scenario 2A (Fig.4.3) show that there are two distinct flow patterns. At the center of the rift between fault H and fault F (A5), cold downflow dominates and separates two hot upflow zones. C3 layer is shown to host supercritical fluids where temperature is equal to or above 400°C (Fig.4.2 and Fig.4.3).

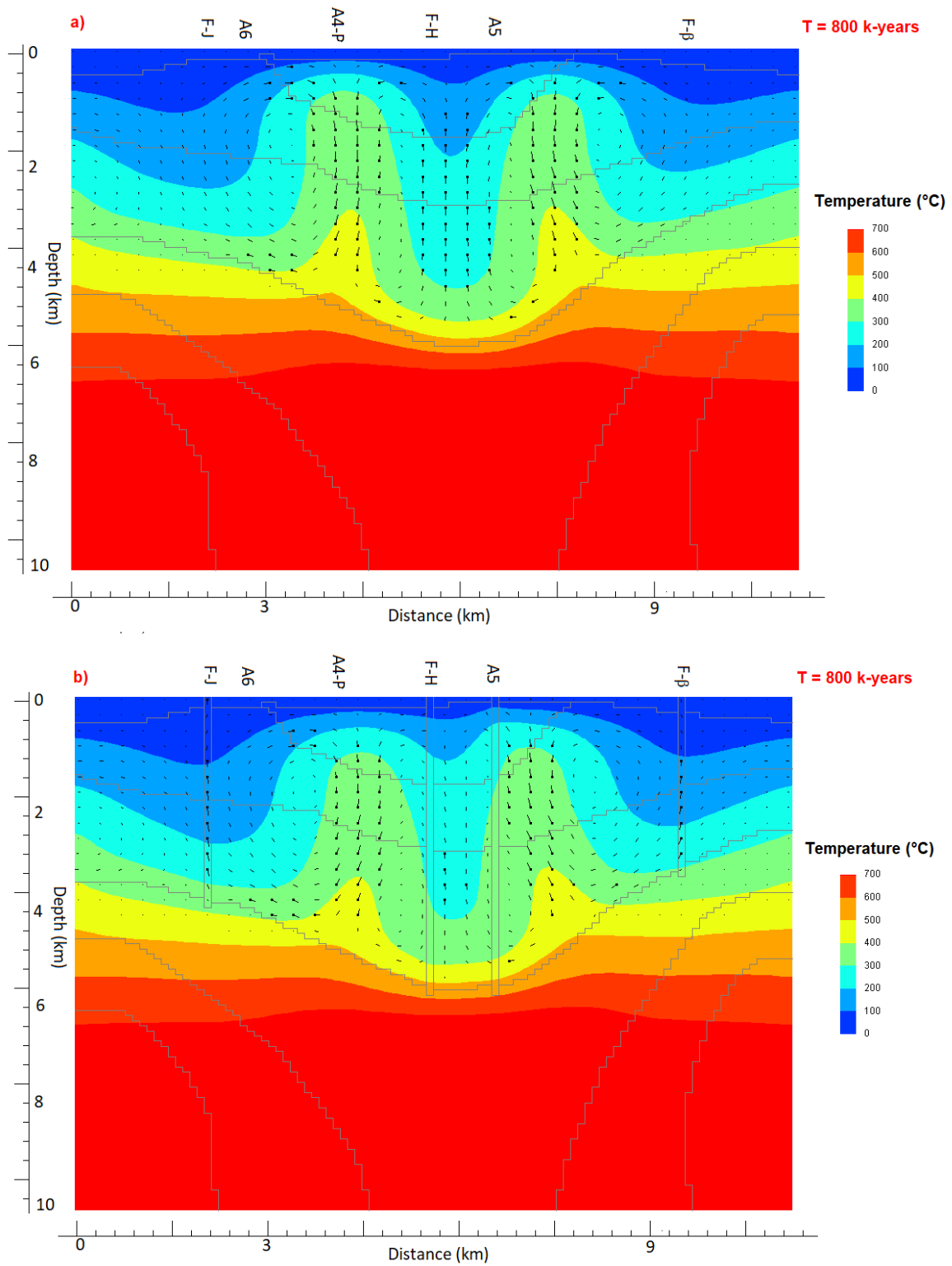


Fig.4.3. Simulated temperature and flow vectors at time 800 000 years for a) scenario 1 and b) scenario 2A. The direction of flow is from the point to the end of straight lines. The length of each line indicates the flow vector magnitude, where $1.2 \text{ km} = 10^{-6} \text{ g s}^{-1} \text{ cm}^{-2}$.

The cold downflow is toward the center of C3 layer and due to the temperature increase, the flow direction reverses and the hot upflow circulation toward the overlying units takes place and migrate according to the development of the high temperature zones. When considering the presence of faults (scenario 2A), there is less cold downflow at the center between faults H and F than in the scenario 1 without faults but the outermost faults (F-J and F-β) acts as a preferred path for the downflow circulation. In scenario 3 (Fig.4.4), the hot upflow takes place along fault H whereas faults F-J and F-β exhibit a preferred path for the downflow circulation. Additionally, fault F (A5) experiences a mixture of cold and relative hot downflow. In scenario 4 (Fig.4.4), the pattern of flow is quite similar to scenario 2A but between faults F and β, the hot upflow circulate toward the north-east direction (toward fault β) and the system at the center of the rift is hotter between faults H and F where a hot upflow replace the downflow when compared to scenario 3. In scenarios 5A and 6A (Fig.4.5), due to the horizontal permeability increase, lateral flow is more pronounced than for the preceding simulations. Moreover, the direction of flow is different in each layer (C2 and C3; Fig.4.2) and inside the fault systems. At the center of the rift in the C2 layer, the hot upflow is toward the rift margins (toward north-east and south-west) direction, while the downflow originates from the rift margins and is toward the center of the rift. There is a significant lateral flow toward the rift center in the C3 layer while the hot upflow is directed vertically toward the C2 layer and is concentrated inside the 300-400 °C isotherms. Furthermore, the flow vectors inside the faults show two different patterns in scenario 5A. The first pattern is a dominant downflow circulation inside the outermost faults (F-J and F-β), whereas the second pattern illustrates upflow and discharge and is localized in the upper part of the faults (F-J and F-β) close to the surface (Fig.4.5). For this same simulation scenario 5A, the fault H (F-H) does not seem to act as a preferred path for fluid flow while there is an important hot upflow taking place along the fault F (F-F). In scenario 6A, significant lateral and vertical flow co-exist in C3 unit. At the center of the rift, there is a hot and wide zone with significant oblique upflow (azimuthal direction). It is obvious that each hot upflow area is surrounded by cold downflow areas but lateral flow toward the center of the rift also exists, particularly inside the C3 layer.

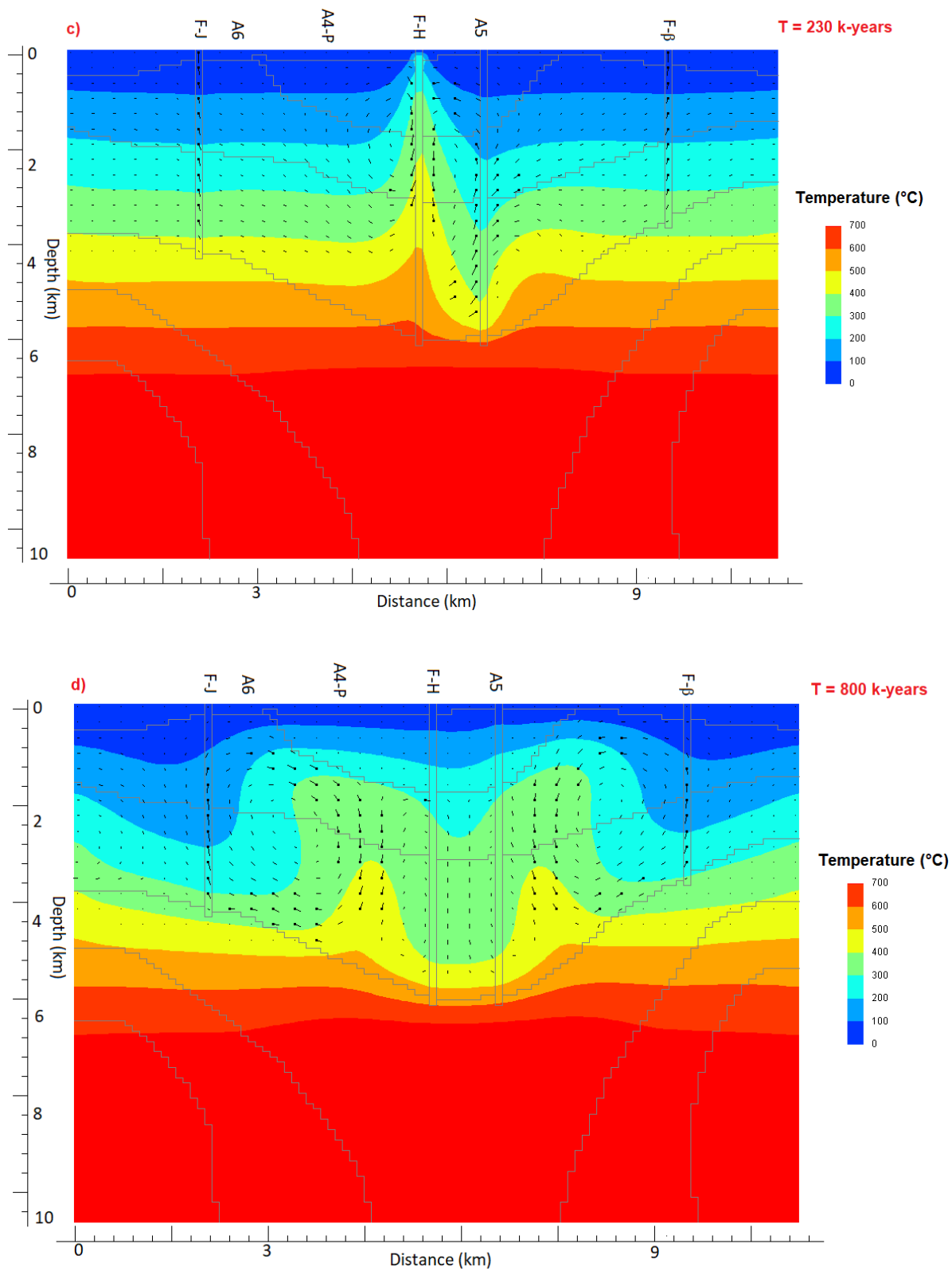


Fig.4.4. Simulated temperature and flow vectors for c) scenario 3 at time 230 000 years, and d) scenario 4 at time 800 000 years. The direction of flow is from the point to the end of straight lines. The length of each line indicates the water vector magnitude, where $1.2 \text{ km} = 10^{-6} \text{ g s}^{-1} \text{ cm}^{-2}$.

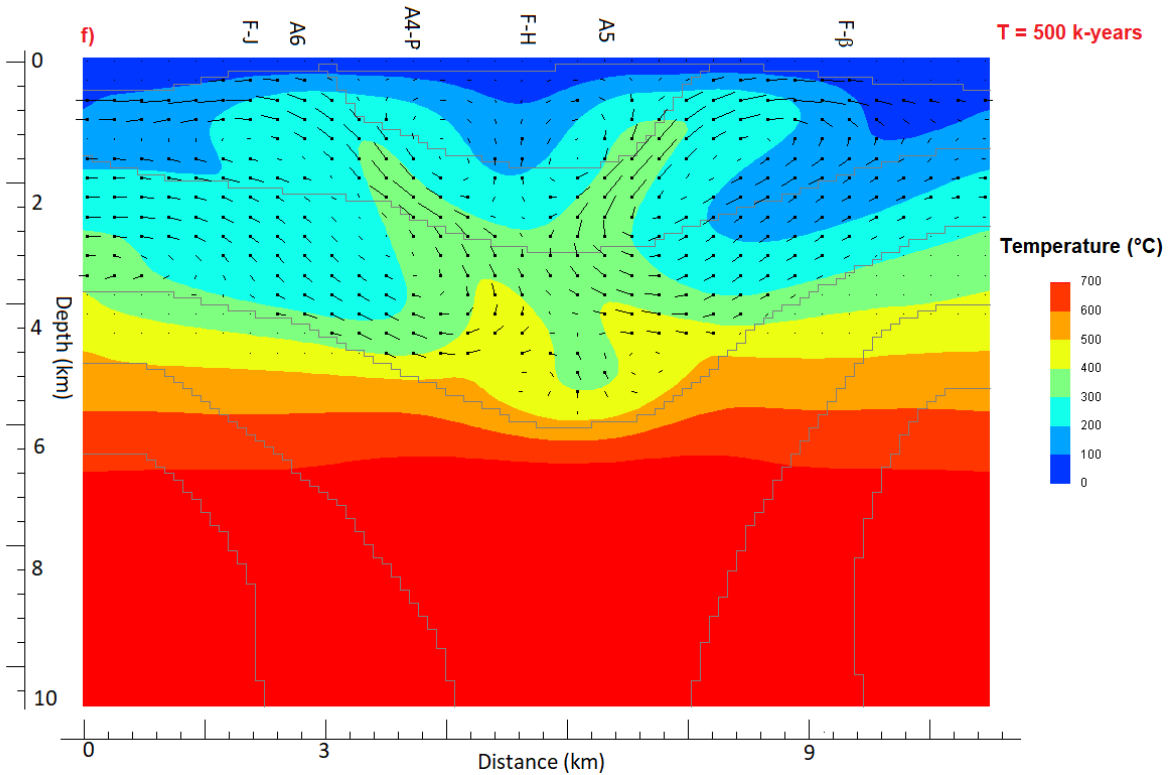
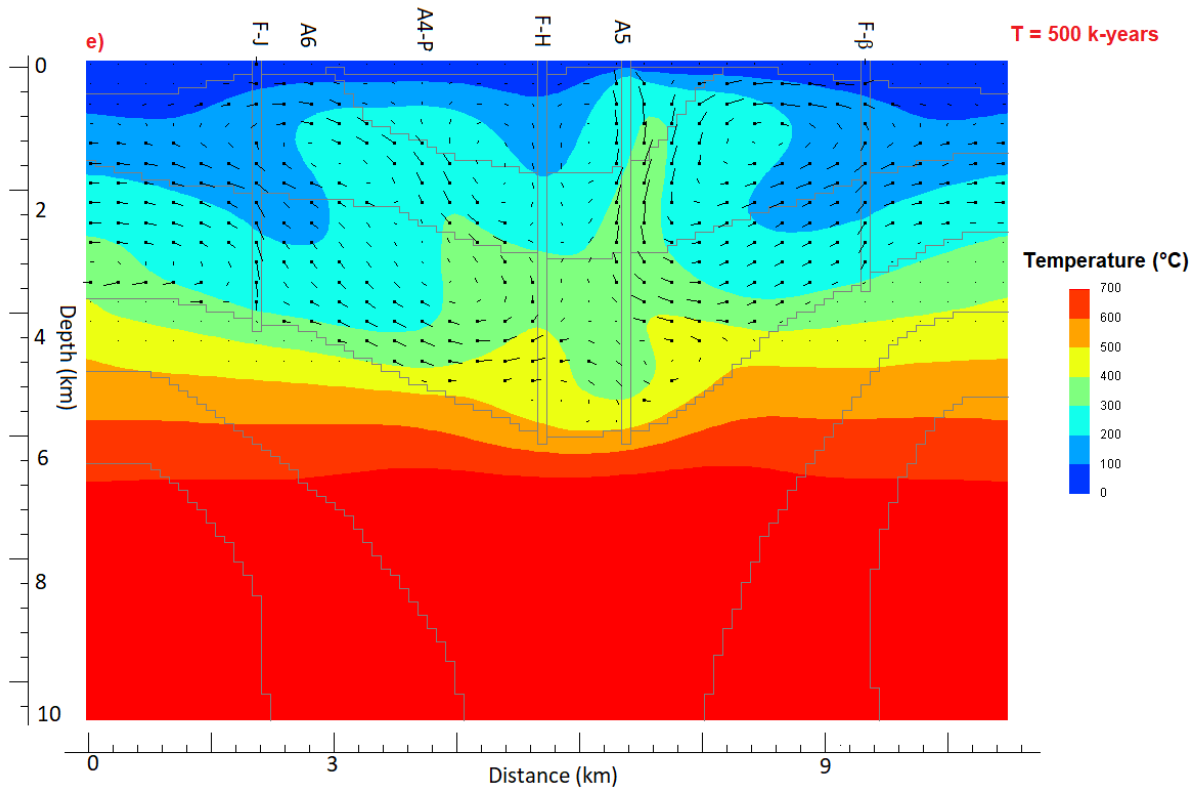


Fig.4.5. Simulated temperature and flow vectors at time 500 000 years for e) scenario 5A and f) scenario 6A. The direction of flow is from the point to the end of straight lines. The length of each line indicates the water vector magnitude, where $1.2 \text{ km} = 10^{-6} \text{ g s}^{-1} \text{ cm}^{-2}$.

Results obtained with scenario 5B show that both the deep and shallow hydrothermal circulations are directed toward the south-west rather than the north-east of the rift. Thus, one main hot upflow zone exists in the south-west of the rift whereas the north-east of the rift seems less hydrothermally active with potential cooling (Fig.4.6). Results obtained with scenario 6B are somehow similar to those of 5B but in the case of 6B we can observe high magnitude of fluid vectors at the edge of the south-west of the rift which can be considered as a zone of high discharge rate (Fig.4.6).

Fluid circulation in scenarios 7 and 8 (Fig.4.7) presents common features and similarities. In scenario 7, the hot upflow area is concentrated in the 300-400 °C isotherms and part of the fluid is discharged at the surface close to the area of faults H and F (F-H and F-F), whereas in the other parts of the rift, fluid is flowing laterally and directed toward the north-east and south-west before recirculation with vertical downflow that take place at depth. Additionally, the high temperature gradient at the center allows the formation of convection cells which transforms the downflow into a hotter upflow toward the upper unit. Scenario 8 displays approximately the same flow patterns, but the outermost faults (F-J and F-β) are in this case the preferred path of fluid to be discharged at the surface and the main upflow is concentrated between faults H and F.

Measured temperatures in geothermal wells A6 and A4 best match with the simulated temperature at the locations of the wells for scenarios 5A, 5B, 6A and 6B (Fig.4.8). Notably the simulated temperature for both wells A6 and A4 best match in scenarios 5B and 6B. This confirms that layered anisotropy of horizontal permeability reproduces better the observed thermal state in the geothermal wells of Asal rift.

It can be concluded that horizontal anisotropic permeability (higher horizontal permeability than the vertical) of the upper geological units impacts the observed thermal state in the deep geothermal wells. Moreover, the general flow pattern illustrated by scenarios 5B and 6B is believed to be most representative of hydrothermal fluid circulation in Asal rift (Fig.4.5). In addition, simulated temperature and observed temperature at well A6 are in good agreement for both scenarios 5B and 6B (Fig.4.8b). It is interesting to note that those modified scenarios (5B and 6B) better reproduce the observed thermal state of the upper part of well A6 than the original scenarios (5A and 6A), whereas the observed thermal state of the lower part are almost the same (Fig.4.8). This suggest that the permeable north-east part of the rift can facilitate recharge while hydrothermal up flow would concentrate in the south-west part of the rift.

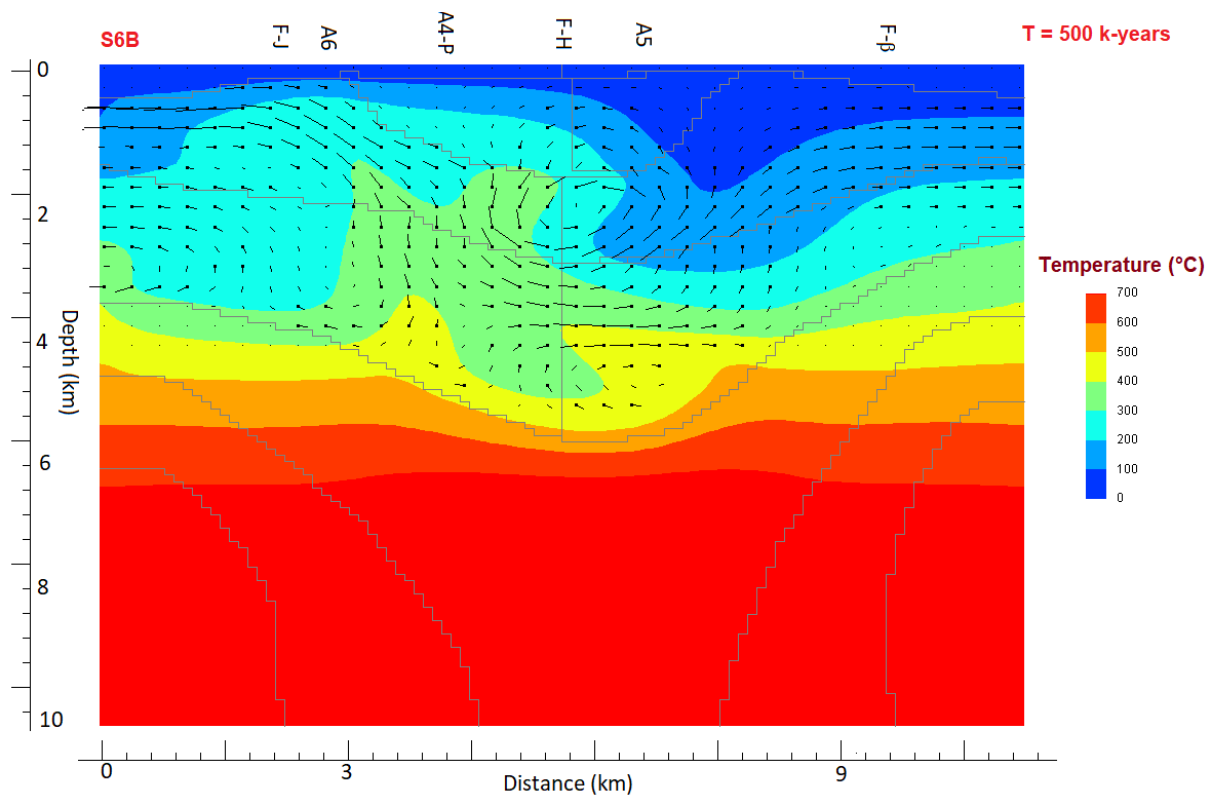
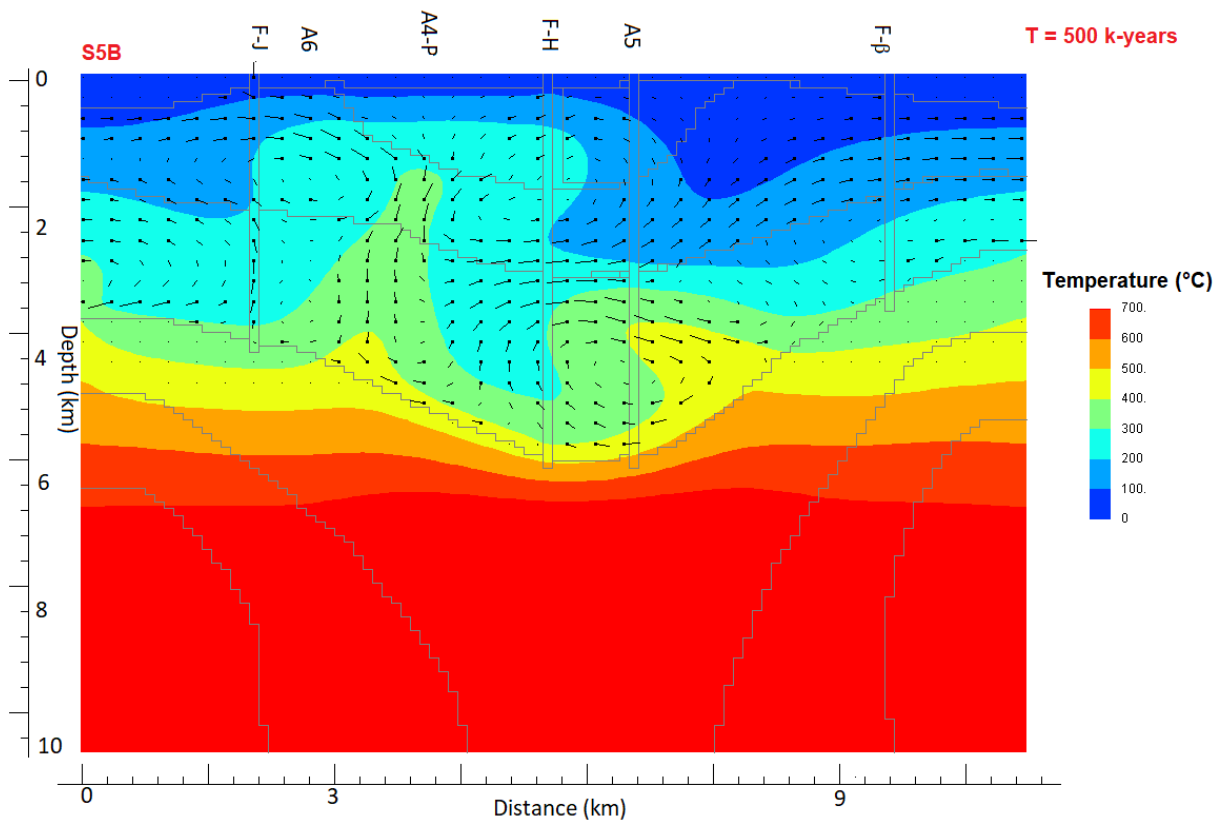


Fig.4.6. Simulated temperature and flow vectors at time 500 000 year for S5B) scenario 5B and S6B) scenario 6B. The direction of flow is from the point to the end of straight lines. The length of each line indicates the water vector magnitude, where $1.2 \text{ km} = 10^{-6} \text{ g s}^{-1} \text{ cm}^{-2}$.

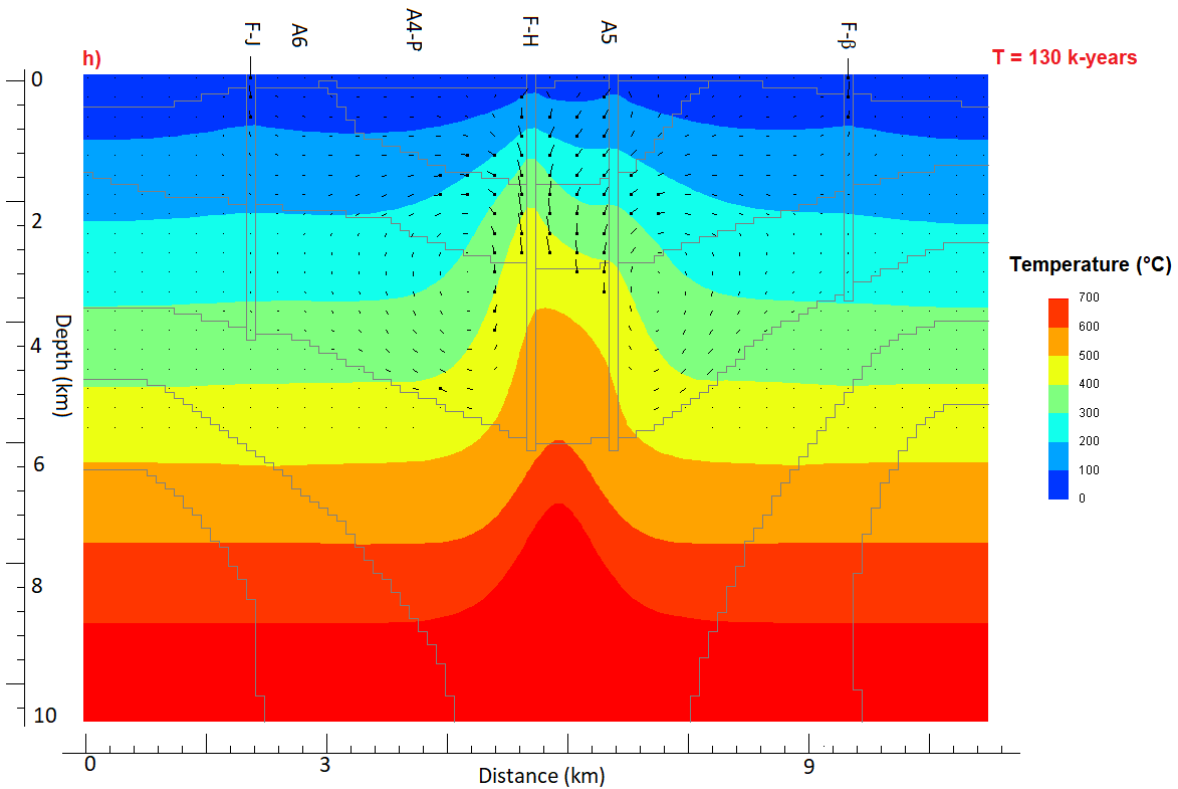
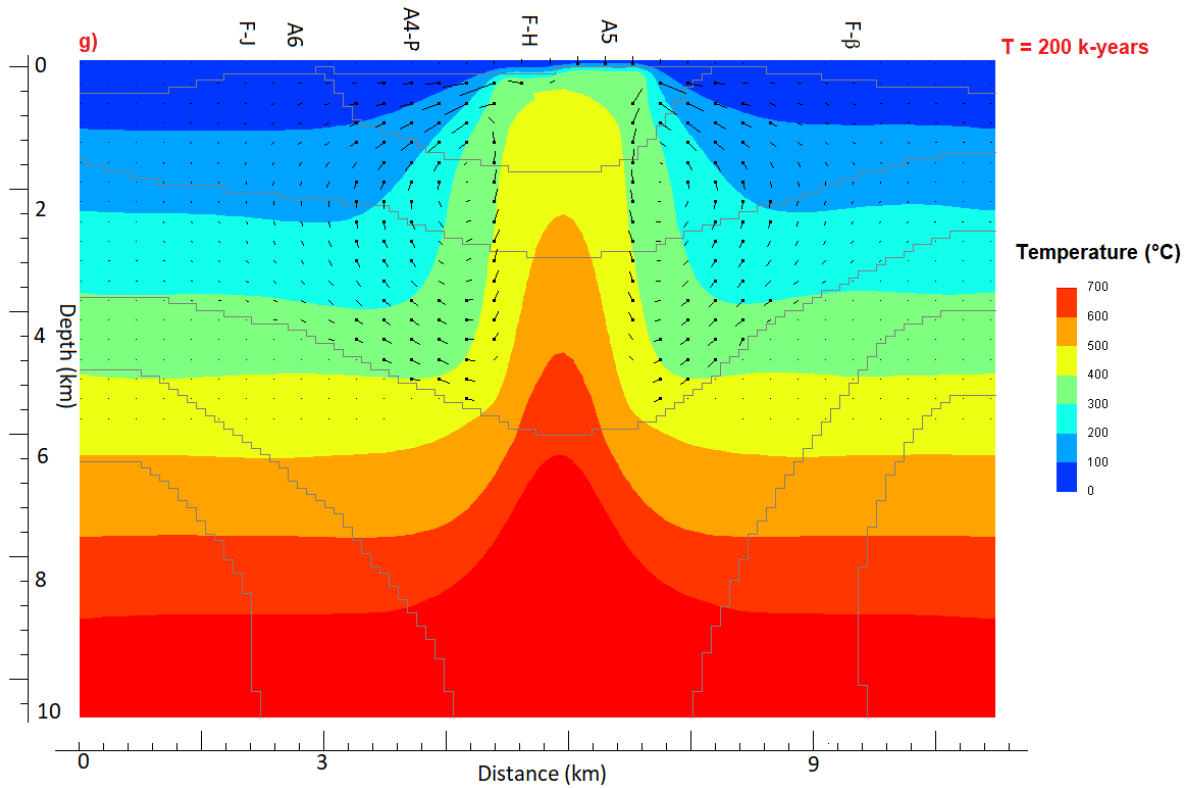


Fig.4.7. Simulated temperature and flow vectors for g) scenario 7 at time 200 000 years and h) scenario 8 at time 130 000 years. The direction of flow is from the point to the end of straight lines. The length of each line indicates the water vector magnitude, where $1.2 \text{ km} = 10^{-6} \text{ g s}^{-1} \text{ cm}^{-2}$.

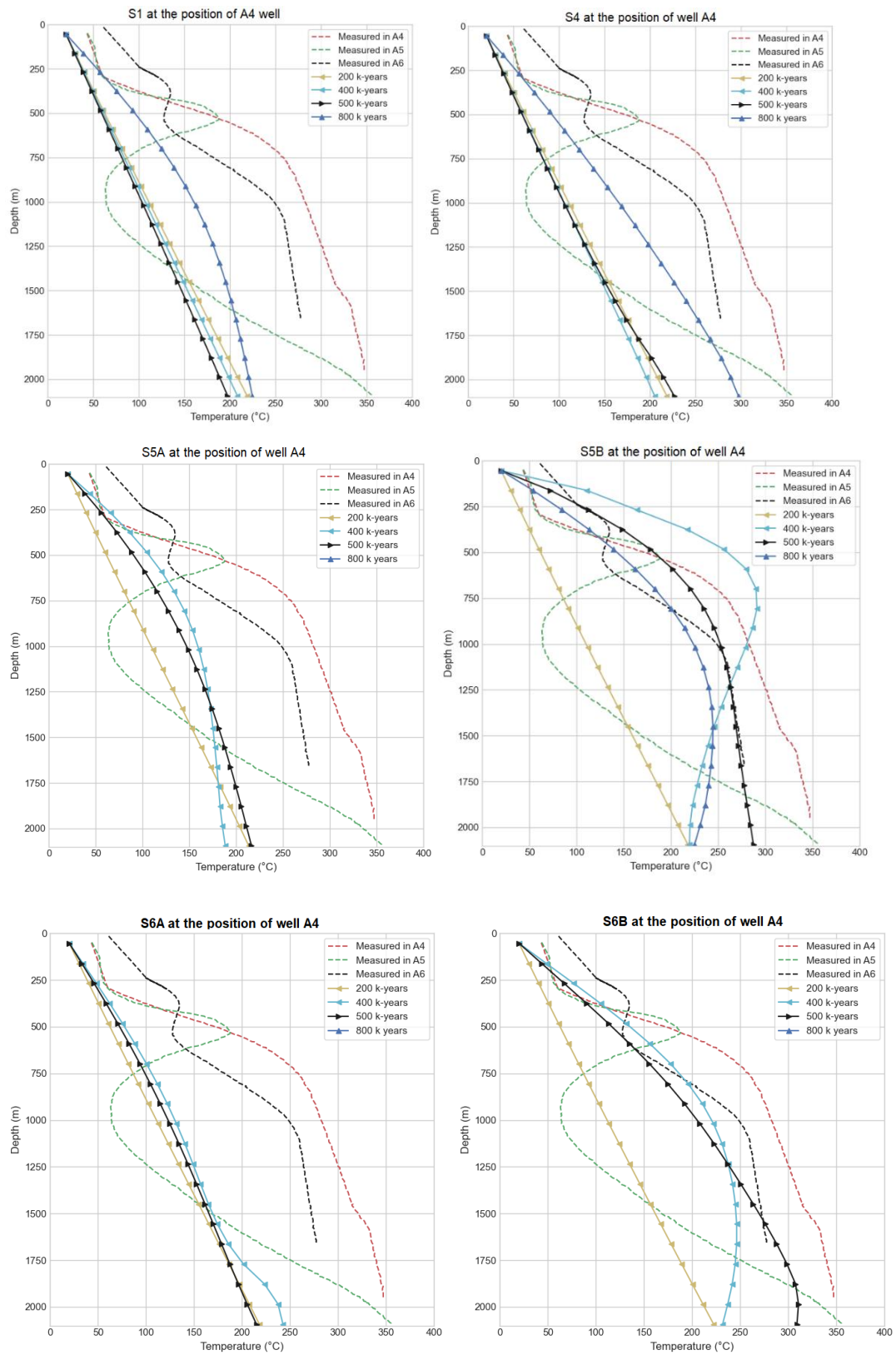


Fig.4.8a. Comparison between the observed and simulated temperatures at well A4. The word S represent scenario.

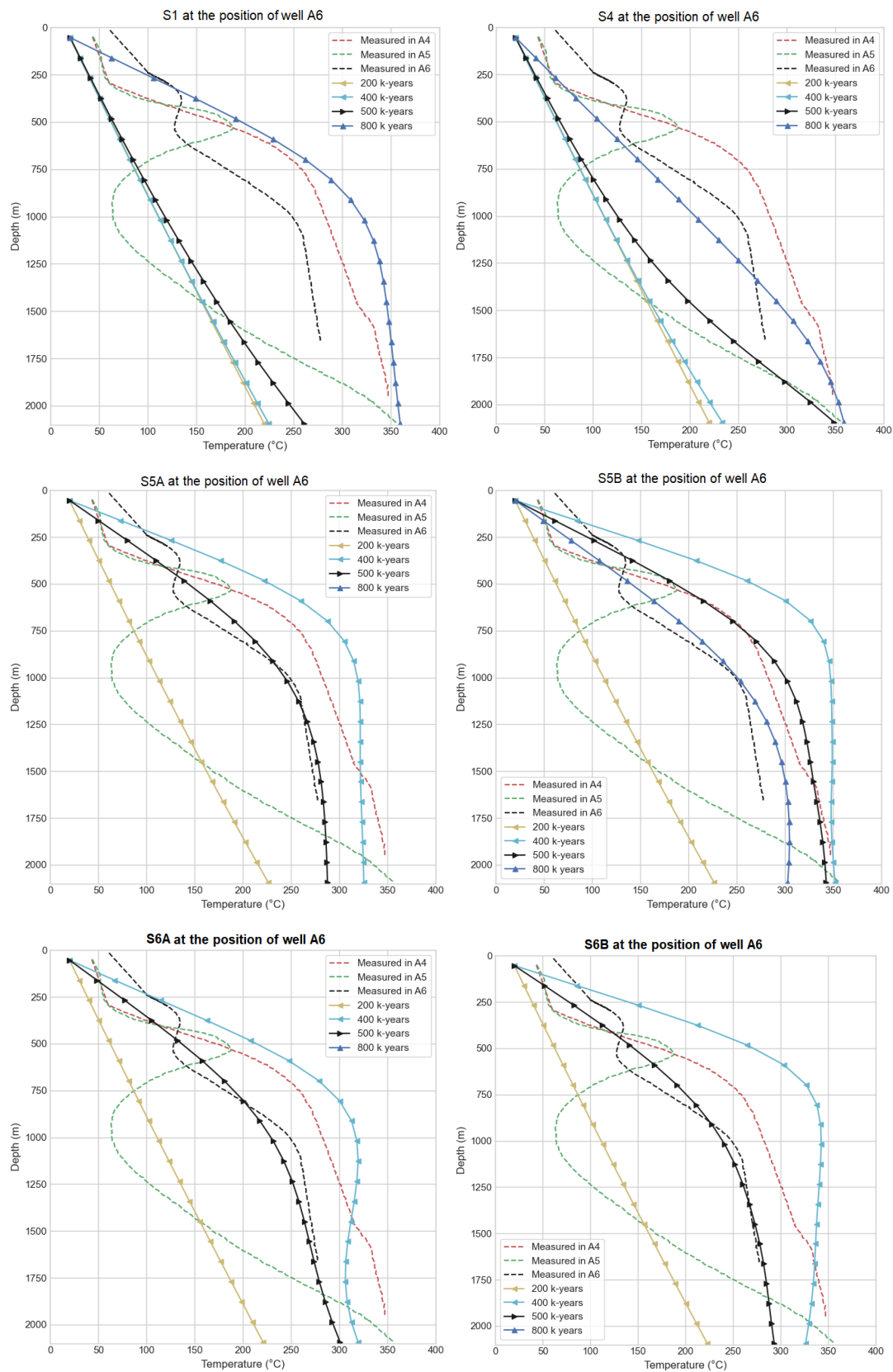


Fig.4.8b. Comparison between the observed and simulated temperatures at well A6. The word S represent scenario.

4.5. Discussion

4.5.1. Rock permeability

In all scenarios simulated in this study, the main property that was subject to variations is permeability. Furthermore, the complexity of the model is increased from scenario 1 to 8 in order to understand the overall behavior of fluid circulation inside the 2D conceptual model to give a reliable interpretation of the features that controls fluid flow. Permeability plays important role in the development of hydrothermal systems (Driesner and Geiger 2007; Rojstaczer et al. 2008). The presence of a cap rock (low permeable unit), represented in this study with layer C1, allows the formation of high temperature inside C2 and C3 layers (scenario 4). This confirms the well-known theory that favorable high temperature hydrothermal system needs a cap rock at a shallow depth and above the vertical projection of the heat source to trap heat in the underlying units. As postulated previously by Hayba and Ingebritsen (1997), the presence of cap rock facilitates the maximum steam saturation with the formation of a vapor dominated system. Moreover, the increase pore pressure commonly occurs under a capped hydrothermal system (Okubo and Kanda 2010). The importance of the moderate host rock permeability and seafloor topography as the major factors controlling the long live hydrothermal circulation and venting temperature were also inferred for the lost city hydrothermal system (Titarenko and McCaig 2016).

A uniform permeability was assumed in each unit for this study but permeability can be affected by dynamic process like alteration, metamorphism and diagenesis (Rojstaczer et al. 2008). The long life time of hydrothermal systems suggests that a dynamic permeability evolving with time is more representative than a fix value based on actual physical system state (Scott et al. 2016). In cases of moderate to low permeability as in scenario 4 (with cap rock), a high temperature system is developed with a wider 400 °C isotherm resulting from the slow flow velocities. When the permeability of rock increases (as in scenarios 5A and 6A), the duration of development of the hydrothermal system with high fluid enthalpy decreases from 800 ky to 500 ky, which is the time needed for the hydrothermal system to approach steady state. In other words, temperatures and life span of hydrothermal systems decrease with increasing permeabilities, which is corroborated by our simulation results. This was previously demonstrated by Weis (2015) and Scott et al.(2016). A high permeability of geological units favors the formation of low enthalpy hydrothermal system because heat advects away from the heat source. As suggested by Hayba and Ingebritsen (1997), Driesner and Geiger (2007) and Scott et al. (2015), the most favorable location for the development of a two-phases fluid zone is expected to occur within intermediate rock permeability ranging between 10^{-16} to 10^{-15} m^2 as evidenced in scenarios 5A and 6A. In our simulations, a low permeability was assigned to deep model units (C4, R2 and R3) and the driving

forces of fluid flow is consequently governed by fluid density variation due to temperature differences. Development and formation of brine lenses above volcanic conduits in hydrothermal systems requires narrow and high permeability pathway, high salinity and elevated temperature of magmatic fluid where the extension and depth of brine lenses can also be associated to zones of high hydraulic conductivity at shallow depth (Afanasyev et al. 2018). This corroborates with the results of scenarios 7 and 8 (Fig.4.7 and Table 4.2), where narrow hot zone can be observed at the center of the rift. It is also surprising that Afanasyev et al. (2018) found consistent correlation between the extension of brine lens and high conductivity zone close to the surface. This kind of consistent correlation may exist in Asal rift because the extension and the width of the high conductive layer (C1 layer in Fig.3.9 of Hassan Aden et al. 2022a or chapter 3) correspond to zones of upflowing fluids with high enthalpy between the H and F faults in Fig.4.7 that could potentially correspond to the brine lens formation.

4.5.2. Fault permeability and number of active faults

Fault permeability plays an important role for the circulation of fluids between the heat source and the surrounding geological units. Increasing fault permeability like in scenario 3, creates a selective switch mechanism in which previously less hydrothermally active faults (H and F) act as a preferred path of fluid flow compared to the previous scenario 2A. As illustrated in scenario 3, the fault H acts as discharge for the hot up flowing fluids whereas the outermost faults (F-J and F- β) remain recharge conduits as in scenario 2A. In this case of scenario 3, the fault F becomes a new recharge conduit at the center of the rift. Increasing fault permeability decreases the life span of the hydrothermal system whereas increasing the number of faults with the addition of two others minor faults in the numerical simulations (this scenario is not presented above, see Appendix A for more details) allows high velocities of hot discharged fluid between faults J and H and a rising hot upflow area between faults F and β with relatively low velocities. That means if more faults are added in the numerical simulations (assuming all faults are active and permeable), the convection scheme is modified and asymmetric hydrothermal fluid circulation pattern can be expected in which the south-west part of the rift is hotter than the north-east and is the host of fluid discharge at the surface (Appendix C).

Fluid velocity increases in the Asal rift with increasing fault permeability affecting fluid flow pattern. Similar characteristic was found in mid-ocean ridge-flank where the relative space between adjacent faults controlled the wavelength of the heat flow variation and consequently the hydrothermal fluid circulation (Yang 2002). Additionally, high fault permeability leads to a narrower upflow zone whereas low fault permeability allows the development of wider upflow zone (Lupi et al. 2010). This same pattern indicating rising hot upflow where the shape and extension depends

primarily on fault permeability was found with in a tectonically active rift-ridge of Iceland with numerical simulations of hydrothermal fluid circulation (Lupi et al. 2010). A comprehensive review including mechanical behavior, structure and flow properties of faults zones was presented by Faulkner et al. (2010), who argue that fluid flow is mainly controlled by 3D architecture of faults zones which can be heterogeneous. The latter authors concluded that, in crystalline rock at depth, significant flow along faults can be observed where flow is controlled by a small number of fractures within the surrounding damage zone of faults. The latter conclusion may correspond to the conditions of simulated scenarios in this study that can be considered realistic.

4.5.3. Permeability anisotropy and asymmetry

Volcanic context with subparallel layered lava flows and pyroclastic units suggest potentially higher horizontal permeability than in the vertical direction (Hurwitz et al. 2007). This condition may be present in Asal rift where vertical and horizontal deformation were recorded (Cattin et al. 2005; Vigny et al. 2007). Horizontal deformation is related to the extension of plates motion that controlled the development of shear zones in which higher horizontal permeability should be expected in the upper crust. This phenomenon was previously inferred in many tectonically active areas where fluid-filled oriented fractures or shear zone induced electrical anisotropy (see paragraph 5.2 in Hassan Aden et al. 2022a). This was correlated with the recent dimensionality analysis of MT data suggesting the presence of anisotropic layers in the upper crust and continuous conductive subparallel layered inferred with the 2D conductivity model (Hassan Aden et al. 2022a). Additionally, volcanic layering can cause permeability anisotropy with higher horizontal permeability or fluid accumulation in sills extruded under the ductile regime can also be a possible mechanism for permeability anisotropy (Coulon et al. 2017). Interestingly, we found that a greater horizontal permeability (scenarios 5A and 6A, 5B and 6B) better reproduced the fluid flow pattern as evidenced by the thermal state that was better matched to temperature of the geothermal wells (Fig.4.8). Additionally, regional stretching can facilitate high temperatures with magma intrusion and fault creep (Cattin et al. 2005). Those authors calculated the deviatoric stress along a 2D thermo-mechanical model parallel to the 2D conceptual model built in this study. It is surprising that the high deviatoric stress determined by those authors (see Fig.7a in that paper) correlates with the isotherms of the two hot upflow zones (scenarios 5A and 6A) and may likely result in poroelastic effects induced by hydrothermal fluid circulation inside anisotropic layers. The horizontal permeability higher than the vertical favor lateral fluid flow with additional stress originating from the thermal state and the activity of the magma system. Regional stretching further implies formation of regional fracture patterns where permeability anisotropy can emerge and be maintained by regional stress direction at shallow depth and by the supply rate of the

overpressure magma system at great depth. The co-existence of regional stress direction and injection of hot magmatic materials may likely accommodate the general pattern of fluid circulation in an anisotropic medium like rock units of the Asal rift. Similar structural controls playing important role for the hydrothermal fluid circulation was inferred for the Taupo Volcanic Zone of New Zealand (Rowland and Sibson 2004). The latter authors postulated that the preferred direction of extensional structures and their distribution in parallel striking array imply the development of permeability anisotropy where enhanced axial or lateral flow in the shallow crust and enhanced vertical permeability in the basement rocks is expected.

Surprisingly, an interesting dynamic is observed when we consider that the north-east part of Asal rift is more permeable than the south-west part with the results of scenarios 5B and 6B (Fig.4.6). These simulations result demonstrate unexpected hydrothermal fluid flow direction which is mainly directed toward the south-west part of the rift instead toward the north-east that is more permeable. This may be the first time where numerical modeling of multiphase flow and heat transfer demonstrates how the general pattern of regional hydrothermal fluid circulation can be changed and modified if asymmetry distribution of rock permeability is assigned in a 2D conceptual model. This pattern of fluid circulation may occur in Asal rift where the north-east of the rift is supposed to be more deformed and permeable than the south-west (Dobre and Peltzer 2007; Dobre et al. 2007; Hassan Aden et al. 2021). It appears important to recall that asymmetry distribution of basaltic rocks where the thickness of the crust is higher in the south-west of the rift than the north-east was suggested previously by Stein et al. (1991), which can imply higher porous thickness and consequently higher transmissivity.

4.5.4. Heat source and magmatic volatile release

Magmatic fluid release or addition of magmatic volatile represented in the model with a boundary condition of higher heat flow as in scenarios 7 and 8 changed the dynamic flow and the behavior of faults (F-J and F- β). For example, in scenario 8, the faults F-J and F- β act as a preferred path for the hot discharged fluid at the surface while the rising hydrothermal fluid in the inner faults (H and F) seems to flow laterally near the surface and toward the rift shoulders (north-east and south-west) instead of flowing vertically and to be discharged at the surface. It is also important to note that the presence of magmatic fluid flux modified the convection pattern of faults systems as shown in scenario 8. As presented in the majority of scenarios, the inner faults (F-H and F-F) and the surrounding areas hosted the main hot upflow zones. An additional scenario (not presented here) was considered in which the entire bottom boundary of the 2D model was assigned with a constant heat flow of 0.13 W.m^{-2} to verify if this convection scheme is related to the strata topography or to the boundary conditions. Surprisingly, the convection scheme is similar

to the above previous scenarios when high heat flow is assigned at the center of the lower boundary of the C4 layer. It can be interpreted as an evidence of convection scheme that is more impacted by the basement shape or by the depth distribution of the layers in the initial conceptual model. Relative importance of basement shape was previously highlighted with 2D numerical simulations in a mid-ocean-ridge where there are no active faults (Yang 2002). Furthermore, magmatic fluid release created a super-critical geothermal system with a vertical upflow zone extending in the upper crust that originated from the underlying overpressure fluid flow driven by the magma system providing the heat source (scenarios 7 and 8; Fig.4.7). Also, simulation results of scenario 7 corroborate with previous numerical simulations conducted in a magmatic hydrothermal ore deposits with hydrothermal circulation (Weis 2015). In this case, the magmatic fluid release can create hydrological barriers separating the inner system dominated by ascending magmatic fluids under near-lithostatic pressures from surrounding outer systems dominated by convection of colder meteoric fluids under near-hydrostatic pressure (Weis 2015).

Another interesting hidden dynamic that can be deduced from numerical simulations is the nature of the magma system beneath Asal rift. The presence of cooling magma system at the center of rift was proposed by Hassan Aden et al. (2022a) in their 2D electrical conductivity model while multiphase flow modeling conducted in this study suggest that the preferred path of the magmatic fluids is likely confined at the inner faults (scenarios 7 and 8), where hot ascending magmatic fluid can migrate before reaching the surface. Faults H and F are the largest major faults located at center of rift and fault F aligns with the volcanic chain (Fig.4.1) that preceded the eruption of Ardoukoba volcano in 1978 (Dobre et al. 2007). The axial upper and lower basaltic deposit series and youngest volcanic deposits have an average deposition date of 30 k years and are mostly present between the fault H and Fieale caldera (Stein et al. 1991; Manighetti et al. 1998). Thus, as the youngest volcanic deposits are located at the center close to the faults H and F, we hypothesized that the preferred actual path of magmatic volatile release is somehow limited between fault H and Fieale Caldera (Fig.4.1), which has important implication for simulation results of scenarios 7 and 8. Moreover, simulations without magmatic fluid releases but with high heat flow at the lower boundary of the rift (scenarios 1, 2A, 4, 5A, 6A) demonstrated that two hot upflow zones can co-exist, one between fault H and well A6 (F-H and A6; Fig.4.5) and another one between well A5 and Fieale caldera (Fig.4.5 and Fig.4.1). The latter upflow is evidently aligned with the volcanic chain and the seismogenic crust inferred by tomography inversion of passive seismic waves (Dobre et al. 2007). Thus, that upflow can be interpreted as a permeable zone with over pressured vertical conduits. Also, the hot upflow zone between fault H and well A6 is correlated with the main hot upflow zone determined from 2D numerical modeling of multiphase flow aligning with the rift axis and recently presented by Hassan Aden et al. (2021).

Ground surface deformation rate in the Asal rift is believed to be controlled by the injection of magma at shallow depth over geological time (Smittarello et al. 2016), while this kind of deformation in volcanic/tectonic context was also suggested to result from the transient poroelastic variation induced by the hydrothermal fluid circulation (Hurwitz et al. 2007). The latter indicates that injection of hot aqueous fluid (not necessarily magmatic fluid) can induce ground surface deformation observed in some calderas. This corroborates to the results of scenario 5A without magmatic fluid injected at its base that reproduced the thermal state observed in geothermal wells of the Asal rift. Measured temperatures in geothermal wells are in agreement with the simulated temperature for scenario 5A, where the hot upflow zone in the north-east part of the rift (Fig.4.5) coincide with the inferred source of deformation at depth below the Fieale caldera (Cattin et al. 2005; Doubre et al. 2007; Smittarello et al. 2016). Additionally, we suppose that the temperature measured in well A4 corresponds to an early stage of the simulated temperature of well A6 (see Fig.4.8b scenarios 5A, 5B, 6A and 6B). One possible explanation is that A4 located at the center of the rift is closer to the heat source than A6 (Fig.4.2, 4.5 and 4.6). That means the regional thermal state is uniform and can be perturbed by the episodic volcanic activity which influences measured temperature relative to the distance between the heat source and the location of geothermal wells.

4.5.5. Fluid flow pattern and thermal state of the Asal hydrothermal system

General pattern of fluid flow along the 2D model developed in this paper can be combined with the previous simulations of fluid flow in Asal rift that was investigated by numerical modeling along a 2D profile parallel to the rift axis and aligned to the shallow groundwater circulation believed from the Ghoubbet sea to the lake Asal (Hassan Aden et al. 2021). The main findings in that study were the existence of superimposition permeable zones where a deep hydrothermal circulation is covered by a shallow topography driven flow toward the Asal Lake and Ghoubbet sea. Simulation results parallel and perpendicular to the rift axis can be reinterpreted together to globally understand hydrothermal fluid flow circulation. All simulations presented in this study demonstrated ascending hot upflow concentrated in the inner part of the rift. Lateral and descending fluid flow co-exist inside geological units (C1, C2 and C3) that hosted the potential hydrothermal system. Additionally, the direction of flow is somehow different and varying in each unit. In C3, fluid flow direction is toward the center of rift whereas in C2 and C1, the main fluid flow direction is toward the rift shoulders (north-east and south-west), where part of this fluid is recirculated and going downward. This means we can expect four different flow direction that can be regrouped in a whole circular convection scheme. In other words, the system is recharged by the cold downflow (mainly by faults systems) and the cold downflow mixes with the density driven

flow at the deeper level of the system to form a hot upflow area. The latter is flowing laterally close to the surface toward the rift margins (north-east and south-west) before fluid mixes through the cold downflow toward the deeper unit. The important features with this convection pattern when considered in complement to the previous simulation work (Hassan Aden et al. 2021) is the existence of a saddle point where lateral fluid flow at shallow depth is toward the rift margins and toward both Asal Lake and Ghoubbet bay (Fig.4.1). In geothermal areas of New Zealand, the same pattern of fluid flow is anticipated where the deep fluid flow is influenced by magmatic intrusion and conveyed at shallow depth by faults to allow the formation of localized convection cells where the brittle-ductile transition at the base of the seismogenic zone limits downflow of meteoric water (Rowland and Simmons 2012).

4.5.6. Implications for geothermal energy exploration

Potential areas for future geothermal exploration drilling targets could be the two upflow zones illustrated in Fig.4.5. The deepest geothermal well A5 was not productive and this is consistent with the results of the majority of scenarios simulated in this study (scenarios 1, 2A, 4, 5A, 5B, 6A and 6B), where high enthalpy fluid circulation is not present in the surrounding of well A5. A complementary exploration option is to determine with geophysical methods and structural analysis if faults H and F are actives and permeable to determine where they can act as preferred path for fluids. In cases where these major faults are actives, further analysis should be undertaken to determine the permeability of their damage zone by drilling exploration wells across the faults and estimate the in-situ permeability with hydraulic tests. If high permeability inside fault zones is inferred as hypothesized in scenario 3, then fault H should be considered as a potential drilling target. Moreover, in case where the relative amount of magmatic fluid release can be determined with joint inversion of electrical resistivity and seismic velocity to better characterize the rheological parameters of porous rocks and the potential amount of molten rock. Geochemical methods with detailed analysis of notable isotopes gas and their relative spatial degassing distribution may give a first order indication of the magmatic fluid release. All those methods could confirm with the amount of fluid release assumed in this study. If the approximate location of magmatic fluid release can be found, then, the area between the inner faults F-H and F-F can be a drilling target where high enthalpy fluid flow and supercritical geothermal system are expected as shown in Fig.4.7 (scenarios 7 and 8).

The temperature log measured in geothermal well A5 close to fault F is more difficult to explain (Fig.4.1). Hydrothermal mineral assemblages identified in drill cuttings correlate with the temperatures measured in all geothermal wells of Asal rift, except for well A5 where a chlorite-epidote mineral assemblage was identified (Zan et al. 1990). This mineral assemblage is

representative of a high temperature and was observed at a depth between 500 and 1200 m, where a temperature inversion is observed in the well. Thus, a pre-existing high temperature reservoir must have existed before at the location of well A5 before it cooled down (see Fig.4.2 in Hassan Aden et al., 2021). One option to explain this temperature decrease could be the recent infiltration of seawater (Hassan Aden et al. 2021).

4.6. Conclusions

Numerical modeling of multiphase flow was performed in this study in order to understand the role of hydrothermal fluid circulation inside Asal rift hydrothermal system. Intermediate and moderate permeability of host rock was shown to facilitate the formation of a two-phase fluid zone whereas the presence of a low permeability cap rock unit above the heat source allows the development of a high enthalpy system. Moreover, fault permeability and the total number of faults create selective switch mechanisms between the faults with respect to their location and their hydrothermal activity. Some faults zones switched from discharged to recharged area depending on the simulation scenarios. Greater fault permeability and higher total number of faults in the 2D model decreased the life span time of the hydrothermal system. Magmatic fluid release implies the development of super-critical fluid flow zones at the rift center and can change the behavior of fault zones acting as recharge or discharge. The assumption of higher horizontal permeability inside an anisotropic porous medium incorporated in some simulations best reproduced the observed thermal state measured in geothermal wells A4 and A6. The expected general fluid flow pattern under these simulation scenarios is a hydrothermal fluid flow direction toward both the north-east and south-west of the rift. Comparison between the inferred fluid flow direction of this study with the previous work developed by Hassan Aden et al. (2021) allow us to hypothesize the presence of a saddle point in the Asal rift where fluid flow direction is toward south-west, north-east, north-west and south-west. A full picture of topography driven flow and density driven flow in the hydrothermal system of the Asal rift could be better evidenced as a next step with 3D multiphase flow and heat transfer simulations to confirm the presence of the saddle flow point and the general pattern of fluid circulation. Our multiphase flow model is based on the assumption of a single pure water component for the fluid. The presence of non condensable gas (CO₂) or dissolved salt (NaCl) that could have been taken into account in the numerical simulations with multicomponent would likely increases the rate of ground surface deformation and extend the boiling and condensation conditions of fluid (Scott et al. 2017). In addition, all faults in the Asal rift could be modeled and studied to understand their relative contribution to the discharge and recharge of fluid and heat. Buried faults that are not visible at surface could further contribute to

the hydrothermal fluid circulation and could also be taken into account with proper seismic monitoring.

5. DISCUSSION GÉNÉRALE ET CONCLUSIONS

Les travaux réalisés dans cette thèse de doctorat ont contribué à l'identification et l'évaluation d'un large système hydrothermal qui se localiserait sous le rift d'Asal. L'ensemble des trois articles de cette thèse et l'interprétation conjointe des résultats obtenus ont permis de mieux définir les structures conductrices profondes et de développer des modèles conceptuels 2D qui ont amélioré notre connaissance et compréhension sur la dynamique, le fonctionnement et la structure du système hydrothermal.

5.1. Les principaux résultats de la thèse et ses contributions

Une faille majeure parallèle à l'axe du rift appelée faille H serait la limite entre deux zones de résistivité distincte au sein du rift d'Asal. La zone du nord-est du rift serait plus conductrice et plus perméable que la zone du sud-ouest du rift. De plus, les résultats d'inversion 1D des données MT suggèrent que la Calera Fieale aurait une résistivité caractéristique de roches moins poreuse montrant l'absence d'écoulement souterrain significatif. Par ailleurs, la faille H agirait comme une frontière hydrogéologique délimitant deux zones, soit le nord-est du rift qui est plus conducteur et le sud-ouest qui est moins conducteur et serait une zone préférentielle pour l'écoulement des fluides hydrothermaux. L'augmentation du gradient de conductivité électrique (du sud-ouest au nord-est du rift) mise en lumière par le modèle d'inversion 1D développé dans le deuxième chapitre est corroboré avec l'augmentation du taux de déformation horizontale et verticale du rift dans la même direction qui a été estimée à partir des mesures géodésiques (Vigny et al. 2007). La présence de formations plus conductrices au nord-est du rift par rapport au sud-ouest a été corrélée par l'existence d'une déformation horizontale et verticale importante au nord-est et qui serait susceptible d'influencer la variation de la conductivité électrique en profondeur. Un modèle conceptuel hydrogéologique 2D parallèle à la direction d'écoulement régionale admise (de la mer de Ghoubbet vers le Lac Asal) a été construit à partir de l'interprétation du modèle d'inversion 1D de résistivité électrique développé dans le chapitre 2. Ce modèle conceptuel a fait l'objet de simulations numériques multiphasiques d'écoulement et de transfert de chaleur. Les résultats des simulations mettent en évidence l'interaction entre l'écoulement régional, la circulation hydrothermale profonde et l'injection de fluide au niveau de la source de chaleur. Cependant, ces résultats montrent que l'écoulement latéral de l'eau de mer vers le Lac Asal n'a pas d'importance significative sur la circulation hydrothermale à l'échelle régionale. Cette circulation hydrothermale régionale indiquerait que la direction des fluides hydrothermaux est à la fois vers le Lac Asal et vers la mer de Ghoubbet. Les meilleurs résultats de simulations

ont été obtenus en considérant une perméabilité du milieu qui varie avec la température dans les unités géologiques correspondant au potentiel réservoir hydrothermal et à la source de chaleur. La corrélation du profil de température simulé à l'emplacement du puits Asal 6 avec le profil de température mesuré démontre que les résultats de simulations reproduisent globalement l'état thermique actuel du système hydrothermal présent sous le rift d'Asal.

Les méthodes et concepts développés dans le chapitre 3 ou dans l'article 2 apportent plus de précision sur les structures géo-électriques profondes et mettent en évidence l'existence de deux directions géo-électriques bien définies. De plus, ces deux directions géo-électriques correspondent aux deux directions d'anisotropie électriques inférées par l'analyse de la dimensionalité des données MT. Cette analyse de dimensionalité démontre la présence d'anisotropie électrique qui dépend également de la période d'investigation des champs électromagnétiques naturels. Pour les courtes périodes, la direction d'anisotropie électrique dominante est de nord-est alors que pour les longues périodes la direction d'anisotropie électrique dominante est sensiblement nord-sud. Il a été suggéré que l'anisotropie de direction nord-est pour la croûte terrestre supérieure serait due à l'activité tectonique et notamment à la déformation horizontale qui résulte de l'extension du rift dans la direction nord-est. Par ailleurs, l'anisotropie électrique de direction nord-sud serait associée à la déformation verticale du rift qui résulte de l'activité magmatique suivie par une activité tectonique qui donne naissance aux failles. En outre, le rift d'Asal se trouve dans la dépression d'Afar qui forme la jonction triple entre trois structures majeures qui sont en extension, à savoir la vallée du grand rift, le golfe d'Aden et la mer Rouge. Ainsi la direction d'extension et de mouvement des deux plaques arabe et somalienne est $N40^\circ$ (Manighetti et al. 1998) et correspond à la direction d'anisotropie électrique pour les courtes périodes montrée dans le chapitre 3 de cette thèse. La direction de propagation du rift de la mer Rouge vers la dépression Afar est nord-sud et correspondrait sensiblement à la direction d'anisotropie électrique pour les longues périodes. De plus, la direction principale des failles normales est nord-ouest – sud-est, ce qui est proche de la direction nord-sud d'anisotropie électrique pour les longues périodes des données MT. Il est raisonnable de suggérer que la direction des mouvements des plaques et le changement de direction ou rotation des contraintes liées aux mouvements des plaques génèrent une anisotropie électrique dont la direction est parallèle aux directions des contraintes maximales induites par l'activité magmatique et tectonique.

Un modèle d'inversion 2D des données MT développé dans l'article 2 confirme la présence d'un large système/réservoir hydrothermal dans le rift d'Asal et hypothétise l'existence d'un système de magma au centre du rift, plus particulièrement à la projection verticale de la faille H. Ce système de magmatisme migrerait latéralement vers le nord-est et vers le sud-ouest du rift d'Asal comme déjà proposé dans des contextes géologiques similaires à celui d'un rift

(Ebinger and Casey 2001; Doubre and Geoffroy 2003; Keir et al. 2009). Le système/réservoir hydrothermal mis en évidence par le modèle d'inversion 2D abriterait des fluides hydrothermaux et son épaisseur serait plus important au centre du rift d'Asal, notamment entre les failles majeurs F et H.

Afin de mieux confirmer la présence des fluides hydrothermaux et leurs directions d'écoulements au sein du large réservoir hydrothermal déterminé dans l'article 2, le dernier article de cette thèse qui est l'article 3 a été présenté.

Le but principal de l'article 3 ou le chapitre 4 est atteint et confirme l'hypothèse de la présence d'un large réservoir hydrothermal avec la modélisation numérique multiphasique d'écoulement et de transfert de chaleur selon un modèle conceptuel qui a été développé à partir des résultats du modèle d'inversion 2D élaboré dans l'article 2 de la thèse. L'anisotropie électrique mise en évidence dans l'article 2 est interprétée en termes d'anisotropie hydraulique afin de mieux cerner son rôle dans l'évaluation des fluides hydrothermaux. Les principaux paramètres pouvant affecter la circulation hydrothermale régionale et qui ont été étudiés sont la perméabilité, les failles majeures normales, le nombre de failles normales actives perméables, l'anisotropie horizontale de la perméabilité et l'injection de fluide magmatique. Les résultats des simulations de l'article 3 permettent une meilleure compréhension du fonctionnement du système hydrothermal et des mouvements des fluides hydrothermaux dans ce contexte d'extension de la croûte terrestre. L'interprétation conjointe des résultats de simulations de l'article 1 et article 3 ont montré qu'il existerait quatre principales directions d'écoulement du fluide hydrothermal qui sont de nord-est, nord-ouest, sud-ouest et sud-est en provenance du centre du rift d'Asal. Par la suite, l'interprétation d'anisotropie électrique en termes d'anisotropie hydraulique illustre que le fluide hydrothermal profond serait un fluide monophasique (à dominance de liquide) et reproduit l'état thermique régionale. L'augmentation du nombre de failles perméables et l'assignation d'une valeur de perméabilité élevée dans les systèmes des failles modifient le comportement hydrogéologique de ces failles. Par ailleurs, l'injection d'un fluide magmatique change aussi le comportement hydrothermal de ces failles. En effet, des failles perméables qui agissaient comme des zones de recharge des fluides deviennent des zones de décharge des fluides. De plus, le rôle de la distribution de la perméabilité des roches évalué dans l'article 3 montre l'intérêt de considérer une anisotropie horizontale de perméabilité afin de reproduire les températures mesurées dans les puits géothermiques et de présenter un modèle de circulation régional des fluides hydrothermaux permettant de localiser les zones propices pour une éventuelle exploration/exploitation de l'énergie géothermique. Les travaux ont permis de confirmer l'extension d'un réservoir hydrothermal profond et la présence d'un système de magma qui serait à l'origine de la source de chaleur dont le gradient de température influencerait la circulation des eaux souterraines sous le rift d'Asal.

L'ensemble des trois articles de cette thèse ont contribué à quantifier les mouvements verticaux et horizontaux des fluides hydrothermaux dans le système hydrothermal d'Asal par le biais d'une interprétation conjointe de la résistivité électrique, du développement d'un modèle conceptuel, de l'écoulement multiphasique et de transfert de chaleur et l'analyse du fonctionnement et de la structure thermique du système hydrothermal d'Asal. Le lien entre la variation du gradient de déformation et celui de la conductivité électrique est suggéré. Le rôle des failles majeurs dans l'écoulement régionale et leurs contributions ont été quantifiées sous différentes hypothèses de simulations. L'intérêt d'associer l'anisotropie électrique à l'anisotropie hydraulique dans un contexte d'ouverture de rift est mis en évidence avec les travaux de modélisation. L'existence d'un large système hydrothermal qui serait compartimenté est montré à l'aide de la modélisation numérique multiphasique sous l'hypothèse d'anisotropie électrique et hydraulique. La dynamique des fluides souterrains et leurs directions d'écoulements sont inférées pour la première fois dans la zone d'étude et confirment la prépondérance de la circulation hydrothermale.

5.2. Implications pour l'exploration de l'énergie géothermique

Les meilleures options pour d'éventuelles opérations d'exploration de l'énergie géothermique ont été proposées à la fin de chaque article en réévaluant de façon qualitative et quantitative le rôle des failles majeurs, de l'extension des structures conductrices, de l'anisotropie électrique, de l'anisotropie perméabilité et de l'injection du fluide magmatique dans un modèle conceptuel 2D inféré à partir de la résistivité électrique régionale. L'article 1 de cette thèse de doctorat propose d'orienter les travaux d'explorations dans le nord-est du rift en évitant la zone de la Caldera de Fiaele. Et d'après les résultats de simulations numériques multiphasique de l'article 1, il serait judicieux de faire des forages profonds allant jusqu'à 3 km de profondeur. L'article 2 montre l'intérêt de la direction d'anisotropie électrique et le modèle 2D de conductivité électrique développé dans cet article montre des couches conductrices ayant une épaisseur importante au centre du rift et notamment à la projection verticale de la faille H. Des forages déviés vers la direction d'anisotropie électrique pourraient capter le fluide hydrothermal présent ou circulant en profondeur. L'article 3 nous montre clairement les zones préférentielles d'écoulement des fluides hydrothermaux et confirme que deux zones des fluides hydrothermaux ascendant existent sous le rift d'Asal et hypothétise que la zone entre les failles H et F serait le conduit préférentiel du fluide magmatique ascendant qui serait un intérêt pour la recherche et l'exploration géothermique. Il serait judicieux de cibler les zones de décharge du fluide hydrothermal mises par les simulations numériques de l'Article 3.

5.3. Suggestions des travaux futurs

Des travaux scientifiques complémentaires pourront être effectués dans le futur afin de parfaire les résultats obtenus dans cette thèse de doctorat. Par exemple, les résultats du modèle d'inversion 1D de conductivité électrique développé dans l'article 1 seraient nettement plus réalistes en ajoutant plus de stations MT qui couvrent l'ensemble du rift d'Asal-Ghoubbet, notamment dans la mer de Ghoubbet et à l'ouest du Lac Asal. Cela permettrait de comprendre si la faille H agit bien comme une limite et/ou barrière hydrogéologique séparant la région en deux zones de conductivité électrique distinctes dans la zone immergée du rift. Donc, si cette hypothèse émise pour la partie émergée du rift est valable dans la mer de Ghoubbet et à l'ouest du lac Asal, il serait naturellement envisageable de considérer l'ouest du lac Asal comme une zone potentielle pour l'exploration de l'énergie géothermique. Toutefois, la probabilité de trouver à l'ouest du lac Asal un fluide hydrothermal ayant moins de salinité ou n'ayant pas réagi avec l'eau de mer ne serait pas faible. Le modèle conceptuel 2D d'écoulement et de transfert de chaleur développé dans l'article 1 ne tient pas compte la salinité du fluide provenant de l'eau de mer et/ou du lac Asal. De ce fait, il serait intéressant d'évaluer si la circulation hydrothermale régionale et les directions d'écoulement seraient modifiées si la salinité des fluides est considérée dans la modélisation numérique multiphasique. En plus, cela faciliterait le choix d'endroits pour d'éventuelles opérations de forage afin d'éviter les zones ayant des fluides hydrothermaux qui ont totalement ou partiellement réagi avec l'eau de mer.

Les résultats de l'article 2 élucident la présence de deux directions d'anisotropie électrique pour une section perpendiculaire à l'axe du rift en extension ainsi que l'épaisseur des structures conductrices profondes. Il serait envisageable de faire une étude sismique approfondie mettant en évidence l'existence de l'anisotropie sismique pour la corrélérer avec l'anisotropie électrique. Cela permettrait de confirmer d'avantage si l'anisotropie électrique montrée dans cette thèse est de nature macro-anisotropie ou anisotropie structurale. Généralement, l'anisotropie sismique est associée à l'anisotropie macroscopique. Le modèle d'inversion 2D de conductivité électrique développé dans l'article 2 est un modèle d'inversion isotrope qui ne tient pas compte de l'anisotropie des données MT. Par conséquent, un modèle d'inversion anisotrope pourrait être développé afin de mieux imager les structures géo-électriques profondes et confirmer les résultats d'inversion en cas de présence des structures anisotropes. De plus, cela servirait à quantifier le facteur ou le ratio d'anisotropie électrique entre le maximum et le minimum de résistivité électrique. Un autre modèle d'inversion 3D qui tient compte la topographie et de l'anisotropie électrique serait également envisageable mais serait difficile à développer puisqu'il nécessiterait un code d'inversion 3D difficile à trouver. Idéalement, ce serait mieux de commencer par un modèle 3D isotrope et si les structures anisotropes ne sont pas bien imagées de tenter par la suite un modèle 2D anisotrope. Dans le pire de cas, si ni le modèle 2D anisotrope et ni le modèle 3D isotrope ne peuvent pas restituer convenablement les structures anisotropes, un

modèle 3D anisotrope pourrait être envisagé. Par ailleurs, il serait intéressant de vérifier si les tippers (vecteurs d'induction) calculés à partir de la modélisation et/ou inversion conjointes avec les résistivités et phases répliqueraient les tippers observés.

Les résultats présentés dans l'article 3 permettent de mieux quantifier l'écoulement multiphasique à partir d'un modèle conceptuel 2D et présentent une vue d'ensemble sur le fonctionnement et la structure thermique d'un système hydrothermal. Toutefois, les scénarios simulés ne tiennent pas compte la salinité du fluide et la présence d'un fluide magmatique qui pourrait contenir des gaz magmatiques dissouts. Il serait souhaitable de considérer dans le futur des modèles conceptuels 2D considérant ces aspects. En effet, comme déjà démontré par Coumou et al. (2009), la séparation des phases du fluide est conditionnée par la pression du fluide, sa composition et la profondeur hydrostatique. En réalisant un tel modèle d'écoulement qui tient compte la salinité et la possibilité de présence de saumure hypersaline, on pourrait mieux comprendre si le fluide de décharge est essentiellement monophasique à dominance de vapeur ayant un faible degré de salinité ou si le fluide de décharge est un fluide diphasique avec la présence simultanée de vapeur et de saumure hypersaline. De plus, le modèle d'écoulement 2D multiphasique développé dans l'article 3 ne tient pas compte de la déformation horizontal et verticale déjà mise en évidence dans le rift d'Asal (Vigny et al. 2007). Et un modèle qui considérerait cet aspect serait probablement plus réaliste. En effet, la régénération et l'augmentation de la perméabilité dans les zones des failles et de fractures par le processus de la déformation facilite la redistribution des fluides entre les réservoirs d'un système hydrothermal fracturé (Cox 2010). Un modèle 3D d'écoulement multiphasique et de transfert de chaleur pourrait ultimement élucider la présence d'un point de selle telle que suggérée dans cette thèse. De plus, il serait souhaitable de faire un tel modèle 3D pour bien quantifier les directions d'écoulement dans un environnement complexe comme celui du rift d'Asal. Incorporer les failles dans un modèle 3D d'écoulement multiphasique serait une tâche complexe mais permettrait de bien préciser leurs contributions dans l'écoulement des fluides. Également, un modèle numérique multiphasique pourrait être proposé ultérieurement afin de représenter les failles par des fractures discrètes ou avec l'utilisation d'un modèle à double porosité. Des travaux de modélisation numérique simulant l'exploitation des ressources géothermiques et considérant l'analyse de sensibilité des paramètres contrôlant la productivité d'un réservoir géothermique (tel que le débit d'injection de fluide, la température d'injection, le débit de production du fluide hydrothermal et la distance entre le puits d'injection et le puits de production) pourrait être entrepris afin de mieux cerner les facteurs qui conditionnent le rendement, la productivité et la durée de vie du réservoir géothermique. Une modélisation multiphasique similaire a été récemment réalisée par Aliyu et Chen (2017) avec un modèle 3D d'un réservoir géothermique fracturé hétérogène et profond qui est couvert par des couches imperméables avec des fractures discrètes. Ces derniers ont conclu que le débit d'injection de

fluide joue un rôle important sur l'efficacité de production d'énergie géothermique. Finalement, il serait intéressant de considérer les variations de conductivité thermique des unités du modèle conceptuel d'écoulement et de transfert de chaleur pour mieux reproduire les profils de température observés. Et cela pourrait donner une bonne corrélation entre les températures simulées et observées notamment sur le 700 premiers mètres de profondeur. Par conséquent, un ajustement de la conductivité thermique permettrait possible d'avoir une meilleure corrélation. Une analyse de sensibilité de la conductivité thermique serait suggérée pour bien saisir son impact sur le profil de température observé.

6. References

- Abdallah A, Courtillot V, Kasser M, et al (1979) Relevance of Afar seismicity and volcanism to the mechanics of accreting plate boundaries. *Nature* 282:17
- Abdallah S, Utsugi M, Aizawa K, et al (2020) Three-dimensional electrical resistivity structure of the Kuju volcanic group, Central Kyushu, Japan revealed by magnetotelluric survey data. *Journal of Volcanology and Geothermal Research* 400:106898. <https://doi.org/10.1016/j.jvolgeores.2020.106898>
- Afanasyev A, Blundy J, Melnik O, Sparks S (2018) Formation of magmatic brine lenses via focussed fluid-flow beneath volcanoes. *Earth and Planetary Science Letters* 486:119–128. <https://doi.org/10.1016/j.epsl.2018.01.013>
- Aliyu MD, Chen H-P (2017) Optimum control parameters and long-term productivity of geothermal reservoirs using coupled thermo-hydraulic process modelling. *Renewable Energy* 112:151–165. <https://doi.org/10.1016/j.renene.2017.05.032>
- Arnason K The Static Shift Problem in MT Soundings. 12, Proceedings World Geothermal Congress 2015 Melbourne, Australia, 19-25 April 2015
- Árnason K, Eysteinnsson H, Hersir GP (2010) Joint 1D inversion of TEM and MT data and 3D inversion of MT data in the Hengill area, SW Iceland. *Geothermics* 39:13–34. <https://doi.org/10.1016/j.geothermics.2010.01.002>
- Audin L, Manighetti I, Tapponnier P, et al (2001) Fault propagation and climatic control of sedimentation on the Ghoubbet Rift Floor: insights from the Tadjouraden cruise in the western Gulf of Aden. *Geophysical Journal International* 144:391–413. <https://doi.org/10.1046/j.0956-540x.2000.01322.x>
- Awaleh MO, Boschetti T, Soubaneh YD, et al (2017) Geochemical study of the Sakalol-Harralol geothermal field (Republic of Djibouti): Evidences of a low enthalpy aquifer between Manda-Inakir and Asal rift settings. *Journal of Volcanology and Geothermal Research* 331:26–52. <https://doi.org/10.1016/j.jvolgeores.2016.11.008>
- Bahr K (1987) Interpretation of the magnetotelluric impedance tensor: regional induction and local telluric distortion. *J Geophys* 62:119–127

- Bahr K, Bantin M, Jantos Chr, et al (2000) Electrical anisotropy from electromagnetic array data: implications for the conduction mechanism and for distortion at long periods. *Physics of the Earth and Planetary Interiors* 119:237–257. [https://doi.org/10.1016/S0031-9201\(00\)00134-5](https://doi.org/10.1016/S0031-9201(00)00134-5)
- Bahr K, Simpson F (2002) Electrical Anisotropy Below Slow- and Fast-Moving Plates: Paleoflow in the Upper Mantle? *Science* 295:1270–1272. <https://doi.org/10.1126/science.1066161>
- Bellani S, Brogi A, Lazzarotto A, et al (2004) Heat flow, deep temperatures and extensional structures in the Larderello Geothermal Field (Italy): constraints on geothermal fluid flow. *Journal of Volcanology and Geothermal Research* 132:15–29. [https://doi.org/10.1016/S0377-0273\(03\)00418-9](https://doi.org/10.1016/S0377-0273(03)00418-9)
- Bellani, S.; Gherardi, F. Thermal Overview of an Area NW of the Larderello Geothermal Field, Italy. *GRC Trans.* **2013**, 37, 231–236.
- Bibby HM, Caldwell TG, Brown C (2005) Determinable and non-determinable parameters of galvanic distortion in magnetotellurics. *Geophysical Journal International* 163:915–930. <https://doi.org/10.1111/j.1365-246X.2005.02779.x>
- Bischoff JL, Pitzer KS (1989) Liquid-vapor relations for the system NaCl-H₂O: summary of the P-T-x surface from 300° to 500°C. *American Journal of Science* 289:217248
- Booker JR (2014) The Magnetotelluric Phase Tensor: A Critical Review. *Surv Geophys* 35:7–40. <https://doi.org/10.1007/s10712-013-9234-2>
- Boschetti T, Awaleh M, Barbieri M (2018) Waters from the Djiboutian Afar: A Review of Strontium Isotopic Composition and a Comparison with Ethiopian Waters and Red Sea Brines. *Water* 10:1700. <https://doi.org/10.3390/w10111700>
- Brasse H, Kapinos G, Li Y, et al (2009) Structural electrical anisotropy in the crust at the South-Central Chilean continental margin as inferred from geomagnetic transfer functions. *Physics of the Earth and Planetary Interiors* 173:7–16. <https://doi.org/10.1016/j.pepi.2008.10.017>
- Caldwell TG, Bibby HM, Brown C (2004) The magnetotelluric phase tensor. *Geophysical Journal International* 158:457–469. <https://doi.org/10.1111/j.1365-246X.2004.02281.x>

- Cattin R, Doubre C, de Chabalier J-B, et al (2005) Numerical modelling of quaternary deformation and post-rifting displacement in the Asal–Ghoubbet rift (Djibouti, Africa). *Earth and Planetary Science Letters* 239:352–367. <https://doi.org/10.1016/j.epsl.2005.07.028>
- Constable SC, Parker RL, Constable CG (1987) Occam's inversion: A practical algorithm for generating smooth models from electromagnetic sounding data. *GEOPHYSICS* 52:289–300. <https://doi.org/10.1190/1.1442303>
- Correia, H.; Demange, J.; Fabriol, R.; Gerard, A.; Varet, J. *Champ Géothermique d'Asal: Synthèse des Données Disponibles au 1^{er} Janvier 1983; Final BRGM Report 83 SGN 022 GTH; BRGM: Orleans, France, 1983*
- Coulon CA, Hsieh PA, White R, et al (2017) Causes of distal volcano-tectonic seismicity inferred from hydrothermal modeling. *Journal of Volcanology and Geothermal Research* 345:98–108. <https://doi.org/10.1016/j.jvolgeores.2017.07.011>
- Coumou D, Driesner T, Weis P, Heinrich CA (2009) Phase separation, brine formation, and salinity variation at Black Smoker hydrothermal systems. *Journal of Geophysical Research: Solid Earth* 114:. <https://doi.org/10.1029/2008JB005764>
- Cox SF (2010) The application of failure mode diagrams for exploring the roles of fluid pressure and stress states in controlling styles of fracture-controlled permeability enhancement in faults and shear zones. *Geofluids* 10:217–233. <https://doi.org/10.1111/j.1468-8123.2010.00281.x>
- Cox SF, Knackstedt MA, Braun J (2001) Principles of Structural Control on Permeability and Fluid Flow in Hydrothermal Systems. <https://doi.org/10.5382/Rev.14.01>
- D'Amore F, Giusti D, Abdallah A (1998) Geochemistry of the high-salinity geothermal field of Asal, Republic of Djibouti, Africa. *Geothermics* 27:197–210. [https://doi.org/10.1016/S0375-6505\(97\)10009-8](https://doi.org/10.1016/S0375-6505(97)10009-8)
- De Chabalier J-B, Avouac J-P (1994) Kinematics of the Asal Rift (Djibouti) Determined from the Deformation of Fieale Volcano. *Science* 265:1677–1681. <https://doi.org/10.1126/science.265.5179.1677>
- Demange, J.; Puvilland, P. *Champ Géothermique d'Asal. Synthèse des Données; Rapport C.F.G; BRGM: Orleans, France, 1993.*

- Dobre C (2004) Structure et mécanismes des segments de rift volcano-tectoniques: études de rifts anciens (Ecosse, Islande) et d'un rift actif (Asal-Ghoubbet). Thèse de doctorat, Le Mans, France.
- Dobre C, Geoffroy L (2003) Rift-zone development around a plume-related magma centre on the Isle of Skye (Scotland): a model for stress inversions. *Terra Nova* 15:230–237. <https://doi.org/10.1046/j.1365-3121.2003.00494.x>
- Dobre C, Manighetti I, Dorbath L, et al (2007) Crustal structure and magmato-tectonic processes in an active rift (Asal-Ghoubbet, Afar, East Africa): 2. Insights from the 23-year recording of seismicity since the last rifting event. *Journal of Geophysical Research: Solid Earth* 112:. <https://doi.org/10.1029/2006JB004333>
- Dobre C, Peltzer G (2007) Fluid-controlled faulting process in the Asal Rift, Djibouti, from 8 yr of radar interferometry observations. *Geology* 35:69–72
- Driesner T, Geiger S (2007) Numerical Simulation of Multiphase Fluid Flow in Hydrothermal Systems. *Reviews in Mineralogy and Geochemistry* 65:187–212. <https://doi.org/10.2138/rmg.2007.65.6>
- Duba A, Constable S (1993) The electrical conductivity of Iherzolite. *J Geophys Res* 98:11885–11899. <https://doi.org/10.1029/93JB00995>
- Ebinger CJ, Casey M (2001) Continental breakup in magmatic provinces: An Ethiopian example. *Geology* 29:527–530. [https://doi.org/10.1130/0091-7613\(2001\)029<0527:CBIMPA>2.0.CO;2](https://doi.org/10.1130/0091-7613(2001)029<0527:CBIMPA>2.0.CO;2)
- Einarsson P (1991) Earthquakes and present-day tectonism in Iceland. *Tectonophysics* 189:261–279. [https://doi.org/10.1016/0040-1951\(91\)90501-l](https://doi.org/10.1016/0040-1951(91)90501-l)
- Eisel M, Bahr K (1993) Electrical Anisotropy in the Lower Crust of British Columbia: an Interpretation of a Magnetotelluric Profile after Tensor Decomposition. *J geomagn geoelec* 45:1115–1126. <https://doi.org/10.5636/jgg.45.1115>
- Eisel M, Haak V, Pek J, Červ V (2001) A magnetotelluric profile across the German Deep Drilling Project (KTB) area: Two- and three-dimensional modeling results. *Journal of Geophysical Research: Solid Earth* 106:16061–16073. <https://doi.org/10.1029/2000JB900451>

- Faulds J, Hinz N (2015) Favorable tectonic and structural settings of geothermal systems in the Great Basin region, western USA: Proxies for discovering blind geothermal systems. Proceedings World Geothermal Congress, Melbourne, Australia, 19-25 April 2015
- Faulkner DR, Jackson CAL, Lunn RJ, et al (2010) A review of recent developments concerning the structure, mechanics and fluid flow properties of fault zones. *Journal of Structural Geology* 32:1557–1575. <https://doi.org/10.1016/j.jsg.2010.06.009>
- Fouillac, C.; Fabriol, R.; Lundt, F. Champ Géothermique d'Asal. Synthèse des Données Hydrogéologiques et Géochimiques Disponibles au 1er Janvier 1983; Final BRGM Report 83 SGN 022 GTH; BRGM: Orleans, France, 1983.
- Frederiksen AW, Ferguson IJ, Eaton D, et al (2006) Mantle fabric at multiple scales across an Archean–Proterozoic boundary, Grenville Front, Canada. *Physics of the Earth and Planetary Interiors* 158:240–263. <https://doi.org/10.1016/j.pepi.2006.03.025>
- Gadalia, A.; Traineau, H. Deux Champs Géothermiques de Rifts Océaniques Emergés: Krafla (Islande) et Asal (République de Djibouti. Une Étude Comparative des Contextes Géologiques et des Méthodes d'Exploration; Final BRGM Report 84 SGN 216 IRG; BRGM: Orleans, France, 1984.
- García Juanatey MA, Hübert J, Tryggvason A, et al (2019) 2D and 3D MT in the central Skellefte Ore District, northern Sweden. *Tectonophysics* 764:124–138. <https://doi.org/10.1016/j.tecto.2019.04.003>
- Gasse F, Fontes J-C (1989) Palaeoenvironments and palaeohydrology of a tropical closed lake (Lake Asal, Djibouti) since 10,000 yr B.P. *Palaeogeography, Palaeoclimatology, Palaeoecology* 69:67–102. [https://doi.org/10.1016/0031-0182\(89\)90156-9](https://doi.org/10.1016/0031-0182(89)90156-9)
- Gatzemeier A, Tommasi A (2006) Flow and electrical anisotropy in the upper mantle: Finite-element models constraints on the effects of olivine crystal preferred orientation and microstructure. *Physics of the Earth and Planetary Interiors* 158:92–106. <https://doi.org/10.1016/j.pepi.2006.01.009>
- Gaudin D, Finizola A, Delcher E, et al (2015) Influence of rainfalls on heat and steam fluxes of fumarolic zones: Six months records along the Ty fault (Soufrière of Guadeloupe, Lesser Antilles). *Journal of Volcanology and Geothermal Research* 302:273–285. <https://doi.org/10.1016/j.jvolgeores.2015.06.015>

- Giroux B, Chouteau M, Descloîtres M, Ritz M (1997) Use of the magnetotelluric method in the study of the deep Maestrichtian aquifer in Senegal. *Journal of Applied Geophysics* 38:77–96. [https://doi.org/10.1016/S0926-9851\(97\)00016-5](https://doi.org/10.1016/S0926-9851(97)00016-5)
- Gómez-Treviño E, Esparza FJ, Muñiz Y, Calderón A (2014) The magnetotelluric transverse electric mode as a natural filter for static effects: Application to the COPROD2 and COPROD2S2 data sets. *GEOPHYSICS* 79:E91–E99. <https://doi.org/10.1190/geo2012-0522.1>
- Harris RN, Fisher AT, Chapman DS (2004) Fluid flow through seamounts and implications for global mass fluxes. *Geol* 32:725. <https://doi.org/10.1130/G20387.1>
- Hassan Aden A, Raymond J, Giroux B, Sanjuan B (2021) New Insights into Hydrothermal Fluid Circulation Affected by Regional Groundwater Flow in the Asal Rift, Republic of Djibouti. *Energies* 14:1166. <https://doi.org/10.3390/en14041166>
- Hayba DO, Ingebritsen SE (1997) Multiphase groundwater flow near cooling plutons. *Journal of Geophysical Research: Solid Earth* 102:12235–12252. <https://doi.org/10.1029/97JB00552>
- Hedenquist JW, Lowenstern JB (1994) The role of magmas in the formation of hydrothermal ore deposits. *Nature* 370:519–527. <https://doi.org/10.1038/370519a0>
- Heise W, Caldwell TG, Bertrand EA, et al (2013) Changes in electrical resistivity track changes in tectonic plate coupling. *Geophysical Research Letters* 40:5029–5033. <https://doi.org/10.1002/grl.50959>
- Heise W, Caldwell TG, Bibby HM, Brown C (2006) Anisotropy and phase splits in magnetotellurics. *Physics of the Earth and Planetary Interiors* 158:107–121. <https://doi.org/10.1016/j.pepi.2006.03.021>
- Heise W, Pous J (2001) Effects of anisotropy on the two-dimensional inversion procedure. *Geophysical Journal International* 147:610–621. <https://doi.org/10.1046/j.0956-540x.2001.01560.x>
- Hermance JF (1982) Magnetotelluric and geomagnetic deep-sounding studies in rifts and adjacent areas: constraints on physical processes in the crust and upper mantle. In: *Continental and oceanic rifts*. AGU Washington, DC, pp 169–192

- Houssein DE, Axelsson G (2010) Geothermal resources in the Asal Region, Republic of Djibouti: An update with emphasis on reservoir engineering studies. *Geothermics* 39:220–227. <https://doi.org/10.1016/j.geothermics.2010.06.006>
- Houssein, I.; Sanjuan, B.; Michard, G. Indices Géochimiques de l'Existence d'un Fluide à 210 °C dans la Région d'Obock (République de Djibouti); Note au C.R.A.S, t.316, Série II; Note au C.R.A.S: Paris, France, 1993; pp. 771–776.
- Hurwitz S, Christiansen LB, Hsieh PA (2007) Hydrothermal fluid flow and deformation in large calderas: Inferences from numerical simulations. *Journal of Geophysical Research: Solid Earth* 112:. <https://doi.org/10.1029/2006JB004689>
- Ingebritsen SE, Flinders AF, Kauahikaua JP, Hsieh PA (2021) Modeling Groundwater Inflow to the New Crater Lake at Kīlauea Volcano, Hawai'i. *Groundwater* 59:7–15. <https://doi.org/10.1111/gwat.13023>
- Jalludin, M. State of Knowledge of Geothermal Provinces of Republic of Djibouti; UNU training KENGEN: Naivasha, Kenya, 2007
- Jalludin M. State of knowledge of geothermal provinces of the Republic Djibouti; UNU-GTP, GDC and KenGen Geothermal training programme NU training KENGEN: Naivasha, Kenya, 2012.
- Karato S (1990) The role of hydrogen in the electrical conductivity of the upper mantle. *Nature* 347:272–273. <https://doi.org/10.1038/347272a0>
- Keir D, Hamling IJ, Ayele A, et al (2009) Evidence for focused magmatic accretion at segment centers from lateral dike injections captured beneath the Red Sea rift in Afar. *Geology* 37:59–62. <https://doi.org/10.1130/G25147A.1>
- Kellett RL, Mareschal M, Kurtz RD (1992) A model of lower crustal electrical anisotropy for the Pontiac Subprovince of the Canadian Shield. *Geophysical Journal International* 111:141–150. <https://doi.org/10.1111/j.1365-246X.1992.tb00560.x>
- Kipp, K.L.; Hsieh, P.A.; Charlton, S.R. Guide to the Revised Ground-Water Flow and Heat Transport Simulator: HYDROTHERM—Version 3; USGS: Reston, VA, USA, 2008.
- Kirkby A, Heinson G, Holford S, Thiel S (2015) Mapping fractures using 1D anisotropic modelling of magnetotelluric data: a case study from the Otway Basin, Victoria, Australia. *Geophysical Journal International* 201:1961–1976. <https://doi.org/10.1093/gji/ggv116>

- Krivochieva S, Chouteau M (2003) Integrating TDEM and MT methods for characterization and delineation of the Santa Catarina aquifer (Chalco Sub-Basin, Mexico). *Journal of Applied Geophysics* 52:23–43. [https://doi.org/10.1016/S0926-9851\(02\)00231-8](https://doi.org/10.1016/S0926-9851(02)00231-8)
- Lilley FEM (2020) Magnetotellurics: the CBB or phase tensor and Bahr's 1988 analysis. *Exploration Geophysics* 51:401–421. <https://doi.org/10.1080/08123985.2020.1717333>
- Lupi M, Geiger S, Graham CM (2010) Hydrothermal fluid flow within a tectonically active rift-ridge transform junction: Tjörnes Fracture Zone, Iceland. *Journal of Geophysical Research: Solid Earth* 115:. <https://doi.org/10.1029/2009JB006640>
- Manighetti I, Tapponnier P, Courtillot V, et al (1997) Propagation of rifting along the Arabia-Somalia Plate Boundary: The Gulfs of Aden and Tadjoura. *Journal of Geophysical Research: Solid Earth* 102:2681–2710. <https://doi.org/10.1029/96JB01185>
- Manighetti I, Tapponnier P, Gillot PY, et al (1998) Propagation of rifting along the Arabia-Somalia Plate Boundary: Into Afar. *Journal of Geophysical Research: Solid Earth* 103:4947–4974. <https://doi.org/10.1029/97JB02758>
- Marini, L. Geochemistry of North Ghoubbat-Asal Region; *Geothermica Italiana Report 551-9-LUI; Geothermica: Reykjavík, Iceland, 1987.*
- Medynski S, Pik R, Burnard P, et al (2016) Magmatic cycles pace tectonic and morphological expression of rifting (Afar depression, Ethiopia). *Earth and Planetary Science Letters* 446:77–88. <https://doi.org/10.1016/j.epsl.2016.04.014>
- Meju MA (2002) Geoelectromagnetic Exploration For Natural Resources: Models, Case Studies And Challenges. *Surveys in Geophysics* 23:133–206. <https://doi.org/10.1023/A:1015052419222>
- Mlynarski M, Zlotnicki J (2001) Fluid circulation in the active emerged Asal rift (east Africa, Djibouti) inferred from self-potential and Telluric–Telluric prospecting. *Tectonophysics* 339:455–472
- Moorkamp M, Avdeeva A, Basokur AT, Erdogan E (2020) Inverting magnetotelluric data with distortion correction—stability, uniqueness and trade-off with model structure. *Geophysical Journal International* 222:1620–1638. <https://doi.org/10.1093/gji/ggaa278>

- Nam MJ, Kim HJ, Song Y, et al (2009) Three-dimensional topographic and bathymetric effects on magnetotelluric responses in Jeju Island, Korea. *Geophysical Journal International* 176:457–466. <https://doi.org/10.1111/j.1365-246X.2008.03993.x>
- Nurhasan, Ogawa Y, Ujihara N, et al (2006) Two electrical conductors beneath Kusatsu-Shirane volcano, Japan, imaged by audiomagnetotellurics, and their implications for the hydrothermal system. *Earth Planet Sp* 58:1053–1059. <https://doi.org/10.1186/BF03352610>
- Okubo A, Kanda W (2010) Numerical simulation of piezomagnetic changes associated with hydrothermal pressurization. *Geophysical Journal International*. <https://doi.org/10.1111/j.1365-246X.2010.04580.x>
- Padilha AL, Vitorello Í, Pádua MB, Bologna MS (2006) Lithospheric and sublithospheric anisotropy beneath central-southeastern Brazil constrained by long period magnetotelluric data. *Physics of the Earth and Planetary Interiors* 158:190–209. <https://doi.org/10.1016/j.pepi.2006.05.006>
- Partzsch GM, Schilling FR, Arndt J (2000) The influence of partial melting on the electrical behavior of crustal rocks: laboratory examinations, model calculations and geological interpretations. *Tectonophysics* 317:189–203. [https://doi.org/10.1016/S0040-1951\(99\)00320-0](https://doi.org/10.1016/S0040-1951(99)00320-0)
- Pedersen LB, Engels M (2005) Routine 2D inversion of magnetotelluric data using the determinant of the impedance tensor. *GEOPHYSICS* 70:G33–G41. <https://doi.org/10.1190/1.1897032>
- Piña-Varas P, Ledo J, Queralt P, et al (2018) On the detectability of Teide volcano magma chambers (Tenerife, Canary Islands) with magnetotelluric data. *Earth Planets Space* 70:14. <https://doi.org/10.1186/s40623-018-0783-y>
- Pinzuti P, Humler E, Manighetti I, Gaudemer Y (2013) Petrological constraints on melt generation beneath the Asal Rift (Djibouti) using quaternary basalts. *Geochemistry, Geophysics, Geosystems* 14:2932–2953. <https://doi.org/10.1002/ggge.20187>
- Pinzuti P, Mignan A, King GCP (2010) Surface morphology of active normal faults in hard rock: Implications for the mechanics of the Asal Rift, Djibouti. *Earth and Planetary Science Letters* 299:169–179. <https://doi.org/10.1016/j.epsl.2010.08.032>

- Prawirodirdjo L, Bock Y (2004) Instantaneous global plate motion model from 12 years of continuous GPS observations. *Journal of Geophysical Research: Solid Earth* 109:. <https://doi.org/10.1029/2003JB002944>
- Ragueneil M, Driesner T, Bonneau F (2019) Numerical modeling of the geothermal hydrology of the Volcanic Island of Basse-Terre, Guadeloupe. *Geotherm Energy* 7:28. <https://doi.org/10.1186/s40517-019-0144-5>
- Raymond J, Langevin H, Comeau F-A, Malo M (2022) Temperature dependence of rock salt thermal conductivity: Implications for geothermal exploration. *Renewable Energy* 184:26–35. <https://doi.org/10.1016/j.renene.2021.11.080>
- Rojstaczer SA, Ingebritsen SE, Hayba DO (2008) Permeability of continental crust influenced by internal and external forcing. *Geofluids* 8:128–139. <https://doi.org/10.1111/j.1468-8123.2008.00211.x>
- Roux E, Moorkamp M, Jones AG, et al (2011) Joint inversion of long-period magnetotelluric data and surface-wave dispersion curves for anisotropic structure: Application to data from Central Germany: JOINT INVERSION OF MT AND SW DATA. *Geophys Res Lett* 38:n/a-n/a. <https://doi.org/10.1029/2010GL046358>
- Rowland JV, Sibson RH (2004) Structural controls on hydrothermal flow in a segmented rift system, Taupo Volcanic Zone, New Zealand. *Geofluids* 4:259–283. <https://doi.org/10.1111/j.1468-8123.2004.00091.x>
- Rowland JV, Simmons SF (2012) Hydrologic, Magmatic, and Tectonic Controls on Hydrothermal Flow, Taupo Volcanic Zone, New Zealand: Implications for the Formation of Epithermal Vein Deposits. *Economic Geology* 107:427–457. <https://doi.org/10.2113/econgeo.107.3.427>
- Rung-Arunwan T, Siripunvaraporn W, Utada H (2017) Use of ssq rotational invariant of magnetotelluric impedances for estimating informative properties for galvanic distortion. *Earth Planets Space* 69:80. <https://doi.org/10.1186/s40623-017-0665-8>
- Rung-Arunwan T, Siripunvaraporn W, Utada H (2016) On the Berdichevsky average. *Physics of the Earth and Planetary Interiors* 253:1–4. <https://doi.org/10.1016/j.pepi.2016.01.006>
- Sakindi, G. Three-Dimensional Inversion of Magnetotelluric Data: Geological-Geothermal Interpretation of Asal Geothermal Field, Djibouti. Master's Thesis, United Nations University, Reykjavik, Iceland, 2015.

- Sanford WE (2005) A simulation of the hydrothermal response to the Chesapeake Bay bolide impact. *Geofluids* 5:185–201. <https://doi.org/10.1111/j.1468-8123.2005.00110.x>
- Sanjuan, B. Use of a new Sodium/Lithium (Na/Li) geothermometric relationship for High-Temperature (HT) geothermal fluids derived from seawater/basalt interaction processes: Application to the Djibouti case. In *Proceedings of the Third East African Rift Geothermal Conference, Djibouti, Djibouti, 22–25 November 2010*; p. 22.2
- Sanjuan B, Michard G, Michard A (1990) Origine des substances dissoutes dans les eaux des sources thermales et des forages de la région Asal-Ghoubbet (République de Djibouti). *Journal of Volcanology and Geothermal Research* 43:333–352
- Schardt C, Large R, Yang J (2006) Controls on Heat Flow, Fluid Migration, and Massive Sulfide Formation of an Off-axis Hydrothermal System—the Lau Basin Perspective. *American Journal of Science* 306:103–134. <https://doi.org/10.2475/ajs.306.2.103>
- Scott S, Driesner T, Weis P (2016) The thermal structure and temporal evolution of high-enthalpy geothermal systems. *Geothermics* 62:33–47. <https://doi.org/10.1016/j.geothermics.2016.02.004>
- Scott S, Driesner T, Weis P (2017) Boiling and condensation of saline geothermal fluids above magmatic intrusions. *Geophysical Research Letters* 44:1696–1705. <https://doi.org/10.1002/2016GL071891>
- Scott S, Driesner T, Weis P (2015) Geologic controls on supercritical geothermal resources above magmatic intrusions. *Nat Commun* 6:7837. <https://doi.org/10.1038/ncomms8837>
- Shalivahan, Bhattacharya BB (2005) Electrical anisotropy of asthenosphere in a region of window to mantle underneath Eastern Indian Craton. *Physics of the Earth and Planetary Interiors* 152:43–61. <https://doi.org/10.1016/j.pepi.2005.06.001>
- Simpson F (2000) A three-dimensional electromagnetic model of the southern Kenya Rift: Departure from two dimensionality as a possible consequence of a rotating stress field. *Journal of Geophysical Research: Solid Earth* 105:19321–19334. <https://doi.org/10.1029/2000JB900106>
- Simpson F, Bahr K (2005) *Practical Magnetotellurics*, 1st edn. Cambridge University Press
- Smittarello D, Grandin R, Chabalier J-BD, et al (2016) Transient deformation in the Asal-Ghoubbet Rift (Djibouti) since the 1978 diking event: Is deformation controlled by magma

- supply rates? *Journal of Geophysical Research: Solid Earth* 121:6030–6052. <https://doi.org/10.1002/2016JB013069>
- Spichak V, Manzella A (2009) Electromagnetic sounding of geothermal zones. *Journal of Applied Geophysics* 68:459–478. <https://doi.org/10.1016/j.jappgeo.2008.05.007>
- Stein RS, Briole P, Ruegg J-C, et al (1991) Contemporary, Holocene, and Quaternary deformation of the Asal Rift, Djibouti: Implications for the mechanics of slow spreading ridges. *Journal of Geophysical Research: Solid Earth* 96:21789–21806. <https://doi.org/10.1029/91JB02118>
- Stieltjes L, Joron J-L, Treuil M, Varet Ja (1976) Le rift d'Asal, segment de dorsale émergé: discussion pétrologique et géochimique. *Bull Soc Géol Fr* 18:851–862
- Szarka L, Menvielle M (1997) Analysis of rotational invariants of the magnetotelluric impedance tensor. *Geophysical Journal International* 129:133–142. <https://doi.org/10.1111/j.1365-246X.1997.tb00942.x>
- Titarenko SS, McCaig AM (2016) Modelling the Lost City hydrothermal field: influence of topography and permeability structure. *Geofluids* 16:314–328. <https://doi.org/10.1111/gfl.12151>
- Tong X, Liu J, Li A (2018) Two-dimensional regularized inversion of AMT data based on rotation invariant of Central impedance tensor. *Earth and Planetary Physics* 2:430–437. <https://doi.org/10.26464/epp2018040>
- Tournerie B, Chouteau M, Marcotte D (2007) Magnetotelluric static shift: Estimation and removal using the cokriging method. *Geophysics* 72:. <https://doi.org/10.1190/1.2400625>
- Triahadini A, Aizawa K, Teguri Y, et al (2019) Magnetotelluric transect of Unzen graben, Japan: conductors associated with normal faults. *Earth Planets Space* 71:28. <https://doi.org/10.1186/s40623-019-1004-z>
- Usui Y, Ogawa Y, Aizawa K, et al (2017) Three-dimensional resistivity structure of Asama Volcano revealed by data-space magnetotelluric inversion using unstructured tetrahedral elements. *Geophys J Int* 208:1359–1372. <https://doi.org/10.1093/gji/ggw459>
- Usui Y, Uyeshima M, Ogawa T, et al (2021) Electrical Resistivity Structure Around the Atotsugawa Fault, Central Japan, Revealed by a New 2-D Inversion Method Combining Wideband-MT

- and Network-MT Data Sets. *Journal of Geophysical Research: Solid Earth* 126:e2020JB020904. <https://doi.org/10.1029/2020JB020904>
- Van NP, Boyer D, Le Mouél J-L, Courtillot V (1981) Identification of a magma chamber in the Ghoubbet-Asal Rift (Djibouti) from a magnetotelluric experiment. *Earth and Planetary Science Letters* 52:372–380
- Vigny C, Chabalier J-B de, Ruegg J-C, et al (2007a) Twenty-five years of geodetic measurements along the Tadjoura-Asal rift system, Djibouti, East Africa. *Journal of Geophysical Research: Solid Earth* 112:. <https://doi.org/10.1029/2004JB003230>
- Vigny C, de Chabalier J-B, Ruegg J-C, et al (2007b) Twenty-five years of geodetic measurements along the Tadjoura-Asal rift system, Djibouti, East Africa. *Journal of Geophysical Research: Solid Earth* 112:
- Vosteen H-D, Schellschmidt R (2003) Influence of temperature on thermal conductivity, thermal capacity and thermal diffusivity for different types of rock. *Physics and Chemistry of the Earth, Parts A/B/C* 28:499–509. [https://doi.org/10.1016/S1474-7065\(03\)00069-X](https://doi.org/10.1016/S1474-7065(03)00069-X)
- Wannamaker PE (2005) Anisotropy Versus Heterogeneity in Continental Solid Earth Electromagnetic Studies: Fundamental Response Characteristics and Implications for Physicochemical State. *Surv Geophys* 26:733–765. <https://doi.org/10.1007/s10712-005-1832-1>
- Wannamaker PE, Hasterok DP, Johnston JM, et al (2008) Lithospheric dismemberment and magmatic processes of the Great Basin–Colorado Plateau transition, Utah, implied from magnetotellurics. *Geochemistry, Geophysics, Geosystems* 9:. <https://doi.org/10.1029/2007GC001886>
- Weaver J.T., Agarwal A.K., and Lilley F.E.M. 2006. The relationship between the magnetotelluric tensor invariants and the phase tensor of Caldwell, Bibby and Brown. *Exploration Geophysics* 37: 261–7.
- Weis P (2015) The dynamic interplay between saline fluid flow and rock permeability in magmatic-hydrothermal systems. *Geofluids* 15:350–371. <https://doi.org/10.1111/gfl.12100>
- Yamaya Y, Alanis PKB, Takeuchi A, et al (2013) A large hydrothermal reservoir beneath Taal Volcano (Philippines) revealed by magnetotelluric resistivity survey: 2D resistivity modeling. *Bull Volcanol* 75:729. <https://doi.org/10.1007/s00445-013-0729-y>

Yang J (2002) Influence of normal faults and basement topography on ridge-flank hydrothermal fluid circulation. *Geophysical Journal International* 151:83–87.
<https://doi.org/10.1046/j.1365-246X.2002.01741.x>

Zan L, Gianelli G, Passerini P, et al (1990) Geothermal exploration in the republic of djibouti: thermal and geological data of the hanlé and asal areas. *Geothermics* 19:561–582.
[https://doi.org/10.1016/0375-6505\(90\)90005-V](https://doi.org/10.1016/0375-6505(90)90005-V)

7. ANNEXES

Appendix A for Chapter 2

Table A1. Verification of mesh independence for simulation of scenario 1.

Number of Elements	Temperature at 1600 m Depth in Asal 6 Well T (°C)	Absolute Value of Relative Difference (%)
1200	238.931	---
2400	248.257	0.039
4000	254.387	0.024
4800	256.327	0.007
10,000	255.095	0.004

Appendix B for Chapter 3

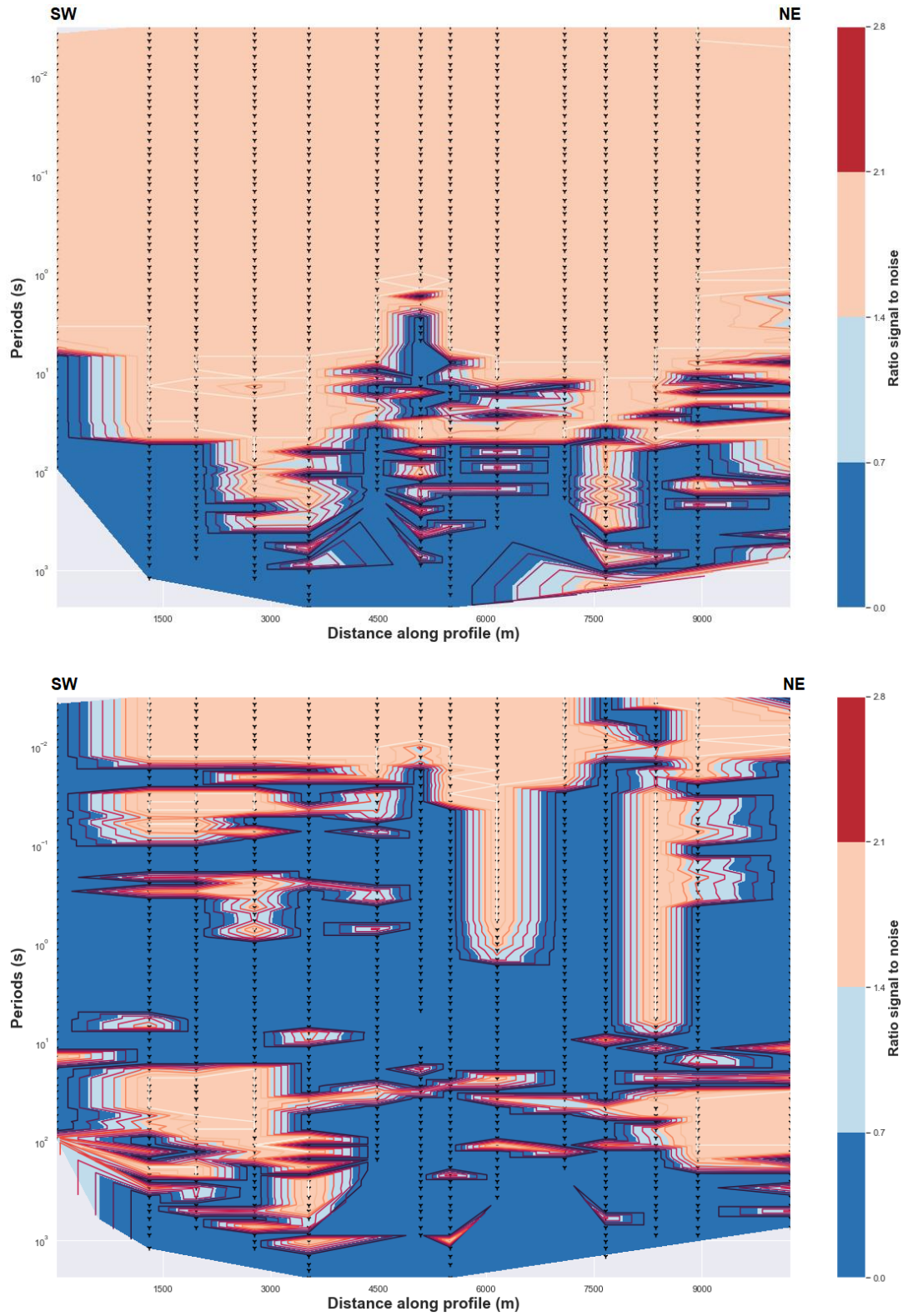


Fig. AB2. Above) Uncertainty of the impedance estimates. Below) Uncertainty of the tipper estimates.

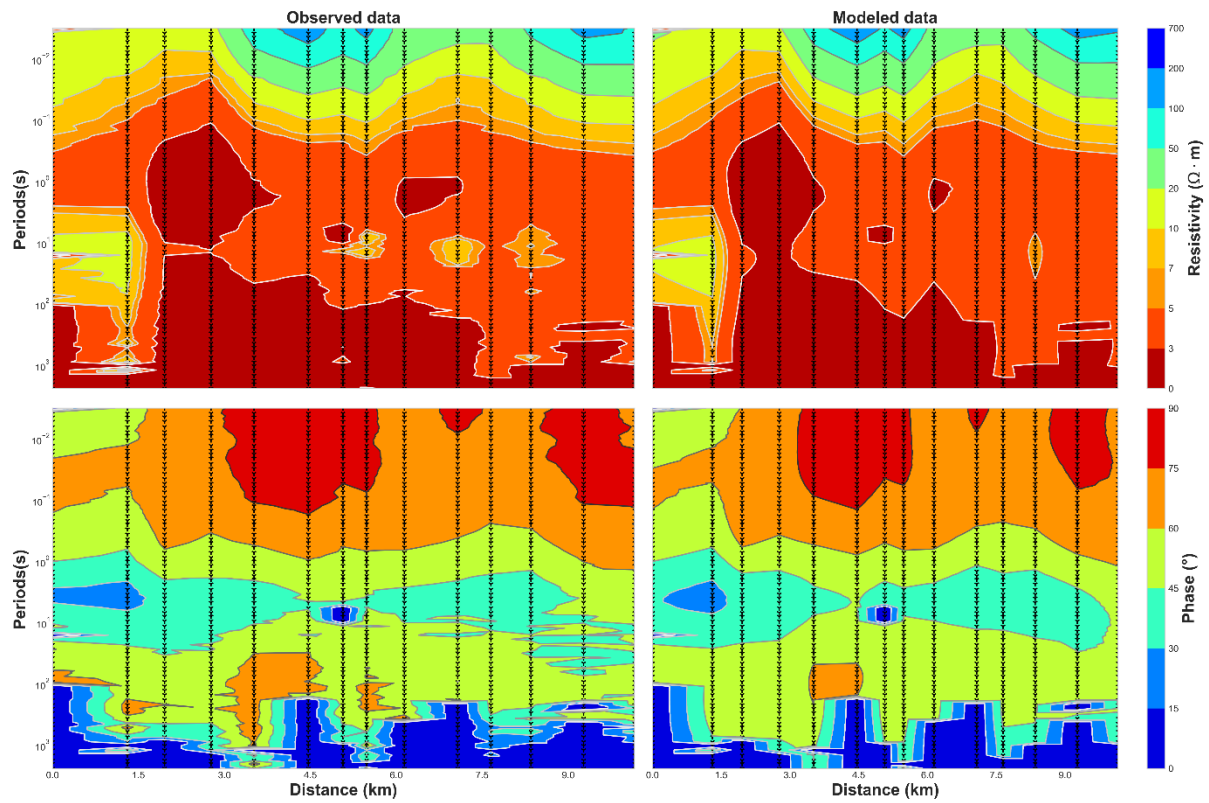
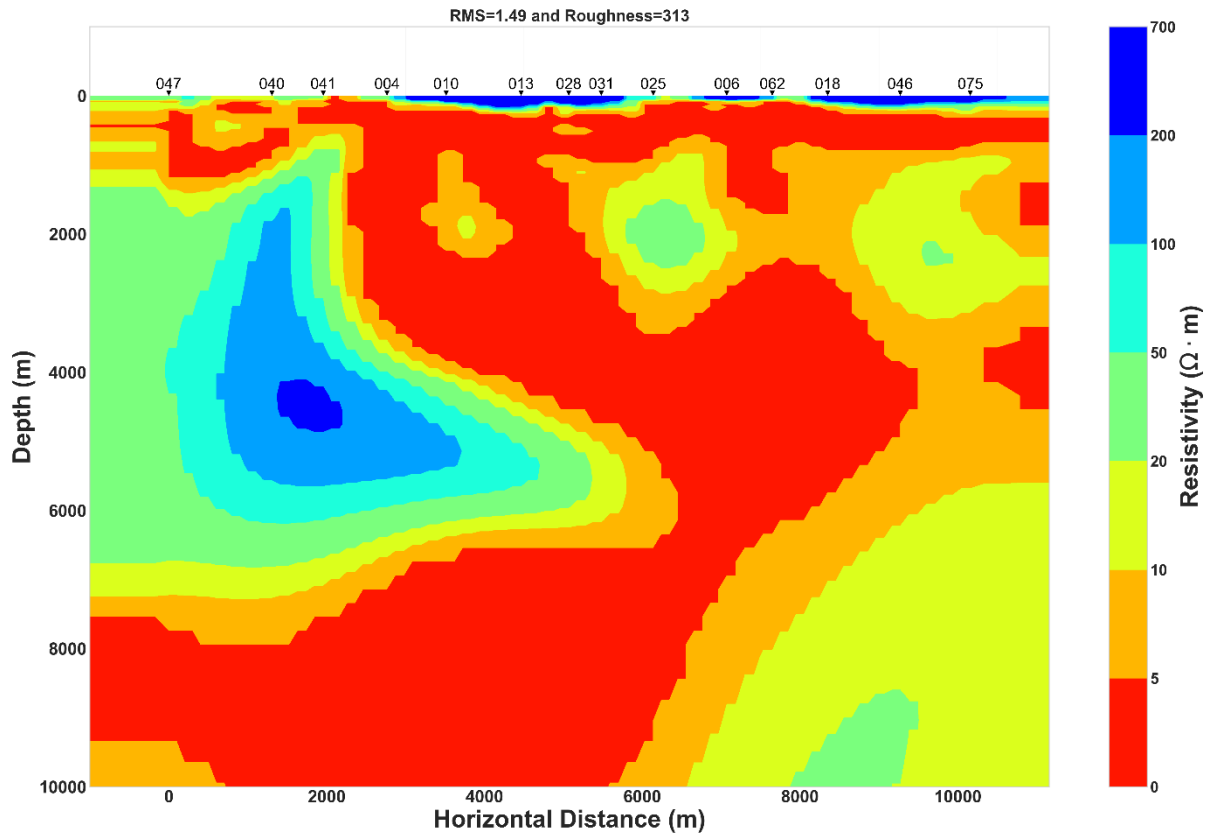


Fig. A2B. Above) Joint Inversion model of TE and TM data for geo-electric strike of N120°E. Below) Comparison between observed and modeled data.

Appendix C for Chapter 4

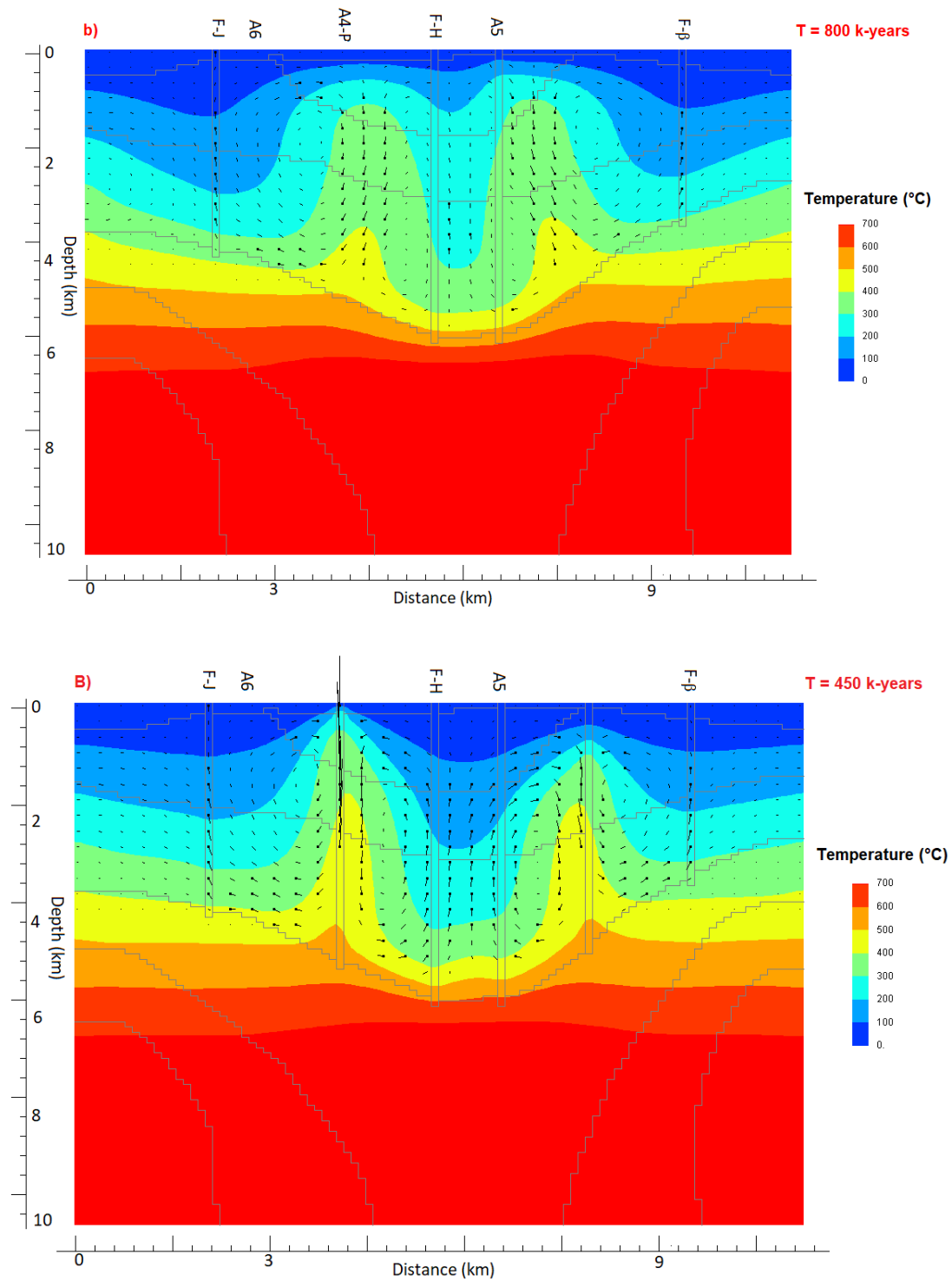


Fig.AC.a). Simulated temperature and flow vectors for b) scenario 2 at time 800 000 years and B) the same scenario 2 with two additional minor faults (6 faults instead of 4 faults) at time 450 000 years. The direction of flow is from the point to the end of straight lines. The length of each line indicates the water vector magnitude, where $1.2 \text{ km} = 10^{-6} \text{ g s}^{-1} \text{ cm}^{-2}$.

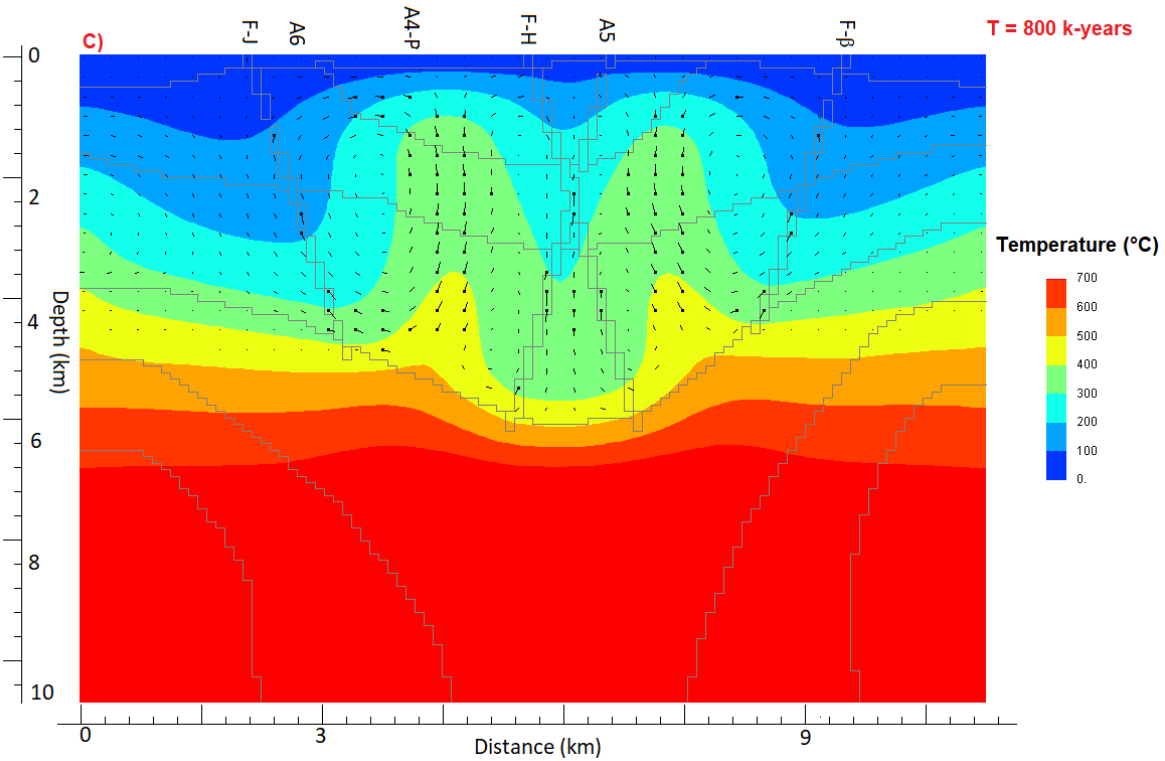
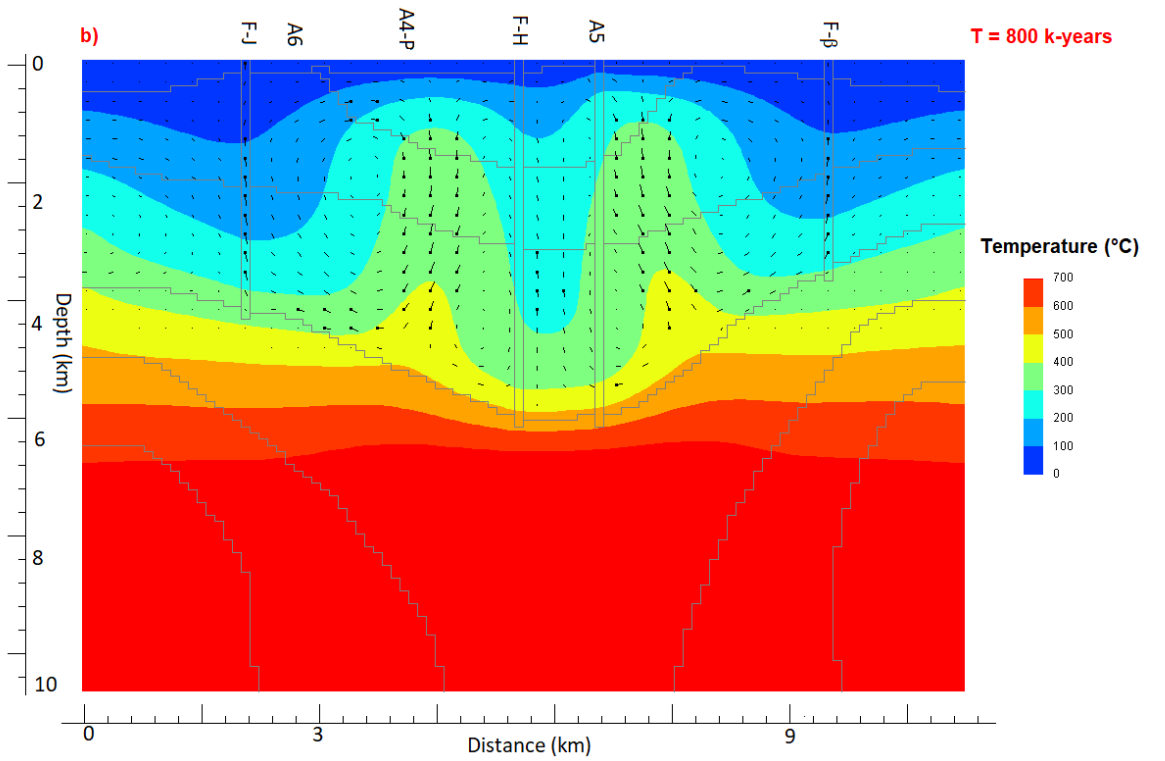


Fig.AC.b). Simulated temperature and flow vectors for b) scenario 2 at time 800 000 years and C) the same scenario 2 with a dipping angle of faults equal to 60 ° at time 800 000 years. The direction of flow is from the point to the end of straight lines. The length of each line indicates the water vector magnitude, where $1.2 \text{ km} = 10^{-6} \text{ g s}^{-1} \text{ cm}^{-2}$.

Table AC.1. Verification of mesh independence for simulation of scenario 1 at the location of geothermal A6 well.

Number of Elements	Temperature at 1480 m Depth T (°C)	Absolute Value of Relative Difference (%)
1 200	390.484	---
3 700	351.897	0.098
5 700	365.068	0.037
8 000	372.647	0.020

Table AC.2. Verification of mesh independence for simulation of scenario 1 at the location of geothermal A4 well.

Number of Elements	Temperature at 1480 m Depth T (°C)	Absolute Value of Relative Difference (%)
1 200	199.784	---
3 700	259.183	0.297
5 700	234.065	0.096
8 000	233.427	0.002